Realistic Lightning Exposure System For Optimized Wind Turbine Reliability

Vogel, Stephan

Publication date:
2018

Document Version
Publisher's PDF, also known as Version of record

Link back to DTU Orbit

Citation (APA):
Vogel, S. (2018). Realistic Lightning Exposure System For Optimized Wind Turbine Reliability. Technical University of Denmark, Department of Electrical Engineering.

Technical University of Denmark

Stephan Vogel

Realistic Lightning Exposure System For Optimized Wind Turbine Reliability

PhD Thesis, November 2017

DTU Electrical Engineering
Department of Electrical Engineering

Stephan Vogel

Realistic Lightning Exposure System For Optimized Wind Turbine Reliability

PhD Thesis , November 2017

Realistic Lightning Exposure System For Optimized Wind Turbine Reliability

Author(s):
Stephan Vogel

Supervisor(s):
Joachim Holbøll, Søren Find Madsen

Department of Electrical Engineering
Centre for Electric Power and Energy (CEE)
Technical University of Denmark
Elektrovej, Building 325
DK-2800 Kgs. Lyngby
Denmark

www.elektro.dtu.dk/cee
Tel: (+45) 45 25 35 00
Fax: (+45) 45 88 61 11
E-mail: cee@elektro.dtu.dk

Release date: November 2017

Class: 1 (Public)

Edition: 1. edition

Comments: This report is a part of the requirements to achieve the Doctor of Philosophy (PhD) at Technical University of Denmark.

PREFACE

This thesis documents the academic progress of three years research related to the interaction of lightning flashes to wind turbines. The main focus was to improve high current testing procedures in order to enhance wind turbine reliability.

The content of this thesis provides state of the art knowledge for wind turbine manufacturers, operators and researchers in the area of lightning testing of wind turbine components. The project was funded by the public Danish foundation Energiteknologiske Udviklings- og Demonstrationsprogram (EUDP) and the private corporation Global Lightning Protection Services (GLPS).

The content of this thesis is to the best knowledge original, apart from the sections which are marked with references and acknowledgments.

First of all, I would like to thank my supervisors Prof. Joachim Holbøll from the Danmarks Tekniske Universitet (Technical University of Denmark) (DTU) and Søren Find Madsen, PhD from GLPS for their excellent cooperation, many technical discussions, and valuable guidance throughout the project.

The second deep appreciation is directed towards the team of GLPS in Hedehusene and Herning, Javier Lopez, Anna Candela Garolera, Lisa Carloni, Jiawei Liu, and Kim Bertelsen which supported me with many conversations, opened my mind to the opportunities of simulation of lightning effects, and treated me as a peer in the premises of GLPS.

I would also liked to thank the people responsible for the technical implementation of the new testing equipment and the laboratory crew of DTU, Victor Rosenberg (GLPS), Gert Lading (GLPS), Tommy Larsen (GLPS), Anders Martinsen (GLPS), and Flemming Juul Petersen (DTU).

Highly appreciated was the possibility to extend the hand-in of the thesis for six weeks and the related funding originating from my group leader Prof. Vassilios Agelidis.

Lastly, my deepest gratitude is sent to my mentors Prof. Ishii from the University of Tokyo and to Dr. Saito from the Central Research Institute of Electric Power Industry in Japan where I was able to study the effects of winter lightning to wind turbines during a four month external stay. The kindness and professionalism experienced in this country was truly exceptional.

ABSTRACT

High current impulse testing of full-scale wind turbine components like blades or nacelles is the optimal tool to verify the proper functionality of a Lightning protection system (LPS) during lightning exposure. The continuous development of the wind power industry increases the physical size of wind turbine components, leading to a higher load for the impulse generator. Due to this reason, a new lightning exposure system was developed which is able to inject realistic lightning currents into full-scale wind turbine components.

Lightning current measurement data from wind turbines and tall structures were gathered in order to define the actual current parameters of a realistic lightning flash. Downward and upward lightning flashes are characterized by significant differences between the current parameters. Testing both types of flashes is necessary to validate the impact of lightning to wind turbines.

The data revealed further that certain wind power plants and towers are exposed to frequent upward lightning attachment. It is investigated why certain wind power plants are affected and it is concluded that four factors increase the upward lightning probability which are the height of the structure, the elevation, the meteorological properties, and the nearby flash density. Special attention is attributed to the meteorological properties of sites and a dedicated section refers to winter thunderstorms and their effects on wind turbines.

The work investigates further the difference between a static tower and a rotating wind turbine in terms of lightning exposure. Space charges created by ionization of air due to high electric field from thunderclouds may influence the likelihood of upward lightning attachment. A Finite Element Analysis (FEA) simulation and laboratory experiments validate the impact of air flow to space charges.

Finally, the design of the novel exposure system is documented. Wind turbine blades are characterized by the largest expected impedance due to their long slender structure. Resistances and inductance are calculated for blades with different LPS solutions and return conductor arrangements. The limitations of high current testing are defined. Finally, the design, control, and validation of the exposure system are described. It is divided into three physical generators that represent the first return-stroke, continuous currents, and the subsequent return-stroke. One of the key elements for the generator is modularity in order to adapt the generator to the load. Selected topics related to the development process and the challenges in the design are discussed.

ACRONYMS

BrasilDat Brazilian National Network.

CFRP Carbon fiber reinforced plastic.
CG Cloud-to-ground.
CLDN Canadian Lightning Detection Network.

DE Detection efficiency.
DF Direction finding.
DTU Danmarks Tekniske Universitet (Technical University of Denmark).
DUT Device under test.
DWC Down conductor.

ELF Extra low frequency.
ELITE Enhanced LIghtning effect TEsting capabilities for optimized wind turbine reliability.
EMC Electromagnetic compatibility.
EMI Electromagnetic interference.
EUCLID European Cooperation for Lightning Detection.

FEA Finite Element Analysis.
FOV Flashover voltage.

GFRP Glass fiber reinforced plastic.
GLD360 Global Lightning Dataset 360.
GLPS Global Lightning Protection Services.

HF High frequency.

IC Intra/inter-cloud.
ICC Initial continuous current.
IEC International Electrotechnical Commission.

JLDN Japan Lightning Detection Network.

LA Location accuracy.
LEMP Lightning electromagnetic pulse.
LF Low frequency.
LINET Lightning detection Network.
LKDS Lightning Key Data System.
LLS Lightning location system.
LMA Lightning mapping array.
LPL Lightning protection level.
LPS Lightning protection system.

LPZ	Lightning protection zone.
NEDO	New Energy and Industrial Technology Development Organisation.
NLDN	National Lightning Detection Network.
PCS	Peak current sensor.
PD	Partial discharge/s.
SAWS	South African Weather Service.
SLIM	Self-consistent leader inception and propagation model.
TOA	Time of arrival.
UV	Ultraviolet.
VHF	Very high frequency.
VLF	Very low frequency.
WRF	Weather Research & Forecasting Model.
WWLN	World Wide Lightning Location Network.

TABLE OF CONTENTS

1 INTRODUCTION

At the 21st yearly meeting of the United Nations, the historic Paris Agreement was formed that aims to form a global response to climate change and to reduce greenhouse gas emission on a global scale [1]. The agreement states that within this century, the global temperature increase shall be limited to $2°C$. As of August 2017, 197 United Nation members have signed and 158 have ratified the Paris Agreement on a national level. The signed countries correspond to more than 85% of the global emissions [2].

One key element for countries to reduce greenhouse gases is to replace fossil fuels such as oil, gas, and coal with renewable energy. The wind turbine industry grows globally and provides a key element for clean renewable energy. New lightweight materials such as carbon fibers enable larger rotor diameters that enable an improved energy output per turbine. As of the end of 2016, the global cumulative installed wind power capacity grew to 486.7 GW. Alone in 2016, 54.6 GW have been newly built with main markets located in China, USA and Germany [3].

The high demand for clean energy opens the markets for international wind turbine manufacturers. The International Electrotechnical Commission (IEC) 61400: Wind turbine standard series provides design guidelines for wind turbine manufacturers in order to define a benchmark to the industry. Most crucial for the social and economic acceptance of wind energy is the reliability and safety of wind turbines. Even though these properties have steadily increased due to advanced engineering methods in the last years, there is still need for technical advances.

According to an investigation of a globally operating insurance company for wind turbines, lightning flashes are the second most common reason for wind turbine failure only preceded by gearbox failures [4]. The high failure rates indicate that lightning protection is still a salient issue for the wind turbine industry which is also addressed in academia [5][6][7].

A lightning flash is an electric spark discharge of several hundreds or thousands of meters in the atmosphere, occurring between the cloud and the ground or between two opposing electrostatic potentials in the cloud. A lightning flash is characterized by one or several high current impulses with a magnitude of up to several hundred kiloamperes and it is driven by a multi-megavolt potential gradient.

Lightning flashes can develop and propagate from the cloud to the ground or vice-versa. Due to their exposed nature and structural height, wind turbines are frequently a lightning termination point on ground. Once a flash is attached, a combination of electromagnetic, thermal, and mechanical stress is imposed on the structure within a fraction of a second due to the transient lightning current. Most often, wind turbine blades are struck by a lightning flash due to their extended dimensions and the resulting electric field enhancement at the tip of the blade [8]. Lightning attachment to nacelles and hubs are also reported, however, with a significant lower rate.

Nowadays, practically every modern wind turbine is equipped with a LPS that is designed to safely conduct the lightning current from the attachment point to the ground. Wind turbines can be damaged due to the direct effects of the lightning current, such as melting or mechanical deformation of conductors, or the indirect effects of the lightning, such as malfunctioning electronic components due to induced voltages. In an attempt to characterize the effects of lightning flashes, the properties of an incident can be described with five current derivatives which are the peak current I_P, the charge Q, the specific energy $\frac{W}{R}$, the rate of rise of current $\frac{di}{dt}$, and the current rise-time T_f. All lightning related damages on wind turbines should, in theory, result from an excess of one or multiple current derivatives, inappropriate LPS design, or lapsing maintenance. Another factor could be that existing lightning protection standards do not represent the natural lightning environment according to the experienced stress of a wind turbine.

In order to identify the reason for failure of wind turbine components, a careful investigation of lightning data seems mandatory. Due to this reason, the first cornerstone of this thesis is to analyze lightning exposure data from wind turbines and tall structures. In the next section, an introduction to the types of lightning exposure data is given.

1.1 Data related to lightning exposure of wind turbines

There are several technologies available in order to quantify the impact of lightning discharges on wind turbines. Direct current measurements via a shunt resistor or a Rogowski coil, provide the most precise information regarding a lightning flash since they are able to capture the current waveform as well as the frequency of lightning attachment to the structure. Current derivatives can be calculated for a single flash or accumulated over the lifetime of a wind turbine. Unfortunately, up till today, only a few measurement campaigns recorded lightning current measurements on wind turbines. One major measurement campaign was performed with the New Energy and Industrial Technology Development Organisation (NEDO) project in Japan [9][10] where 27 wind turbines where equipped with Rogowski coils and lightning flashes were measured over a five year period.

Since direct lightning measurement data from wind turbines are limited, often tower measurements are used to quantify the expected lightning parameters to wind turbines. Pioneering with lightning measurements was Berger in the 1970s who published comprehensive statistics from tower measurements at San Salvatore in Switzerland [11][12][13]. Currently, continuous current measurements are performed, for instance, at the Gaisberg Tower in Austria [14], the Peissenberg Tower in Germany [15], and the Säntis Tower in Switzerland [16].

The second possibility to assess the impact of lightning flashes on wind turbines is by utilizing LLS networks which detect the magnitude and shape of the emitted electromagnetic wave from a current impulse [17][18]. Unlike direct current measurements, typically only the peak current magnitude, the timestamp, and the estimated location of the current impulse are output variables. Lightning data from LLS networks are useful to determine the general lightning activity in a predefined area. Furthermore, lightning pattern of intensified activity can be identified [19][20][21], leading to research related to the reason for such enhanced lightning activity.

Apart from the two mentioned technologies, there are possibilities to classify the impact of lightning flashes on wind turbines by means of Peak current sensor (PCS) cards which are attached in the vicinity of the down conductor in a wind turbine, as well as a range of SCADA integrated sensors operating via a magnetic link. Correlations between the direct measurements (or LLS data) show limited accuracy for these technologies [22][23].

Nevertheless the technology, it is crucial to review and elaborate on the currently available lightning data in order to understand the implications of lightning flashes to the LPS of a wind turbine.

1.2 Towards improved wind turbine reliability

In order to improve the reliability of wind turbine components, the possibility of testing new designs in the laboratory is a crucial step towards a decreased number of damages in the field. The test procedures as well as the test parameters determine directly whether a prospective wind turbine design can withstand lightning flashes in natural conditions. Existing lightning protection standards such as IEC 61400-24: Lightning Protection of Wind Turbines [24] base their reference test values mainly on Berger's dataset of lightning current measurements from static tower measurements [12][13]. This example highlights that there is a need to further research whether lightning exposure performed on towers is in fact comparable to wind turbines.

Another aspect to enhance wind turbine reliability is to further improve the lightning test procedures, where related guidelines are again published in the IEC 61400-24: Lightning Protection of Wind Turbines [24] standard. It should be implicit that lightning testing should represent the natural conditions of lightning flashes as realistically as possible. High-current tests are currently focused on evaluating the effects of the first return-strokes of downward lightning flashes since they are characterized by the highest peak current I_P, charge Q, and specific energy $\frac{W}{R}$. However, also continuous currents and fast subsequent return strokes expose wind turbines to individual characteristic stress components. Furthermore, wind turbines may also be exposed to a high fraction of upward lightning discharges, which are initiated with a long continuous current discharge, followed by a return-stroke sequence. To the knowledge of the author, there is no comprehensive evaluation regarding the failure modes of lightning termination systems of wind turbine blades when exposed to different combined sequences of current waveforms. Approaches towards this direction were performed on small metallic test samples by Tobias [25], Bellaschi [26], Iwata [27], and Kern [28]; however, it is difficult to conclude from the results. One of the reason for a missing evaluation may be the lack of adequate and affordable testing equipment for sequential lightning current exposure.

At this point, it should be noted that the IEC 61400-24: Lightning protection for wind turbine standard is currently under revision and the recent committee draft [29] of the standard includes a test description for long duration current discharge in winter lightning. The new version of the standard aims to be released in 2018.

A third method how to improve wind turbine lightning protection design relates to the transition from partial towards full-scale wind turbine component lightning testing. The benefits and challenges of this approach shall be discussed in the next Section.

1.3 Full-scale high current wind turbine testing

High current testing in the laboratory is an essential tool to help understanding the origin of physical damage caused by lightning flashes to wind turbine components. There are two test procedures for performing high current tests as defined by IEC 61400-24 [24]. The first is the arc entry test where the generator electrode is placed 50 millimeters above the counterpart electrode of the test object. Due to the open arc, the lightning termination system is stressed and superficial damages or punctures can be investigated. The second test is the conducted current test. In this test, the generator electrode is directly connected to the Device under test (DUT) and no open arc is formed. This test is used to verify the mechanical and physical integrity of down conductor systems or connection components which are not exposed to the influence of open arcs. Furthermore, the test can show bonding issues in wind turbine design.

The term full-scale relates to the physical size of the DUT and refers to an entire blade or nacelle. In the next years, it is expected that wind turbine blades reach a length of up to 100 meters and nacelles will be characterized by generation units of up to ten megawatt. The cooperation partner GLPS has performed full-scale high current tests of multi-megawatt nacelles and blade lengths exceeding 70 meters.

There are several benefits in testing an entire full-scale wind turbine component with high current impulse instead of evaluating only a section. For instance, in the case of a wind turbine blade, the voltage distribution between the down conductor and a semi-conductive carbon fiber spars can be evaluated. If a flash-over appears inside the blade during lightning impact, additional bonding between conductive parts need to be established. Furthermore, the position and functionality of sensors during lightning impact can be validated. High current testing of nacelles can be used to validate current distribution simulations. Additionally, the nacelle can be powered-up by an external generator and the functionality of electronic equipment inside the nacelle can be validated. Lastly, voltages induced in cables close to the main discharge part in the nacelle can be recorded and potentially rearranged.

The challenges of full-scale testing are the physical dimensions of the DUT and the resulting high electrical impedance. Especially blades are characterized by large inductance values due to their physical size. This limits the peak current magnitude and decreases the current rise-time of the current impulse. As a rule of thumb, the self-inductance of a round solid conductor with a radius of a 7.8 millimeter can be approximated by $L_s = 1.1uH$ each meter [30]. The accumulated inductance of the DUT and the current return path determines the resulting properties of the current waveform. Similar to the concept of a coaxial cable, the total circuit inductance can be reduced through optimization of the location and the position of return conductors.

Compared to the inductance, the influence of stray capacitance between blade and ground is negligible if the current time to peak remains in the order of several microseconds or more [31]. Capacitive effects appear to influence the current and voltage waveform with current time-to-peak values of 1 microsecond or lower. The resistance of wind turbine blades typically also increases in larger test samples which reduces the specific energy in the test sample.

In the future, it is expected that full-scale lighting tests are the new mean of testing final wind turbine blades and nacelles, however, already today, lightning testing equipment is incapable of injecting the current waveform as defined by IEC 61400-24 [24]. In the next section, the objectives and the structure of this PhD thesis are outlined.

1.4 Objectives and structure of this thesis

The overall aim of the present thesis is to form the academic base for the development process of a realistic lightning current test system for full-scale wind turbine components which will enable the cooperation partner GLPS to test next generation wind turbine nacelles with output powers of five to ten megawatt and wind turbine blades up to 100 meters. Such a test system is the foundation for future high current impact verification which will ultimately enhance the reliability and safety of wind turbine components.

In order to approach a structured realization of the project, the work is divided into the following cornerstones.

The first academic focus is to determine the current waveform that a realistic test system needs to generate and to review if the present lightning protection standard provides adequate representation of the lightning current waveform. The research question could be stated as follows:

> *Which current parameters and waveforms define a realistic lightning current impulse system?*

In order to approach an answer to this question, in Chapter 2, lightning data recorded with Rogowski coils or shunt resistors are evaluated and compared. Unfortunately, there are only few lightning current measurement campaigns performed on wind turbines. Due to this reason, current data from tall towers are also included as a source for this investigation.

The second focus of this thesis, debated in Chapter 3, is related to lightning exposure of wind turbines. The predominant type of lightning, the attachment frequency, and why certain turbines are more exposed than others are crucial factors to determine where a prospective damage is expected. These factors should also be incorporated in a realistic impulse current system by adapting the amount of tests and the location of lightning attachment to the expected exposure of a wind turbine.

> *Which external factors determine the frequency, type, and magnitude of lightning discharges to wind turbines and what are the consequences for the lightning protection system?*

In order to answer this question, lightning data mainly originating from electromagnetic measurement systems are evaluated since they provide a broader view of a thunderstorm and are available for large areas. Each detection technology is characterized by individual performance indicators and the data need to be interpreted accordingly. Meteorological parameters are a key component to differentiate between summer and winter thunderstorms. The characteristics and effects of winter lightning are further discussed in order to reach a conclusion.

The third focus of this thesis, documented in Chapter 4, relates to the impact of blade rotation of a wind turbine. There is an academic discussion whether wind turbines are more exposed to lightning attachment compared to static towers since the shielding effect caused by a removal of corona space charge is mitigated [32]. If such a difference exists, there should be another debate in how accurate lightning current data measured on towers represents lightning observations on wind turbines. This would have eventually also an impact on the current parameters for the new lightning current impulse system. To break-down the topic, the following research question has been defined.

> *Does air flow around the receptor of a rotating wind turbine blade affect the electric field due to a shift in space charge concentration?*

The research question was approached by a literature review of corona modes and how they distribute below a thundercloud. An overview between the situation on the tip of a static tower and a wind turbine is provided. A finite element simulation is performed which evaluates the impact of wind to the space charge concentration. Subsequently, a laboratory experiment is performed which validates the impact of the air flow.

Finally, based on the input from the previous chapters, the design and development of the high current impulse generator is documented as the last cornerstone of the thesis in Chapter 5. A research question can be defined as follows:

> *What are the technological means to realize a high current impulse generator for realistic lightning current verification?*

The first step towards the novel test generator is to estimate impedance of the expected test objects. Wind turbine blades are characterized by the highest expected stray inductance value due to their elongated shape. Therefore, they are considered as the most challenging load for the test generator. Subsequently, the limitations of high current testing are provided to get an overview of the design space. Finally, the design concept of the generator is given and validation of the concept is provided by laboratory measurements.

This PhD project is a part of the so called Enhanced LIghtning effect TEsting capabilities for optimized wind turbine reliability (ELITE) project which was funded by the Danish Ministry of Energy, Utilities and Climate within the scope of EUDP. The aim of the project was to develop a new full-scale lightning test system for validating the LPS performance of full size wind turbine components like blades and nacelles. The project was initialized in August 2014 in a cooperation between DTU and GLPS and completed with a full-scale demonstration of the new test system in October 2017. An overview of the different work packages and further information regarding ELITE are provided in Appendix A.

2 CURRENT PARAMETERS OF LIGHTNING DISCHARGES

The first step towards the design of a realistic lightning exposure system for wind turbines is to review and collect data regarding lightning discharges to wind turbines and tall structures.

The properties of a lightning flash can be described with a few key current derivatives such as the peak current I_p, the charge Q, the specific energy $\frac{W}{R}$, the duration T and the current steepness $\frac{di}{dt}$. There are various technologies available to record such information regarding lightning, each of them characterized by individual performance characteristics. For instance, Rogowski coils enable the measurement of the current waveform from a lightning discharge and are easy to be installed in a LPS of a wind turbine but are inaccurate when measuring current components below the lower cut-off frequency of the coil. This can introduce measurement errors during long duration continuous currents in lightning flashes. A low ohmic shunt resistor, on the other hand, provides an accurate lightning current measurement but has the disadvantage to be difficult to integrate in a LPS of a wind turbine since the entirety of the current needs to pass though the resistor. Lightning data accumulation is expensive and time demanding. Especially current waveform data are not a public asset and often protected by non-disclosure agreements that prevent the data from being published.

This chapter is structured as follows. At first, the considerate reader is presented with background information regarding the process of cloud electrification, different types of lightning flashes, as well as their characteristic current components. Subsequently, a meta data analysis regarding lightning current parameters is presented which concludes in a section describing the requirements of the new lightning test system.

2.1 The lightning discharge

This first section introduces the reader to the fundamental principles of lightning discharges. General theories of thunderstorm electrification are explained. Subsequently, the terms downward and upward lightning are introduced and properties of these discharges are provided. The differences between positive and negative polarity are emphasized and the different trigger mechanisms for upward lightning are highlighted. This section aims to be an introductory section especially valuable for non-professional interested readers.

2.1.1 Cloud charging mechanisms

A lightning discharge is a conductive plasma channel that develops as the result of a high electrostatic potential between cloud and ground. There are several hypotheses how charged ions are created in such quantities that an electrical breakdown of air can form. The two main theories are the convection mechanism theory and the graupel-ice mechanism theory. The interested reader can find more information on the topic in [33]. Here a short summary is given. The first theory is based on the mechanics that during fair weather, positive space charge is lifted to the top of a growing cumulus cloud by warm air currents (updrafts). Positive accumulation of ions attract nearby negative ions, which are created beforehand by cosmic ray radiation. On the boundary of the cloud, the negative ions fall to lower altitudes by means of downdrafts, caused by cooling and convective circulation. The lowered negative charged particles create an electric field on ground, which enables the creation of partial discharges on the ground, leading to the creation of positive space charge which propagate towards the cloud and creates the typical tripolar charge structure of a cumulonimbus cloud. In the second theory, the graupel-ice mechanism, charges are created between precipitating particles (graupel) and cloud particles (small ice particles). In essence, falling particles create ions due to collision between particles (also called rimming). The temperature in the cloud is crucial to determine which polarity is created. Laboratory experiments demonstrated that graupel particles acquire a negative polarity below a specific reversal temperature T_R, whereas the particles acquire a positive polarity if the temperature is above T_R [34]. The threshold for T_R is between $-10°C$ and $-20°C$. Apart from the temperature, other factors such as cloud water density, ice crystal diameter, relative velocity of the collision, and chemical impurification have an impact on the amount of charge and the polarity. There is still no common consent in the scientific community on how the collision processes are interacting exactly and which properties determine the magnitude and polarity of the thundercloud in the different cloud layers. Agreement among the scientists exists regarding the idealized model of a cumulonimbus thundercloud, which initiates the most of the lightning discharges during summer thunderstorms. The model is characterized by a typical tripolar charge structure with a positive charge layer of approximately $40C$ in a height of $8 - 15km$, a negative charge layer of approximately $-40C$ in a height of $5 - 8km$, and a smaller positive charge layer of around $3C$ in a height of $4 - 5km$. In depth information about charging processes and charge distribution in clouds can be found, for instance in [35].

The location where the first streamer and consequently leader is created and where this discharges propagates to, determines the terminology of the lightning discharge. In the literature, three different cases are differentiated:

1. The discharge starts in the cloud and the discharge develops towards the ground. The so called downward lightning strike is termed as Cloud-to-ground (CG) lightning.
2. The discharge starts on the ground and the leader develops towards the cloud. The so called upward lightning strike is termed also as CG lightning.
3. The discharge starts in the cloud and the leader develops towards the opposite polarity in the cloud which is known as Intra/inter-cloud (IC) lightning.

Each type of lightning discharge has characteristic current parameters, as further discussed in section 2.2. Ground truth current measurements data are available for downward and upward lightning discharges, whereas current parameters from IC lightning may be inferred from measurements of electromagnetic waves. Before providing detailed parameters of the individual characteristic current components, an overview of the two lightning discharge types is given.

2.1.2 Downward lightning

Once a sufficiently high charge is apparent in the cloud, the electrical breakdown strength of air may be exceeded leading to small partial discharges in the cloud, which may form around ice particles or on sharp objects on the ground. A further increase in the electrical field can result in the formation of a streamer which may develop into a lightning leader. By definition streamers are long filamentary partial discharges of air which are driven by space charges. The magnitude of ions in the head of the avalanche impacts the local electric field around the boundaries of the plasma which starts to dominate the ionization process of the discharge instead of the background electric field [36]. A leader is the subsequent mode of a streamer in long gaps and is characterized by sufficient charge to heat-up the stem above a critical temperature, which is necessary to sustain the discharge [37] [38]. The radius of the plasma in a lightning leader is estimated between 0.1 m and 0.5 m [39]. The polarity of the charge center in which the leader forms determines the polarity of the flash. On the way towards ground, the leader may form several branches in air. Negative leaders show typically more branching compared to positive lightning leaders. Typically, a negative leader propagates in steps of between 10 to 100 meters with about $10\mu s$ - $50\mu s$ delay between the expansions [35]. Positive lightning leaders propagate in a rather continuously manner. When the lightning leader approaches the ground, the electrical field increases and typically one or several answering leaders develop from the ground [33]. The origin of the answering leader is often a protruding object where the electric field is concentrated due to the shape of the object. The length of the answering leader can be a few meters [40] [41] up to several hundred meters [42]. Answering leaders starting from tall objects are typically longer compared to leaders on flat ground. The junction point where sky leader and the answering leader meet establishes an electrical connection between the two plasma channels. This can be seen similar to a switch connecting a charged capacitor bank. From this point, two return-stroke waves are generated which propagate towards the ground and the cloud [33]. The current wave propagating towards the ground requires to travel a much smaller distance compared to the upwards directed wave. On ground, a part of the wave (determined by the characteristic impedance of the flash channel and the ground) is reflected. The reflected wave also starts to propagate upwards and catches up with the initial created upward propagating wave. The resulting current wave travelling upwards represents the current magnitude of the first return stroke of a downward lightning strike. The speed of the return-stroke propagation is between $5.5 \cdot 10^7 \frac{m}{s}$ and $2 \cdot 10^8 \frac{m}{s}$, whereas leader speeds are between $8 \cdot 10^4 \frac{m}{s}$ - $1.1 \cdot 10^6 \frac{m}{s}$ (negative stepped leader) [33]. After the first return stroke which usually takes several tens to hundreds of microseconds, the lightning flash may end or continue with a constant charge displacement between the cloud and the ground which is called continuous current. The charge displacement triggered by the first return stroke has also an effect in the potential distribution inside the cloud. IC discharges, several kilometers away from the return stroke channel, may be triggered after return strokes. In literature, these IC discharges are named "K-changes" or sometimes "recoil leaders". If such a IC discharge connects to the return stroke channel, the ionized particles contained in the plasma are conducted towards the ground. The state of the return stroke channel determines whether an M-component or a dart leader is created. M-components are current surges with moderate current rise time whereas dart leaders trigger subsequent lightning strokes with a high current rise time. M-components are created if the return-stroke channel from the first discharge is still conducting current (continuous current mode). In this case, there is no subsequent return stroke sequence, however, the incident current wave may be reflected from the ground. In case the first return-stroke channel is extinguished, a so called dart leader may be created. Usually, the dart leader follows the path of the previous first-return stroke in a continuous manner; however, it is also possible that the dart leader forms a new channel and propagates similar to a stepped leader [35]. As soon as the dart leader approaches the ground, similar physics as in the first return stroke sequence appears and a return-stroke sequence is initiated. Typically, subsequent return stroke currents are characterized by a fast $\frac{di}{dt}$ and a short duration as further discussed in Section 2.2. There can be more than 10 subsequent return stroke sequences following a first return-stroke current. Typical median negative downward flash durations are approximately 60 milliseconds in duration [43]. An illustration of the current waveform from a negative downward lightning flash is shown in Figure 2.1a.

Positive lightning can be characterized by a return-stroke sequence similar to negative downward lightning as depicted in Figure 2.1b. Positive lightning discharges show rarely subsequent lightning activity and are possibly followed by long continuous currents. Another occurrence of positive lightning is described in [33], where a very long negative upward leader is created and the connection between answering leader and sky leader happens several hundred meters above the ground. The current waveform of the latter lightning type is characterized by a very long current rise time which can be associated with a M-component current pulse. Berger's lightning current parameters [12] for positive downward lightning did not differentiate between the two types of positive lightning. Unfortunately, there are no comprehensive datasets of positive downward lightning currents available except of the data by Berger. The median positive downward flash duration is 94 milliseconds [43].

In summer thunderstorms, it is assumed that 90% of all discharges lower negative charges to ground (negative stepped leader, positive answering leader, negative return-stroke) whereas only 10% lower positive charge to the ground (positive leader, negative answering leader, positive return-stroke) [33].

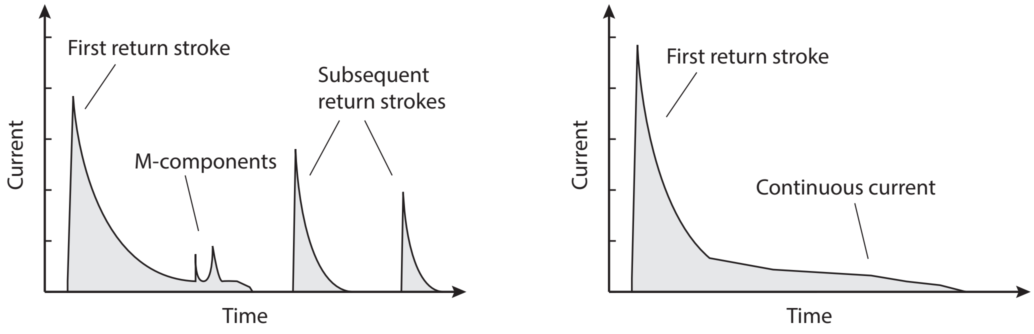

(a) Negative downward lightning (b) Positive downward lightning

Figure 2.1: Illustrations of current waveform from typical positive and negative lightning flashes

2.1.3 Upward lightning

Upward lightning discharges are created if the electric field on ground exceeds the breakdown strength of air over a critical distance [33]. Furthermore, a minimum charge criterion of $C = 1\mu C$ must be contained in the streamer head in order to fulfill the streamer to leader transition [37]. An upward lightning leader propagates from the ground to the cloud with approximately $8 \cdot 10^4 \frac{m}{s}$ to $4.5 \cdot 10^5 \frac{m}{s}$.

Upward lightning always starts with an upward lightning leader that propagates towards the cloud. The current waveform is characterized by an Initial continuous current (ICC) of a few tens to thousands of amps due to the propagation of the leader [14]. The waveform is possibly superimposed with M-components. The current duration of the initial phase can span several milliseconds. After the current ceases, there may be subsequent return-strokes preceded by dart leader sequences. M-components and dart leader/subsequent return-stroke sequences are similar as described in Section 2.1.2. An illustration of the current waveform is depicted in Figure 2.2.

Wang et al. [44] differentiated between two different upward lightning types by means of electric field measurements. The first one are self-initiated upward lightning discharges, which develop during a constant electric field. The second type are upward lightning discharges that are preceded by nearby lightning activity. Wang et al. concluded with his work that upward lightning flashes can be created irrespective of whether the electric field is built up slowly or rapidly. Self-initiated upward lightning discharges require a very high electric field on ground, which is characteristic for low-altitude thunderclouds seen during winter thunderstorms, whereas other-triggered lightning events are reported during winter [44] and summer thunderstorms [45][46].

Upward lightning leaders may start from several locations simultaneously [23]. Typically, only one leader connects to the charge regime in the cloud. As soon as one leader branch establishes a connection, the electric field decreases and the remaining leaders cease to develop. These stagnated leaders are also called aborted leaders. During the collapse of the leader, the charge used for expanding the leader flows back through the lightning channel to the starting point of the flash [47]. An evaluation of the consequences of these back flow currents in terms of EMC interference to electrical systems (for instance, in wind turbines) is missing in the scientific literature.

Advancements in the classification of upward lightning discharges were made from direct tower measurements at the Gaisberg Tower in Austria [14]. The author differentiated between three different types of upward lightning discharges:

- Initial continuous currents only (ICC_{only})
- Initial continuous currents with pulses (ICC_{pulses})
- Initial continuous currents with return-strokes (ICC_{rs})

ICC_{only} pulses are defined as upward lightning discharges with pure initial continuous currents.ICC_{pulses} are upward lightning discharges with M-component pulses superimposed to the initial continuous current. ICC_{rs} have subsequent return-strokes sequences in the current waveform and, additionally, may have M-component pulses. The individual types of upward lightning are important since they have distinct different characteristics in the detection of lightning flashes with LLS and Rogowski Coils. In the case of the Gaisberg Tower, 30% of flashes are characterized as ICC_{rs}, 22% of flashes are ICC_{pulses}, and 48% are ICC_{only}. The ratio between the types of upward lightning strokes may differ between locations. Charge amounts for all types are significantly lower during the summer months compared to winter months.

Current properties of upward lightning discharges are well known due to various measurement towers around the world which mainly intercept upward lightning discharges (exception is Tokyo Skytree, Japan). At this moment (2016), continuous tower measurements are performed in Germany [15][48][49], Austria[50], Switzerland [51][52], and Japan [53][54] which record the waveform of the current. Upward lightning discharges are typically characterized by a low peak current I_p and a long duration T. Flashes with a high charge and specific energy are observed in winter lightning areas, as described in Section 3.6. To the knowledge of the author, there are no reported differences between current parameters of self-initiated or other-triggered lightning events. For information about current parameters of upward lightning flashes can be found in Section 2.2.3.

2.2 Lightning current parameters

A lightning discharge is a transient high current impulse which creates an electromagnetic field along the discharge channel and in the struck object. Each flash varies in intensity and in particular downward and upward flashes have distinct different discharge characteristics. As discussed in section 3.1, wind turbines are exposed to both flash types.

This section provides statistical information about downward and upward lightning parameters. Current parameters from LLS are not included in this chapter. Before the data are presented, an overview of the characteristic current derivatives is provided which are crucial to define the impact of a particular lightning flash. Thereafter, current parameters of downward and upward lightning from measurements on static towers from the literature are presented. A dedicated section for current parameters measured in wind turbines lists the available data for wind turbines. Subsequently, the contemporary test current waveform characteristics from the IEC 61400-24: Lightning Protection of Wind turbine standard are given. The section is concluded with an argumentation regarding the differences between current measurement from static towers, wind turbines and the IEC 61400-24 standard. Finally, the proposed current parameters of a realistic lightning current exposure system are defined.

2.2.1 Current derivatives

In engineering applications, it is necessary to evaluate the characteristics of a discharge in order to estimate the consequences of the event. For this reason, key parameters are derived from the current measurement of a discharge. In this section, the four most important key parameters are highlighted and the immediate consequences connected to the parameter are discussed. All of the mentioned parameters are to some degree interconnected since the current waveform itself is responsible for possible damages. The information of this section is mainly based on the IEC 62305-1 Ed.2: Protection against lightning - General

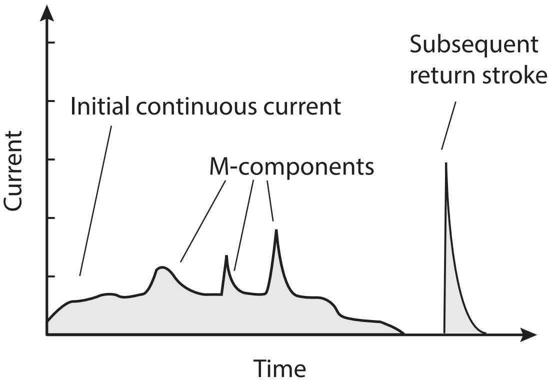

Figure 2.2: Typical upward lightning flash

principles [55]. The current derivatives discussion is included in this section, in order to debate the implications of different lightning types later in the thesis.

2.2.1.1 Peak current

The peak current value is defined by the amplitude of a given current waveform and is related to the maximum electromagnetic force between two conductors with following relationship:

$$F(t) = \frac{\mu_o}{2\pi} i^2(t) * \frac{l}{d} \tag{2.1}$$

where $F(t)$=electromagnetic force [N], i=current [A], μ_0=magnetic permeability of vacuum, l=length of conductor [m], and d=the distance between the wires [m]. In a LPS of a wind turbine, often several parallel discharge paths exist where the current is distributed in a resistive-inductive network. In the case of a wind turbine, for instance, the blade may contain a metallic down conductor and a semi-conductive carbon fiber layer, whereas the tower is characterized by a steel network. Mechanical fixations need to withstand the transient force impulse which is associated with the square of the current. The instant of maximum current also represent the point of maximum force impact. In general, metallic LPS may be exposed to elastic and plastic deformation whereas the former is a reversal process. An important aspect here is the eigenfrequency of the component; however, natural lightning impulses are usually characterized by much smaller natural frequencies compared to the mechanical eigenfrequencies of LPS. Deformation due to electromagnetic forces may occur in soft metallic materials like copper or aluminum where edges and loops may be displaced.

Apart from the force on conductors, the peak current is linked, together with the current steepness, to the acoustic expansion in the surrounding media of the arc. The metallic conductor system is unlikely to be influenced by this effect; however, adjacent composite materials may loose mechanical integrity.

In the industry, the quantity peak current is often used as a general assessment of the severity of a discharge which can be misleading. The reason for this circumstance may be the intuitive understanding and the wide accessibility of the parameter through LLS. Nevertheless, to relate to a specific damage because of a high peak current should never be the only mean to validate a damage. Very high peak currents can be characterized by small impulse energy. On the other hand, a lightning flash with a small peak current can have high energy content. Laboratory experiments show that high peak current lightning impulses with low duration cause less melting damage on the LPS compared to low peak current magnitudes with a long duration as demonstrated by Hernandez [56].

Therefore, a damage assessment should not be performed solely by the peak current magnitude. Deterministic for a damage may also be the following current parameters, as well as the general condition of the LPS.

2.2.1.2 Maximum current steepness

The maximum current steepness $\frac{di}{dt}$ is related to induced voltages in the electronic system of a component. While the lightning current propagates towards earth, the electromagnetic energy stored in the stray inductance of the LPS may be induced in loops and circuits. This can cause overvoltages in low voltage equipment.

$$U_i = M\frac{di}{dt} \tag{2.2}$$

where U_i is the magnitude of induced voltage in the system, M is the mutual inductive coupling of two circuits, and $\frac{di}{dt}$ is the transient current derivative.

To protect a circuit from Electromagnetic interference (EMI) several measures can be taken. The current steepness of the lightning stroke itself can not be varied; however, optimized lightning down conductor placement can prevent overvoltages in sensitive areas. Electromagnetic 2D/3D simulation can be performed to compute the current path in a component and optimize the routing of cables and bonding positions. Furthermore, shielding of cables and boxes enhances EMI performance. Additionally, low voltage circuits, which are frequently exposed to EMI, can be protected with surge arresters or over-dimensioned in terms of voltage capabilities in order to ensure proper functionality.

2.2.1.3 Charge

The charge $Q = i(t) * dt$ is mainly responsible for the erosion at the current injection and exit point. In the case of a wind turbine, the points are usually the tip receptor and the grounding electrodes. Given that the surface area of the grounding electrode is far higher than that of the tip receptor, the latter is exposed to a higher current and charge density and the impact of erosion is dominant at that point.

The magnitude of the charge determines, together with the anode/cathode voltage, the energy of the arc which affects the melting of the conductor. The voltage drop over the arc $u_{a,c}$ is rather constant and has usually a value of a few tens of volts.

$$W = \int u_{a,c} i dt = u_{a,c} \int i dt = u_{a,c} Q \tag{2.3}$$

Assuming that all the energy created in the arc is used for melting of material, the volume of melted material can be calculated. The equation below estimates the dissipated volume; however, the loss is slightly overestimated.

$$V = \frac{u_{a,c}Q}{\gamma} \frac{1}{C_w(\Theta_s - \Theta_u) + C_s} \tag{2.4}$$

where V is the volume of melted metal $[m^3]$, $u_{a,c}$ is the anode or cathode voltage drop $[V]$, Q is the total charge of the lighting $[C]$, γ is the material density $[\frac{kg}{m^3}]$, C_w is the thermal capacity $[\frac{J}{kgK}]$, Θ_s is the melting temperature $[K]$, Θ_u is the ambient temperature $[K]$, C_s is the latent heat of melting $[\frac{J}{kg}]$.

The impact of the current waveshape was also analyzed by Kern [28]. The author exposed several metal sheets with varying thickness and materials to impulse currents (typical: $I_p = 200kA$, $Q = 100$, $\frac{W}{R} = 10\frac{MJ}{\Omega}$) and DC-components ($Q = 200C$, $T = 0.5s$) and measured the loss of volume to the sample. Impulse currents were observed to cause wide-spread melting over a large area (1 cm up till 10 cm) due to the high specific energy of the arc; however, the depth of damages was very low (0.1 - 0.4 mm) depending on the material of the sheet. Interestingly, the loss of volume was independent of the polarity of the discharge, except for steel. Long duration DC discharges, on the other hand, exposed the metal sheet to a smaller melted area (1 cm - 2 cm) and deeper penetration into the test sample. Temperature measurements revealed a maximum temperature of up to $1000°C$ whereas impulse current caused temperature rises of typically $100°C$. The author further investigated the impact of the distance between electrodes to the produced damage. The results of the observation show that damages increase drastically if the counter electrode is closer to the test sample. According to his research, the existence of plasma rays enhances the effect of melting to the test object; however, in natural downward lightning the distance between the potentials are immense and there is no influence of plasma rays in the discharge. For the purpose of this experiment, the author used isolated electrodes to avoid the influence of plasma rays as best as possible.

Similar investigations regarding the impact of the impulse and the DC component of the current waveform were performed, for instance, by Bellaschi and Baranov [26][57].

2.2.1.4 Specific energy

The specific energy, also known as action integral, is used as a proxy to determine the ohmic heating due to lightning impact. The unit of the parameter may be expressed as $\frac{J}{\Omega}$ or A^2s. Similarly to the force calculations on two conductors, the specific energy is calculated with the square of current.

$$\frac{W}{R} = \int i^2 dt \tag{2.5}$$

Also the local resistance of the DUT determines the point of maximum heating along the LPS. Special attention should be given to fixtures and clamps along the conducting path since local resistivities may be enhanced. Also cross-sectional considerations are crucial to prevent overheating since the specific temperature is determined by the current density.

Since lightning discharges are fast transient processes, the skin effect impacts the current distribution which reflects on the current density. Heating of metallic down conductors can be controlled with sufficient cross-sectional diameter A specific for used material. For instance, $10\frac{MJ}{Ohm}$ applied to one meter of a $50mm^2$ conductor leads to a temperature rise of $\Delta T = 52°C$ with aluminum whereas the same properties lead to a temperature rise of $\Delta T = 940°C$ for stainless steel.

2.2.2 Current parameters of downward lightning measured on static towers

Statistical information about current parameters of downward lightning flashes can be found from various sources. In order to distinguish the parameters between downward and upward lightning, current measurement techniques which capture the current waveform need to be employed. At stationary towers, usually the voltage is measured across a shunt resistor in order to derive the current waveform. Recently, also specialized Rogowski coils are introduced for lightning current measurement which are able to measure the frequency spectrum of a lightning impulse [58].

The most comprehensive lightning data acquisition was performed by Berger at Mount San Salvatore, Switzerland [12]. The author based his work on direct measurements with a shunt resistor and separated his data into first negative strokes, first positive strokes, subsequent strokes, and flash duration. Table 2.1 and 2.2 show the cumulative probability distribution of the 5%, 50% and 95% values, separated by stroke type. For his analysis, the author used up to 101 first negative strokes, 135 subsequent strokes and 26 positive strokes. The actual cumulative distributions of peak current I_p, charge Q, specific energy $\frac{W}{R}$, rate of rise of current $\frac{di}{dt}$, and front duration of the impulse T_f can be found in Appendix B. By direct comparison between the graphs in Appendix B and the values of Table 2.1 and 2.2, it can be seen that data in the Tables are originating from the linearized curves. This has the effect that minor discrepancies exist between the tabulated values and the actual data. For instance, the five percentile value of the peak current of the first stroke is given in Table 2.1 with 80 kA, however, comparing it with the graph in the Appendix B, the peak current value is rather 70 kA.

The highest peak current amplitude which was ever measured at a tower was determined by Berger K. with a magnitude of 270 kA [11]. The observation period for this measurement was 1946 - 1971.

Since the measurements of Berger, several lightning measurements on tall structures at different places on earth were performed including Italy, South Africa, Japan, Brazil, Switzerland, Austria, and Germany. The results of the measurements are gathered and further discussed in the comprehensive CIGRE report: Lightning Parameters for Engineering Applications [60]. If all global data measurements are compared, the median return-stroke peak current for negative first strokes is about 30 kA and for subsequent return-strokes about 10-15 kA. Positive downward flashes report slightly higher median peak current amplitudes of approximately 35 kA, however the data population of positive lightning is rather low globally. As can be seen by Berger's data, the positive peak current is characterized by a high statistical 5% magnitude of up to 250 kA from the

Table 2.1: Downward lightning stroke parameter for negative flashes. Data: [12], Table adapted from [59].

Parameter	Units	Sample Size	% Exceeding Tabulated Value		
			95%	50%	5%
Peak Current (minimum 2kA)	$[kA]$				
First strokes		101	14	30	80
Subsequent strokes		135	4.6	12	30
Charge (total charge)	$[C]$				
First strokes		93	1.1	5.2	24
Subsequent strokes		122	0.2	1.4	11
Complete flash		94	1.3	7.5	40
Impulse charge (excluding continuing current)	$[C]$				
First strokes		90	1.1	4.5	20
Subsequent strokes		117	0.22	0.95	4
Front duration (2kA to peak)	$[us]$				
First strokes		89	1.8	5.5	18
Subsequent strokes		118	0.22	1.1	4.5
Maximum di/dt	$\frac{kA}{us}$				
First strokes		92	5.5	12	32
Subsequent strokes		122	12	40	120
Stroke duration (2kA to half peak value on the tail)	$[us]$				
First strokes		90	30	75	200
Subsequent strokes		115	6.5	32	140
Action integral ($\int i^2 dt$))	$\frac{J}{\Omega}$				
First strokes		91	$6.0 \cdot 10^3$	$5.5 \cdot 10^4$	$5.5 \cdot 10^5$
Subsequent strokes		88	$5.5 \cdot 10^2$	$6.0 \cdot 10^3$	$5.2 \cdot 10^4$
Time interval between strokes	$[ms]$	133	7	33	150
Flash duration	$[ms]$				
All flashes		94	0.15	13	1110
Excluding single-stroke flashes		39	31	180	900

Table 2.2: Downward lightning stroke parameter for positive flashes. Data: [12], Table adapted from [59].

Parameter	Units	Sample Size	% Exceeding Tabulated Value 95%	50%	5%
Peak current (minimum 2kA)	$[kA]$	26	4.6	35	250
Charge (total charge)	$[C]$	26	20	80	350
Impulse charge (excluding continuing current)	$[C]$	25	2.0	16	150
Front duration (2kA to peak)	$[us]$	19	3.5	22	200
Maximum di/dt	$\frac{kA}{us}$	21	0.2	2.4	32
Stroke duration (2kA to half peak value on the tail)	$[us]$	16	25	230	2000
Action integral ($\int i^2 dt$)	$[\frac{J}{\Omega}]$	26	$2.5 \cdot 10^4$	$6.5 \cdot 10^5$	$1.5 \cdot 10^7$
Flash duration	$[ms]$	24	14	85	500

cumulative probability distribution (80 kA for negative first strokes). His dataset is based on 101 negative and 26 positive downward flashes which leads to an approximate 25% positive flashes ratio. Other publications which investigate a mixed-global dataset of flashes observed a negative/positive flash ratio of roughly 10% [61]. Therefore, it may be noticed that Berger's location in Switzerland experienced a higher than usual ratio of positive strokes. Furthermore, Berger measured only two positive lightning flashes which exceeded a current amplitude of 120kA, which had a magnitude of 205 kA and 270kA [11], however, from Berger's dataset, standardization committees derive their lightning protection requirements [24][55].

More recently, direct current measurements were also performed in South-Eastern Brazil [62]. In total 79 flashes were registered. Only two positive downward lightning flashes were recorded and a cumulative probability was presented for negative first-strokes. The highest peak current did not exceed 100kA in this investigation. Compared to the measurement of Berger, Brazil reports slightly higher median peak current values with 45 kA and 18 kA, respectively.

Another measurement campaign measured downward lightning currents with Rogowski coils on transmission line towers in Japan [63]. In total 120 current waveforms were measured from 1994 - 2004 including three measurements exceeding 100kA. The author correlated that greater current amplitude results in a longer front duration.

All lightning current parameters for wind turbines, which are listed in IEC 61400-24 [24], originate from measurements on tall towers.

Nowadays, it should be noted that current lightning observation towers (Gaisberg Tower - Austria [14], Säntis Tower - Switzerland [16][64], and Peissenberg Tower, Germany [48]) are recording nearly exclusively upward lightning discharges. The reason for this observation is that these towers are constructed on elevated mountain rides. Wind turbines in similar areas are also expected to receive a high amount of upward lightning discharges. On the contrary, Berger's tower at Mount San Salvatore in Switzerland is located in an area where downward and upward lightning discharges can appear. As can be seen, the location of the tower/construction is of crucial importance for the amount of upward and downward lightning strikes. Interestingly, as recently published by Poelman [65], the annual flash density of negative flashes with peak currents higher than 100 kA is higher in coastal and offshore areas, as well as in the surroundings of the measurement tower of San Salvatore, compared to the rest of Europe. This indicates that also Berger may have measured a statistically higher amount of high peak current events during his measurement campaign than typically observed in continental locations.

2.2.3 Current parameters of upward lightning measured on static towers

Similarly to the downward lightning statistics, upward lightning discharges were measured on towers and statistical information is provided from several sources.

One of the first evaluations was again published by Berger in 1978 [13] where polarity dependent current parameters of 1196 upward lightning flashes were evaluated. In his work, he also stated the differences between upward and downward lightning leaders as discussed in section 5.57b. The most important values of his work are gathered in Table 2.3.

As can be seen in Table 2.3, the author observed different current parameter depending on whether a return-stroke followed or only the leader current was apparent. Upward lightning leaders which lowered positive charge towards the ground are characterized by higher peak current, charge and specific energy compared to the negative charge transport. Anderson

Table 2.3: Current parameters of upward lightning discharges from [13].

Flash Type	Polarity	Amount	10%	50%	90%
Parameter: Peak Current			A	A	A
Only Leader	Negative	639	1030	203	40
Connected Leader	Negative	176	25000	10000	4200
Only Leader	Positive	132	11000	1510	206
Connected Leader	Positive	35	127000	36300	10400
Parameter: Charge			C	C	C
Only Leader	Negative	638	69	11.6	1.94
Connected Leader	Negative	172	100	23	5.4
Only Leader	Positive	137	187	26.4	3.7
Connected Leader	Positive	35	348	84.2	20.4
Parameter: Current steepness			$\frac{kA}{\mu s}$	$\frac{kA}{\mu s}$	$\frac{kA}{\mu s}$
Connected Leader	Negative	710	123	26.4	5.6
Connected Leader	Positive	24	12.2	1.9	0.28
Parameter: Specific Energy			$\frac{J}{\Omega}$	$\frac{J}{\Omega}$	$\frac{J}{\Omega}$
Connected Leader	Negative	398	$1 * 10^4$	$2.3 * 10^3$	$5 * 10^2$
Connected Leader	Positive	35	$9 * 10^6$	$6.6 * 10^5$	$5 * 10^4$

[61] pointed out that it is likely that several positive downward lightning discharges were falsely declared as upward lightning discharges in Berger's data. This could explain the very high peak current magnitudes of Connected Leader type flashes in Table 2.3 In terms of observation frequency, negative discharges appeared six times more frequent compared to positive discharges. Compared with downward lightning, upward lightning discharges in general are characterized by lower peak currents, lower specific energy, high charge amounts, and lower current steepness compared to the first return-stroke. This pattern may be different in winter lightning areas as further discussed in Section 3.6. The author further analyzed bipolar lightning flashes (values not included in Table 2.3) and concluded that these discharges usually start with negative current pulses. With increasing leader length, also positive charge pockets are connected to the same plasma channel and a bipolar charge transfer is established.

As mentioned in the previous section, there are several measurement towers in Europe which record the lightning environment for a specific location (Gaisberg Tower - Austria [14], Säntis Tower - Switzerland [16][64], and Peissenberg Tower, Germany [48][49]). Due to their height and their location in elevated territories, these towers receive nearly exclusively upward lightning discharges. The majority of the discharges lower negative charge to the ground. Extensive statistical evaluations for the towers are available in the above mentioned papers and the interested reader is referred to them. The observed values of upward lightning flashes from the towers have to some degree similarities to Berger's current parameters for "Only leader" types flashes shown in Table 2.3.

The Säntis towers shows lightning activity mainly in the convective period from June until September [51][16]. The Gaisberg tower, on the other hand, shows lightning activity more or less evenly distributed throughout the year [14]. Similarly, the Peissenberg tower receives upward lightning flashes in both convective and non-convective seasons [49]. The average lightning activity of the Gaisberg and the Säntis tower is 51 [66] and 115 [16] upward lightning flashes/year, respectively. The number of the Säntis tower was derived from statistics of 21 months only. The Peissenberg tower receives fluctuating amounts of upward lightning flashes, however, on certain days during winter as much as 9 flashes discharge on the structure.

These numbers show that lightning environments are distinctly different between observation towers, even though the Peissenberg tower, the Gaisberg tower, and the Säntis tower are located within a similar latitude and are separated by only a few hundred kilometers, distinct differences between the seasonal lightning activity can be observed.

The reason why the Säntis is not exposed to frequent lightning during the winter season may potentially be explained by the elevation of the site. The tower (124 meters) is located 2500 meters above sea level, whereas Gaisberg (100 meters) and Peissenberg (160 meters) tower are located at 1287 meters and 940 meters, respectively. Climatology in summer may rather represent a winter lightning site at the Säntis tower with daily mean temperature values between $0°C$ and $6°C$ between May and October [67]. In winter, on the other hand, the temperature drop and daily mean values of $-7°C$ to $-4°C$ are observed. The meteorological aspects of upward lightning discharges are further discussed in Section 3.3.

The threat of upward lightning discharges to the LPS of a structure may not be explained by individual current parameters alone. Measurements at the Gaisberg Tower in Austria document that upward lightning discharges accumulate up to $C = 8800C$ of charge within one year [66]. The consequence of such extensive charge transfers are degraded lightning termination systems. In wind power plants, usually the upward lightning flashes are distributed among several wind turbines, however, there are usually certain turbines more exposed than others, as discussed in Section 3.1.

2.2.4 Current parameters measurements on wind turbines

There is a lack of quality lightning data from wind turbines. So far, only a few measurements campaigns on wind turbines were performed and published. Wind turbines may be equipped with simple PCS that record the peak current amplitude with a magnetic film, or more advanced Rogowski coils [58], however, often the data are owned by the wind turbine operators or manufacturers and the data are protected against publishing. To the knowledge of the author, there are no shunt current measurements in wind turbines performed due to noise and installation issues.

2.2.4.1 PCS card evaluation of lightning flashes

An evaluation of lightning current measurements with a correlation of peak current detector and PCS cards was performed by [7] for a dataset from an offshore wind farm (Nysted - Baltic Sea). In general, there was poor correlation between the readings of the PCS and the peak current detector and vice versa; however, a general trend in the peak current magnitude can be reported. In a period of three years (2003-2006), a total of 51 lightning current detections were registered in 72 wind turbines. 33 out of 51 events were recorded in the winter months. This observation gives support to the hypothesis that lightning during winter is a threat for wind turbine reliability also in the Northern European countries. The mean peak current amplitude recorded was $I_p = 6 - 8kA$ which is much less than documented return-stroke currents in the literature. The highest peak current recorded was approximately $I_p = 62kA$ during a summer thunderstorm.

Furthermore, [7] analyzed a global dataset of 1800 PCS cards. The majority of lightning amplitudes was below $I_p = 15kA$ and 40 out of 1800 discharges recorded a peak current amplitude of $I_p \geq 50kA$. The highest measured peak current was $I_p = 120kA$ which occurred once ($I_p = 120kA$ is also the highest detectable peak current magnitude, so the actual peak current may have been higher).

PCS cards capture the magnitude of nearby electromagnetic fields by erasing a section of the magnetic strip of the card. When placed in the immediate vicinity of the down conductor of a wind turbine blade, the lightning current peak amplitude can be estimated subsequently by using a commercial card reader. The cards are restricted by certain limitations such as: a low detection rate for lightning currents below 5 kA, variations in the peak current magnitude, no temporal footprint, and only the highest peak current is recorded on the card. The performance of commercially available PCS cards was evaluated in [22]. Laboratory waveforms showed poor agreement between oscilloscope readings and the detected peak current. There was often no reading detectable or a much too high value recorded. Rocket-triggered experiments show a better agreement, however, the dataset was very limited. [7] performed also cross-correlation in the laboratory. The author concluded that PCS cards are generally reliable when tested with impulse currents and peak currents above $I_p = 5kA$; however, no peak current test was performed with a current waveform that resembles a upward lightning discharges.

2.2.4.2 Winter lightning in Japan

A Comprehensive lightning current measurement campaign was established in Japan within the frame of the NEDO measurement campaign from 2008 - 2013 [9] (Summary in English:[10]). This section relates entirely to the previously named sources. The current measurements recorded in Japan relate nearly exclusively to winter lightning observations.

27 wind turbines were equipped with Rogowski coils, and continuous current measurements were performed. 21 out of the 27 turbines were located in the high risk zone of winter lightning as depicted in Figure 2.3. Furthermore, records of lightning damages on wind turbines and video recordings of lightning flashes were gathered and evaluated.

In total 834 lightning flashes were recorded during the observation period. Current measurements are available from 681 lightning flashes whereas video recordings are available from 153 incidences. More than 86% of all flashes were recorded in the month November to March, however, winter lightning can also appear in October and April in Japan. Therefore, 98.5% of all current recordings are associated with upward lightning caused by winter thunderstorms. Figure 2.4 shows the cumulative probability of charge, specific energy and peak current measured in winter lightning.

As can be seen in Figure 2.4a, approximately 5% of all flashes exceeded a charge Q magnitude of $300C$ and 1% exceeded $600C$. The specific energy $\frac{W}{R}$ plot in Figure 2.4b reveals that 5% of flashes exceeded a magnitude of $2\frac{MJ}{\Omega}$ whereas 1% of the flashes exceeded $5\frac{MJ}{\Omega}$. The peak current I_p depicted in Figure 2.4c show that 5% of all flashes are characterized by amplitudes above $30kA$ whereas 1% of all flashes are bigger than $50kA$. Furthermore, it may be noticed that bipolar flashes are typically characterized

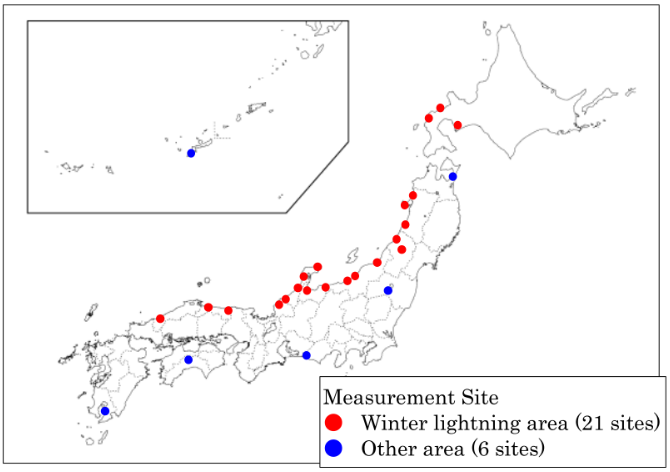

Figure 2.3: Locations of wind turbines equipped with Rogowski coils in NEDO measurement campaign - adapted from [10]

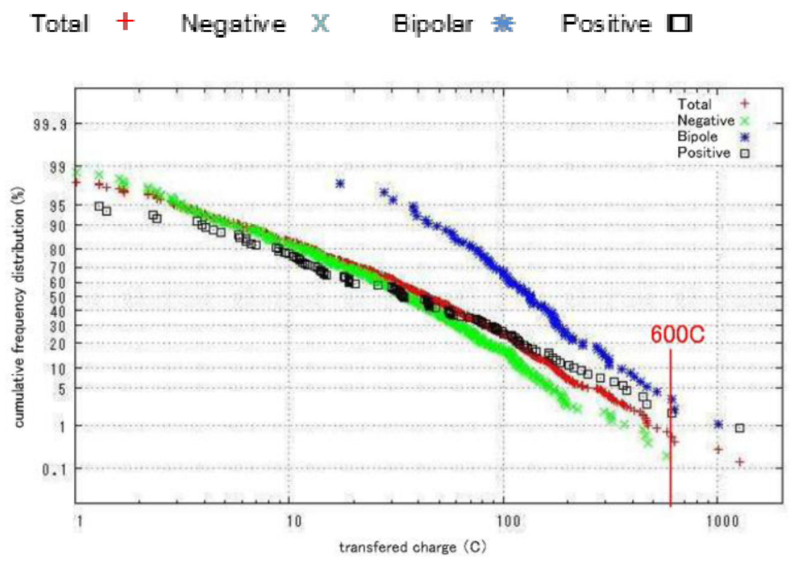

(a) Cumulative probability of charge measured during NEDO campaign - adapted from [10]

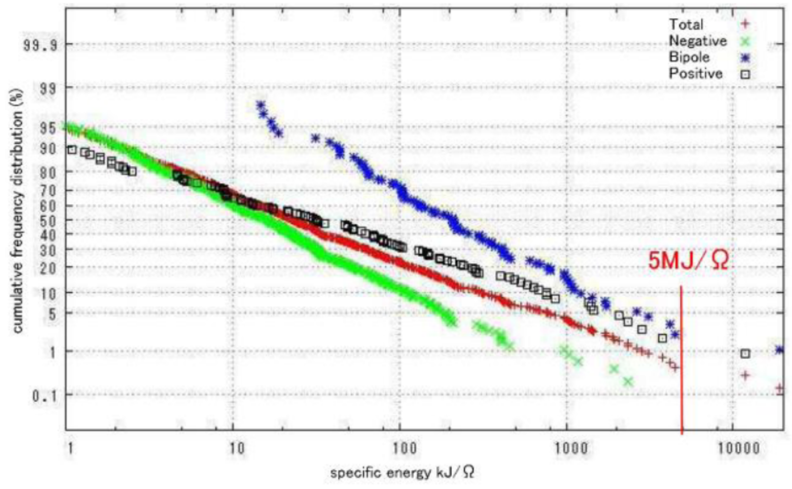

(b) Cumulative probability of specific energy measured during NEDO campaign - adapted from [10]

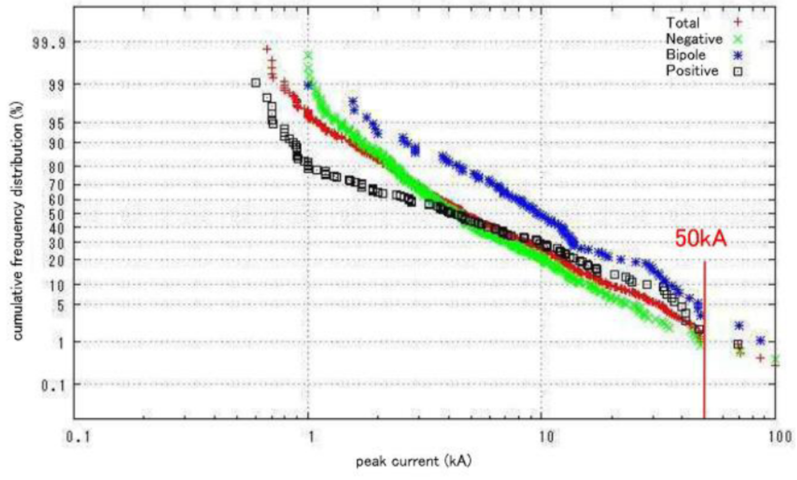

(c) Cumulative probability of peak current measured during NEDO campaign - adapted from [10]

Figure 2.4: Statistics of winter lightning current parameters observed at wind turbines in Japan - adapted from [10]

by above average charge, specific energy, and peak current values, followed by positive lightning, and lastly negative lightning. Median values for the current parameters are: $Q = 45C, \frac{W}{R} = 20kJ\frac{kJ}{\Omega}$ - ($\frac{W}{R} = 200\frac{kJ}{\Omega}$ for bipolar lightning), and $I_p = 4.5kA$ (double for bipolar lightning).

2.2.5 Current parameters according to IEC 61400-24

The standard IEC 61400-24 Wind turbines - Part 24: Lightning protection [24] provides various guidelines directly related to lightning protection of wind turbines. The standard is currently under revision and a new version is expected in 2018. The information regarding current parameter are taken from the latest available committee draft (88/613/CD).

The main topics of the IEC 61400-24 standard are:

- Lightning environment for wind turbines
- Lightning exposure assessment
- Lightning protection of components
- Earthing of wind turbines

Two different high current tests are described which are the arc entry and the conducted current tests. Arc entry tests are used to determine the physical damage of the open arc to the lightning attachment location on a LPS of a wind turbine component such as air termination systems, metal foils, diverter-strips, or connectors. On the other hand, conducted current tests are used to determine the lightning current conduction abilities of the LPS, as well as temperature rises in conductors and connections, arcing and sparking in bearings, sliding contacts, brushes and general connection components.

For both tests, the current characteristics defined by IEC 61400-24 are the same. Both tests correspond to current parameter values of Lightning protection level (LPL) 1. The requirements are listed in Table 2.4. In total, six shots are injected into the test sample. Three out of six shots are characterized by a peak current of $I_p = 200kA$, a specific energy $\frac{W}{R} = 10\frac{MJ}{\Omega}$, and a charge of $C = 100C$ which represents the first positive return-stroke current. The last three test pulses are defined by a charge content of $C = 200C$ which represents the long continuous current in either downward or upward lightning. The latter pulses are used to evaluate the effect of wear due to the increased charge content.

Table 2.4: IEC 61400-24 requirements for arc entry or conducted current tests.

Test Id.	Peak current [kA]	Specific Energy [$\frac{MJ}{\Omega}$]	Charge per test [C]
1-3	200	10	100
4-6	-	-	200
Accumulated charge content			900

A novel addition is introduced in the new version of the IEC standard which accounts for lightning strikes during winter lightning conditions. This type of lightning appears in certain areas in the world and is characterized by long duration discharges with relatively low peak current amplitude and high charge content. The requirements for high current testing of winter lightning exposure are listed in Table 2.5. The maximum stroke duration to inject the current impulse is one second. With this test, the lightning termination (receptor in blades, Franklin rods on nacelle) are stressed since charge is the main driver for material removal during high current testing as described in Section 2.2.1.3.

Table 2.5: IEC 61400-24 requirements for winter lightning testing.

Test Id.	Peak current $[kA]$	Specific energy $[\frac{MJ}{\Omega}]$	Charge per test $[C]$
$7-X$ $(X \geq 9)$	-	-	600
Accumulated charge content (winter lightning)			3 (minimum) times 600

Regarding the current rise time, the current standard IEC 61400-24: Ed.1 [24] relates to the IEC 62305-1: Ed.2 [55] which defines a current rise time T_f of $10\mu s$ and a half time of $T_h = 350\mu s$ for the current waveform of all LPL.

Testing of negative first return-strokes is not performed physically but may be evaluated with simulation. It should be noted that the recommendation of IEC 62305-1: Ed.2 [55] of the current rise-time from negative first return-strokes is defined with $T_f = 1\mu s$ which is a too small value considering that larger peak currents are also associated with larger rise times [63].

As can be seen, the IEC standard is oriented mainly on the current parameters based of positive downward lightning from Berger's [12] measurements.

2.3 Current parameters for the new lightning test equipment

In the previous subsections, research regarding current measurements on tall towers and wind turbines was gathered. Due to the limited time of the PhD and the necessary financial efforts, it was not possible to conduct own current measurement on wind turbines.

In order to approach a solution for finding the necessary current parameters, a realistic lightning exposure system needs to generate, the following information from this chapter are highlighted.

- A downward lightning flash can be divided into up to three different components which are a first-return stroke, continuous current, and a subsequent stroke. An upward lightning flash, on the other hand, is divided into an initial continuous current and possible return-stroke sequences which show similar characteristics to first-return strokes or subsequent return-strokes.
- Wind turbines are exposed to downward and upward lightning. The amount and type of discharge a wind turbine is exposed to seems to vary distinctly between the different locations. Unfortunately, there are only a few direct lightning current measurements performed on wind turbines. It is known that in some areas of the world, upward lightning, in particular during the cold season, dominates the annual lightning activity. Tower measurements in Austria [14], Germany [15], and Switzerland [64] provide an indication of the expected lightning impulses a wind

power plant may experience on very mountainous territories. As is stated in Section 2.2.3, most of received discharges were upward initiated. Especially isolated and elevated wind power plants may be struck very frequently. During several years of operation, the accumulated charge transfer of lighting discharges is likely to affect the efficiency of air termination system on wind turbine blades. On the other hand, wind turbines may also be affected by downward lightning. Convective thunderstorms are the most common source of this type of discharge. The amount of downward lightning flashes to a wind turbine can vary distinctly depending on the average flash density of the wind turbine's location.

- Following these observations, it can be stated that a realistic lightning exposure system needs to be able to create both types of lightning current patterns.
- Downward and upward lightning are characterized by significantly different current waveforms and current derivatives. High-current testing of wind turbines should be performed for both types of lightning separately.
- Regarding the test parameters of downward lightning flashes: Up till today, beside Berger's dataset of tower measurements in Switzerland, there are only few conclusive direct current measurements for downward lightning. Standardization committees derive their recommendations for impulse current tests on the highest 5% of positive return-strokes from Berger's dataset. For instance, the standard IEC 61400-24: Lightning Protection of Wind Turbines recommends to test the impact of the first return-stroke current with a peak current amplitude of $I_p = 200kA$, a charge of $Q = 100C$, and a specific energy of $\frac{W}{R} = 10\frac{MJ}{\Omega}$. These values are slightly lower than the 5% values of Berger. However, considering the small dataset of positive flashes in his data, there is room for some variance. Since there is only one reliable and comprehensive data source of downward lightning and the standardization recommendations derive their values in a reasonable manner from that source, it is difficult to argue that testing parameters should be different from the existing values. It is therefore recommended to keep the current parameters for validation of first-return stroke currents as suggested by IEC 61400-24. Regarding subsequent strokes, it is recommended to test the effect of subsequent lightning currents especially in case of full-scale nacelles. The current waveform may induce harmful voltages in cables or circuits. Currently, the effect of subsequent return strokes are validated by means of swept channel (subsequent stroke) attachment tests by utilizing a high voltage waveform with a rise-time of $T_f = 1.2\mu s$ (blades only). The new test generator system shall also attempt to generate realistic current components of subsequent strokes. Regarding the parameters for such a stroke, the dataset of Berger's lightning measurements provides also the best available orientation.

  If the rise time of subsequent return-strokes is also increased with higher peak currents (similar to first return-strokes [63]) is not confirmed.
- Regarding the test parameters of upward lightning flashes: With the Japanese lightning current measurement campaign conducted by NEDO, direct current measurements of upward lightning discharges on wind turbines are available. This can be used to define the current parameters for high-current testing of upward lightning discharges. If a similar approach was selected compared to the case of downward lightning and the highest 5% of bipolar upward flashes determines the current derivatives of a test waveform, the characteristics would be $I_p = 45kA$,

$Q = 300C$ $\frac{W}{R} = 3\frac{MJ}{\Omega}$. The current impulse pulse is initiated with a low amplitude continuous current and a return-stroke sequence is applied after the DC sequence. By direct comparison to the determined current derivatives of downward lightning flashes, the parameters for upward lighting are all lower. Two differences exist between the potential testing of upward lightning. First, the continuous current is conducting through the structure before the return-stroke. This heats-up the LPS and the arc entry location. Potentially, different damage-modes can be observed on the LPS compared to the downward lightning sequence. Second, the upward lightning waveform would need to be injected into a test sample much more often compared to the downward lightning flash waveform. Extreme locations for wind turbines, such as the Gaisberg tower in Austria, resemble the highest documented exposure with an accumulated charge of up to $Q = 8800C$ yearly.

- Upward lightning from winter thunderstorms in Europe and Japan have similarities. For instance, the Gaisberg tower reports 50% and 5% charge values from negative upward lightning flashes of $38C$ and $300C$ [14], respectively, whereas measurements of negative upward lightning flashes measured on Japanese wind turbines report values of $35C$ and $200C$ [10]. The median values of specific energy from negative upward lightning flashes for the Gaisberg Tower and Japan are $9.6\frac{kJ}{\Omega}$ and $20\frac{kJ}{\Omega}$, respectively.

In order to represent a realistic lightning flash, a lightning exposure system for wind turbines should be able to inject three different lightning current components which are:

- A return-stroke sequence which is characterized by a peak current amplitude of $I_p = 200kA$, a charge of $Q = 100C$, and a specific energy of $\frac{W}{R} = 10\frac{MJ}{\Omega}$.
- A DC current component with an amplitude of $I_p = 600 - 2000A$, with a duration up to one second, representing continuous currents which may appear after return-stroke sequences or as initial stage in upward lightning discharges. The possibility of varying the current amplitude during the discharge is considered valuable.
- A fast current component similar to the most intense 5% current derivative values of subsequent return-strokes. Peak current I_p, maximum current derivative $\frac{di}{dt}$, and rise-time T_f are the most crucial current parameters for the subsequent flash. Following Berger's investigation: $I_p = 30kA$ and $T_f = 0.25\mu s$ (rounded from $T_f = 0.22us$). Charge and specific energy are not crucial for this current component.

Each of these lightning current components shall be injected into the DUT separately, in order to examine the individual effects each current component has on the performance of the LPS. Additionally, in order to create a realistic lightning current exposure system, it is suggested that the current components shall be injected as a combined current impulse, preferably in a user defined sequence, in order to create a current waveform that resembles downward lightning or upward lightning. The possibilities and limitations for a practical high current impulse generators are further discussed in Chapter 5.

This summarizes the return-stroke parameter selection for the test generator. In the next chapter, a closer look at the frequency of lightning discharges to wind turbines is provided. This ultimately reflects on the testing procedures in how often a DUT needs to be tested in order to verify the accumulated lightning exposure during the operational time of a turbine.

3 LIGHTNING EXPOSURE OF WIND TURBINES

The study of current parameters from lightning flashes, as mentioned in the previous section, is an important element in order to determine the consequence a discharge has on the reliability of a wind turbine. The data shows that wind turbines are exposed to both downward and upward lightning. In the first chapter, factors which are reported to increase the amount of upward lightning discharges are gathered. The exposure for each type of lightning seems to vary significantly from site to site. Therefore, it is crucial to further investigate the factors that influence the exposure and identify related characteristics.

In this context, LLS data can provide valuable information regarding the overall lightning activity of a thunderstorm, an estimation of the location of the discharge, as well as the peak current magnitude of the discharges. As discussed in the first chapter, downward lightning can be detected with a high reliability with this technology. The technology, on the other hand, has difficulties to detect current discharges with a low amplitude and low di/dt which are characteristics for some types of upward lightning discharges. The quality of the data depends on several parameters such as sensor baseline and post-processing algorithms. Furthermore, there are various types of LLS technologies available. Therefore, the second section of this chapter presents an analysis on how to use and interpret LLS data for wind turbines.

Another disadvantage of LLS data is that lightning discharges are detected without the information whether it is downward or upward lightning. This information, on the other hand, is crucial since the damage characteristics between the two types vary distinctly. Due to this reason, in Section three and four, correlations between meteorological and LLS data highlight the differences between summer and winter thunderstorms and show that individual storms trigger different types of lightning flashes.

The fifth and sixth section of this chapter are dedicated to properties of winter lightning. Lightning data, mainly from the north-west coast of Japan, which is a typical winter lightning area, were used to determine properties from the storms. An attempt has been made to provide a meteorological model to localize winter thunderstorms. It is shown that different winter thunderstorm types exhibit the environment with different current parameters. Furthermore, an in depth video analysis of the lightning attachment process during winter lightning strikes provides statistics about the attachment process of upward lightning discharges. The section is concluded with possible reasons and remedies for the increased failure rate of wind power plants in winter lightning areas.

3.1 Downward and upward lightning estimation of wind turbines

Wind turbines are exposed to both downward and upward lightning. In order to design appropriate lightning testing equipment for wind turbines it is crucial to estimate the maximum yearly exposure for each type of lightning strikes. As discussed in Section 2.2, current parameters and their related physical consequences for the LPS of wind turbines are distinctly different between downward and upward lightning. Observations show that the ratio of appearance of these two types may vary drastically depending on the wind farm location. The background processes for the initiation of upward lightning are still considered as ongoing research, however, a classification of other-triggered and self-triggered lightning discharges is frequently used [44].

In general, the amount of downward lightning flashes N_D a wind turbine receives can be estimated by utilizing the average flash density N_g of the area where the wind power plant is erected. The average flash density N_g can be obtained reliably by requesting LLS data from a major commercial provider. More information regarding detection efficiency of LLS can be found in Section 3.2. Downward lightning is initiated several kilometers above the ground in a random location in the cloud where the electric field is sufficiently high. The leader propagates towards the ground in a random path. Only if the downward lightning leader happens to propagate within the striking distance of the wind turbine, and a connecting leader develops from the tip, the wind turbine intercepts the flash [68]. Various empirical models exist that attempt to infer the striking distance like the rolling sphere method or the collective volume method. A model based on the physical properties of a lightning leader showed that the perspective peak current of the first-return stroke, the height of the structure, and the lateral position of the downward leader impact the striking distance [69]. IEC 61400-24 define a radius r of three times the turbine height as an attractive radius around the wind turbine.

The amount of upward lightning discharges, on the other hand, can vary drastically among different wind turbine sites. Four factors are observed to increase the amount of upward lightning discharges experienced by a wind turbine. Firstly, the height of the structure has an impact, where taller objects are more frequently exposed to upward lightning. Eriksson [70] derived an empirical relation between the height of the structure and the expected proportion of receiving upward lightning strikes.

$$P_u = (52.8 \cdot lnH) - 230 \tag{3.1}$$

where P_u in [%] is the proportion of upward flashes to a structure, as a function of structure height H in $[m]$. The source of his data are lightning observations from several free standing structures (mostly instrumented towers or chimneys) ranging from heights of 22 to 500 meters. The formula is valid from a structural height of approximately 100 meters. At this point, the structures are estimated to receive a fraction of upward lightning discharges (approximately 13%) whereas structure which are higher than 500 meters receive only upward lightning discharges. Equation 3.1 provides a first estimation in the amount of receiving upward lightning discharges; however, the empirical relation does not include certain effects such as the environmental impact of the topography. Furthermore, recent publications show that very tall towers such as the Tokyo Skytree ($H = 634m$) also receive downward lightning strikes [54]. These findings indicate that the amount of upward lightning strikes to a structure can not be inferred by the height of the structure alone. Secondly, the topography of the wind power plant and its environment can impact the amount of upward lightning strikes. Elevated terrain such as mountain ridges promote the appearance of upward lightning [45][71]. Thirdly, the meteorological conditions and local effects have a distinct impact in the amount of receiving upward lightning discharges, as documented at the west coast of Japan [10][72][73][74] or in Basque country [75]. The meteorological conditions which promote upward lightning discharges are all connected with thunderclouds of low altitude which effectively increase the electric field on ground.

The first three factors (increase in structural height, increase in elevation, and low cloud height) refer to a decrease between the distance of structure and thundercloud which increases the electric field. These factors promote the formation of an upward leader from ground before the initiation of the downward lightning process is observed.

The fourth factor which increases the possibility of upward lightning discharges relates to the local ground flash density which may, together with the characteristics of the structure, be responsible for upward lightning triggered by nearby CG or IC activity [46].

Several publications attempted to infer the amount of upward lightning discharges to tall structures by analyzing the intensification of lightning detections around tall structures [76][21][77]. These publications enable an understanding of the frequency of upward lightning discharges to tall structures. There are, however, limitations to the detection of upward lightning discharges with LLS as further discussed in Section 3.2. Furthermore, a reliable prediction method to infer the number upward lightning discharges before a wind power plant is constructed is missing. Suggestions to indicate which areas may be prone to upward lightning discharges are given in Section 3.5. Furthermore, more information which power plants are prone to upward lightning discharges are documented in Section 3.3.

3.2 Detection of lightning with LLSs

LLS data are a versatile tool to investigate the lightning exposure properties of a particular wind turbine site. It can be used to identify the lightning environment before wind power plants are erected in order to adapt a particular LPS solution or maintenance intervals can be scheduled according to the expected wear of the wind turbines. Furthermore, the data are used to conduct post-lightning exposure analysis in order to clarify the reason for a possible damage. The detection of lightning and the interpretation of lightning data are not straightforward. There are a variety of different technologies for lightning detection available. Each of them is characterized by different performance indicators such as Detection efficiency (DE) and Location accuracy (LA). Furthermore, the current waveform of the lightning incident and the resulting Lightning electromagnetic pulse (LEMP) determines if a stroke can be detected. There are also vast differences in the performance indicators of a LLS between downward lightning and upward lightning.

This section was motivated by the observation that LLS data from wind power plants obtained from various locations in Europe showed different patterns. Some of the wind power plants showed severe lightning cluster formation around the turbines whereas other did not. The question arose if also the quality of LLS data has an influence on the observations.

In this section, different technologies for lightning detection are analyzed, compared, and the suitable technologies for wind turbines lightning exposure analysis are highlighted. Furthermore, there are practical examples of lightning data around wind power plants highlighting the effect of varying performance indicators. This section aims to improve the understanding of using LLS data for wind turbines exposure analysis. The content of this section relates to publication [c.2].

3.2.1 Types of LLS data for the evaluation of lightning exposure to wind turbines

The technology for geo-location of lightning can be divided into two major categories: ground-based and satellite based LLS. Ground-based LLS are divided into Time of arrival (TOA), Direction finding (DF), or a combination of both technologies. Satellite-based LLS utilize optical imaging to locate lightning. The performance characteristics for the networks are usually defined with DE, LA, polarity and peak current estimation accuracy, and lightning type classification accuracy. A thorough review of the technologies was performed by [17]. When evaluating the risk of a wind turbine to be struck by lightning, ground-based LLS technology should always be preferred compared to satellite-based LLS. Reasons against satellite-based LLS are general inferior performance characteristics, the inability to differentiate between CG and IC lightning, and the limited spatial and temporal resolution. The DE of a low-earth orbiting satellite varies from 38% to 88% percent, depending on the instrument and time of day. LA ranges from ten to several tens of kilometers which is not sufficient to correlate a distinct lightning event to a wind turbine site [18]. For this reason, this evaluation of the usability of LLS data for lightning exposure of wind turbines is focused on ground-based LLS. Since the ability of ground-based LLS to detect and allocate downward lightning is substantially different from upward lightning, the topic is divided into two parts which address first the downward lightning and then the upward lightning.

3.2.1.1 Performance characteristic of ground-based LLS for downward lightning

Ground-based LLS are divided by the frequency ranges in which they are able to detect the radiated LEMP. They can be classified into long-range, medium-range, short-range, and very short range systems. A comprehensive state of the art summary about the LLS technologies with performance indicators can be found in the work of [18]. From his work, the performance characteristics from different ground-based LLS are listed by different frequency bands in Table 3.1. Three main observations can be made when evaluating the usability of different LLS technologies:

- With increasing frequency band, the DE and LA is increasing
- With increasing frequency band, the necessary sensor baseline is decreasing
- With increasing frequency band, the CG stroke peak current error decreases

Table 3.1: Characteristics and performance of different ground-based- LLS for cloud-to-ground lightning (From [17][18]).

Range	Frequency Band	Sensor Baseline	Detection Efficiency			Median Location Accuracy	Peak current error
			CG Stroke	CG Flash	IC Flash		
Long range	VLF (1 - 2 kHz)	Several thousand kilometers	3 - 40 %	10 - 70 %	<10 %	2 km to more than 10 km	25 - 30%
Medium range	ELF - HF (3 Hz - 3 MHz)	150 - 400 km	70 - 90 %	85% to >95%	About 50%	About 100m to less than 1 km	15 - 20%
Short range	ELF - HF (3Hz - 3MHz)	50 - 75 km	>90%	>95%	About 75%*	About 100m to few hundred meters	15 - 20%
Very short range	VHF mapping (30MHz - 300MHz)	10 - 40 km for TOA, 150 km or less for interferometry	Total flash DE >95%			Several tens to few hundred meters	N/A

*=Estimated performance characteristics derived from the characteristics of sensor, associated instruments, and algorithms

Long range LLS The DE of long range LLS like the World Wide Lightning Location Network (WWLN) is strongly dependent on peak current and polarity. Current amplitudes bigger than ± 35 kA are detected in 10% of the events. Current amplitudes in between 0 and -10 kA are detected in 2% of the events [78]. Another long range LLS is the Global Lightning Dataset 360 (GLD360) which provides global real time lightning data for tracking of severe weather. Recently, an algorithm upgrade in the software enabled a performance leap, leading to an improved DE and LA [79]. The CG detection efficiency for downward lightning increased from 55-75% to 75%-85%. The median location accuracy decreased from 2.4 km to 1.8 km, and the 90th percentile decreased from 12.9 km to 6.4 km. However, for small peak current magnitudes, the DE is still below 75%. Furthermore, upward lightning discharges can not be located with this technology. These performance characteristics indicate that the data from these networks are too inaccurate to perform exposure assessment for wind turbines, especially since the median LA is several kilometers.

Medium range LLS Medium range LLS, which normally operate in a Low frequency (LF) band (approx. f= 1 – 350 kHz), are the best choice to evaluate the lightning incidences to wind turbines. They cover a big part of the frequency spectrum of lightning which is not biased by propagation effects of LEMP. Low frequency electromagnetic signals (<100kHz) are able to propagate over conductive ground without major losses of amplitude. The high frequency components (>100kHz) in a LEMP, however, are subjected to propagation effects due to soil conductivity. The radiated amplitudes of those waveforms lose some of their energy while propagating over soil with finite conductivity which decreases the amplitude of the LEMP. This effect is especially pronounced in LEMP from subsequent strokes. Globally, there are over 60 Very low frequency (VLF)-LF LLS networks operating which provide commercial lightning detection data. Examples of major networks are the National Lightning Detection Network (NLDN) covering North America, European Cooperation for Lightning Detection (EUCLID) and Lightning detection Network (LINET) covering Europe, Japan Lightning Detection Network (JLDN) covering Japan, Brazilian National Network (BrasilDat) covering Brazil, the Canadian Lightning Detection Network (CLDN), and the LLS of South African Weather Service (SAWS) [17]. It needs to be highlighted that performance characteristics of such networks can vary vastly, especially for small peak current amplitudes. According to [80], the five most important parameters that influence DE are:

- Sensor baseline and network geometry
- Sensor sensitivity, noise handling, thresholds, and dead time
- Signal treatment and discrimination
- Procedures for correlation of signals belonging to the same stroke
- Numerical location software

State of the art commercial ground-based mid-range LLS are able to detect peak currents $>$ 20 kA of downward lightning very reliably within their interior boundaries. LA varies between 100m and 1000m where lower peak currents are usually associated with higher location uncertainties. Depending on the network properties, current magnitudes lower than 10 kA are also detected. Looking at the peak current distribution from Section 3.2.2, however, it becomes apparent that the majority of detected lightning discharges around wind turbines are below 20 kA and often below 10 kA. Therefore, it is crucial to verify the mean LA and DE of the network at the wind turbine site with the LLS data provider in order to interpret the lightning data correctly. Subsequent strokes are characterized by 5 – 10% lower DE and LA compared to the first return-strokes, due to lower mean current amplitudes and higher impulse frequencies which increases attenuation of LEMP due to propagation effects [81]. The lowest possible first return-stroke peak current amplitude which can occur in nature was previously determined to be within a range of 1.5 - 3 kA [82].

Short range and very short range LLS For the purpose of defining the exposure of lightning to a wind turbine, high DE, low LA, and low stroke peak current estimation error are advantages. Therefore, short range and very short range LLS data may be optimal to perform exposure assessments. Unfortunately, these systems have a short sensor baseline and do not cover large areas. They are used to study the individual breakdown process of virgin air and provide lightning information for research purposes for designated locations [83]. Furthermore, due to their high operating frequency range, large amount of data are collected for each lightning discharge which makes the data processing tedious. High frequency (HF) and Very high frequency (VHF) LLS need to be located within a short distance to the observed object due to the propagation effects of the LEMP.

3.2.1.2 Performance characteristic of ground-based LLS for upward lightning

In this section, recent research regarding the ability of mid-range LLS to detect upward lightning is stated. Recently, few publications evaluate the performance of VLF-LF LLS to detect upward lightning. In the work of [50], the author stated a local DE of 42% to detect upward lightning which was derived from 713 upward lightning events measured in the Gaisberg tower (Austria) in a time period from 2000-2013. This low percentage is a result of the low efficiency of LLS to detect the most common characteristic upward lightning current waveform which is ICC_{only}. Out of 713 upward lightning events, 338 were of the type ICC_{only} which is 47%. The probability of an LLS to detect upward lightning ICC_{pulses} and ICC_{rs}, are 58% and 96%, respectively. The author does not provide information about LA of detected upward lightning events. A similar study was performed for the Säntis Tower in Switzerland by [84] where an overall DE to detect upward lightning is stated to be 97%. However, ICC_{only} events were removed from the scope of the study which limits the validity of the evaluation with respect to the lightning exposure of wind turbines. The publication included an analysis of LA for upward lightning events. The author reported a strong correlation of larger location errors for peak currents below 10kA. Most of them were associated with ICC_{pulse} waveforms. On the other hand, the current rise time does not influence the LA with a clear tendency; however, current rise times larger than $8\mu s$ are reported to be detected by the network in only 3% of the cases. Furthermore, the LA decreases with an increased number of reporting electromagnetic sensors. Both studies mentioned previously used the EUCLID network in the alp region for performance evaluation which consists of about 150 lightning detection sensors. Other parts of Europe, which are also covered by EUCLID, may vary in performance characteristics due to different sensor technologies [65], varying sensor baselines, and the geographic region being considered [18].

Another commercial European lightning detection networks is the LINET system which is comprised out of 130 crossed-loop antennas which measure variation in the magnetic flux due to lightning [85]. The network has the capability to detect lightning events with peak currents well below 5 kA within the central part of the network according to [80]. March [20] documented the process of data quality improvements due to an increase of nearby sensors close to two wind power sites in Spain. Throughout the observation period from 2006-2013, the stepwise increase in the amount of nearby LINET sensors showed improvements of DE and LA for the LLS. Furthermore, lower peak-current magnitudes were able to be detected after more sensors were installed. The median, mean, and first percentile peak current magnitude around the wind turbines (after the sensor update in 2010) as detected with LINET data were ranging from: 5.9 – 7.8 kA, 6.1 – 10.2 kA, and 2.2 – 2.4 kA, respectively. These values were recorded in the years 2010-2013. For comparison, in 2006, before additional sensors were installed in the area, the median, mean, and first percentile peak current magnitude were: 15.9 kA, 19.2 kA, and 9.5 kA, respectively. This study highlights the importance of low baselines between sensors in LLS in order to detect low peak current amplitudes.

A comparison between measurements conducted with Rogowski coils in 16 wind turbines in Japan and LLS data from the JLDN revealed DE of 18% for lightning currents with less than 100C and 23% for lightning currents above 100C [19].

The performance of the NLDN in respect to upward triggered lightning was investigated in [46] during the time period 2004-2010. Time-stamped optical sensors of ten tall towers revealed that due to nearby lightning activity observed by the NLDN, upward lightning was triggered in 83% of the cases. The analysis further showed that 44% of the upward flashes were reported by the NLDN as subsequent negative CG strokes or IC events.

The following observations can be made regarding the DE of upward lightning by ground based VLF-LF LLS.

- ICC_{only} events are not detected due to their very low frequency electromagnetic fields and their weak peak current amplitude. According to measurements performed by [50], at the Gaisberg tower, 47% of all upward initiated lightning flashes are of type ICC_{only}.
- ICC_{pulse} events are detected in 58% of all cases. A high amount of reporting sensors, a high peak amplitude, and low rise times promote the DE and LA for this type of upward lightning. 21% of the lightning strikes measured in [50] were of type ICC_{pulse}
- ICC_{rs} events feature similar characteristics like subsequent return-strokes in natural downward lightning and the DE is reported to be above 95%. 32% of the lightning strikes in [50] are of type ICC_{rs}.
- March [20] reported direct improvements of DE and LA for upward lightning by LLS by reducing the sensor baseline in the network.

Furthermore, it should be noticed that VLF-LF LLS often classify upward lightning as IC discharges. For instance, out of 2036 detected pulses at the Säntis Tower, 73% of the pulses were classified as cloud discharges by the EUCLID network [84].

3.2.2 Practical LLS data evaluation to wind turbines

In the following section of the thesis, the implication of varying data quality from LLS is evaluated. In the previous section, medium range VLF-LF LLS were identified as the best suitable solution for lightning data evaluation for wind turbines since they are able to detect downward lightning very reliably and additionally, they are able to detect a fraction of upward lightning discharges. This section aims to provide practical information about how to interpret lightning data as well as identify wind turbine locations which are impacted by winter lightning.

In the first example, LLS data from 13 wind power plants which are scattered in Europe were compared. The locations of the wind power plants were: Norway, Denmark, UK, Germany, North-Sea, Poland, France (2 wind power plants), Spain, Italy (2 wind power plants), Croatia, and Greece. The size of the wind power plants varied between 3 and 130 wind turbines. For each site, the peak current detections and uncertainty ellipses r_s are analyzed. Each location is unique in terms of LLS performance. Generally, wind power plants which are located in the center of Europe are characterized by a lower uncertainty ellipse r_s (high location accuracy) whereas wind power plants on the outskirts of Europe are characterized by a higher r_s (low location accuracy). It is shown that low peak currents are only recorded in wind power plant sites which are characterized by a low uncertainty ellipse r_s. The average reported peak current is increasing with increasing r_s.

In the second example, stroke and flash density plots from three different wind turbine sites are provided. LLS data is used to identify if a wind turbine site is exposed to frequent winter lightning discharges and which impact r_s has on the classification of upward lightning strikes.

3.2.2.1 The influence of the uncertainty ellipse

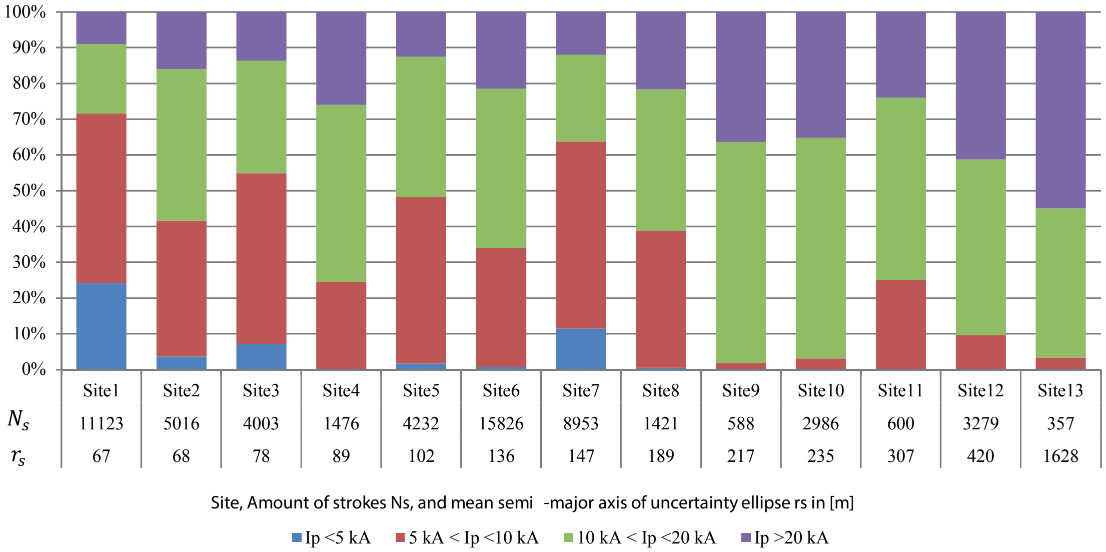

Figure 3.1: LLS data of detected peak currents from 13 wind power plant locations sorted by increasing semi-major axis of uncertainty ellipse r_s

As an example to highlight the differences in LLS data for an exposure assessment, the lightning detection data for 13 random wind power plants are used. The data were obtained from a major VLF-LF LLS network. The purpose of the analysis is to examine only the data quality differences and the effect to the peak current distribution. This analysis can provide information regarding the differences of LA and may imply some tendencies for DE. The wind power plant locations are scattered within a rectangular area with the longitudinal and latitudinal distance of approximately 2400 and 2900 kilometers, respectively. The lightning data covers a radial distance of five kilometers around the wind power plants and is recorded in a time frame of 5 years. Intra-cloud lightning detections were removed from the dataset. For each lightning stroke detected, the network provided an uncertainty estimation r_s which is the semi-major axis of the elliptical confidence region of the detected lightning stroke. This confidence region is a measure that the detected lightning stroke is within the boundaries of the radius r_s with a probability of p. Usually, but not exclusively, the reference probability level p of a LLS network is 50% [86]. In Figure 3.1, the detected peak current distribution of the 13 wind power plant sites is illustrated. The data are sorted with increasing semi-major axis of the uncertainty ellipse. Furthermore, the amount of detected strokes is presented. The following observations can be made :

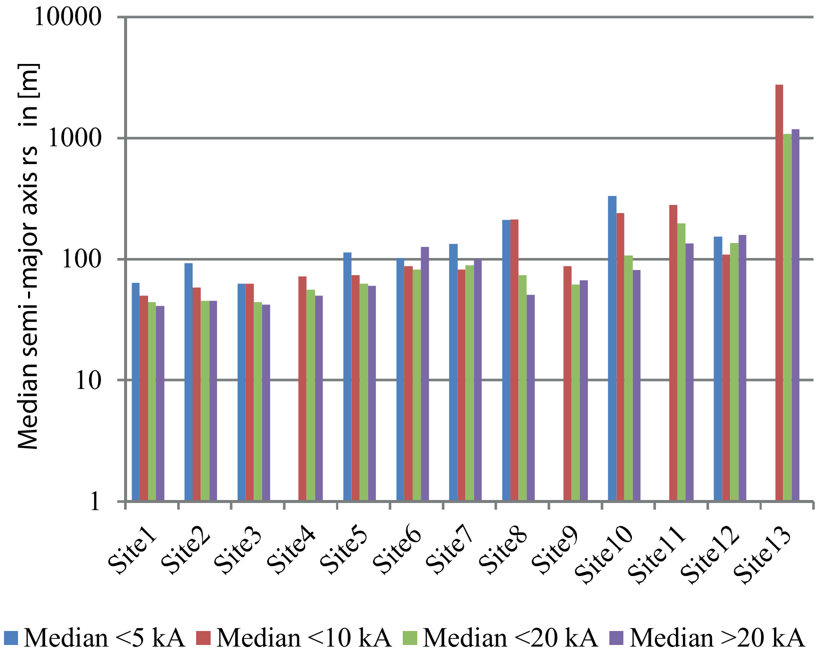

Figure 3.2: Median error ordered by detected peak current amplitude. Usually lower peak currents are associated with lower location accuracy.

- The calculated mean uncertainty estimation r_s from all detected lightning strokes within one sites varies from 67 – 1628 meters. This is a considerable difference of LA.
- With increasing r_s, the absolute percentage number of detected lightning strikes above 20kA is increasing (purple color).
- With increasing r_s, the ability to detect small current amplitudes below 5 kA is decreasing. From Site 9 – Site 13, no lightning currents below 5 kA are detected.
- With increasing r_s, there is a trend that the absolute percentage of lightning strikes between 5 and 10 kA is decreasing.

A smaller uncertainty ellipse r_s is generally combined with improved LLS network properties. This can be due to smaller sensor baseline, more reporting sensors, and improved sensor technology. The sites 1 – 7 are characterized by a mean stroke LA error of less than 147 meters. At site 1, 3, and 7, 5% or more of the total detected lightning strokes are characterized peak currents magnitudes below 5 kA; however, at sites 2, 4, 5, and 6, no or very few peak currents below 5 % are detected. Without more details about the properties of the LLS, no definite conclusions can be made if there are simply no lightning currents below 5 kA in this area or if the network is not able to detect them, however, the latter seems more likely. Several studies report observations of triggered or self-initiated upward lightning leaders with low peak currents starting from wind turbines blades which seldom are detected by LLS [32][23][87]. At sites 8 – 13, the mean LA is bigger than 190 meters. The majority of detected lightning discharges are above 10 kA. At site 13, very high location accuracies are detected and the majority of detected lightning amplitudes are above 20kA. There is a high probability of missed lightning detections with small peak current amplitude / low current rise time at sites 8 – 13.

In Figure 3.2, the median error is illustrated for the individual peak current interval with a logarithmic scale. Low peak currents are generally characterized by the highest uncertainty value r_s and hence, the LA is the lowest. With increasing peak current the LA is increased. This result follows observations reported in [84]. Site 6, 7, 9, and 12 do not follow a clear trend in this perspective. The example given above emphasis the differences which are attributed to different local LLS performances even within the same network.

3.2.2.2 Hot spot formation due to low current amplitude strokes

As observed in the previous example, the mean semi-major axis of the uncertainty ellipse r_s can be used as an indicator if low peak current amplitudes are able to be detected by a LLS network.

In this example, five years of LLS data from three different wind power plants are compared. Two sites are characterized by low r_s, whereas one site is characterized by a high mean r_s. For all three sites, the average flash density N_g and the average stroke density N_st are illustrated in Figure 3.3a to Figure 3.3f. Wind turbines positions are marked with a black triangle facing down and lightning detections are marked with a colored dot or circle related to the peak amplitude and polarity.

In Figure 3.3a, the lightning flash detections for the first wind farm are illustrated and hence strokes are removed from the observation. The lightning detections in the map are fairly distributed in the map with a slight intensification around certain turbines. The intensification can be attributed to either intercepted downward lightning or upward lightning. On the contrary, Figure 3.3b shows the same dataset for lightning stroke occurrences. It can be observed that cluster formations are more prominent compared to Figure 3.3a and subsequent events do influence the exposure. These events can be attributed to triggered upward lightning, repeated self-initiated events or to subsequent strokes.

The second wind power plant is also characterized by a good LA. In this example, the lightning environment is different. In Figure 3.3c and Figure 3.3d, the flash density and stroke density are illustrated, respectively. It can be observed that no intensification of lightning events around the wind turbine is apparent. It appears that the wind turbines are mainly influenced by downward leaders in this location.

Table 3.2: The calculated average flash and stroke densities for the three investigated sites illustrated in Figure 3.3a - Figure 3.3f. The term area refers to the lightning environment of the surrounding of the wind power plant whereas A_d refers to the lightning activity in the close vicinity of the wind turbines inside the collection area defined by IEC 61400-24

	r_s [m]	Average flash density $N_G[1/km^2yr]$		Average stroke density $N_{st}[1/km^2yr]$	
		Area	A_d	*Area*	A_d
Site 1	111	3.0	5.0	5.0	11.0
Site 2	78	1.4	1.1	2.5	2.6
Site 3	420	0.6	0.9	0.8	1.5

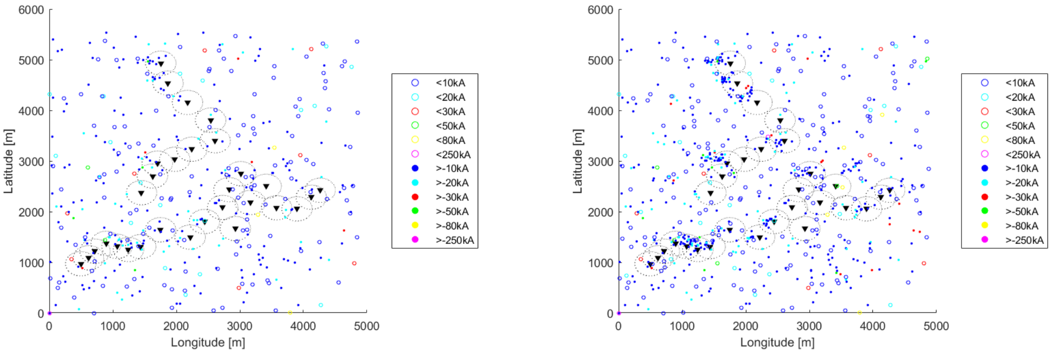

(a) Site 1: Flash detections for a wind power plant which is influenced by upward lightning. LLS data with high accuracy. Small intensification of lightning discharges around wind turbines.

(b) Site 1: Stroke detections for a wind power plant which is exposed to upward lightning. LLS data with high accuracy. Distinct intensification of lightning discharges around wind turbines

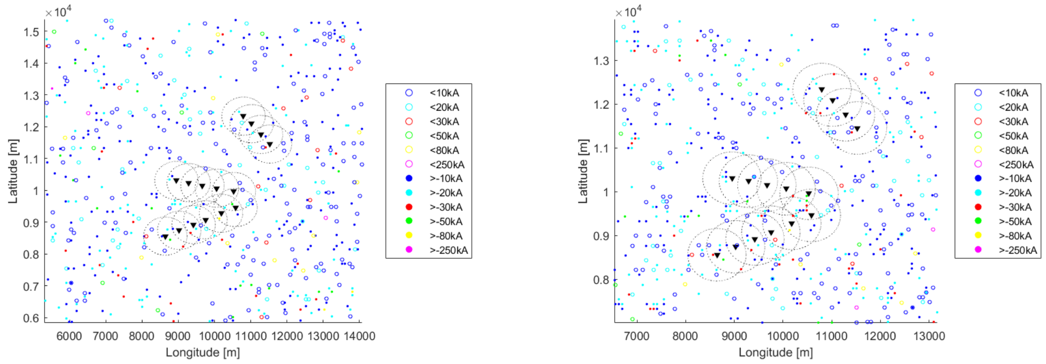

(c) Site 2: Flash detections for a wind power plant which is not affected by upward lightning. LLS data with high accuracy. No intensification of lightning discharges around wind turbines.

(d) Site 2: Stroke detections for a wind power plant which is not affected by upward lightning. LLS data with high accuracy. No intensification of lightning discharges around wind turbines

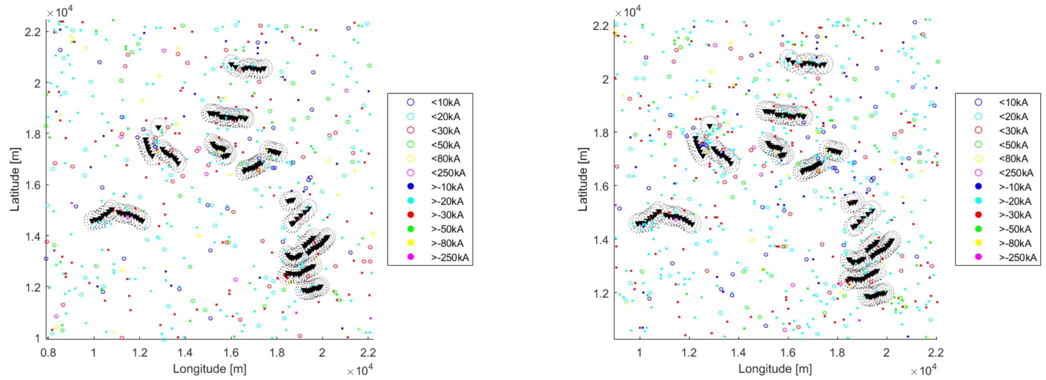

(e) Site 3: Flash detections for a wind power plant which is may be affected by upward lightning. LLS data has low accuracy, so low amplitude flashes are maybe not recorded.

(f) Site 3: Flash detections for a wind power plant which is may be affected by upward lightning. LLS data has low accuracy, so low amplitude flashes are maybe not recorded.

Figure 3.3: LLS data from three different wind power plant sites with individual lightning environment.

The third wind power plant is characterized by a high r_s and hence low DE and LA. In this example, it is not possible to predict the effect of upward lightning to the wind power plant based on Figure 3.3e and Figure 3.3f. Similar to the second study, none or only limited cluster formation around the wind power plants can be identified. However, in Table 3.2, it is apparent that the lightning density inside the collection area r_s is higher than the surrounding area for both flash and stroke occurrences. This is an indication that the wind turbines at this location are exposed to a certain enhancement in lightning activity, however; due to the limited data quality, it is difficult to conclude to which extend the site is really exposed.

In this example, three different locations are investigated and two main conclusions can be obtained. Firstly, there are wind turbine sites which are affected frequently by subsequent lightning activity and upward lightning, and there are other sites which are not influenced. Secondly, the data quality of a LLS has a big impact in the DE and LA. From the performance characteristic review of Section 3.2.1.1, it can be assumed that in all three cases the high peak currents of downward lightning strikes are detected and located with a high percentage. The biggest unknown of lightning exposure of wind turbines based on LLS data is attributed to low peak amplitudes which are often related to upward lightning events. Even though, hot spot formation is apparent in Site 1 and partially in Site 3, only a fraction of upward lightning discharges are able to be detected and hence, an even higher lightning density is expected in reality due to ICC_{only} events which cannot be detected by any medium-range LLS.

3.2.3 Concluding remarks regarding the detection efficiency of LLS

This section reviewed information which are relevant if a detailed exposure assessment for wind turbines shall be conducted with LLS data.

From the evaluation of performance characteristics of different LLS technologies of downward, upward lightning, several characteristics of LLS in respect to lightning exposure of wind turbines can be concluded:

- Due to the low DE, especially for low peak current amplitudes, very long range LLS are not suitable to provide LLS data for exposure assessment of wind turbines. They are able to detect mainly high peak current return-strokes.
- Satellite LLS are characterized by a low DE and LA. A classification between upward and downward lightning is not possible. Furthermore, only certain parts of the world are currently observed with low earth orbiting satellite. Therefore, an exposure assessment is not recommended.
- HF / VHF LLS cover only a limited area and generate high amount of data which may require long time to evaluate; however, the technology records lightning processes in a very high detail. In general, the technology may be seen as research technology to investigate the individual breakdown processes during lightning formation or to benchmark other LLS.
- Downward lightning: Benchmarks of VLF-LF LLS to towers with measurement equipment indicate very good flash DE of 85% till over 95%. Stroke DE vary from 70 – 90% depending on the network. Often low peak currents < 10 kA are missed by LLS. The median LA of flashes and strokes can be estimated in a range of 50 meters – 2000m depending on the sensor network.

- Upward Lightning: Upward lightning performance characteristics vary vastly among VLF-LF LLS. Approximately 50% of upward lightning strikes are of type ICC_{only} which cannot be detected by any VLF-LF LLS. For the remaining 50% of type ICC_{pulse} and ICC_{rs}, the DE and LA of the strokes depend on the sensor baseline, peak current, current rise-time, and evaluation algorithm. From the numbers in the studies, a DE of 0-40% with a possible LA accuracy of 100 m – 5 km may be assumed for all lightning events, depending in the location and the type of LLS.

The factor r_s in the lightning exposure assessment is introduced to account for the inability of LLS to detect upward lightning, however, since network technology steadily improves, upward lightning events may be included already in LLS data nowadays. A careful investigation needs to be conducted before an exposure assessment to avoid the overestimation of the total number of estimated strokes to the turbine.

The fact that also first return-strokes can have low peak current amplitudes which are not detected by an LLS may foment the overestimation of the current peak amplitudes from lightning strikes attaching to wind turbines.

The performance characteristics of the data have a distinct impact in the ability to detect small current amplitudes. Furthermore, the occurrence of upward lightning to wind turbines depends heavily on the location observed.

3.3 Comparative evaluation of meteorological data from summer and winter thunderstorms related to lightning exposure of wind turbines

In the previous section, the data quality of LLS data from wind power plants from different locations was compared and the uncertainty ellipse r_s was related to the ability to detect small peak current magnitudes. Particular sites with a low r_s showed a cluster formation of low amplitude discharges around the wind turbines (Figure 3.3a - 3.3b) whereas other sites with low r_s did not (Figure 3.3c - 3.3d).

With the desire to research why certain wind power plants are exposed to these lightning intensification and others are not, an investigation of the meteorological conditions at five wind power plants was performed. The results of this section are also published in paper [c.3]. LLS data with a rather small r_s (78m - 190m) were available for all five sites. Each of the sites are characterized by individual characteristic properties in terms of topography, elevation and average ground flash density. The selected locations are a site in north Croatia which is located close to the sea on an up-slope ridge, a flat-inland site in north France, a site in Italy on a mountain top, an offshore site in the North sea and three wind power plants in the north of Spain which are located on top of mountain ridges. Meteorological data of the atmosphere where thunderstorms developed were obtained from radio sounding measurements. Figure 3.4 illustrates the position of the wind farms and the closest radio sounding station. Wind power plants are located within the indicated circle. No absolute positions are given due to data privacy reasons for particular sites. For each of the sites, five years of LLS data were obtained within a radius of ten kilometers around the wind turbine sites from the VLF/LF network LINET.

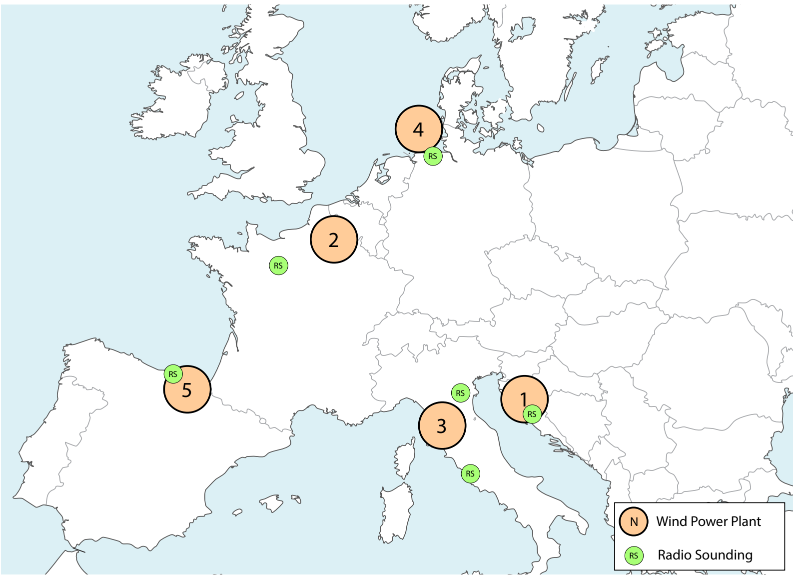

Figure 3.4: Overview of the five selected wind turbine sites in Europe with closest radio sounding location for atmosphere probing. Wind power plants are located within the indicated circle. No absolute position are given due to data privacy reasons for particular sites.

Table 3.3 summarizes geographical information of the sites as well as a quality assessment of the LLS data. The average elevation of the site and the total height of the turbine is stated. The value h is the sum of the elevation and the height of the turbines. This value is used later in this work as the evaluation point for weather data. The data quality assessment is conducted through the 2D error ellipse r_s. For the investigated sites, the mean radius r_s of all lightning registrations for each particular site varies between 78 and 190 meters which is a rather good margin compared to other LLS [18].

3.3.1 Seasonal variations of lightning occurrences throughout Europe

In order to begin the meteorological evaluation of the five sites, a short overview of lightning detections as a function of the months is provided. In Figure 3.5, two diagrams show the normalized lightning activity in the collection area A_d of the wind turbines. The area A_d is determined by 3 times the turbine height, as defined in the IEC 61400-24 exposure assessment guidelines.

Basically, two different site types can be distinguished. In Figure 3.5a, the lightning activity of France and Italy is illustrated. As can be seen, the active months are mainly during the summer and autumn months. The lightning activity may be dominated by large scale convective storms in the warm season. On the other hand, Figure 3.5b illustrates the seasonal occurrence of lightning at the location in Spain, Croatia and in the North Sea. Here, the lightning activity is more distributed throughout the year and also in the colder months, lightning is observed. Interestingly, the corresponding latitude does not have an influence on this observation. Lightning detections in the colder months are registered in the northern offshore wind farm as well as in Spain and Croatia. On the other hand, France and Italy seems to be mainly exposed during the summer and autumn. This observation indicates that some sites are mainly exposed to lightning discharges in

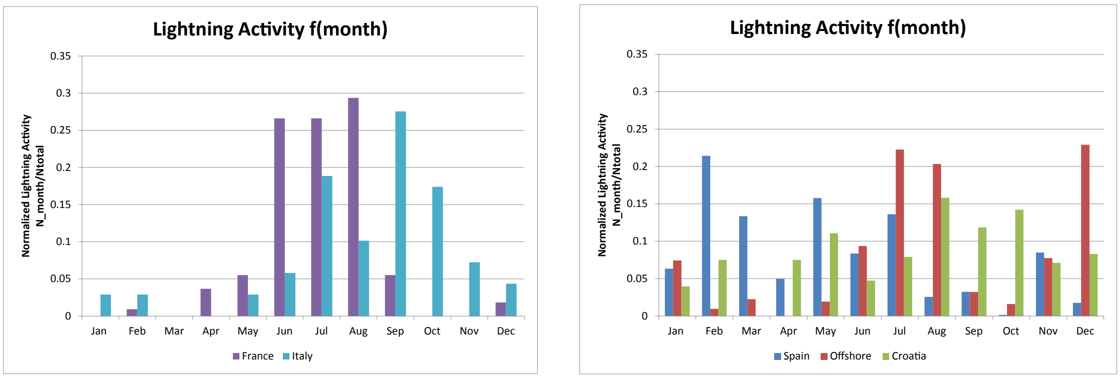

(a) Lightning detections around wind turbines of the investigated site in France and Italy mainly in the warm season

(b) Lightning detections around wind turbines in Spain, Croatia and in the North Sea are distributed in the warm and in the cold season.

Figure 3.5: Monthly variation of lightning activity in the vicinity of wind turbines

the warm season whereas other locations are also prone to thunderstorms in the cold season.

As a second approach to evaluate the sites, the ambient temperature at ground level as a function of months were investigated in order to see if a correlation between the ambient temperature and the monthly lightning exposure can be made. Figure 3.6 shows the average temperature at the individual sites. The sites in France, Spain, and the North Sea experience similar average temperatures throughout the year, whereas Croatia and Italy are experience warmer average temperatures. From this graph, no correlation between the average ambient temperature (Figure 3.6) and the lightning activity (Figure 3.5) can be found. The data has been extracted for the particular sites in the last 10 years from the National Oceanic and Atmospheric Administration (NOAA) - GHCN CAMS dataset which provides high resolution temperature data based on satellite surveillance.

Table 3.3: Data from the investigated wind power plants: Elevation, Height, the sum of Elevation and Height h, the mean 2D error estimation r_s, and distance to the closest radio sounding d_{rs}.

#	Site	Terrain Classification	Elevation $[m]$	Height $[m]$	h $[m]$	r_s $[m]$	d_{rs} $[km]$
1	Croatia	Slope, Close to sea	750	150	900	146	110
2	France	Flat, Inland	140	200	340	78	170
3	Italy	Mountain Top	600	91	691	136	160
4	North Sea	Offshore	0	151	151	190	106
5	Spain1	Mountain Top	1000	80	1080	113	117
5	Spain2	Mountain Top	1000	105	1105	112	110
5	Spain3	Mountain Top	1000	80	1080	118	101

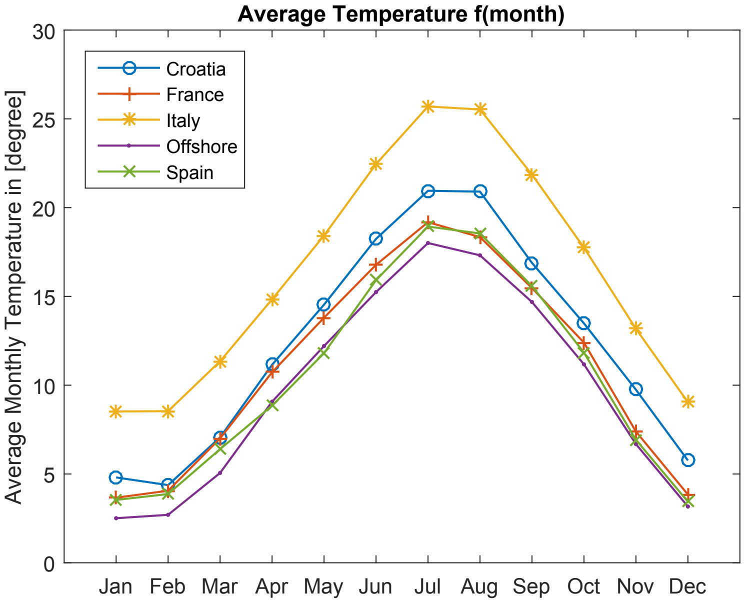

Figure 3.6: The plot of average surface temperature for the different sites. The probability of winter storms can not be correlated with the temperature.

3.3.2 Meteorological characteristics of summer thunderstorm compared to winter thunderstorms

The monthly analysis of lightning activity revealed that France and Italy are typical summer thunderstorm sites, whereas in Spain, Croatia and the Offshore site, lightning activity was also observed in the winter months.

In order to get a better understanding of the meteorological characteristics of each site, five to seven particular dates were selected which exposed the sites to the highest amount of discharges to the turbines (A_d). In some of the sites, the most severe thunderstorms to the wind turbines were reported in the warm season only (France, Italy), whereas the wind power plants in Spain and in the North Sea were also exposed to a high number of lightning detections within A_d in the cold season.

In order to study the differences between warm and cold season storms, the weather conditions in which the storm developed have been studied by two means: radio sounding of the atmosphere and radar data analysis (only available for the sites in Spain).

3.3.2.1 Radio sounding measurements

Before the radio sounding data from different sites are compared, some more details regarding the technological properties of radio soundings are provided in order to enable an understanding of the limitations of the data.

Radio soundings measure the vertical distribution of physical properties of the atmosphere and several parameters such as pressure, humidity, temperature, wind speed and wind direction can be obtained as a function of the height. The measurements are performed by sensors that transmit the data via radio communication. These sensors are lifted by means

(a) Spain

Parameter	Var.	Unit	Warm 2011- 05-11	Warm 2013- 07-19	Warm 2014- 09-07	Cold 2014- 03-26	Cold 2012- 11-28	Cold 2014- 02-25	Cold 2013- 02-02
Amount of discharges	#		51	23	6	49	26	25	23
Time first discharge	t_1	HH:MM	18:56	17:47	13:58	2:40	10:05	14:39	9:21
Time last discharge	t_2	HH:MM	19:21	18:48	16:51	21:15	23:25	15:56	21:37
$t_2 - t_1$	Δ t	HH:MM	0:25	1:01	2:53	18:35	13:20	1:17	12:16
Temperature at h	T_a	$[degC]$	**10.6**	**19.3**	**20.7**	**1.8**	**2.3**	**1.2**	**1.9**
Pressure at h	p_a	$[hPa]$	912	907	900	900	895	893	904
Relative humidity at h	$\%rh$	[%]	96	36	52	87	88	94	69
Wind direction at h	$\angle\vec{v}$	$[deg]$	245	77	170	335	353	305	340
Wind speed at h	$\lvert\vec{v}\rvert$	$[ms^{-1}]$	**2.6**	**6.1**	**7.1**	**15.8**	**12.2**	**12.8**	**17.9**
Height of 0°C iso. - h	h_0	$[m]$	**2331**	**2720**	**2951**	**265**	**316**	**143**	**120**
Height of -10°C iso. - h	h_{-10}	$[m]$	**3853**	**4161**	**4365**	**1802**	**1773**	**1594**	**344**
Sounding measurement	t_s	HH:MM	12:00	12:00	12:00	12:00	12:00	12:00	12:00

(b) North Sea

Var.	2012- 07-30	2013- 06-19	2013- 08-02	2013- 12-05	2014- 12-11
#	54	27	29	22	17
t_1	4:15	10:05	19:48	12:42	1:35
t_2	5:13	10:17	22:07	21:34	22:28
Δt	0:58	0:12	2:19	8:52	20:53
T_a	**16.7**	**18.6**	**30.2**	**4.9**	**4.1**
p_a	993	998	990	986	980
$\%rh$	75	95	35	81	85
$\angle\vec{v}$	170	265	172	232	253
$\lvert\vec{v}\rvert$	**8.2**	**10.7**	**15.3**	**28.6**	**15.8**
h_0	1925	N/A	4045	520	638
h_{-10}	**3685**	**N/A**	**5256**	**2982**	**1936**
t_s	12:00	12:00	00:00*	12:00	12:00

(c) Croatia

Var.	2010- 12-09	2011- 04-12	2011- 10-07	2013- 08-28	2013- 01-14
#	16	18	20	11	9
t_1	13:50	20:37	13:16	12:10	4:14
t_2	14:23	23:56	13:48	12:20	6:08
Δt	0:33	3:19	0:32	0:10	1:54
T_a	**11.7**	**7.7**	**5.4**	**14.8**	**5.9**
p_a	900	907	903	910	904
$\%rh$	66	66	65	75	79
$\angle\vec{v}$	256	288	286	298	184
$\lvert\vec{v}\rvert$	**12.2**	**16.3**	**13.8**	**4.1**	**12.9**
h_0	1388	1169	1123	2230	682
h_{-10}	**3102**	**3032**	**2635**	**4765**	**2373**
t_s	12:00	00:00*	12:00	12:00	0:00

(d) France

Var.	2010- 06-06	2011- 08-22	2011- 08-26	2013- 07-27	2014- 08-12
#	9	5	15	8	12
t_1	8:40	20:07	4:02	20:07	15:07
t_2	9:23	20:26	4:31	20:18	16:17
Δt	0:43	0:19	0:29	0:11	1:10
T_a	**15.0**	**22.2**	**19.2**	**20.2**	**14.2**
p_a	975	977	967	968	974
$\%rh$	87	60	72	75	92
$\angle\vec{v}$	274	0	120	269	221
$\lvert\vec{v}\rvert$	**3.1**	**3.6**	**9.2**	**9.0**	**4.1**
h_0	2555	3826	3205	3362	2017
h_{-10}	**4579**	**5228**	**4868**	**5232**	**3504**
t_s	12:00	12:00	0:00	12:00	12:00

(e) Italy

Var.	2010- 07-29	2010- 09-13	2013- 08-24	2013- 09-29	2014- 10-11
#	8	6	4	7	8
t_1	21:52	13:48	21:37	11:26	19:00
t_2	22:06	14:03	21:42	23:42	19:53
Δt	0:14	0:15	0:05	12:16	0:53
T_a	**18.9**	**16.3**	**19.0**	**21.3**	**18.0**
p_a	938	939	932	937	938
$\%rh$	63	73	73	51	63
$\angle\vec{v}$	282	N/A	298	225	200
$\lvert\vec{v}\rvert$	**2.3**	**N/A**	**6.6**	**3.1**	**1.8**
h_0	3521	2323	2879	3280	2734
h_{-10}	**5134**	**3916**	**4431**	**5132**	**5080**
t_s	12:00	12:00	0:00	12:00	0:00

Table 3.4: Meteorological parameters from radio sounding measurements and LLS data information of severe thunderstorm days for 5 different wind turbine sites in Europe. Warm convective storms are highlighted light grey, whereas cold thunderstorm days are marked dark grey. Important factors for the thunderstorm development are the ground temperature T_a, the altitude of the -10°C isotherm to the site h_0 and the wind speed $|\vec{(v)}|$. * indicates that radio sounding data was obtained after the thunderstorm event and is hence representative for the decay conditions of the thunderstorm.

of a balloon. Radio soundings are available globally. Several hundred stations contribute to the data accumulation. Typically, two soundings are launched from a station every day, at 12:00 UTC and 00:00 UTC. The data is publically available from different sources, such as the University of Wyoming [88] and the National Oceanic and Atmospheric Administration [89]. The methodology for retrieving meteorological information from radio soundings has been adapted from [75]. The distances from the radio sounding launching sites to the wind power plants under investigation d_{rs} vary between 100 and 170 km and are listed in Table 3.3 and illustrated in Figure 3.4.

In Table 3.4, data extracted from LLS like the amount of discharges # within the area of A_d, and the time between the first and last discharge Δt are given. Additionally, meteorological parameters from nearby extracted radio sounding observations are listed. In some cases, the thunderstorm was active during the ascent of the radiosonde, whereas in other cases, the thunderstorm was in the development phase. The information provided by the soundings is considered to be valuable in order to understand the atmospheric conditions which are apparent during a thunderstorm - or led to the development of a thunderstorm - in different seasons and over the areas under study. The following variables were extracted at the height h (average elevation of the wind farm + turbine height) of the wind power plant: temperature T_a, pressure p_a, relative humidity $\%rh$, wind direction $\angle\vec{v}$, wind speed $|\vec{v}|$, the distance between the height of the 0°C isotherm and h, and the distance between the height of the $-10°$C isotherm and h. The last two variables are frequently used to estimate the height of the charge region in a thundercloud [73].

Significant differences between warm and cold season thunderstorm days can be observed from the data presented in Table 3.4.

- As it can be expected, the temperature at ground level T_a is significantly different, being in the range from 10°C to 30° in the warm season and close to the freezing point in the cold season. These differences also depend on the location of the site, being more homogeneous in sites close to the sea (e.g. Italy) and with larger differences between season in mountainous areas (e.g. North of Spain) and northern latitudes (e.g. North Sea). The temperatures at surface level can largely affect the inception of the convection that can lead to the development of a thunderstorm.
- The distance between the wind power plant and the $-10°$C isotherm is usually larger than 3500 m in warm thunderstorm days, whereas it remains usually below 2000 m in cold thunderstorm conditions. This matches with the observations of winter lightning in Japan [73].
- The observed wind speed $|\vec{v}|$ at the height of the wind power plant during cold season storm days is always high. This observation might be a crucial prerequisite for moisture to get in higher altitudes, which is an important factor for the formation of snow and graupel. According to the rimming theory of cloud electrification, these particles are believed to create negative and positively charged ions in the atmosphere [72].
- The time duration Δt between the first observed discharge and the last observed discharge is typically much longer in the cold season compared to the warm season. The thunderstorm conditions in the warm season usually imply fast development and decay phases, and therefore the lightning discharges to the wind turbine sites are

concentrated over short periods of time. In the cold season, however, the lightning environment appears to be much more steady and discharges are distributed over time periods of a day or more.

3.3.2.2 Radar data observations

As can be seen from the previous section, warm season thunderstorms and cold season thunderstorm are formed in completely different meteorological environments. Fortunately, the possibility to study radar data plots for the surroundings of the Spanish wind power plant sites was given. The data were available for all seven thunderstorm days which were analyzed. It covered a radius of 100 km with a temporal resolution of 10 min during the thunderstorm activity. Additionally to the maximum echo reflectivity values, the LLS data for the area was superimposed to the radar data.

Radar measurements are used to provide information about the water content of a cloud which can be manifested liquid or solid state. In general, the higher the reflectivity of the cloud, the higher the precipitation experienced at ground. The term reflectivity specifies the amount of transmitted power returned to the radar receiver. The range of detectable reflectivity starts from light mist in the atmosphere to extreme hail and is measured in dBZ. For this work, the MAX. reflectivity values of seven thunderstorms days in Spain were used to relate the parameters to the topology of the cloud. As a representative example, three frames of a warm season and cold season thunderstorm are illustrated in Figure 3.7. Each frame inherits a similar structure. In the center of the frame, the 2D horizontal distribution of the clouds is visible. On the upper and right corner of each frame, the vertical 2D profile of the cloud can be followed, as seen from the north-south and east-west direction. The following section describes the properties which could be observed. The observed wind power plants are marked with a bold black X. The red circles provide information about the intensity center of cloud-to-ground lightning.

Warm Season Thunderstorm Figure 3.7a illustrates a typical warm season thunderstorm which developed in the vicinity of the wind power plants on 2011-05-11 around 15:00 UTC. The first picture captures the time frame of 15:50 - 16:00 UTC. In this period, the MAX. reflectivity values reach approximately 60 dBZ which corresponds to heavy rain/moderate hail. The biggest storm center can easily be identified west of the wind power plants, whereas smaller single cells are formed south of the location. Lightning discharges are mainly located where MAX. reflectivity are 40 dBZ or higher. From the vertical profiles of the cloud, the highest point of water content can be estimated with 15 km. These values can also be used to approximate the top of the cloud. In general, as higher the moisture inside the cloud, as higher the risk of frozen particles interacting and promoting the activity of the charge generation inside a thunderstorm. In the second picture of 3.7a, the thunderstorm center with very high precipitation has moved approximately 15 km to the south-east (red circle), whereas the wind in the lower layers pushing the main precipitation of the storm towards the north-east. This observation can be made at tall clouds which are influenced by different wind directions within their vertical profile. The observation is of particular interest since the tri-polar charge structure of a cloud is often assumed to be very static; however, as can be seen, the cloud and

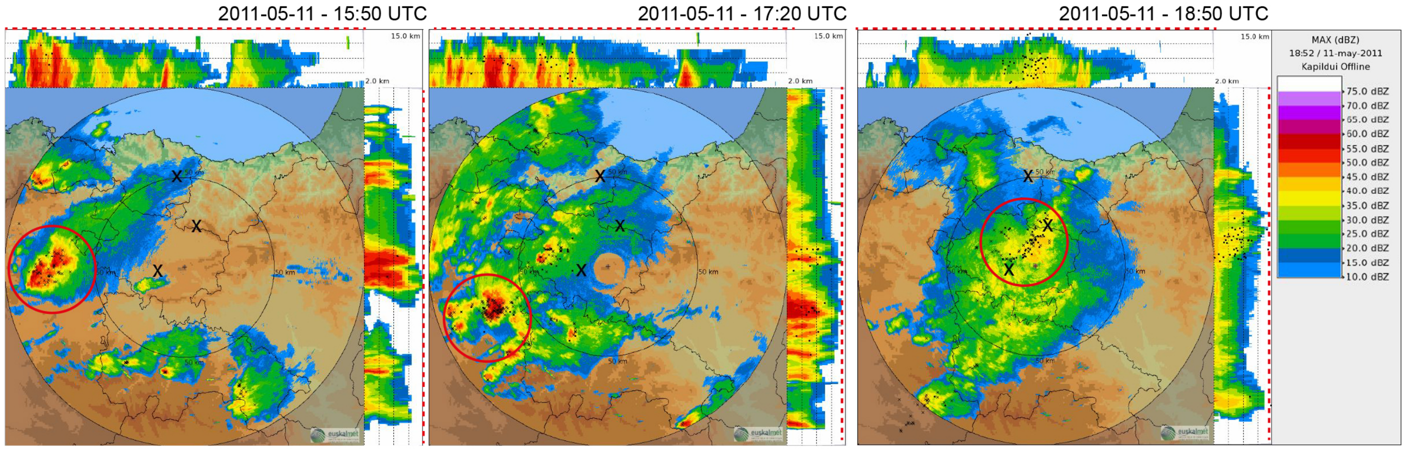

(a) Very high reflectivity values. Lightning registrations are concentrated mainly around MAX. reflectivity values. Very high cloud-top height.

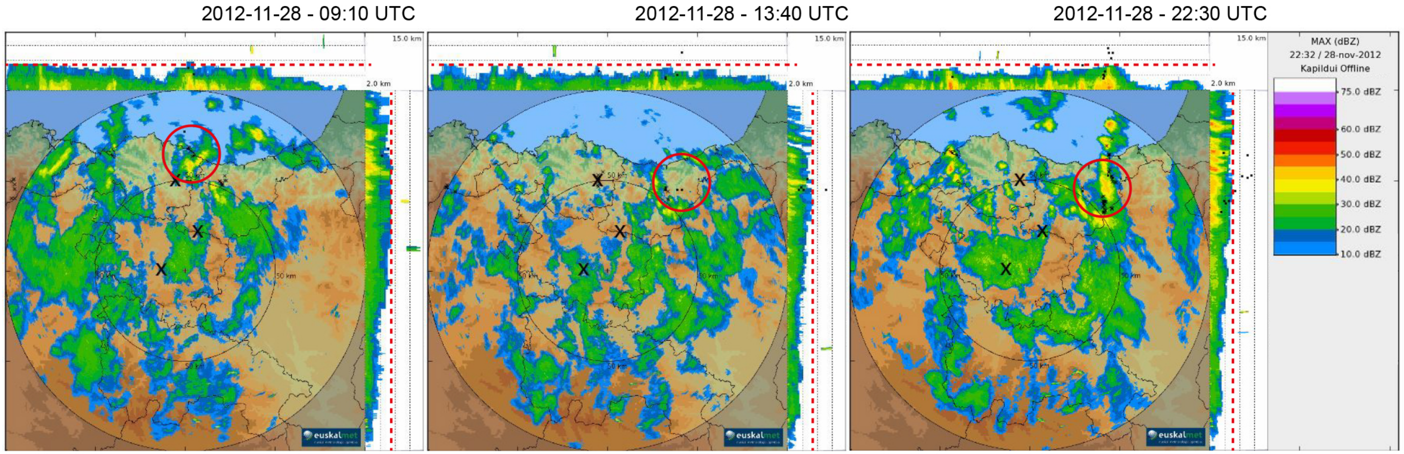

(b) Lightning registrations are recorded throughout over 13 hours over a wide area. Very low cloud base and top heights. Low reflectivity values.

Figure 3.7: MAX. reflectivity radar plots of three time frames from a typical convective warm season thunderstorm and a cold season storm over the north of Spain. The capital X letters are marking three wind power plants. The red circles mark the center of cloud-to-ground lightning. The red dotted line marks the top height of the cloud. Data provided by Basque weather agency Euskalmet.

its charge content can propagate multi-directional. In the third frame, the very high reflectivity values disappeared and the maximum values in the frame reached values of 45 dBZ. Lightning discharges are registered on two wind power plant locations. To summarize the observations, the thunderstorm develops and decays in a time frame from 15:30 UTC to 21:00 UTC. Within the time duration, the storm travels approximately 200 km from west to north-east. Lightning discharges are often created within a very narrow sector only. According to the LLS data, the wind turbines are only exposed to lightning discharges in a time frame from 18:56 to 19:21 UTC.

Cold Seasons Storm In Figure 3.7b, a typical cold season thunderstorm is illustrated. Significant differences in the reflectivity data and in the lightning discharge pattern can be observed compared to the warm season thunderstorm. For the analysis, the 2012-11-28 is chosen as a representative day for such a storm. In fact, all the four investigated dates of cold season storms show similar features. The first characteristic property is the storm does not have one single thunderstorm cell but the reflectivity values indicate that the precipitation is evenly spread over a wide surface. Secondly, lightning discharges are not concentrated but are distributed over a large area. The majority of lightning discharges are recorded in the first 50 km measured from the shore line and are often concentrated where the reflectivity values reach a local maximum. Only few discharges are recorded over sea and further than 50 km inland from the shore. It can be noticed that the discharges are registered during a long time period. In the case of cold season storm from the 2012-11-28, the first lightning discharge in the vicinity of the wind turbines was registered at 10:05 UTC and the last discharge at 23:25 UTC. Within this time period, several hundred lightning discharges are registered in the observed area illustrated in Figure 3.7b. Another noticeable difference is the low cloud-base heights visible in the MAX. reflectivity plots, compared to the summer thunderstorm conditions. This observation is similar to the reported cloud-composition of winter lightning in Japan [35].

3.3.3 Discussion

From the evaluation of weather data of warm and cold thunderstorm days distinct differences of the investigated meteorological parameters are found. From the radio sounding and radar data, the atmospheric conditions were monitored in which these thunderstorms were developed. Warm season thunderstorms are characterized by relatively high ambient ground temperatures T_a and a charge separating $-10°\mathrm{C}$ isotherm h_{-10} which is located above 3500 m. Additionally, they can develop and decay during a short period of time. The lightning activity is often concentrated within a small area. The top height of precipitation in the cloud, which is indicated in the radar plots, is often above 10 km in the cloud. The creation of warm season thunderstorms and precipitation centers may be also influenced by pressure gradients due to a rotating updraft, convective development, storm mergers, and orographic effects [90]. From the radar data observation, the complex propagation and development of warm season thunderstorms is illustrated. In the presented case of Figure 3.7a, the most active thunderstorm region was combined with very high reflectivity values up to 60 dBz. It was observed that this very high located storm center propagated in a different direction than the main precipitation area which is caused by different wind layers directions. The observation shows how diverse an actual composition of a warm season storm may be. From this point of view, in the literature, the often used tri-polar thundercloud structure [33], where the negative regime of charge is perfectly aligned with the positive regime of charge, may not be such an often observed phenomena.

On the other hand, the max. reflectivity values and LLS data recordings observed from cold season thunderstorms show a more homogeneous pattern in the storm structure. Severe lightning observations were registered mainly if the ambient temperatures T_a was slightly above the freezing point, the wind speed $|\vec{v}|$ was high, the relative humidity $\%rh$ was above 80%, and, most importantly, the charge separating $-10°\mathrm{C}$ isotherm h_{-10} was lower than 2000 m to ground. From the radar data evaluation of Spain, it was observable that the cold season thunderstorms cover a wide-spread area, as can be seen Figure 3.7b), and are active within a long time period up to 18 hours.

Another characteristic feature between warm- and cold season thunderstorms can be observed if the LLS data from individual days are compared. In Figure 3.8a, the lightning detections of a single day (2011-05-11) during the warm season in Spain is illustrated. The lightning activity is scattered in the observation area and only 13 discharges are detected within the collection area A_d of the wind turbines. From the meteorological analysis in Table 3.4, it is confirmed that this thunderstorm is characterized as a convective warm-season thunderstorm which mainly exposes the environment to downward lightning. The wind turbines are affected by the storm but the impact is distributed among the entire wind power plant and the observation area.

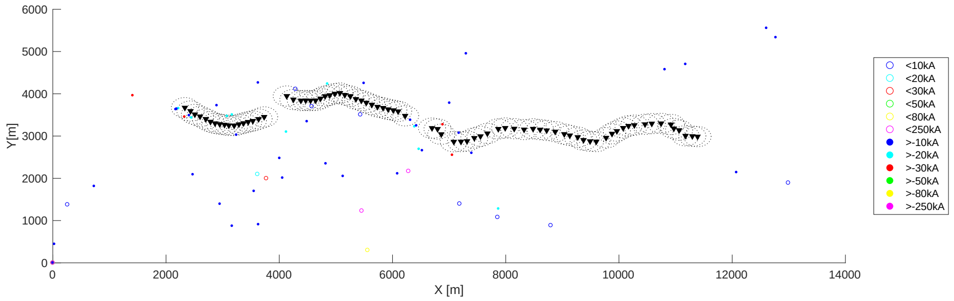

(a) Warm-season thunderstorm (2011-05-11) - Discharges scattered in the observation area. 13 discharges within A_d

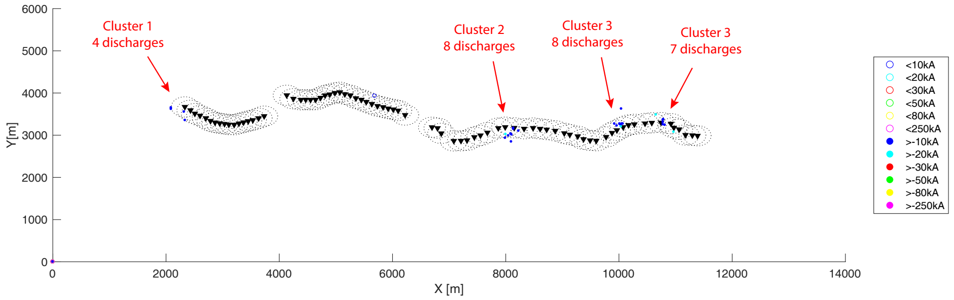

(b) Cold-season thunderstorm (2014-03-26) - Discharges centered around a few wind turbines. 27 discharges within A_d.

Figure 3.8: Reported lightning discharge on a wind power plant in Spain within one day. Circles around wind turbines represent the collection area $A_d = 3h$.

On the other hand, Figure 3.8b shows the lightning detections of a single day (2014-03-26) during the cold season. In total, 27 discharges are reported within the collection area A_d and none is reported in the remote observation area. Most likely several upward lightning discharges were not detected by the LLS due to the reasons discussed in Section 3.2. Furthermore, the data suggests that certain wind turbines are more affected than others and 4 clusters can be identified on that particular day. The meteorological pattern, as indicated in Table 3.4, are similar to the confirmed parameters of upward lightning in Japan [73] and hence, it can be inferred that these discharges are also upward lightning.

This example demonstrates that even if a wind power plant is located in a location where frequent summer thunderstorms develop, the impact of the thunderstorm is distributed between the surrounding area and the wind turbines because of the random propagation nature of downward lightning flashes. On the other hand, during cold season, all generated flashes are initiated at the point where the electric field on ground is highest. Often the same wind turbines are affected, which increases the stress for the LPS.

3.3.4 Conclusion

LLS data from five different wind turbine sites in Europe were analyzed and the exposure as a function of the month is illustrated. It is shown that two sites are exposed to lightning strikes mainly during the summer months (France, Italy) whereas three sites (Croatia, Spain, North Sea) are prone to lightning discharges throughout the entire year. The comparison of average monthly temperature along the year for the different sites does not indicate whether they have lightning activity during the cold season. Radio sounding measurements and radar reflectivity values are used to determine the storm topology.

From the analysis, it can be stated that cold season thunderstorms are characterized by low cloud-base heights, $-10°$C isotherms below 2000 meters above the ground, high wind speeds, and temperatures close to zero degrees. Similar observations are made for winter lightning in Japan [73][72]. Furthermore, radar reflectivity observation show that lightning discharges are recorded throughout several hours and over wide area.

On the other hand, the characteristics of warm season thunderstorm show high cloud-base heights, $-10°$C isotherms more than 3500 meters above the ground, and relatively high ambient temperatures. Warm season thunderstorms develop in shorter time frames than storms in the cold season. The entire life cycle of the warm season thunderstorms can be short, with relatively fast mature and decay stages, or last for longer times in those situations in which thunderstorms organize in systems, where new cells constantly develop while others decay.

3.4 Five years of LLS data from a site frequently exposed to winter thunderstorms

The lightning activity of five years, divided by the convective and non-convective season, is illustrated in Figure 3.9a and 3.9b, respectively.

During summer thunderstorms, the lightning discharges are scattered in the entire area. As elaborated in Section 3.1, downward lightning flashes are initiated by a lightning leader that

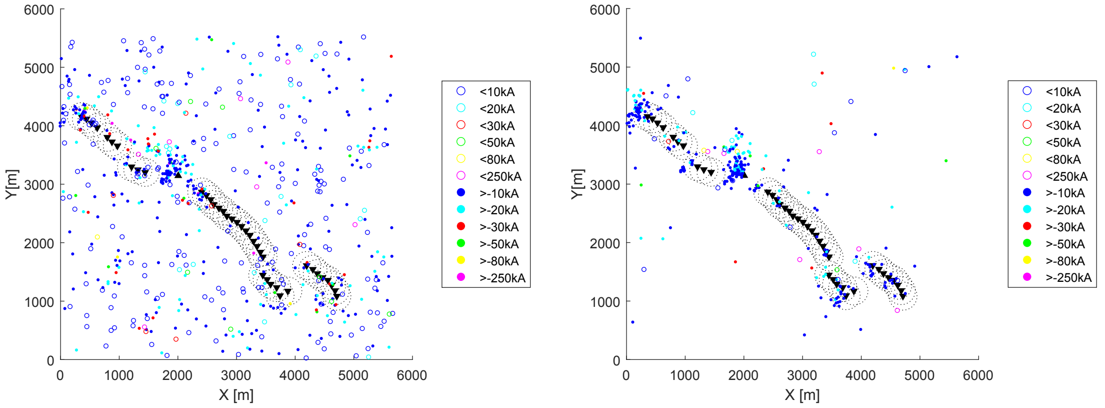

(a) 5 years LLS data in the month March to October (convective season)

(b) 5 years of LLS data in the month November to February (non-convective season)

Figure 3.9: Comparison between LLS pattern observed in the convective and non-convective season.

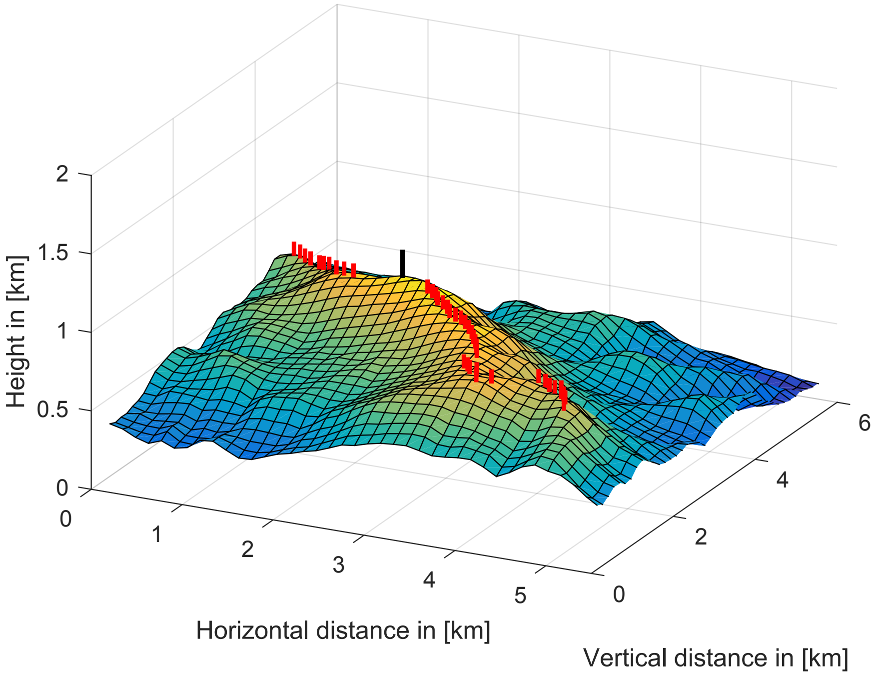

Figure 3.10: Elevation profile and indicated wind turbine (red) and tower position (black) for wind power plant depicted in Figure 3.9.

approaches the ground in a random manner. The attractive radius of a tall structure may vary depending on the height of the object, the elevation and the prospective return-stroke current; however, as can be seen in Figure 3.9b, in summer the cluster formation around the towers are limited.

In the non-convective season and in an area which is prone to winter lightning, on the other hand, lightning strikes attach directly on the wind turbine. Furthermore, the same wind turbine may be struck by lightning several times within a few seconds. For instance, on the 1st of March 2008, a particular winter lightning storm at the Gaisberg Tower initiated 22 flashes within 25 minutes which lowered a total amount of $C = 3735C$ of charge towards the ground. Extreme cases like this explains the potential threat of winter lightning to wind turbines or tall structures. It is not necessarily extreme current parameters of upward lightning but the possibility that one structure is struck several times within a small time span which may degrade the LPS of a wind turbine. Typically, the discharges are spread over several wind turbines, however, as can be seen in Figure 3.9b, the discharges may concentrate at one particular structure. In the case of this wind farm, the hot spot is a static tower which is distinctly higher compared to the wind turbines. The elevation profile with indicated height of the wind power turbines (red) and the tower (black) is illustrated in Figure 3.10.

3.5 Location of winter lightning on continental and global scale

The severe cluster formation of upward lightning appears only in distinct locations on the world. This chapter shows two different maps which may indicate affected areas. Wind turbines constructed in those areas may be impacted by frequent lightning attachment in the cold season with the characteristic discharges pattern as illustrated in Figure 3.9b. Wind farm developers and operators should carefully evaluate if the LPS of the wind turbine can be optimized for cold season lightning.

3.5.1 Global winter lightning map

The first winter lightning map was published by [91] in 2016. The author used two criteria for possible winter lightning occurrence:

1. The temperature at the 700hPa level must be lower or equal than $-10°C$
2. Lightning must be confirmed by the globally operating WWLN LLS

Global temperature data was obtained from the ECMWF Re-Analysis (ERA-Interim) dataset with a tile resolution of $1° \times 1°$. The results of the analysis is illustrated in Figure 3.11.

As can be seen in Figure 3.11, the map highlights several intensification zones of winter lightning areas such as:

- Sea of Japan and west of Japan
- Eastern United States

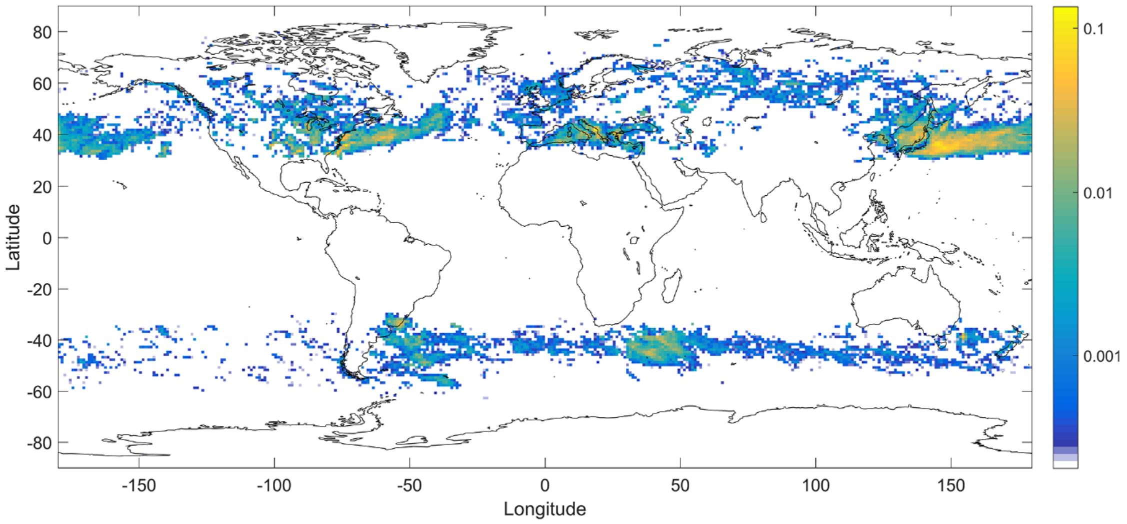

Figure 3.11: Global winter lightning occurence with scale stroke density $\frac{strokes}{km^2 \times yr}$ (adapted from [91])

- Coast of Italy and Croatia
- Eastern parts of China
- Coast of South Brazil and Uruguay
- Coast of New Zealand

It is apparent that most of the intense winter lightning areas are close to the sea, however, also minor winter lightning activity is observed in parts of Russia and China. The interaction between the warm currents of the oceans and the cold dry air from the poles as described in Section 3.6.1.

In the work of the author, it is mentioned that the scale of the map is distinctly underrated due to the limitations of the DE of the WWLN. As described in Section 3.2.1.1, the WWLN is able to detect only a fraction of low peak current amplitude events (About 2% of events with peak current below 10kA). Upward lightning discharges in winter thunderstorms are typically low peak current discharges (See Section 2.2.4.2 - Median value approx. $I_p = 5kA$.) It is expected that the map in Figure 3.11 can identify a fraction of ICC_{rs} during winter thunderstorms which successfully highlights winter lightning regions. Up till today, this map is the only winter lightning map with a global scale.

3.5.2 European winter lightning map based on meteorological data

The second winter lightning map was developed by analysis of meteorological data from winter thunderstorms. Similar weather patterns were observed during winter thunderstorms as described in Section 3.3.2. A model was created that evaluates the meteorological weather patterns in a given area and time frame and subsequently identifies if the meteorological conditions were fulfilled to create upward lightning discharges. Radio sounding measurements were used as the input for the model. The approach to study the meteorological characteristics of a site by means of radio sounding data was also previously used [75][73]. Advantageous for this map is that it may identify an area that is susceptible for winter lightning before a wind power plant is erected whereas the global lightning map

[91] uses LLS pre-recorded data which may show increased lightning activity after the wind power plant was erected. This section relates to paper [c.4].

3.5.2.1 Winter lightning pattern in meteorological data

In Section 3.3, an in-depth analysis of the meteorological conditions of winter thunderstorms conducted by radio soundings and radar observations revealed that the atmospheric conditions of these events were very similar in all cases. These conditions were characterized by ground temperatures slightly above freezing point, a relative distance of the $-10°C$ isotherm above the ground not exceeding $2000m$, a relative distance of the $0°C$ isotherm not exceeding $400m$, and wind velocities above $12\frac{m}{s}$. The temporal analysis of the thunderstorm revealed many low-amplitude discharges of a few kA in the vicinity of the wind turbines which were continuously recorded during a long time period up-till 18 hours. These discharge pattern are characteristics for winter lightning discharges. This observation indicates that winter thunderstorms, which produce lightning discharges, are characterized by steady lightning environments. This gives the possibility to investigate the atmospheric conditions with radio soundings which are usually performed every 12 hours. In addition, radar observations in Spain which were overlaid with LLS data revealed that the electrified clouds were moving from the sea towards the land. These storms are spatially spread over wide areas ($> 200km$). Lightning discharges were detected mainly within a range of $50km$ from the shoreline.

To summarize the observations, the following parameters are used as inputs for the meteorological model. All quantities can be determined from radio sounding measurements. Furthermore, a physical relation of the parameters concerning cold season lightning is highlighted. Microscale effects of the parameters due to topography cannot be modeled with this approach.

- The distance of the $-10°C$ isotherm to ground is based on the observations of cold season lightning which were reported in Japan and Spain. The parameter is used as an indicator to determine at which height the charge is located in the cloud [72]. A threshold value of $2000m$ to ground is used. Furthermore, few lightning activity was observed when the $-10°C$ isotherm was below a distance of $600m$ to ground [73][92][72].
- The distance of the $0°C$ isotherm to ground establishes the conditions of temperatures around the freezing point. Cold season thunderstorms developed in ground temperature below $0 - 6°C$ C. A threshold distance of $400m$ to ground for the $0°C$ isotherm is derived from the analysis of [92] for cold season thunderstorms.
- Wind Speed: Cold season thunderstorms are often, but not exclusively, combined with high wind velocities [93]. To define a threshold level for the model, a minimum value of $12\frac{m}{s}$ at ground level is used as observed in the analysis in [92].
- When cold season lightning was observed, significant humidity up to saturation was reported. Furthermore, precipitation in form of snow or hail was apparent. Often alternating high humidity and dry areas were observed. Since an investigation of the relative humidity $\%rh$ as function of the height during cold season thunderstorms remained inconclusive, the precipitable water content of a cloud provides a better

prediction for the moisture. The value determines the amount of water that can be potentially released by the cloud. The threshold of $9.5mm$ is used from [92].

- As observed in Japan [73], only the northwest coast of the main island is exposed to winter lightning. In Japan the main wind direction during the non-convective season is west-northwest, a correlation between exposure and wind direction is established. The clouds are discharged within the first tens of kilometers after the cloud reaches the main land. Similar observations were recorded with LLS and radar observations in Spain [92].

3.5.2.2 Meteorological model

The model uses the combination of meteorological and topographic data in order to show areas that experience similar meteorological conditions in which cold season lightning has been observed before.

Elevation data Publicly available elevation data are used from the Shuttle Radar Topography Mission (SRTM) dataset. An initial geospatial resolution of 30arc-second is further downscaled to about 2.46 arc-minutes in order to improve the calculation time of the model. The bounding box corner points of Europe are defined as Longitude ($-10°$, $30°$) and Latitude ($35°$, $60°$). This results in a resolution of 960x600 points. In terms of absolute tile sizes, one tile has metric distance of Longitude: 2.2 – 3.8 kilometer and Latitude: 4.4 – 5.3 kilometer, depending on the location (x,y). Since the map illustrates the potential risk for cold season lightning to wind turbines, each elevation point has been increased a difference of $\Delta h = 150m$, which assumes the total height of a recent generation wind turbine.

Meteorological data The weather data of 72 radio sounding stations is used to analyze the condition of the atmosphere. An overview of the locations of the radio sounding stations is presented in Figure 3.12. For the model, 5 years of data from the non-convective season (October 2009 - March 2014) is downloaded from the University of Wyoming. Usually, two measurements per day were obtained for each station at 00:00 UTC and 12:00 UTC; in the event of missing data, the results were interpolated from other radio sounding stations. Following data are available through radio soundings as a function of the altitude: pressure, temperature, dew-point, relative humidity, mixing ratio, wind-speed, wind direction, potential temperature, equivalent potential temperature, and virtual potential temperature. Furthermore, there are several sounding indices available which are derived from the above mentioned parameters. One of the indicators, the precipitable water W for the entire sounding, is used as indicator for a high moisture content which is often observed during cold season lightning. It is defined by the integrated mixing-ratio of water $x_w(p)$ as the function of pressure p multiplied by the inverse of the density of water ρ and acceleration of gravity g:

$$W = \frac{1}{\rho g} \int_{p_1}^{p_2} x_w dp \tag{3.2}$$

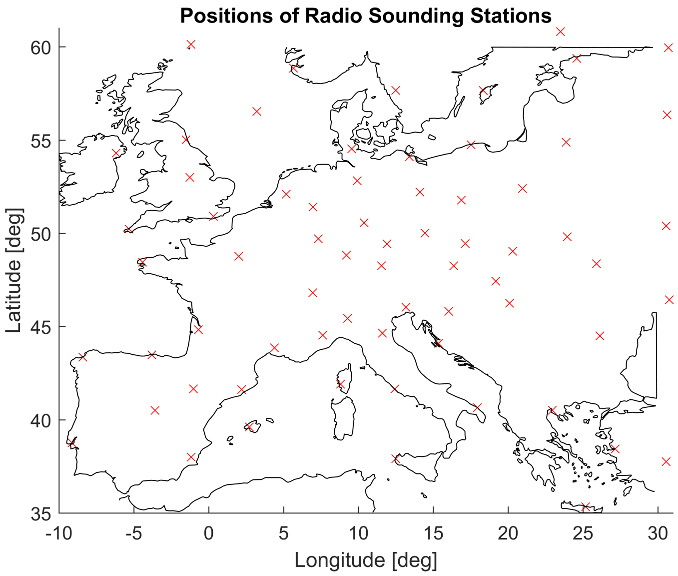

Figure 3.12: Overview of 72 radio sounding used for data analysis.

Implementation To automate the process, a script has been created which downloads the necessary weather data automatically, filters unusable data, sorts the datasets in the right format, and processes the information. For each half-day, one surface map of the $-10°C$ isotherm, one surface map of the $0°C$ isotherm, one surface map of precipitable water, and one streamline vector map of the wind direction were created. Furthermore, the wind velocity was calculated throughout the atmosphere for each step in altitude of $\Delta z = 41$ meters in order to approximate the wind velocities at each layer in the model. The data points of the 72 measurements are then linearly interpolated over the elevation grid (960x600 points) in order to have an evaluation of the weather conditions at each point (x,y). Locations outside the radio sounding stations are extrapolated with the nearest neighbor algorithm in the Matlab environment. After all the datasets were calculated for each day, the position (x,y) in Europe is individually evaluated according to the threshold criteria for cold season thunderstorms (Table 3.5). If the distance of $-10°$ isotherm is below 2000 meters and above 600m relative to the ground, the distance of the $0°$ isotherm is below 400 meters, the wind speed at ground is above 12 meters per second, and the precipitable water content is above 9.5 millimeter, the location is marked as potentially exposed to winter lightning on that day for the given time of the radio sounding (which is either 00:00 UTC or 12:00 UTC).

Table 3.5: Summary of the meteorological conditions which are used to determine if the conditions for cold season lightning conditions are met in a certain site.

Description	Parameter	Unit	Threshold	Source
Distance $-10°C$ isotherm to ground	$h_{-10°}$	$[m]$	600 - 2000	[73] [92] [72]
Distance $0°C$ isotherm to ground	$h_{0°}$	$[m]$	<400	[92]
Wind speed at ground	|v|	$[\frac{m}{s}]$	>12	[73] [92]
Precipitable water	W	$[mm]$	>9.5	[92]
Wind Direction at -10 isotherm	$\angle v$	$[deg]$	f(x,y)	[73] [92]

The analysis of the data revealed that often a cluster of exposed spots was marked, for instance at coastlines at mountainous areas. The influence of the wind direction is applied to deselect positions in the grid which were not facing the wind direction. This emulates the observation that upward lightning typically discharges in the first few kilometers at the coast, whereas there are only few or no discharges further inland. In other words, it reproduces the effect of a cloud with finite charge content which discharges preferably at the first locations where the previous four cold season criteria are met.

To perform the computation, the wind direction at the $-10°$ isotherm is calculated as a streamline vector map. Each grid element, is further classified into one of the cardinal or intermediate directions, as illustrated in Figure 3.13b. Then, the algorithm detects the neighbor elements of the marked position and evaluates whether it is the one of the first five elements towards the wind direction. Cardinal directions relate to the neighbor elements of the grid in horizontal or vertical manner, whereas intermediate directions use the diagonal elements in respect to the neighbor. If the element is equal or bigger than the sixth element in order, the location is deselected. An illustrative example of the process is shown in Figure 3.13a. Green elements indicate locations which are facing the calculated wind direction, whereas red areas are shielded by green locations. The red elements are deselected. The factor five in the model is a measure of distance and represents the movement of the cloud over the ground which presumably discharges within the first kilometers when the meteorological conditions are met. The factor five relates to $10-32$ kilometers of distance, depending on the location on the map. This evaluation is performed for each spot which fulfilled the first four criteria and is thereby marked with a one in the grid. Finally, the analysis is conducted for each time data set (twice a day) and the exposed locations are summed-up and normalized by the amount of years under survey.

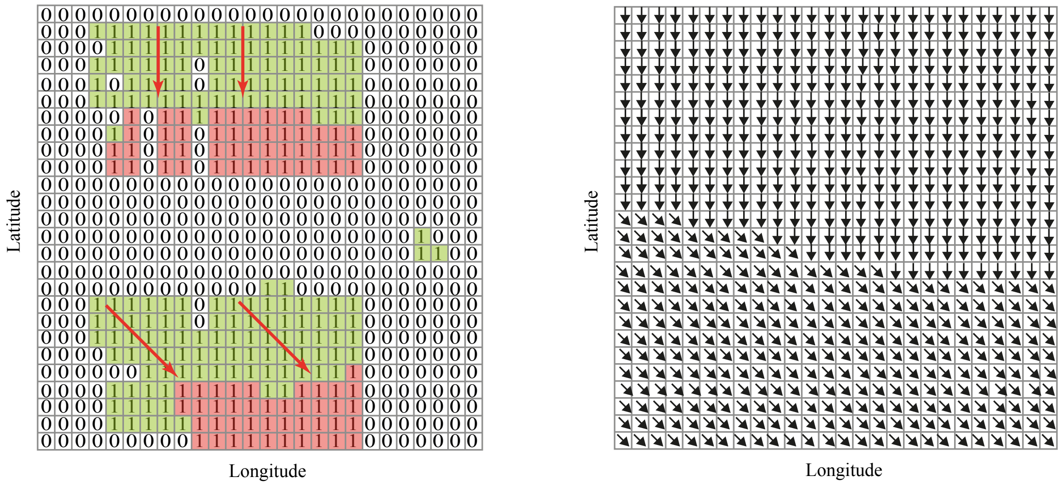

(a) Example of a section of the streamline vector map. The wind direction of the -10°C isotherm is calculated for each element based on the interpolation of the radio sounding data. It is further classified into one of the cardinal or intermediate wind directions. The figure represents only a small section of the map.

(b) Each location classified as exposed (1) is evaluated regarding the wind direction. Only the first 5 elements facing the wind direction (green elements) are kept. Red elements are discarded from the investigation. Notice, in the upper cluster, the wind direction is North, whereas in the lower cluster, the wind direction is North West. Red arrows indicate the apparent wind direction at location (x,y).

Figure 3.13

3.5.2.3 Results and discussion

In Figure 3.14, the results from meteorological assessment of Europe are illustrated. In this map, the x and y axis represent the longitude and latitude of Europe, respectively, and the z axis defines the number of days in which winter thunderstorm conditions are fulfilled. The visualization of the locations is performed with a color scale and an 2D grid according to the data point of the location. Certain hot spots can be identified in the map. The highest values are reported in descending order in the south of Italy around the volcano Etna (38.3 days/year), the mountain formation “Picos de Europa” in north Spain (34.6 days/year), and around the national park “Sierra Nevada” in the south of Spain (34.3days/year). Furthermore, exposed areas are found to be in the mountainous regions around the Alps and in the Pyrenees. These spots are clearly highlighted due to the big elevation difference compared to the adjacent surroundings. Smaller values of around 10 – 20 yearly winter thunderstorm days are indicated in the north of Spain, central/south Italy, the coastline of the Balkans, north of Africa and Scotland. Locations with less than 10 cold season thunderstorms days are Norway, some areas in central Germany, central Spain, south France, and the Transylvanian Alps. It needs to be emphasized that this map aims to indicate upward lightning areas due to meteorological measurements from radio soundings of cold season thunderstorm conditions in Spain and Japan. It does not provide any information of natural downward lightning.

In order to try to approach a validation of this map, several positions are marked with red and magenta color. Red circles indicate locations where frequent cold season lightning (hence cluster formation as indicated in Figure 3.9b) was observed by LLS or tower

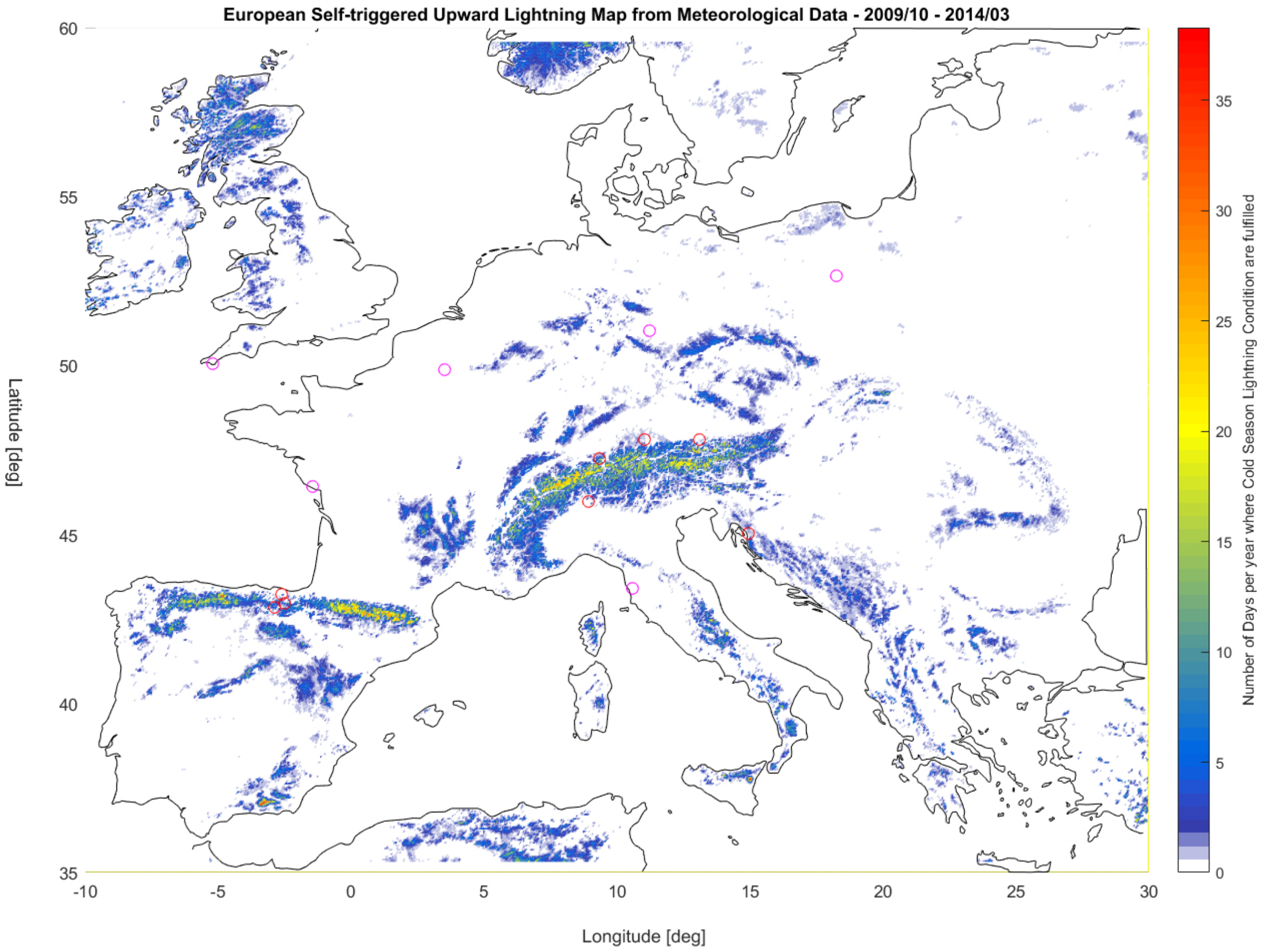

Figure 3.14: European map with locations indicated in which meteorological conditions for self-triggered upward lightning are fulfilled. The color scale on the right indicates the number of days per year, where cold season lightning is possible. Red circles indicate positions, where cold season lightning was observed with a LLS or is known to be apparent by instrumented towers (Wind power plants: Spain and Croatia; Instrumented Towers: Gaisberg Tower, Säntis Tower, Peissenberg Tower, Tower at San Salvatore). Magenta crossed circles indicate positions where no cold season lightning was observed with LLS (Wind power plant in Italy, France (2x), Germany, Poland, UK). Ground elevation offset is $\Delta h = 150m$ in order to evaluate the possible presence of wind turbines.

measurements in the past (Wind power plant in Croatia and Spain, Säntis Tower, Gaisberg Tower, Peissenberg Tower and Tower at San Salvatore) and magenta colored crossed circles indicate locations in which LLS data did not indicate the presence of cold season thunderstorms (Italy, France, Germany, UK, and Poland) [92][74]. Indeed, there is a tendency that positions indicated by red markers are located in the vicinity of predicted cold season thunderstorm areas. The usage of LLS data for verification of this map requires the detailed daily analysis of the meteorological conditions of the thunderstorm. Especially in South Europe, sporadically occurring high temperatures in October – March can trigger convective thunderstorms which cause natural downward lightning. These events are likely to be captured by LLS data which are then erroneously declared as cold season lightning. In order to validate this map further, more lightning current measurements are necessary which are preferably based on on-site measurements instead of LLS data.

3.5.2.4 Conclusion

In this section, the data of the meteorological analysis of cold season thunderstorms in Japan and Spain was used to define threshold values when cold season lightning was recorded in the past. Meteorological data of 72 radio sounding stations in Europe is analyzed for a 5 year period (2009-2014) in the cold seasons of these years from October until March. The data has been used in order to build a model that estimates the probability of exposure to cold season lightning all over Europe. For each tile of the map, the outcome of the model is the number of days in which meteorological winter lightning conditions are fulfilled. This may be used to estimate the risk of a potential wind power plant or structure to be affected by high frequent upward lightning attachments in the cold season. The conditions evaluated are valid for onshore sites only since there were not enough cold season lightning events at offshore wind power plants recorded. Some factors are definitely relevant such as the temperature gradient between the sea surface and the atmosphere layers above. These conditions are difficult to estimate with radiosondes launched from land and should be analyzed in a future work in order to refine the model for offshore sites. The model considers already the existence of tall structures all over the study area and estimates the exposure based on this. In the future, the method of this paper has potential to be improved by using numerical weather prediction models such as the Weather Research & Forecasting Model (WRF) model to obtain better temporal resolution of the cold season lightning conditions. This would also enable to investigate instability factors of the atmosphere, which are the results of convective processes. In general, the methodology to identify cold season thunderstorms directly based on conditional instability would be physically more meaningful instead of the comparison of few cold season measurement samples from radio soundings. Unfortunately, to the knowledge of the author, there is no instability indicator which allows to detect low-convective winter thunderstorms. Furthermore, an extensive amount of data processing resources would be necessary to make such computations on continental level.

3.6 Winter lightning in Japan

The special lightning environment created during winter thunderstorms leads to severe problems for the wind turbine industry. The north-west coast of Japan is one of the most affected areas by winter lightning on the planet.

The decision to dedicate an entire section of this thesis to winter lightning in Japan was motivated by the circumstance that the wind turbine industry reports frequent damages on wind turbines during the winter months in Japan. For instance, alone in the winter season of 2013 – 2014, in total eight severe wind turbine damages (blade rupture and falling, receptor falling, nacelle burnout) due to winter lightning occurred along the Sea of Japan [94]. Also a newly commissioned wind turbine with a certified LPS experienced fatal blade failure (blade collapse) due to lightning impact[95]. Further damages are reported on tall structures such as radar towers [75], transmission lines [96], and wind turbines [76]. Due to this reason, the lightning environment needs to be further studied and the reason for failure of wind turbine components needs to be determined.

A collaboration between the University of Tokyo, the Central Research Institute of Electric Power Industry (CRIEPI), GLPS, and DTU was established and a four month research stay in Japan was conducted from September to December 2016. During this time period, temporary access to the Japanese lightning data of the NEDO project (See Section: 2.2.4.2) and the JLDN LLS [97] was granted.

Two topics from this research stay shall be discussed in this section which are a lightning attachment analysis of upward lightning flashes of rotating wind turbine blades (Paper [j.1]/[c.5]) and an evaluation of the current parameters of active and inactive winter thunderstorms (Paper [c.7]). Subsequently, reasons and remedies or the increased failure rate of wind turbines in Japanese winter lightning areas are provided. Before these topics are discussed, a summary of previous work from researches regarding the classification and development of winter thunderstorms is provided.

3.6.1 Winter thunderstorm characterization

One of the first publications regarding winter lightning was performed by Takeuti and Nakano in 1976 [98]. The author highlighted the particularity that, in the observation period of the study, nine out of ten discharges lowered positive charge to ground. In the following years, international research teams published various research regarding the anomalies of Japanese winter thunderstorms at the Hokuriku coast [99][100].

Characteristic for winter thunderstorms are a rather low cloud height compared to summer thunderstorms combined with a lower located charge region [72]. Recent Lightning mapping array (LMA) measurements indicate that the charge structure of winter thunderstorms can be bipolar or tripolar and the dominant charge structure can alternate between negative and positive polarity in between the same thunderstorm. Unlike summer thunderstorms, the horizontal extension of a winter storm is usually much larger (by a factor of 10) compared to the vertical extension [101]. A high fraction of positive and bipolar CG lightning as well as occasional sprites may be observed [102]. The reduced distance of the cloud to the ground creates a higher electric field on ground, leading to a high fraction of upward lightning discharges initiated at tall structures [103]. An illustration of the resulting electric field of different thunderstorm types is illustrated in Figure 3.15. As can be seen, winter thunderstorms are able to create several times the magnitude of electric field on ground as compared to summer thunderstorms. Since the electric field on ground is higher, also space charge generation from ionization is more pronounced in winter thunderstorms. The average flash density N_g of winter thunderstorms is rather low compared to summer thunderstorms [104][105].

The cloud electrification processes of winter lightning are still not fully defined and are subject to academic discussions. Probably the best studied meteorological driver of winter thunderstorms is the cold air over warm water scenario. In order to create atmospheric instability (creates vertical air motion) which delivers moist air in the colder regions of the cloud, cold dry air has to be located above a warm surface such as a ocean [100]. Snow covered surfaces (on land) reflect the majority of energy back into space and are inappropriate to generate sufficient heat. Due to this reason, most winter lightning observations are located in the vicinity of water which enables a heating process during the cold season. Instability creates turbulent vertical movement inside the thundercloud. The moisture from the warm phase near the ground is transported in higher levels of the cloud where snow and graupel particles are created. By collision of the two particle types, electrically charged regions in the cloud are produced.

Typically, winter thunderstorms develop in a surface temperature range of $-5°C$ to $2°C$ following the Clausius-Clapeyron relationship which dictates the temperature dependence of the equilibrium water vapor concentration [104]. If the surface temperature is lower than $-5°$ insufficient moisture is delivered to the storm which inhibits the possibility of snow. On the other hand, if the surface temperature is too high, the latent heat is to big to create graupel particles.

A classification between the intensity of winter thunderstorms was performed by [73]. The author introduced a separation of two different winter thunderstorms types based on the recorded LLS patterns and the total detected amount of flashes. The "inactive type" with

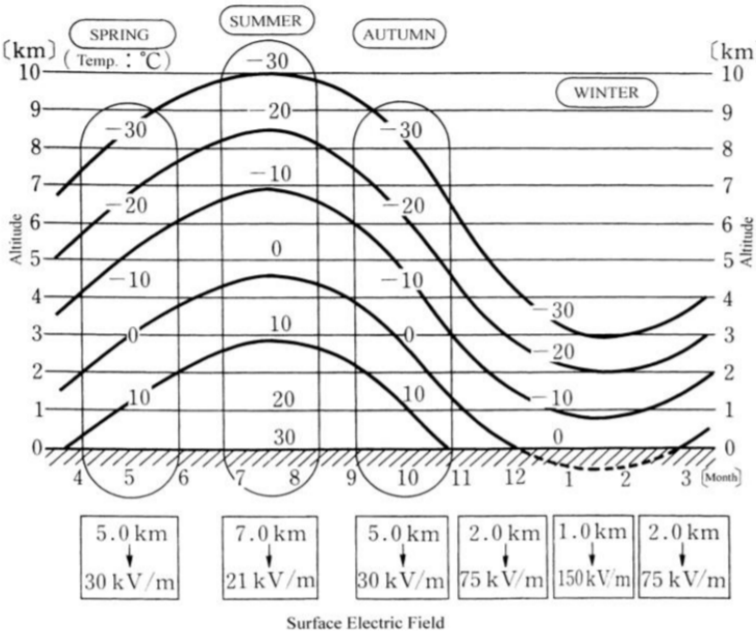

Figure 3.15: Electric field on ground as a result of different thunderstorm types and their characteristic height. Graphic adapted from [105]

less than 100 lightning detections and the “storm type” with more than 1000 lightning detections per day - where the latter is clearly the more dangerous type for wind turbines. This terminology is used in the next section and current parameters of upward lightning discharges measured in wind turbines during winter thunderstorms are cross-correlated with the lightning activity of winter thunderstorms.

3.6.2 Current parameters of active and inactive winter thunderstorms in Japan

During the external stay in Japan, an investigation of the intensity of winter thunderstorms in Japan was performed. Current measurement data from the NEDO project are compared to lightning activity determined by LLS data in order to evaluate if particular types of winter thunderstorms are especially dangerous to tall structures.

3.6.2.1 Method

This work utilizes LLS and lightning current measurement data from Rogowski coils. Both technologies are biased by shortcomings of data acquisition, especially for upward lightning with currents having low time-derivatives. This section elaborates on the limitations of the datasets and provides input for data interpretation. Beforehand, the area under investigation is illustrated and the method for the cross-correlation of the datasets is explained.

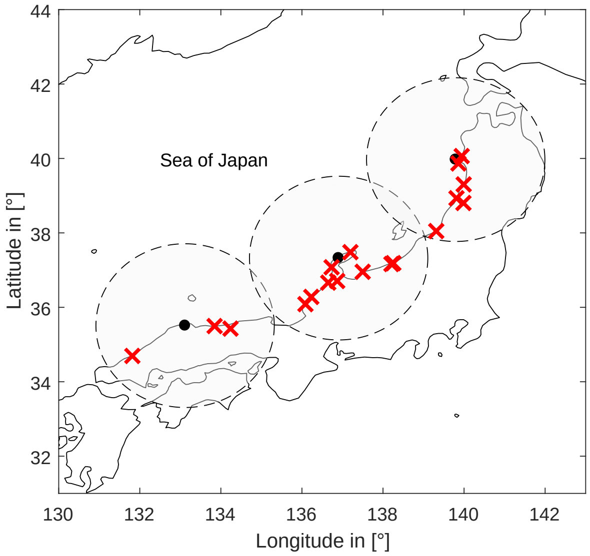

Figure 3.16: Geographical orientation for the study area Japan. The grey circles indicate the area for analysis of JLDN data. The red crosses mark the positions of wind turbines where lightning current measurement was performed.

Overview The area under investigation is on the north-west coast of Honshu Island in Japan. This area is characterized by frequent winter lightning which has been subject to previous studies for instance by Saito et al. [21] or Ishii et al. [10]. In Figure 3.16 the dashed circles indicate the area where the amount of daily lightning flashes are determined by means of LLS data. The red crosses are the locations of wind turbines which are used for the lightning current measurement. For the investigation, data from all sources were available in a time frame of October 2008 - March 2013.

Details regarding JLDN used in this investigation JLDN, a LLS which provides stroke detection data, covers entire Japan, and as of December 2015, it operated six IMPACT ESP sensors, three LPATS-IV sensors, eleven LS7001, and ten TLS200 sensors. The position of the sensors can be found in Sugita and Matsui [97]. The detection efficiency of LLS was previously discussed in Section 3.2.

The classification of active and inactive thunderstorms in this study is based on a fixed number of lightning detections by JLDN as proposed by [73]. As sensor technology improves, however, more flashes are detected, so it is rather unfavorable to use fixed numbers as classification threshold. For this work, the classification aligns with previous work since the observation period and the corresponding technology are similar to those of Fujii et al. [73] (2008 - 2009). For the analysis of JLDN data, no distinction was made between data of CG and IC events in the process of strokes detection since upward lightning is often missed or misclassified as IC lightning by LLS as earlier discussed in Section 3.2.

Details regarding current measurement system Current measurement data used in this work are based on the lightning data obtained in the NEDO project from 2008 - 2013, which measured lightning current at 27 wind turbines with Rogowski coils in Japan [9]. As indicated in Figure 3.16, only current measurements from 18 turbines are used. Data from the remaining nine turbines were not considered since only few or no lightning strokes were measured at these locations. The frequency range of the Rogowski coils used was $0.1Hz$ to $1MHz$. Upward lightning currents may be characterized by long duration continuous DC components. Therefore, the cut-off frequency of $0.1Hz$ was not sufficient and digital compensation down to $0.01Hz$ was applied to the current measurements. One example current waveform of upward lightning is illustrated in Figure 3.17.

Methodology A flow chart of the data analysis to correlate LLS data and current measurement is indicated in Figure 3.18. Initially, the time reference frame of LLS data and current measurement data was aligned to the same time zone. Subsequently, each time stamp of the 814 current measurements was verified if a valid current measurement waveform was available. The timestamp was verified if it was recorded in the non-convective months November, December, January, February, or March. In the next step, the number of JLDN detections is determined in each observation area, a circle having 200km radius shown in Figure 3.16, six hours before and after the lightning incidence was recorded by the current measurement. In fact, this approach differs slightly from the method used in [73] and [97] since the time reference is not determined by the diurnal cycle which can introduce misinterpretation if the discharge appeared around midnight. Instead, the approach of a fixed time interval provides a more accurate investigation of the lightning environment before and after a discharge was measured. With this method, the general lightning activity of the surrounding area during a winter thunderstorm was evaluated.

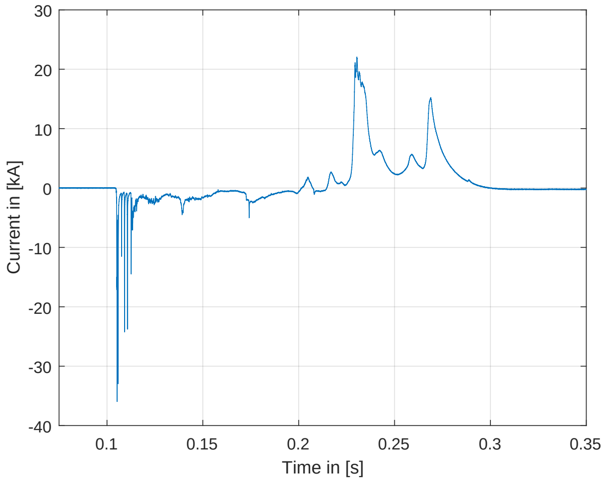

Figure 3.17: Measured bipolar upward lightning current waveform with Rogowski coils. $Q = 628C$, $\frac{W}{R} = 4.2MJ/Ohm$, $I_p = -36kA$. Data from the Nedo project [9].

The calculation terminates when each measured lightning discharge which is characterized by related peak current, charge and specific energy is correlated with the number of nearby detected lightning flashes.

3.6.2.2 Results

Figure 3.19 and 3.20 illustrate the charge, specific energy and peak current distribution as a function of the number of detected LLS sources. From initially presented 834 observed lightning discharges of the NEDO report, the investigated number of discharges was reduced to 814 since only 18 instead of 27 wind turbines were investigated. Furthermore, 123 datasets did not include current measurements and where therefore excluded from the investigation. 50 events were recorded outside the specific months November - March and were consequently removed from the investigation. Additionally, at 10 events, there were no lightning events detected by JLDN in the observation area. 33 events of current measurements had a charge content of less than 3C and were removed from the investigation since flashes with such small charge content may be classified as attempted leaders instead of upward lightning discharges. The remaining 598 events are discharges in the winter months all classified as upward lightning discharges. 214 events were recorded when less than 100 lightning flashes were detected nearby, whereas in 384 events, more than or equal to 100 flashes were detected. In Figure 3.19a, the charge distribution as a function of the number of lightning detections within six hours from the current measurement is illustrated. The vertical red line indicates 100 lightning detections, which was defined as the threshold of inactive thunderstorms as described in [73]. Apart from the individual data points, the average value of each logarithmic tile is determined and illustrated with a black line in the figure. The highest measured charge amount was 1272 C and the analyzed lowest charge amount was 3 C. The average amount of charge of one flash at storms of lightning detections below 100 is 53 C whereas it is 99 C at storms of above 100 discharges. In the charge plot two different areas are highlighted which show particularities in the data. The arrow along I indicates the tendency that the maximum measured amount of charge in flashes increases with the number of JLDN detections. The data suggests

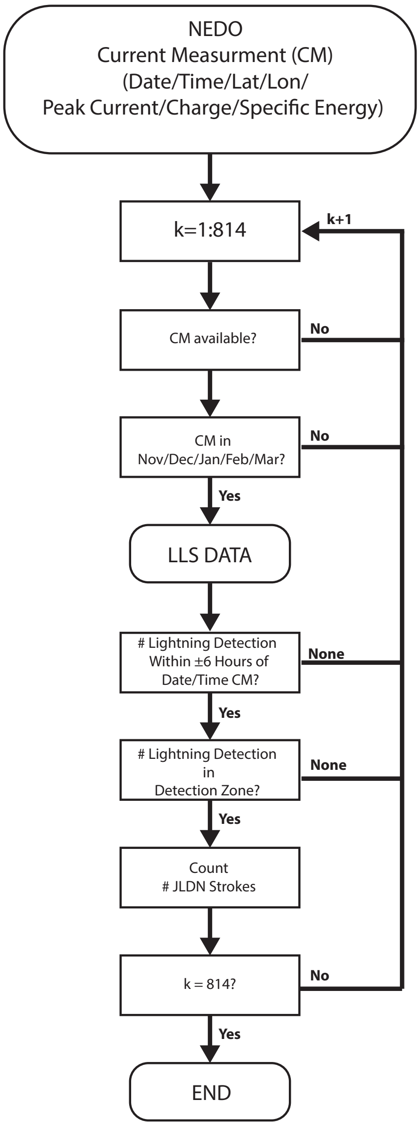

Figure 3.18: Flowchart to derive correlation between current parameters and LLS data (CM = Current Measurement, # = Number)

that inactive winter thunderstorms are characterized by lower amount of charge in a flash compared to active thunderstorms. The arrow along II highlights the tendency for active type thunderstorms that flashes contain statistically lower maximum charge values as more flashes are reported in the nearby environment. One data point, however, lies outside this indicated arrow II and is characterized by a charge transfer of 1272 C. The characteristic of the specific energy as a function of lightning activity is illustrated in Figure 3.19b. The gradient of the arrows in this figure is larger compared to the charge plot.

Lightning from inactive thunderstorms tend to have lower specific energy contained in their flashes and very active thunderstorms above 600 flashes also produce flashes of reduced specific energy values.

Peak current distribution as a function of lightning activity is illustrated in Figure 3.20. Bipolar flashes are included in this analysis, and their polarities are defined by the polarity

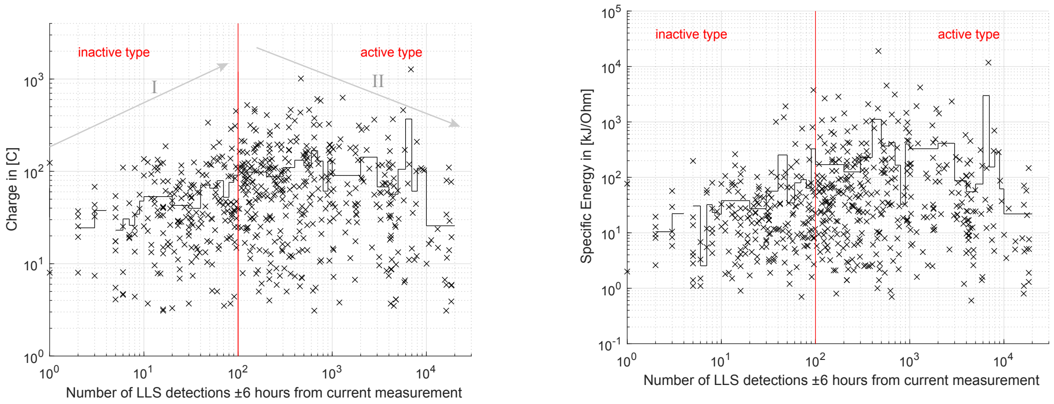

(a) Flash charge as a function of measured lightning activity. Black line indicates mean value of each logarithmic tile.

(b) Specific energy as a function of measured lightning activity. Black line indicates mean value of each logarithmic tile.

Figure 3.19: Current parameters of winter lightning thunderstorms as a function of thunderstorms activity

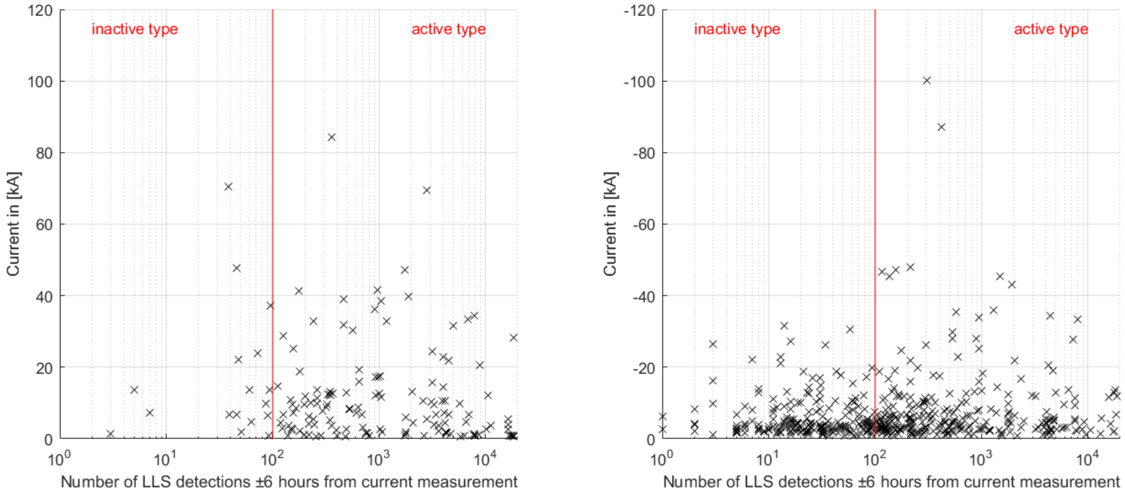

Figure 3.20: Positive (left) and negative (right) peak current distribution as a function of nearby lightning detections. Notice, there are only few positive registrations below 100 discharges.

of highest peaks of currents. 140 positives and 458 negative discharges were recorded. It can be noticed that 17 out of 123 positive discharges (14%) were recorded when inactive winter thunderstorms with less than 100 detections were registered. The reduced amount of positive discharges during inactive winter thunderstorms may also be a reason for the limited charge and specific energy transfer during these storms, since positive thunderstorms are known to lower higher amount of charge to ground. In comparison, discharges of negative polarity occur in 197 out of 214 (92%) events during inactive thunderstorm activity. Inactive thunderstorm activity is evidently dominated by negative polarity events. Dependence of peak currents on activity of storms is not as clear as for the plots of charge and specific energy. Analyzed distributions of charge, specific energy and peak current for active and inactive storms are listed in Table 3.6, as well as the number of strokes.

3.6.2.3 Discussion

From the investigation, approximately 36% (214 of 598) of all winter thunderstorms were classified as the less dangerous inactive type with lower than 100 lightning detection. The remaining 64% lightning incidences at more than 100 nearby lightning locations belong to dangerous type storms with 95 percentile values of charge and specific energy of 318 C and 1 MJ/Ohm, respectively. There is no substantial difference between the peak current values; however, inactive winter thunderstorms show reduced amount of positive discharges. Looking strictly at current parameters, the most dangerous winter thunderstorms are the ones between 400 and 3000 discharges which report the highest specific energy and charge values.

Another discussion can be taken into consideration when investigating the height of the minus ten degree isotherm which is often associated with the height of the negative charge region in the cloud. For each lightning day, the minus ten degree isotherm was extracted from the nearest radio sounding stations which was closest to the measured location of the wind turbine. As can be seen in Figure 3.21, the height of the minus ten degree isotherm increases with the number of LLS locations in the surrounding area. The difference between main charge region in inactive and active thunderstorms can reach up to 3 km and therefore the leader lengths must also be significantly different. This, in turn, may be reflected in different current wave shapes and different current parameters.

Table 3.6: Statistical key parameter derived for active and inactive thunderstorm type (Number = number of events, Mean = average value, 50th pct. = median value, 95th pct. = 95th percentile, Max= maximum value).

	Charge		Specific Energy		Positive Current		Negative Current	
	Inaction [C]	Active [C]	Inactive [kJ/Ohm]	Active [kJ/Ohm]	Inactive [kA]	Active [kA]	Inactive [kA]	Active [kA]
Number	214	384	214	384	17	123	197	261
Mean	53	99	75	275	15.3	12.1	-6.1	-8.7
50th pct.	36	62	15	35	8.5	7.4	-3.8	-4.9
95th pct.	137	322	202	1042	59.1	39.2	-18.3	-31.6
Max	450	1272	3760	19000	70.4	84.5	-31.5	-100.1

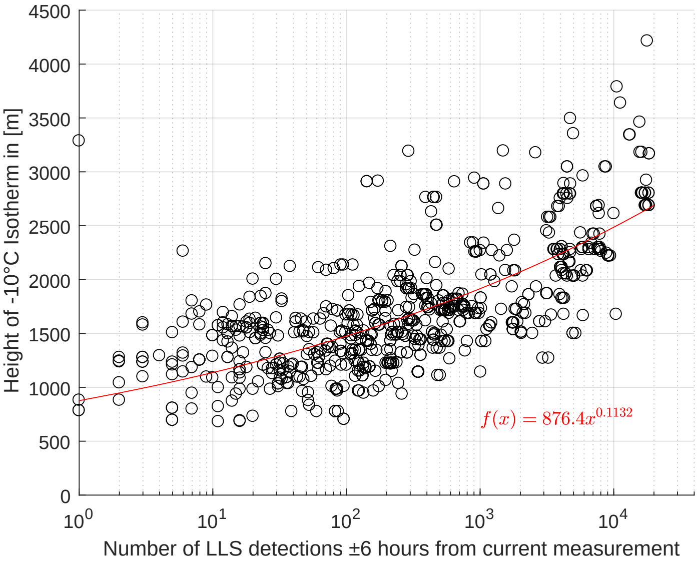

Figure 3.21: Height of the -10 degree isotherm dependent on lightning activity.

The results indicate that lightning flashes from winter thunderstorms of inactive type are typically characterized by lower current parameters in transferred charge and specific energy. This implicates that the threat of damage to a wind turbine blades may also be less and turning-off wind turbines during winter thunderstorms with low flash rate might be critically discussed.

3.6.2.4 Summary

From the investigation of current parameters as a function of lightning activity following conclusions can be drawn. Winter thunderstorms with low lightning activity are characterized by lower amount of charge and specific energy compared to winter thunderstorms with higher flash density. Therefore, not only the frequency of upward lightning attachments is limited in these storms but also the immediate threat of energetic lightning to structures is reduced. It is noticeable that positive discharges are rarely reported at inactive type thunderstorms which are commonly associated with larger charge and specific energy.

3.6.3 Upward lightning attachment analysis on rotating wind turbine blades

In this section, an analysis of video recordings of upward lightning discharges to wind turbines during winter thunderstorms are presented. 172 video recordings of lightning discharges on rotating wind turbines are analyzed and attachment angle, detachment angle, and the resulting angular displacement were determined. A classification between self-initiated and other-triggered upward lightning events is performed by means of video analysis.

The video recordings from upward lightning discharges on rotating wind turbines were analyzed in order to document lightning attachment behavior which can be used to validate or reject numerical models of the attachment location.

All discharges were recorded in the non-convective months from November – April. Swept plasma channels, which form after the upward lightning leader attached to a charge pocket in the cloud (Figure 3.22), are characteristic for long duration lightning flashes on rotating wind turbines. The pictures originate from the NEDO project dataset [9]. The plasma channel, which is attached to the metallic tip receptor, is dragged along the circumference of the rotor and exposing the trailing edge of the blade to a high energetic arc.

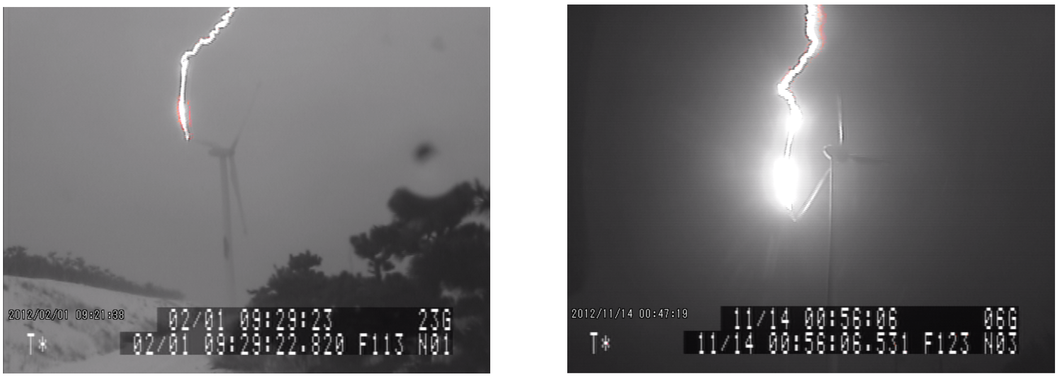

(a) (b)

Figure 3.22: Upward lightning discharges in winter thunderstorms with typical swept channel due to long current pulse duration

This work investigates 12 wind turbines which are located along the Sea of Japan as indicated in Figure 3.23. The video recording system captured images with 30 fps which provides one picture every 33 milliseconds. Even though the frame rate is low, due to the characteristic long duration discharges from the winter discharges in Japan, the recordings provide sufficient quality. Figure 3.24 illustrates the angular reference frame which is used in this work. 180° represents a vertical blade facing upwards, whereas 90° and 270° represent horizontal blade alignment with ascending and descending blade movement, respectively. All angle estimations are derived by visual inspection of video data and may be biased by subjective error. An accuracy tolerance of ±10° may be assumed. The blue area indicates the angle where a lightning stroke was attached to the blade and swept along the trailing edge of the receptor.

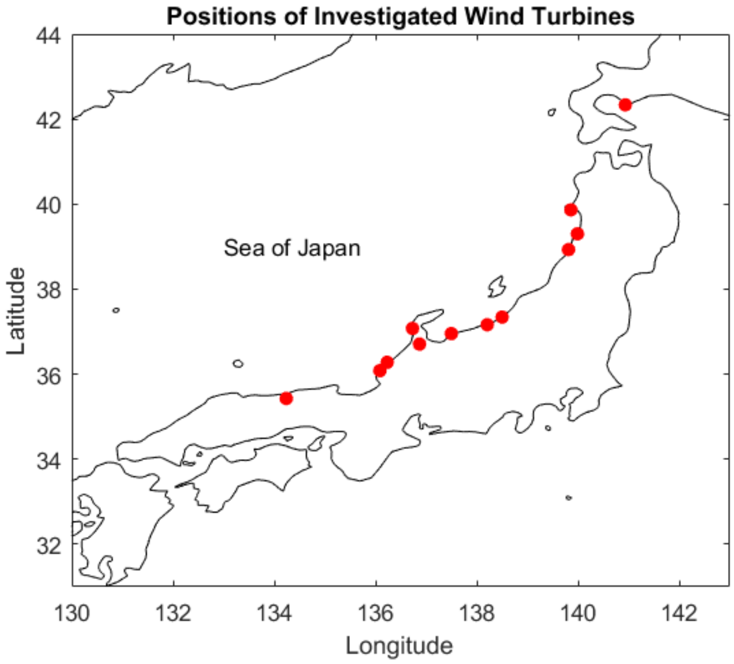

Figure 3.23: Investigated wind turbine locations in Japan.

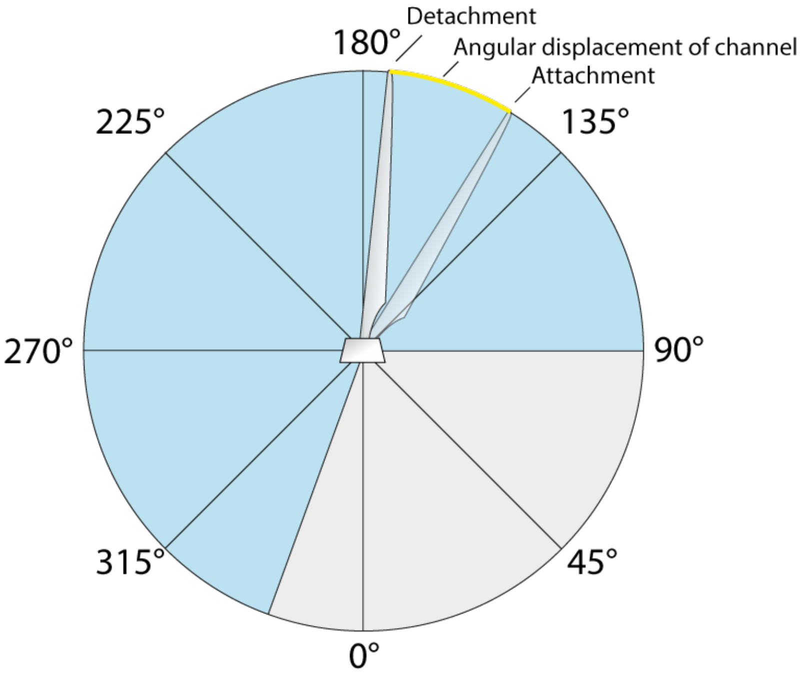

Figure 3.24: Angular reference frame. The blue area indicates the angle where the plasma channel was attached to the blade.

In Figure 3.25 each individual lightning incidence is represented by a bar which provides information about the attachment angle, the detachment angle and the resulting displacement angle. Several observations can be drawn from this figure. Attachment of lightning strokes was recorded from 90° to 270°. The longest observed discharge was

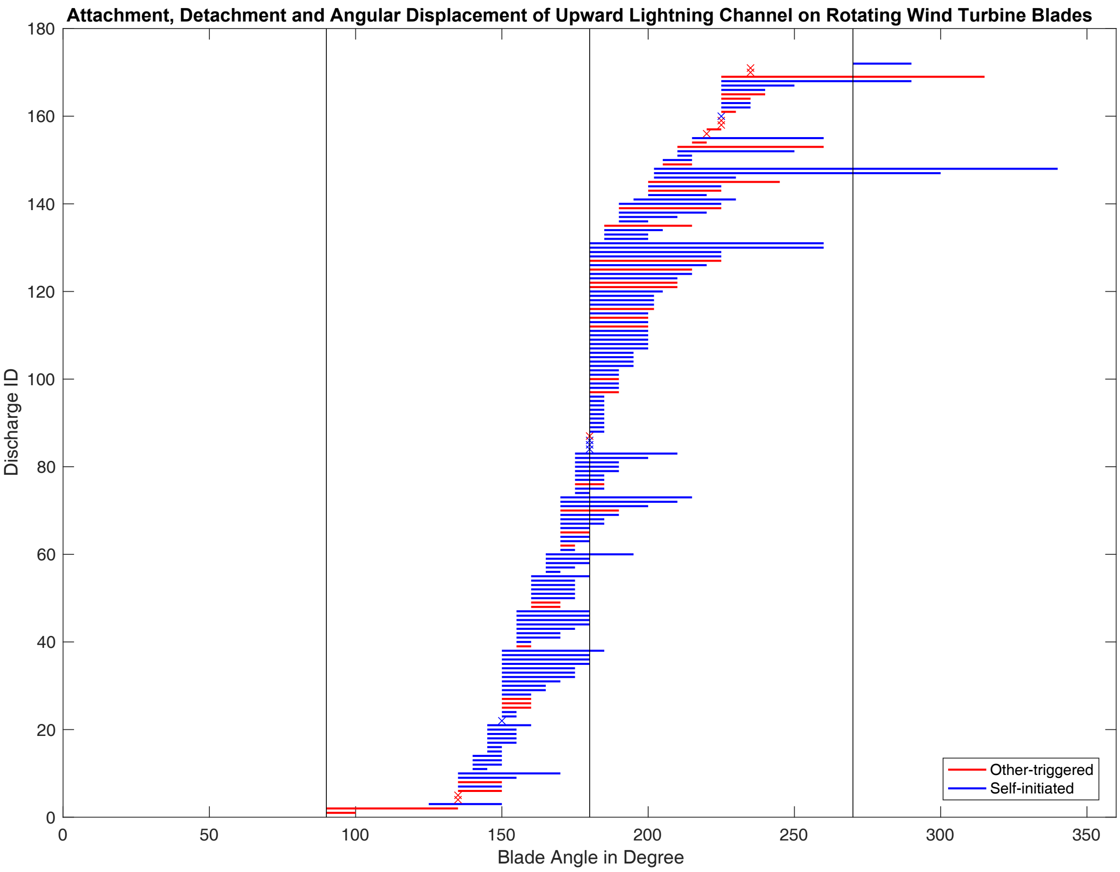

Figure 3.25: Attachment characteristics of 172 upward lightning discharges on wind turbine blades. Each bar represents an individual lightning discharge to a wind turbine. The start and the end positions indicates the attachment and detachment position of the blade, respectively. A cross indicates a short duration (1 frame) lightning event.

characterized by a timespan of 0.63 seconds, attached to the blade around 200°, and detached at an angle of 340°, where the blade was nearly facing vertically towards the ground. The average visible timespan for a discharge was 0.22 seconds. 80 out of 172 (46%) of all incidences appear between an angle of 170° to 190° which represents a vertical blade facing up. In 60 out of 172 (35%) of the cases the attachment happened during the ascending movement ($< 170°$) of the blade whereas in 32 out of 172 (19%) of the cases, the blade was in descending movement ($> 190°$). Therefore, upward lightning initiation is most frequently observed when the blade is vertical, which represents also the condition where the electric field is the highest at the extremities of the blade. The ascending phase of rotation has about double the amount of discharges compared to the descending phase. One explanation for this observation could be that the electric field in the descending phase of the rotation is reduced by lagged space charges which built-up on the trailing edge of the blade. During the ascending phase; however, the electric field around the leading edge of the blade is not biased by space charges since the impact of the rotation sweeps them towards the trailing edge [32].

A short duration attachment, which was visible only for one frame, is indicated with a cross. 159 out of 172 video recordings were longer than two frames whereas the remaining

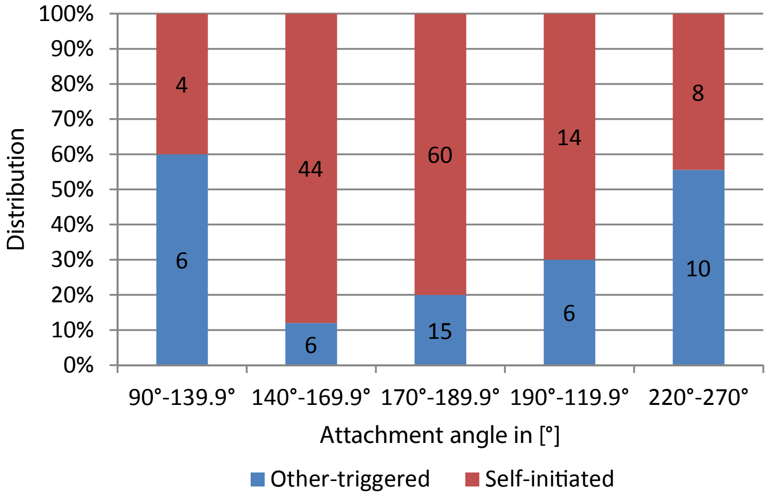

Figure 3.26: Separation of self-initiated and other-triggered lightning discharges according to the attachment blade angle. Amount of events in each category are indicated inside the bar plot.

13 events showed lightning events for only one frame which may be classified as attempted leaders or very short duration incidences. There was no observation of a simultaneous discharge from two blades or a lightning discharge which terminated in a new attachment point during the dart leader period (for instance nacelle or inboard). One out of 172 cases evidently developed an upward lightning leader from the nacelle. In this case, the rotor was in a Y position (blades at 135° and 225°). Furthermore, a classification between self-initiated and other triggered lightning discharges is performed. Each video recording was evaluated weather a visible lightning event was observed prior to the lightning attachment (indication: illuminated one - four frames before the attachment). Limitations apply with this classification since the video observations may not be able to show the preceding flash. Therefore, there is a possibility that a fraction of declared self-triggered lightning discharges

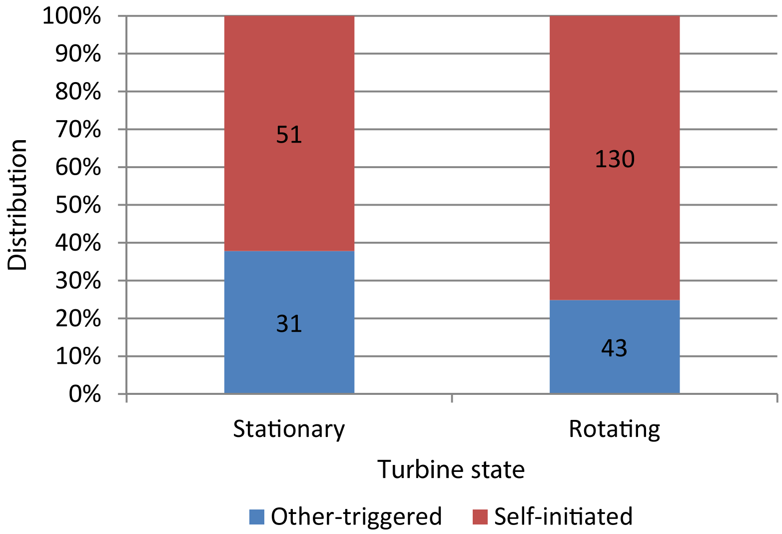

Figure 3.27: Lightning incidences of rotating vs stationary wind turbine blades.

may actually be other-triggered. Nevertheless, Figure 3.25 shows that a high fraction of lightning discharges are self-initiated when the blade is vertical; however, discharges initiated from a horizontal blade experience a higher fraction of other-triggered sources. The angular dependencies between other-triggered and self-initiated upward lightning discharges are also illustrated in Figure 3.26. 43 out of 172 (25%) upward lightning flashes are marked as other-triggered lightning events. Considering the tendency that a higher fraction of upward lightning flashes connect to a horizontal blade when triggered by another flash, the position and the vector of the triggering lightning discharge together with the resulting electric field change of the stroke may impact the starting point (even though the blade may not be vertical) of the upward leader.

The charge and specific energy as a function of flash duration is illustrated in Figure 3.28a and Figure 3.28b, respectively. From the graphs it can be seen that a long flash duration is not automatically correlated to a high value of charge or energy. Initial continuous currents of a few hundred amperes can establish such relatively weak and long duration flashes. Charge values above 300 C were recorded in a with a time period of 0.2 – 0.47 seconds.

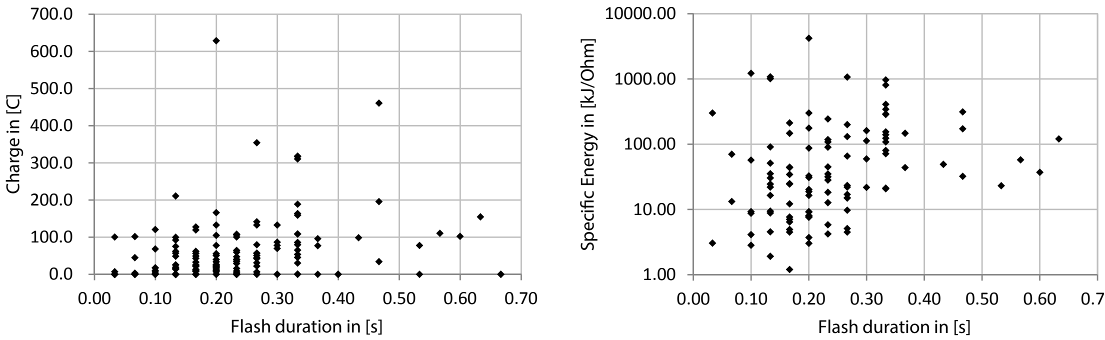

(a) Charge amount of upward lightning flashes as a function of flash duration

(b) Specific energy of upward flashes on rotating wind turbines as a function of flash duration

Figure 3.28

3.6.3.1 Current parameters from stationary and rotating blades

In this section, some derivatives from current parameters of rotating and stationary wind turbines are briefly compared to investigate if there are distinct differences between the two scenarios. Simultaneous current measurements and video recordings were available from 43 flashes on stationary wind turbines and 115 flashes on rotating wind turbines. The data was measured by utilization of Rogowski Coils. Further information about implementation, acquisition and data post processing of the system can be found in [10]. Figure 3.29a and Figure 3.29b illustrate the probability distribution of charge and specific energy, respectively. Seven out of a total of 158 flashes exhibited larger charge amounts than $300C$, which is the maximum charge value for a flash for LPL 1 for wind turbines according to [24]. On the other hand, none of the flashes exceed the specific energy testing requirement of $10\frac{MJ}{\Omega}$. As can be seen, only slight differences between the rotating and stationary discharges can be found. The charge does not show particular differences apart that the two highest values are related to the rotating state. The specific energy of stationary wind turbines is slightly reduced between the 50% to the 90% area; however, above $300\frac{MJ}{\Omega}$ the differences are minimal. Interestingly, all measured upward lightning discharges on stationary wind turbines which exhibited higher charge values ($> 100C$ and $1\frac{MJ}{\Omega}$) were situations when the wind turbine was manually shut-off due to thundercloud warning systems (several wind power plants in Japan need to be turned-off during thunderstorm activity as a safety policy) and not due to of a lack of wind. This statistics shows that disabling wind turbines during stormy conditions does not provide protection from flashes with high charge and specific energy content. Furthermore, flashes which are intercepted on stationary wind turbines due to weak ambient wind speeds are likely to have limited charge and specific energy content. The reason for the occurrence may be a limited charge separation process as a result of the low resulting vertical updraft velocity. Also the peak current parameters show only minor differences, with a tendency that stationary wind turbines experience slightly lower mean peak current values. Peak current values of upward lightning are reported to be well below $50kA$ with only a few exceptions.

Concluding from this statistic, there is no evidence that the exposure intensity (current parameters) vary depending on the rotating and stationary state. From this point of view, the decision to turn-off wind turbines during or before thunderstorm activity as a protection measure might not be justified; however, disabling wind turbines may help to prevent an extension of damages after lightning impact.

3.6.3.2 Conclusion

This work presents the results of an extensive video analysis of upward lightning discharges to wind turbines, which were recorded in the winter months from 2008 – 2013. The attachment point, detachment point and the duration of 172 upward lightning discharges to rotating wind turbines are investigated. Conducted current of upward lightning can be characterized by a long duration and can transfer a high amount of charge to the ground. Shortly after the leader connected to a charge pocket in the cloud, the plasma channel is

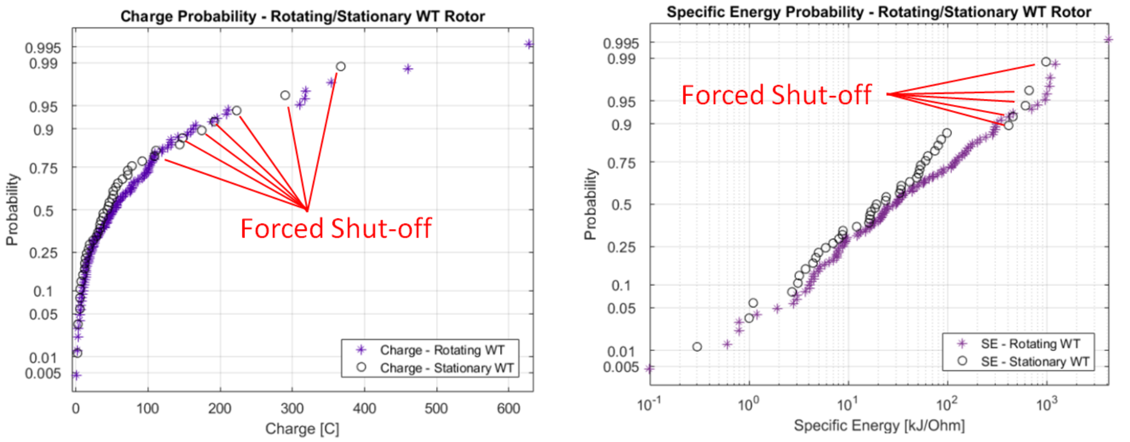

(a) Charge distribution of rotating/stationary wind turbines. On stationary wind turbines, charge values above 100C were measured when turbine was stopped manually.

(b) Specific energy of rotating/stationary wind turbines. On stationary wind turbines, specific energy values above 1 MJ/Ohm were measured when turbine was stopped manually

Figure 3.29

pushed towards the trailing edge due to the resulting velocity of the blade tip. Therefore, the majority of the energy of the flash enters the wind turbine from the trailing edge of the tip receptor. Furthermore, the arc may cause pollution of the non-conducting glass-fiber material around the receptor due to vaporized metal, which, in turn, can influence the susceptibility to blade puncture. Wind turbines manufacturers operating in severe upward lightning areas should address these observations in their receptor design. Flashes were characterized into self-initiated and other-triggered events by means of video analysis. Even though a fraction of flashes may have been misclassified, the tendency that horizontal blade alignments are triggered by other flashes was established. Furthermore, the attachment angle of other-triggered lightning events are scattered throughout the circumference from 90° till 270°. Self-initiated discharges are most frequently observed at vertical blade alignment. A comparison of current parameters from stationary and rotating rotors reveal no substantial differences between the two operational modes.

3.6.4 Reasons and remedies for increased failure rate in winter lightning areas.

This section analysis possible reasons why structural damages on wind turbines from lightning strikes are often reported in winter lightning areas such as Japan. Alone in the winter season of 2013 – 2014, in total 8 severe wind turbine damages (blade rupture and falling, receptor falling, nacelle burnout) due to lightning occurred along the Sea of Japan [94]. Subsequently, suggestions which kind of lightning protection solutions may increase the reliability of wind turbines are provided.

3.6.4.1 Increased rate of lightning attachment

The first crucial point to be made is that wind turbines may get struck several times more often in winter lightning sites compared to a typical site which are exposed mainly during the convective season (natural downward lightning). Typically, the current parameters

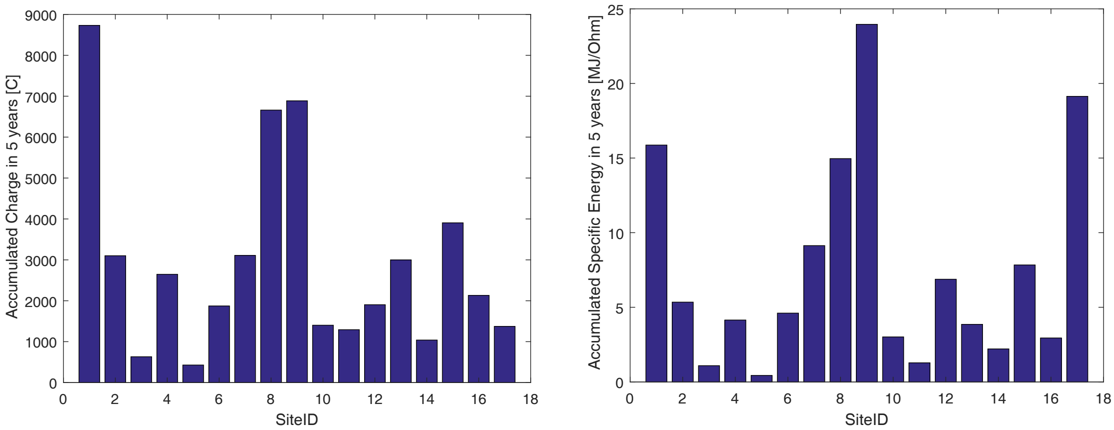

(a) Charge

(b) Specific Energy

Figure 3.30: Accumulated values of 17 wind turbine locations in the winter lightning area in Japan during 5 years period of the NEDO measurement campaign [9].

of upward lightning strikes are well within the standard test requirements of the IEC 61400-24 standard as mentioned in 2.2.4.2. Charge, specific energy or peak current are exceeded only in very few instances. It is evident, however, that the accumulated charge transferred by lightning during a year can exceed a value of more than $8000C$ as reported from the Gaisberg Tower [66]. The accumulated charge in a lightning flash is responsible for material removal around the injection point (receptors), spark gaps in the LPS design and the exit point (grounding electrode). From the data of the NEDO report [9], the accumulated charge and specific energy for 17 wind turbine sites in the winter lightning area is illustrated in Figure 3.30 for a five year period. As can be seen, the maximum accumulated charge for Site 1 was $Q = 8730C$ which corresponds to $Q = 1746C$ in yearly lightning charge exposure. The mean and median yearly charge values of all 17 sites are $Q = 563C$ and $Q = 403C$, respectively. Compared to the Gaisberg Tower [66], the values for charge Q are lower for the individual wind turbine sites in winter lightning region. It should be noted, however, that lightning attachments to the wind turbines sites in Japan are likely to be distributed among several wind turbines (or nearby structures) whereas the Gaisberg Tower is by far the highest elevated structure in the area and is expected to receive the majority of flashes from nearby winter thunderstorms. With this argument, an isolated wind turbine in winter thunderstorms in Japan may receive more charge and specific energy than illustrated in Figure 3.30.

A photograph of a wind turbine tip receptor (cap-type formed as winglet) from a wind turbine which operated in winter lightning area for several years is depicted in Figure 3.31. As can be seen, the trailing edge of the receptor is degraded due to the high amount of upward lightning flashes with high charge content. The functionality of the receptor was not influenced by the removed metal. The deformation of the receptor may even be beneficial since the protruded electrode geometry enables easier formation of upward lightning leaders which helps to reduces attachment failure to undesirable location inside the blade.

From Figure 3.31, it can be seen that the receptors of wind turbines in winter lightning areas need to be designed to withstand a high rate of material removal. Alternatively, a regular inspection of the lightning termination system seem mandatory in order to ensure reliable operation of the wind turbine in winter lightning areas. Wind turbine operators in winter lightning areas report inferior performance of small disk receptors compared to cap-type receptor [106]. Blades with disk type receptors were reported to malfunction frequently. Signification improvements in wind turbine reliability were reported after a retrofit of a disk receptor to a band receptor in the winter lightning area of Japan as depicted in Figure 3.32 [9].

Also changing the electrode material (for instance from Steel to Tungsten) is expected to lead to a reduction of material loss due to flashes with high charge content and to improve winter lightning performance.

3.6.4.2 High fraction of positive lightning discharges

The second reason why winter lightning poses such a severe threat to wind power plants may be explained by the high fraction of positive lightning discharges. It is estimated that 33% percent of all winter lightning discharges in Japan are of positive polarity [105].

Figure 3.31: Cap type receptor (winglet) from wind turbine in winter lightning area after several years of operation. The lightning current degraded the trailing edge of the receptor.

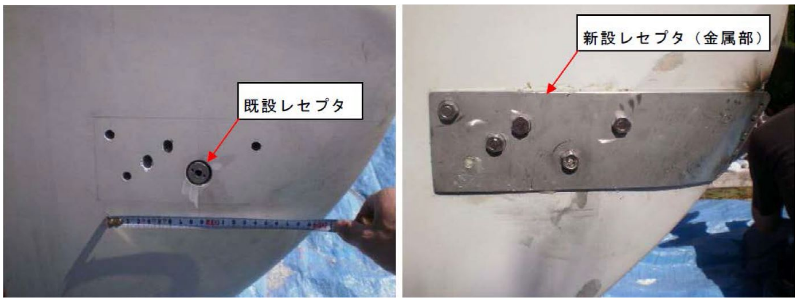

Figure 3.32: Tip receptor retrofit. Initially disk receptors were installed. Retrofit to band type receptors resulted in significant lightning performance improvements (Figure adapted from [9]).

Additionally, about 13% bipolar lightning is observed. Positive upward lightning implies that positive charge in the cloud is neutralized and it is initiated with a negative upward leader from ground. In the laboratory environment, high voltage attachment tests with negative polarity are typically the most critical for wind turbine blades. Polarity depending experiments on wind turbine tip sections were performed in [107]. Repetitive punctures through the laminate were reported with negative polarity on the DUT whereas leader attachment at positive polarity typically started from the metallic tip receptor. Two reasons for the polarity difference are further elaborated in [107]. First, the applied voltage and the resulting electric field around the LPS is distinctly higher (around twice the voltage) with negative polarity. This increases the electric stress for the insulation around the LPS. Second, the fundamental discharge processes between positive and negative polarity are distinctly different as further described in Section 4. The result is that lightning attachment of negative polarity has a significantly higher risk to attach to unintended location inside the blade instead of at intended receptors. Careful insulation coordination of the LPS seem to be mandatory in order to exclude lightning attachment to unintended locations. Furthermore, all conductive elements inside the blade should be characterized by rounded-off edges in order to avoid corona and streamer formation.

3.6.4.3 Lack of laboratory verification in LPS designs

High-voltage and high-current tests, as described in IEC 61400-24: Lightning protection of wind turbines, are the most fundamental tools to verify the effectiveness of a LPS in a wind turbine. If these tests have not been performed, it is not possible to exclude trivial lightning protection design issues such as insufficient insulation coordination around the receptors, deficient receptor implementation or insufficient bonding of electrical conductors inside the blade. Many wind turbines monitored in the NEDO campaign were older wind turbine models which (most likely) did not perform excessive lightning testing in a high-voltage laboratory. Therefore, it is rather difficult to determine the final reason for failure. Several reports after wind turbine damage documented a disconnected down conductor system possibly caused by lightning interaction combined with tensile stress on the down conductor (improper installation) [95]. In the second edition of IEC 61400-24 which will be released in 2018, laboratory testing will become mandatory for wind turbine certification. Therefore, all new wind turbine models are expected to enhance lightning protection performance.

3.6.4.4 Single extreme lightning discharges with high current parameters

During the lightning measurements campaign in the NEDO project [9][10], a few high energetic lightning discharges occurred with specific energy and charge values of up to $\frac{W}{R} = 19\frac{MJ}{\Omega}$ and $Q = 1200C$, respectively. These rare discharges pose a significant threat to the LPS of wind turbines due to their high energy content. The expected failure modes associated with high specific energy and charge may be found in Section 2.2. According to [10], 4% of winter lightning discharges exceeded a charge amount of $Q = 300C$ and only 1% exceeded a specific energy content of $\frac{W}{R} = 2\frac{MJ}{\Omega}$. At this point, it should be mentioned that the recording time of a lightning flashes in the NEDO project was limited to 0.5 seconds. Video observations of winter lightning flashes(See Section 3.6.3) indicate that flash durations exceeded this value occasionally. Since flashes recordings typically include a pre-triggering of up to 0.2 seconds, several recorded current waveforms did not reach the zero values before the current recording terminated. As a result, several current recordings were terminated before the lightning current has ceased. Therefore, it may be speculated that current parameters of winter lightning flashes are higher than mentioned in [9] and potentially, a higher fraction of flashes may exceed the current parameters described by the IEC 61400-24 standard.

3.6.4.5 High electric fields in winter thunderstorms

Another distinct difference between winter thunderstorms and summer thunderstorms is the higher electric field on ground (up to $E = 150\frac{kV}{m}$) caused by the lower cloud height as depicted in Figure 3.15. The implications of high electric fields for composite structures such as wind turbine blades are not very well researched. It can be estimated, however, that partial discharges and space charge effects are more distinct during winter thunderstorms. In [107] a description of the processes related to internal discharges on wind turbine blades was given. In theory, partial discharges created on a metallic object such as a down conductor produce similarly charge ions like the down conductor polarity which move through the air in direction of the resulting background field (towards the cloud) and deposit on the insulating Glass fiber reinforced plastic (GFRP) laminate. This creates a counteracting electric field which theoretical limits the magnitude of electric field inside the blade. In reality, wind turbine blades rotate and the electric field gradient is changing continuously.

3.6.4.6 Insufficient maintenance

Frequent damages may also appear due to practical issues for example a lack of maintenance. Conversations with Japanese wind turbine operators revealed that the procedures of blade inspection by means of rope access were started in Japan from year 2011 [106]. Due to creation of a new branch of industry (from window cleaners on skyscraper to wind turbine inspection specialists), the overall maintenance situation improved. Reoccurring inspection and early repair of small damages on the blade lamination are now a fundamental aspect for the Japanese wind turbine operator service schedule, especially in winter lightning areas.

3.7 Summary

Wind power plants are exposed to downward lightning flashes and upward lightning flashes. The number of downward flashes a wind power plant receives depends on the average flash density of the site location. The amount of upward lightning flashes, on the other hand, depends on four conditions which are:

- The height of the structure
- The elevation profile of the site and the absolute distance to the charge layer in the cloud
- The meteorological conditions of the site
- The average flash density of the site

When examining LLS data from wind power plants, intensification of average flash density in the immediate vicinity of a wind power plant is an indication for upward lightning discharges. It needs to be noticed that LLS data needs to be carefully interpreted. There is a fraction of upward lightning discharges (ICC_{only}) which can not be detected with LLS technology due to the absence of fast current components. (ICC_p) discharges may be detected in approximately half the events, whereas ICC_{rs} flashes have a high probability to be detected [50].

Wind power plants at different locations are exposed to different lightning environments. Certain wind power plants are exposed to lightning discharges mainly in summer whereas other wind power plants also receive lightning discharges during the winter season. The characteristics of warm season thunderstorm show high cloud-base heights, −10°C isotherms more than 3500 meters above the ground, and relatively high ambient temperatures. Characteristic properties for winter thunderstorms locations are a low cloud-base heights, −10°C isotherms below 2000 meters above the ground, high wind speeds, and temperatures close to zero degrees.

An indication of at which location winter thunderstorms may trigger frequent upward lightning discharges was provided in Europe. Wind turbine operators in these areas should be aware of the resulting risk and may potentially retrofit their wind turbine blades with improved lightning protection solutions or improve maintenance/inspection intervals.

The low cloud height during winter thunderstorms trigger upward lightning discharges on the ground. Typically, tall structures such as radio towers or wind turbines are the formation point for these discharges. Exposed locations or tall structures may be struck much more often by upward lightning discharges compared to downward lightning discharges.

Upward lightning discharges during winter thunderstorms in Japan are characterized by median peak current of $5kA$, charge values of $40C$ and specific energy values of $20\frac{kJ}{\Omega}$. Also the 90th percentile values of charge, specific energy and peak current are $20kA$, $170C$,and $350\frac{kJ}{\Omega}$, respectively which is within the testing conditions of IEC 61400-24: Lightning Protection of Wind Turbines. Only in very rare occasions the current parameters exceed extreme values of $50kA$, $600C$, and $5\frac{MJ}{\Omega}$. Due to these reason, the high amount of damages on wind turbine can not be explained by current parameters alone. More likely is a combination of a high fraction of positive lightning discharges which are initiated on unintended locations, receptor erosion due to frequent lightning attachment to the same wind turbine, a lightning protection design not tested according to the current lightning protection standards, and insufficient maintenance of wind turbine components.

The video observation of upward lightning discharges during winter thunderstorms on rotating wind turbine blades showed that lightning attachment happened nearly exclusively to the tip section of the blades. Unfortunately, the video quality did not allow for a more precise differentiation in terms of whether the tip receptor or the laminate was the attachment point. There was only one confirmed nacelle hit out of a dataset of 172 lightning flashes. Lightning attachment happened from rotational angle 90° till 270°. Horizontal lightning attachment had the tendency to be correlated with other-triggered lightning events whereas vertical blade alignment was related to either self-trigger or other-triggered lightning discharges. Characteristic for upward lightning discharges is a flash duration of up to 0.67 seconds. The long duration of the flash drags the illuminated plasma channel along the circumference of the wind turbine blade after the flash connected to the tip receptor. It may be speculated that a multiple attachment of long duration flashes degrades also the composite laminate around the tip receptor.

Reflecting on the number of downward and upward lightning discharges to wind turbines, the data suggests that both numbers are independent from each other. There are sites where nearly no downward lightning is observed in the summer time, however, frequent upward lightning flashes appear in the winter. On the other hand, certain sites are only exposed to summer lightning. Therefore, it seems counter-intuitive that the amount of upward lightning discharges to a structure is calculated as a fraction of downward lightning flashes as suggested by the committee draft version of IEC 61400-24 Ed.2 [29].

Current parameters from downward and upward lightning flashes are also distinctly different which reflects on the risk of failure of the LPS during testing in the laboratory and in real conditions. Furthermore, *LLS* data shows that lightning exposure can be vastly different even within one wind farm. To define a common lightning environment based on more or less arbitrarily chosen environmental factors C_x (due to winter lightning activity, complexity of terrain, height above sea level) and mix again the effects of downward and upward lightning, may not be the right way to represent the realistic amount of dangerous events to a wind turbine N_D. Therefore, it is suggested that the number of dangerous events to a structures N_D, as defined by the standard IEC 61400-24 [29], should be separated into the number of dangerous downward N_{Dd} and upward N_{Du} events.

In the next chapter, the interaction of air flow and space charges around the tip receptor of wind turbine blades is investigated.

4 ON THE IMPACT OF AIR FLOW TO ELECTRIC FIELD ALTERING SPACE CHARGE

Polarized space charges, created by ionization due to a high electric field, can alter the resulting electric field around the point of creation [108]. The lightning receptors of wind turbine blades are constantly exposed to high air velocity up to 80 meters per second. Recently, there has been a discussion in the academic literature whether wind turbines are more exposed to lightning attachment compared to static towers due to the constant removal of polarized space charge from the high air velocity at their tip receptors [32][109].

In this chapter, research regarding the effect of space charge removal due to wind on electrode configurations is performed. At first, relevant background information on corona modes, space charge propagation, and electric field measurements from balloons on various heights is provided. Subsequently, an overview of the differences between static towers and rotating wind turbine blades during thunderstorms conditions is given in order to enable the reader a better understanding of the involved processes. A FEA simulation was performed in order to approach a theoretical solution for the task. Afterwards, a laboratory experiment employing a high air flow wind generator was performed. In order to create space charges, a high voltage DC source was connected to a rod-plane electrode configuration and breakdown of the gap was triggered by a parallel connected Marx-type generator. An analysis of the Partial discharge/s (PD) patterns before breakdown of the gap as well as the breakdown voltage is performed. Subsequently, the theoretical and experimental results are discussed.

4.1 Background

The electric field established between a thundercloud and ground is the initiator for the generation of polarized space charge which affects the total resultant electric field. The space charge, which may be positive or negative ions, have their origin in corona discharges and the polarity of the dominant charge layer in the cloud determines the polarity of them. The overall effective E-field generated by a thundercloud is directed from ground to cloud in about 90% of all cases during summer thunderstorms which implies a dominant negative cloud charge [110], as seen from the ground. If the negative directed electric field at ground level exceeds the ambient corona onset field $\vec{E}_{acor}$, small partial discharges are created on sharp edges such as trees and bushes. As a product of the ionization, positive space charges are injected into the air. These particles drift towards the cloud due to the opposing polarity and create an electric field which counteracts the dominant existing field created by the thundercloud. During the propagation, the charged ions may recombine or reattach to other molecules resulting in the loss of their electrical polarization. The field reduction from the space charge can reach significant values and aggravate lightning attachment. An empirical relation of the ambient corona current has been conducted by [111]:

$$I = c * \vec{E}(\vec{E} - \vec{E}_{acor})^2 \tag{4.1}$$

where c is an empirical determined constant depending on the landscape, $\vec{E}$ is the ambient field at ground, and $\vec{E}_{acor}$ is the ambient onset field. The equation estimates the point-discharge current on a small tree. The author in [111] measured, however, the steady state values of this discharge current which implies the test object was surrounded by a space charge cloud when the measurement was performed. Further accuracy improvements for the equation are provided with a third degree polynomial expression described in [112].

Space charges are not only created on bushes or trees at ground level but also on grounded conducting objects of tall structures such as lightning protection systems of towers or wind turbines. The radius and the apparent electric field around the conductive element determines whether partial discharges are created.

4.1.1 Corona modes

Partial discharges in air, also called corona, are the first observations of an imminent breakdown of a gas insulation in a non-uniform electrode configuration. Partial breakdowns occur in high field regions around sharp edges caused by high voltage sources. Also the lightning protection system of a wind turbine is characterized by sharp edges and high electric fields are observed on conducting surfaces in blades and nacelles due to electrically charged thunderclouds. Corona discharges are a transient or steady state process that changes with increasing electric field strength. Also the polarity of the stressed electrode has a distinct impact on the partial discharge behavior. Corona modes are described below and a through discussion about the topic can be found in [113] and [114].

Negative corona are initiated at the cathode and develop towards the anode in a continuously decreasing field. Due to the high field intensity around the cathode, molecules are separated to positive charged ions and electrons. Electrons are readily available due to the vicinity of the negative potential. The partial discharges stop at a distance S_0 where the ionization coefficient α and the attachment coefficient η are equal. Free electrons are characterized by a lower mass and hence move much faster than ions in an electric field. They are readily swept away towards low field intensity regions of the gap. Due to their high velocity, they collide with oxygen molecules in air and form negative charged ions which travel towards the anode with a lower velocity due to their increased mass. Both positive and negative charged ions bias the electric field in the vicinity of the cathode and create current pulses which depend on the propagation of the space charge. The electric field distribution of a negative corona point is illustrated in Figure 4.1a.

Three different corona modes can be identified which change with increasing applied voltage. The first mode is called a "Trichel streamer" which produces small pulsing conducting channels which are repetitively initiated, developed and suppressed by the space charge. The dead time between pulses is decreased until it disappears with increasing voltage. The second corona mode, the "negative pulseless glow corona", is established which continuously emits electrons as a results of continuous bombardments of ions to the cathode. The electrodes are accelerated from the cathode and form steady ionization in the corona

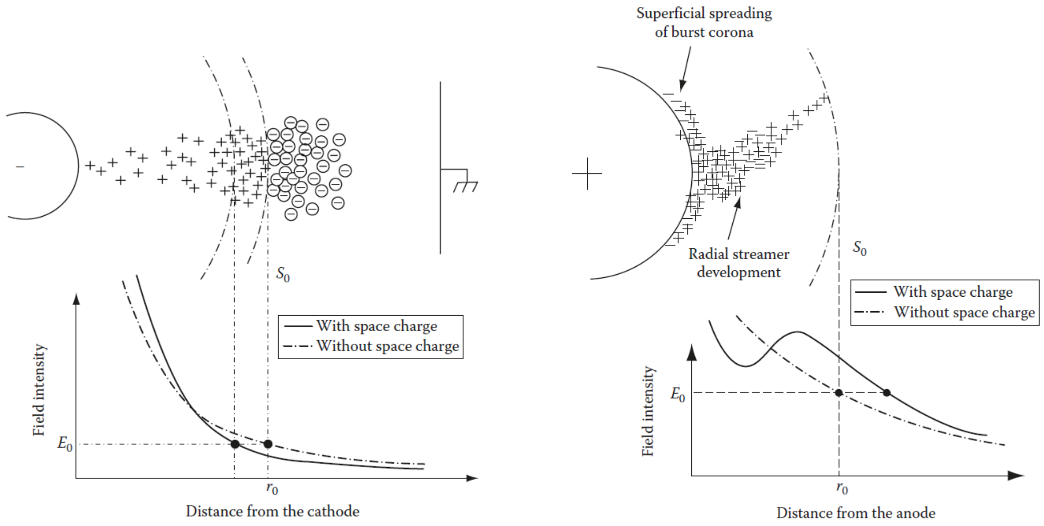

(a) Negative point.

(b) Positive point.

Figure 4.1: Illustrations of positive and negative corona adapted from [113].

volume. Increasing the field even more establishes the third corona mode which is called "negative streamer corona" where ionization becomes more enhanced and space charge start streamer channels which reach far into the gap. The length of the channel varies continuously which causes low frequency pulsation of the discharge current.

Positive corona is initiated at the anode at slightly higher voltages since no electron source is available directly from the electrode. Electrons are attracted from the gap instead. The partial breakdown is initiated at the point in the gap where ionization coefficient α and attachment coefficient η are equal and develops towards the anode in a continuously increasing field. An electrode avalanche propagates towards the anode, leaving positive space charge in the volume which is now propelled away from the anode. The anode is not able to neutralize all incoming electrons at once and an ionization around the electrode begins. If the electric field is high enough, the positive space charge initiates a streamer mechanism which is fed by positive space charge and forms filament channels which are the starting points for the breakdown of the gap. The electric field distribution of a positive corona point is illustrated in Figure 4.1b.

The first corona mode on a positive electrode is the "burst corona". It is characterized as a thin luminous layer that is located close to the anode surface. Incoming high energy electrons may loose their energy in the vicinity of the anode surface by ionization before they neutralize their charge on the electrode. Positive space charge is hereby created which suppresses the ionization locally and provides a pulsing characteristic due to the relatively slow ion propagation. The second corona mode is the "onset streamer corona" where the positive charge around the anode forms a high electric field leading to the initiation of subsequent electron avalanches from photons. The feedback processes by photons enable to create small filaments which extend further into the gap than the bust corona volume. Increasing the voltage further, lower amount of onset streamer are observable since the increasing field removes more positive space charge from the anode and the burst corona zone is pushed further away from the anode. The continuously propagating space charge leads to a field reduction which prohibits streamer discharges from extending farther into the gap. The third stage, the steady "glow corona" is created, which forms an equilibrium between removal and creation of positive ions. The field pushes positive space charges effectively into the gap without having the sufficient concentration to form streamer channels which propagate further into the gap. The final stage of a positive corona is the "breakdown streamer corona" where again similar streamer processes occur compared to the onset streamer corona; however, the discharges are characterized by higher current pulses and they can propagate further into the gap. Streamer processes with photoionization take place and short circuit conditions or breakdown may occur.

4.1.2 Space charge properties

In [115], the author presented a mathematical expression of the propagation of space charge in air. The research concluded that the neutral aerosol charge density of the surrounding air has a distinct influence in the attachment behavior of positive space charge. A high concentration of neutral aerosol particles (as seen in urban areas) leads to a high attachment rate of positive space charge, whereas a low concentration (in rural areas) promotes lower attachment. It can be concluded that rural areas are exposed to thicker positive space charge layers. Furthermore, as described in [115], the neutral aerosol charge density of the surrounding air has a big influence in the attachment behavior of positive space charge. In [116], the author modeled the full ion drift of small positive-ions, big positive-ions, small negative ions, big negative ions and neutral aerosol molecules by means of the continuity equations for particles. The results implied that the majority of the positive space charge does not reach the cloud layer since the particles are more likely to be transformed to neutral aerosol particles, however, the model did not include convective transport of particles which means the charge transport is still possible.

In [117], a comprehensive study of positive glow corona is performed and the main reactions which contribute in the discharge process are evaluated. The research concluded that the biggest charged-particle contribution to the total discharge current was conducted by the positive-ion concentration, whereas electron and negative-ion concentrations contributed only little to the conducted discharge. Therefore, the assumption can be made that measured discharge currents in external circuits are mainly transformed into positive-ion species in a positive corona. Furthermore, the author discussed the distinct impact of the mobility of positive-ion species to the pulse frequency, which is expected if positive-ions carry the biggest contribution of the main current. The concentration of negative-ions and electrons are eliminated readily due to the vicinity of the anode and are not deterministic for the electric field distortion around the conductor. All of the mentioned papers above did not include the effect of the velocity of the wind. Computations were conducted in one-dimension and a symmetric shape of the corona discharge was assumed. This implies limitations of the electric field distribution due to the one-dimensional approximation. Two-dimensional studies dealing with propagation of streamers can be found in [118][119].

Few publications exist which investigate the effect of the wind to the corona. In the work of Ariza[120], a single-needle electrode is exposed to high electric field which triggers positive corona. In the experiment, a fan introduced a wind velocity up to $\vec{v} = 9\frac{m}{s}$ towards the needle. A distinct increase in the corona current was found when the needle was exposed to wind. Bazelyan [121] provided a comprehensive analytical and numerical base for corona currents including the removal of space charge due to ion drift and the movement of the of wind. Abdel Salam [122] studied the influence of axial and transversal wind to positive corona with low wind speeds up to $\vec{v} = 8.6\frac{m}{s}$.

4.1.3 Electric field measurements at varying heights

The impact of space charge can be observed when performing simultaneous electric field measurements below thunderclouds as performed by [123]. In his work, the electric field was measured below a thunderstorm at the Kennedy Space Center, Florida, US. The sensors were located at ground level, 80 meters, 436 meters, and 603 meters above ground and attached to a hovering balloon by means of a tether. During the period, four lightning strokes were recorded at 23:47, 23:53, 23:58, and 00:00, respectively. Figure 4.2 illustrates the impact of the electric field on the different heights.

As can be seen, the electric field measurements are significantly different between the layers. The highest electric field measured during the recording period was $65\frac{kV}{m}$ at $603m$, whereas the simultaneous recorded electric field on ground did not exceed $5\frac{kV}{m}$. On the ground layer, space charges are created on the small radii of vegetation. The particles slowly drift towards the charge in the cloud and are impacted by the electrostatic force as well as the ambient wind velocity. During their ascend, small ions reattach to heavy aerosol particles to form heavy ions with a mobility two orders of magnitude lower [124]. Due to the recombination of space charge and the related reduction of particles density, higher structures are also exposed to higher electric fields on their extremities. This

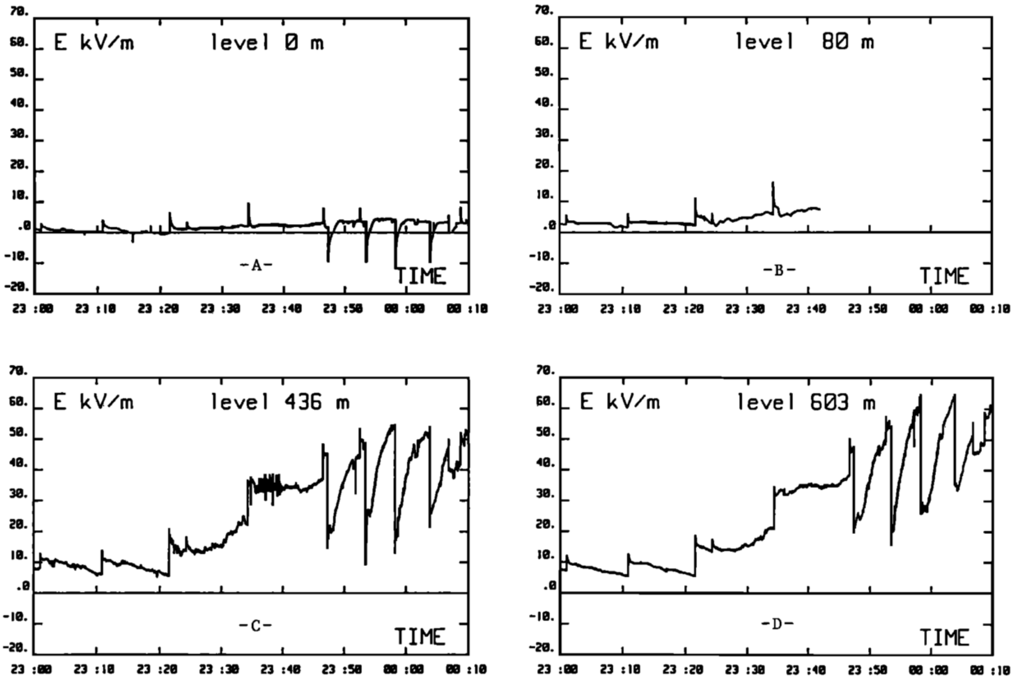

Figure 4.2: The electric field at different heights (ground level,80 meter ,436 meter, and 603 meter above the ground) was measured beneath a thunderstorm versus time. Four lightning strokes were triggered at 23:47, 23:53, 23:58, and 00:00, respectively. Charts adapted from [123]

may also be a reason why higher structures are more exposed to lightning attachment. Considering natural downward lightning, the answering upward lightning leaders are more likely to start from positions of higher electric field intensity. Nowadays, the total structural height of modern wind turbines increases steadily and turbines up to 230 meter height are commissioned. The increased height of wind turbines leaves the extremities less protected by the space charge which increases the risk of interception of downward and upward lightning discharges.

Another mentionable observation regarding space charge effects on electric field magnitudes from thunderstorms was documented by [125]. The author performed electric field measurements over water surfaces and documented values up to $130\frac{kV}{m}$ beneath summer thunderstorms. In this case, the absence of vegetation is the reason for lower space charge densities over water surfaces and increased electric fields. Offshore wind turbines may therefore be exposed to higher electric fields compared to onshore wind turbines, even though their total height is typically lower compared to onshore wind turbines. Small water droplets from rain or sea spray may be a source of corona discharges since the geometry enhances the electric field around these droplets.

4.2 Overview - Static tower vs. rotating wind turbines

Figure 4.3a and Figure 4.3b describes a scenario where, apart from the ambient space charge influence from the ground, tall objects protrude out of the ground. The top parts of these constructions are often equipped with antennas and lightning air termination systems with pointy geometries where a distinct field intensification can be observed. Here, the rule applies, the smaller the diameter of the protrusion, the higher the field amplification. Melted air termination systems on wind turbine blades are also source of E-field intensification. These elevated points are often the source of corona discharges on a structure. The total electric field $\vec{E}$ around a protrusion is composed out of the electric field of the thundercloud and the counteracting field created by the space charge.

In the case of Figure 4.3a, low ambient wind speeds are exposed to the tower and the generated space charge cloud above the tip is only slightly tilted. This implies that the tower is exposed to a lower electric field since the space charge is surrounding the top of the tower. The risk of lightning attachment is reduced. The higher the ambient wind speed, the more the space charge cloud drifts away, leaving the structure more exposed. The resultant drift velocity of positive ions is the sum of the velocity due to the attraction of the electric field $\vec{v}_{e_{field}}$ and the velocity of the wind $\vec{v}_{wind}$.

$$\vec{v}_{ion} = \vec{v}_{e_{field}} + \vec{v}_{wind} \tag{4.2}$$

Where $\vec{v}_{e_{field}}$ is the electric field $\vec{E}$ around the point discharge multiplied with the mobility of positive ions $\mu_p = 1.5 \cdot 10^-4 \frac{m^2}{Vs}$ which is considered constant [126][127].

$$\vec{v}_{e_{field}} = \mu_p \vec{E} \tag{4.3}$$

In the direct vicinity of a sharp edge, $\mu_p E$ dominates the ion velocity. However, the electric field is rapidly decreased when moving away from the anode. At a specific distance d_0, the velocity of the wind dominates the ion drift $\mu_p E < \vec{v}_{wind}$. For low wind speeds $\vec{v}_{wind} \leq 10\frac{m}{s}$, the border electric field intensity E_{crit} can be calculated, at which the ambient wind speed dominates the movement of the particles compared to the electric field.

$$\vec{E}_{crit} \leq \frac{\vec{v}_{wind}}{\mu_p} \leq \frac{10\frac{m}{s}}{1.5 \cdot 10^{-4}\frac{m^2}{Vs}} \leq 0.66\frac{MV}{m} \tag{4.4}$$

In Figure 4.3b, the same scenario is illustrated with a rotating wind turbine. Here, the space charge is readily removed due to the high tip speed $\vec{v}_{rot}$ of the blade. For a standard wind turbine with a rotor diameter of 120 meters and an angular velocity $n = 5 - 12\frac{1}{min}$, the velocity at the tip of the blade varies between $\vec{v}_{rot} = 31 - 75\frac{m}{s}$ which is much higher than the velocity of the ambient wind. Therefore, the wind turbine is more exposed on the leading edge of the blade due to the lack of the counteracting electric field from the space charge. The wake velocity field $\vec{v}_{wake}$, which is the induced air vortex behind a wind turbine, is composed out of the contribution of $\vec{v}_{wind}$ and $\vec{v}_{rot}$. Space charge is transported in the wake which creates a small counteracting electric field. This might influence the attachment of lightning to following structures. Out of this observation, the first wind turbine in a wind farm facing the wind might be most exposed structure. However, a quantitative estimation is hard to obtain due to the various parameters that influence lightning attachment. A wind turbine which does not rotate behaves similarly to a static tower.

4.3 Ion speed vs. rotational speed of wind turbines

With Equation 4.3 in mind, the velocity and traverse time of ions between two electrodes can be approximated with an electrostatic FEA simulation. Subsequently, the ion speed from corona discharges and rotational speed of wind turbines can be compared to see if the air flow can impact the propagation of ions. This is the first step to estimate if the rotation of a wind turbine and the resulting wind speed may be different compared to a stationary tower. The impact of space charge which, in turn, alters the electric field can not be computed with an electrostatic simulation alone.

The model calculates the velocity of ions based on the electric field between the electrodes and the field dependent mobility of charged particles. Following limitations apply to the model:

- The field calculation is only governed by the geometry of the model.
- There is no interaction between charged particles.
- Attachment and recombination of particles is neglected.
- No proximity effects due to cathode or anode reactions are considered.

For this computation, an axis symmetric 2D electrostatic FEA was created with a needle-plane electrode configuration as can be seen in Figure 4.4. After the electric field was calculated for the model, the velocity can be computed following Equation 4.3.

The electric field and hence the ion velocity is highest close to the needle electrode and decreases rapidly farther in the gap as depicted in Figure 4.5. Therefore, also the ion speed is highest close to the needle electrode where the ion is created due to PD. The comparison of the ion velocity between several distances is shown in Figure 4.6. The gap distance (x-axis) is normalized to compare the results. As can be seen, shorter gaps are

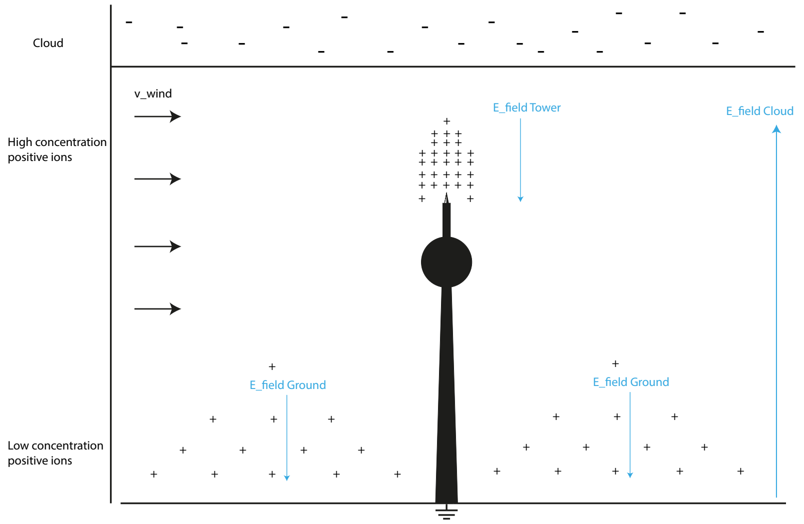

(a) 2D illustration of a static tower at low wind speeds. Space charge covers the tip of the tower and created $\vec{E}_{ftower}$ shields the structure. Lightning attachment probability reduced.

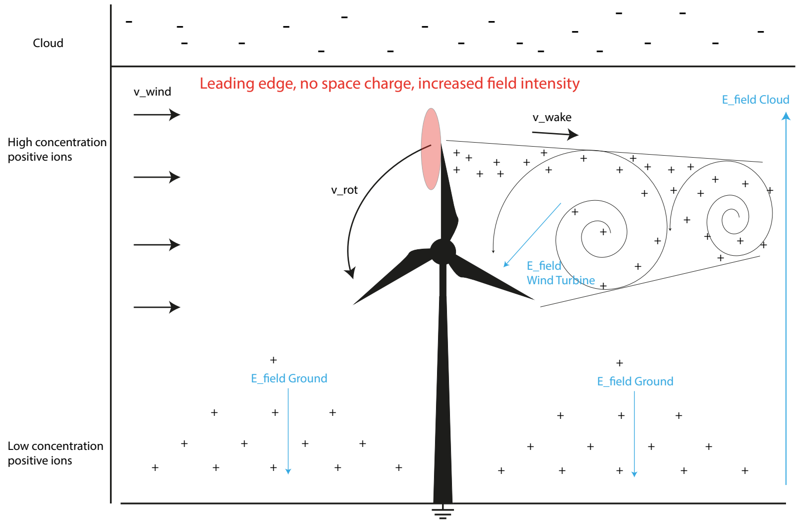

(b) 2D illustration of a rotating wind turbine. Space charge is readily removed at the leading edge due to the contribution of $\vec{v}_{rot}$, hence higher field intensity at the leading edge. Lightning attachment probability increased compared to the tower. Turbulent $\vec{v}_{wake}$ used to transport positive ions away which might lead to shielding of structures in the wake. $\vec{v}_{rot} \gg \vec{v}_{wind}$

Figure 4.3: Illustrations of space charge distribution in case of static towers and wind turbines

characterized by higher velocities as well as shorter distances. Already at a gap distance of about 1 meter, the ion speed due to electrostatic force is reduced to about $v_{is} = 1.8\frac{m}{s}$ at half the distance (0.5 meters). This means that even low magnitude air flow (ambient wind speed) dominates the ion propagation distinctly. In the case of 0.25 meter gap, the ion speed due to electrostatic force is about $v_{is} = 10\frac{m}{s}$ at half the distance (0.125 meter). The increase in ion speed results in a reduced impact of air flow in smaller gaps, however, it is expected that an impact is still observable.

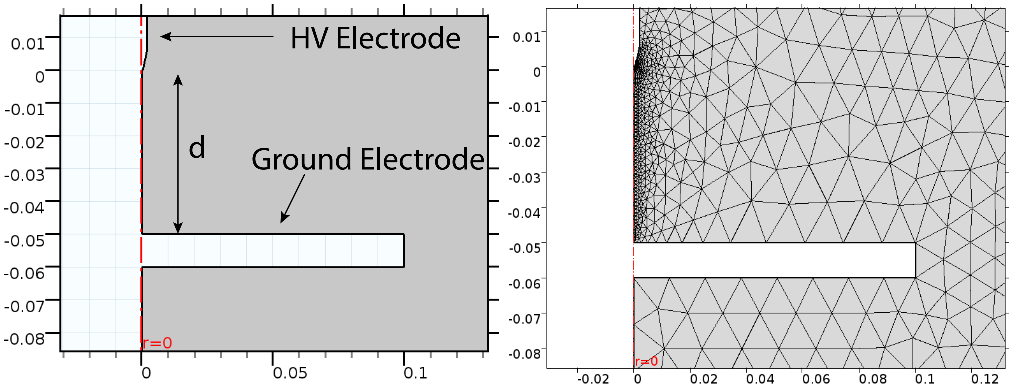

Figure 4.4: Simple 2D axis symmetric model for electrostatic evaluation of the electric field.

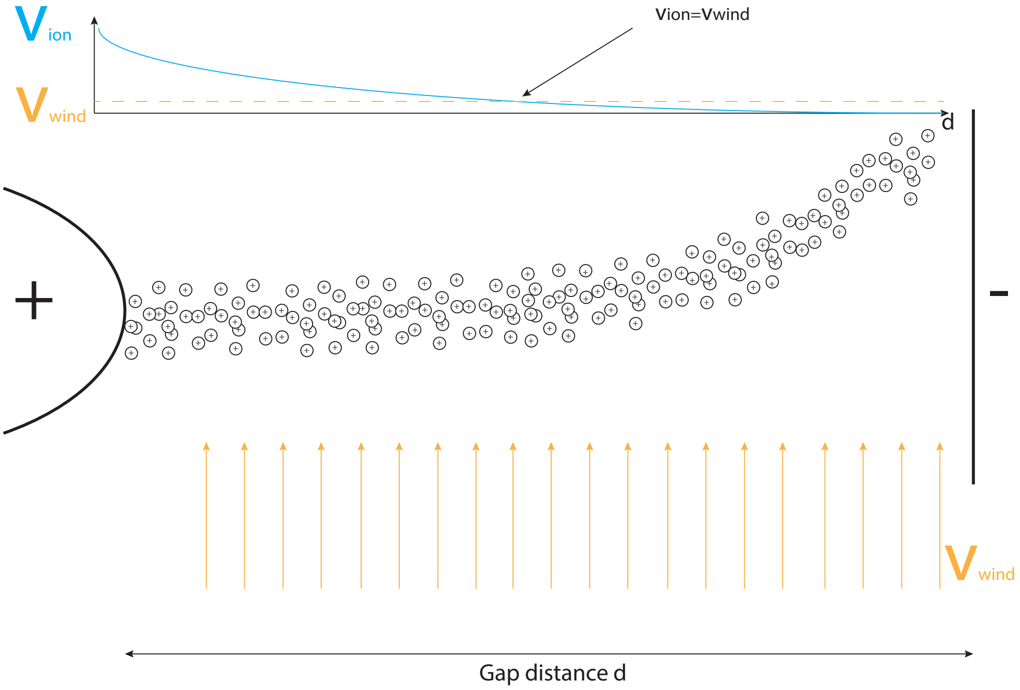

Figure 4.5: Illustration: The velocity of the ions is dominated by the high electric field in the vicinity of the electrodes. Farther in the gap, the wind speed dominates the propagation of the ions since the electric field is weaker.

In case of lightning strikes, the electrode distances are much larger than 4 meters and it is expected that air flow has the biggest impact in the distribution of space charge. The ion speed only dominates the wind speed in the close vicinity of the electrode of PD generator.

The time to traverse the gap can be calculated by dividing the incremental distance ds between the finite elements by the calculated field dependent ion velocity $v(ds, E)$ at each point in the grid. The result is then integrated along the length of the gap.

$$t = \int_0^{gaplength} \frac{ds}{v(ds, E)} \tag{4.5}$$

The results show the travel time as a function of gap distance and the results are given in Table 4.1. As can be seen, the travel time of ions is increased distinctly if the needle-plane electrode is farther apart. The electric field around the needle tip is similar at all gap distances; however, the electric field is reduced significantly in the far regions close to the ground plane, which slows down the ion propagation. A longer travel time also allows the gap to be filled with more space charge before the ions are neutralized on the opposite electrode. This has also an impact on the electric field inside the gap. In Table 4.1, the propagation time and the charge in the gap are provided as a function of the gap length.

This result indicates that as bigger the distance between the electrodes, as bigger is the impact of the space charge and the air flow.

Table 4.1: Dependence of gap length on travel time.

Gap length	[m]	0.25	0.5	0.75	1	2	4
Ion propagation time	[s]	0.0691	0.2600	0.6187	1.1751	5.7574	35.4210
Charge in gap	[C]	6.9189e-6	2.5997e-5	6.1873e-5	1.1751e-4	5.7574e-4	3.5e-3

4.4 Finite element simulation of the effect of wind on space charge propagation

At this point, the effect of strong wind to the space charge propagation is evaluated by means of a FEA simulation. The content of this section relates to paper [c.1].

4.4.1 Space charge drift model

A space charge drift model has been developed in order to simulate the effect of strong winds to the space charge around the surface of an electrically charged conductor. The purpose of the model is to visualize the flow of the space charge and to provide predictions about the electric field distortion around the conductor. Scenarios with and without wind are compared. The model utilizes positive ion concentrations to simulate the change in the electric field around the anode. In order to simplify the model, the creation of positive space charge was performed on the boundary of the conductor in the model. In this way, the computational efforts are reduced significantly since the source of the positive particles are focused on a small area in the model. In a positive corona process, the ionization

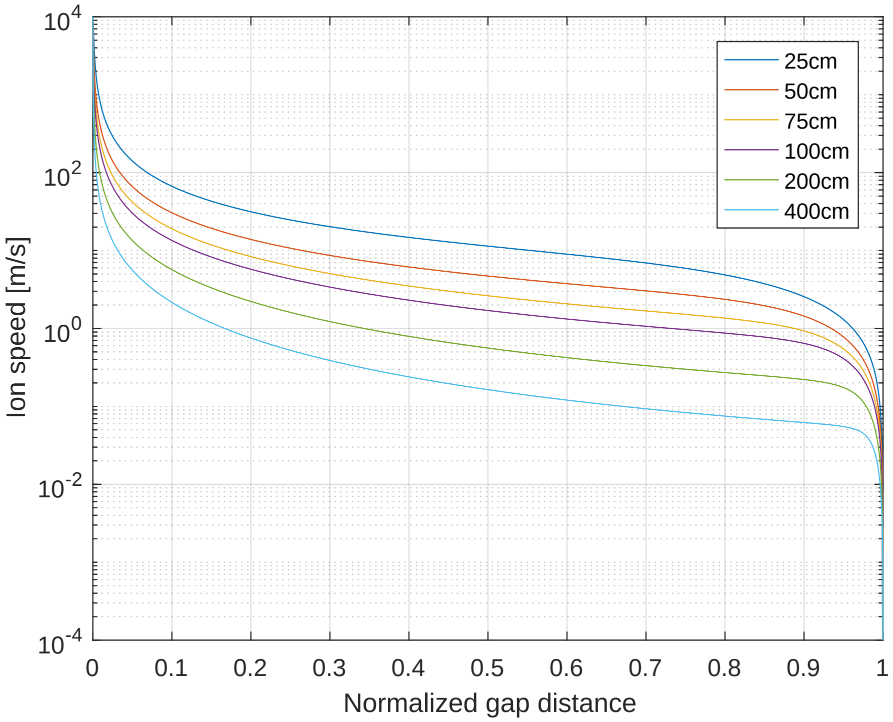

Figure 4.6: The ion speed as a function of normalized gap distance.

is started at a certain distance S_0 through an initial electron. The electron avalanche propagates towards the anode in an increasing field. Due to the higher mobility of electrons, a positive space charge cloud is left behind, which propagates slowly towards the negatively charge cloud. The rate of electron attachment is low because of the high electric field. Negative ions and electrons are readily swept away into the anode [117] and do not have a crucial influence to the electric field. In order to drive the model, it is assumed that the electric field remains on the same level once the corona onset field strength is reached. Other publications use similar approaches which can be found in [120][128][129]. Peek presented a formula which approximates the onset corona electric field $\vec{E}_{cor}$ [130].

$$\vec{E}_1(r,\delta) = 31.53 + \left(\frac{9.63}{\sqrt{\delta r}}\right)\left[\frac{kV}{cm}\right] \tag{4.6}$$

where r is the radius of the conductor and δ is the density of air. The equation was derived for co-axial cylindrical structures. For a conductor with $r_w = 0.04cm$, the corona inception voltage is found to be $\vec{E}_1(0.04cm, 1) = 79.7\frac{kV}{cm}$ [114] assuming an air density factor of $\delta = 1$. The relative air density δ can be calculated with

$$\delta = 0.386 * \frac{p}{273+t} \tag{4.7}$$

p and t are the standard atmospheric conditions of air ($p = 760$torr and $t = 20°$C). For this model, a corona inception field expression for point-plane electrode configuration is used as derived in [131].

$$\vec{E}_2(r,\delta) = 25\cdot 10^3\delta\left(1+\frac{0.35}{\sqrt{\delta r}}+\frac{0.03}{\delta r}\right)\left[\frac{kV}{cm}\right] \tag{4.8}$$

which provides a critical corona inception field of $\vec{E}_2(0.04cm, 1) = 87.5\frac{kV}{cm}$. In Figure 4.7, an illustration of the model is presented. At the top boundary, a negative potential is applied and in 50 cm distance, a grounded conductor is placed which is centred in the domain and measures a radius of $r = 0.04cm$ and a length of $l = 100cm$. Even though the voltage gradient is calculated for a cylindrical structure, since the condition $\vec{E}_2(r, \delta)$ is applied to the boundary, the model treats this representation as a point electrode. The outer surface of the conductor is divided into 24 sections which allows monitoring of the electric field independently around the conductor. To each of the boundaries, equation 4.8 is applied in order to determine if the condition of a corona discharge is fulfilled. In the case $\vec{E}(r) > \vec{E}_2$, a burst of positive ions are exiting the boundary which leads to a decrease of the ambient field $\vec{E}(r)$ around the boundary. The magnitude of the burst is approximated by the volt-current characteristics for stabilized glow discharges in air [132]. This method is repeated until $\vec{E}(r) < \vec{E}_2$. At this instance, no ions are generated at the boundary.

Once the space charge is created on the boundary, the concentration is governed by the continuity equations for particles.

$$\frac{\partial n_p}{\partial t} + \nabla(-D_p \nabla n_p - z_p \mu_p n_p \vec{E}) + \vec{u} \cdot \nabla n_p = S_p \tag{4.9}$$

where n_p, μ_p and D_p are the particle density, the mobility, and the diffusion coefficient, respectively. E denotes the electric field at each point in the domain, Φ is the potential, q is the elementary charge, ϵ_o represents the electrical permittivity of vacuum and $\vec{u}$ is the velocity field of the wind. The latter is modeled via the Navier-Strokes equation for compressible flows.

$$\rho(\vec{u} \cdot \nabla)\vec{u} = \nabla \cdot \left[-pI + \mu(\nabla\vec{u} + (\nabla\vec{u})^T) - \frac{2}{3}\mu(\nabla \cdot \vec{u})I\right] + F \tag{4.10}$$

where ρ is the density of the air, I is the unity tensor, μ is the dynamic viscosity, T is the viscous stress tensor and F is the volume force vector.

Since the positive space charge is directly initiated at the boundary of the conductor, no source terms S_p needs to be defined in the model. This results in further enhancement of computational speed for the model. However, the attachment and recombination of ions needs to be considered with this source term if the propagation exceeds the typical laboratory distances of some centimeters. Especially, the ion attachment to neutral aerosol particles has a distinct influence in the positive space charge distribution if longer distances and time frames are investigated[116][133].

The diffusion coefficients for ion particles are determined with the Einstein relation:

$$D_p = \mu_p \cdot k_b \cdot \frac{T}{q} \tag{4.11}$$

where D_p is the diffusivity, k_b is the Boltzmann's constant and T is the temperate at each specific point in the domain. The specific temperature for positive and negative ions can be computed with:

$$T_i = T_g + \frac{(m_i + m_g) \cdot (3 \cdot (\mu_p \ \cdot |\vec{E}|)^2)}{k_b} \tag{4.12}$$

where T_g denotes the ambient temperature, and m_p and m_g are the ion mass and O_2 molecule mass, respectively [134][135].

These equations are implemented in the FEM simulation software Comsol Multiphysics. The model is implemented in a 2D, time discrete, non-symmetrical, Comsol simulation. Non-symmetry is essential since the wind flow disturbs the particles homogeneity. The drift equations are utilized with the transport of diluted species interface which has a two way coupling to the electrostatic interface. Both interfaces are time dependent. Furthermore, the velocity field is computed via the Laminar Flow interface which has a one way coupling to the model and is set to be stationary. Therefore, the velocity field can influence the charged particles, however, the charged particles are not able to influence the velocity field of the wind. The model is able to simulate the generation and propagation of space charge which is generated at pointy objects such as Franklin rods or other exposed parts of the structure. The model layout, the boundary conditions, and the paths where voltage and electric field distributions were extracted, are illustrated in Figure 4.7. Furthermore, mesh details for the conductor and the domain are shown. The finest mesh is applied close to the boundary of the conductor since the ion drift speed is highest at this position. The simulation time step varies throughout the time frame of the simulation from $t_s = 1 \cdot 10^{-6} s$ to $t_s = 2 \cdot 10^{-7} s$ to ensure convergence. Conductor and earth potential plate are placed in a distance of $50cm$.

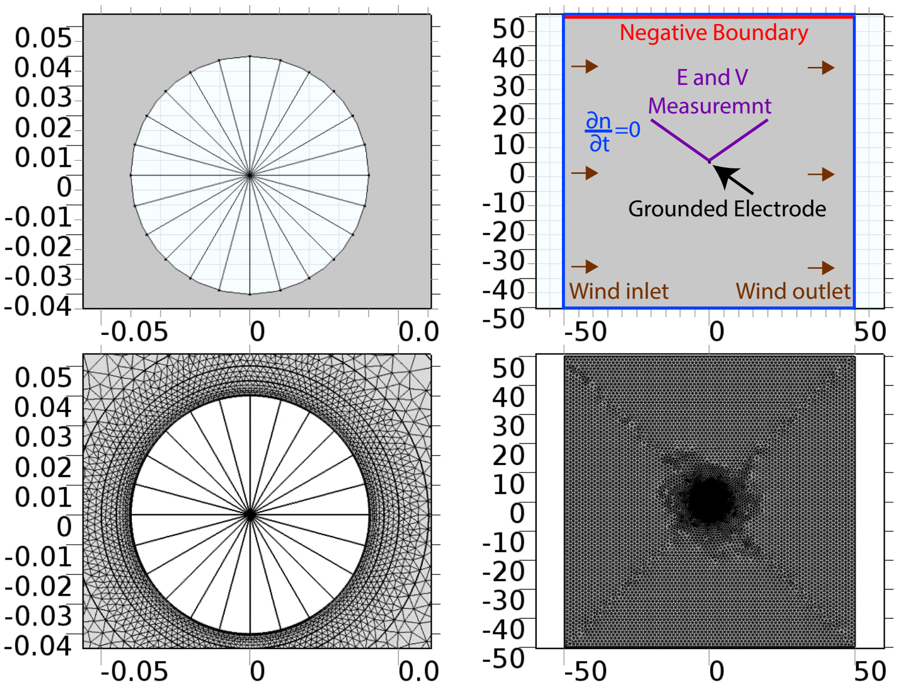

Figure 4.7: Overview of 2D-Model for space charge propagation. Up-left: conductor with 24 separated sections and $r = 0.04cm$, Up-right: overview of domain with anode and cathode, Down-left: mesh around the conductor, Down-right: mesh for entire domain. All distances in [cm].

4.4.2 Simulation results

In order to evaluate the shielding effect of the space charge to structures, the ion velocity determines the propagation of the concentration in the domain. As can be seen in Figure 4.8, in a scenario without space charge, the ion velocity is proportional to the electric field and the ion mobility (See equation: 4.3). Since the electric field drops significantly with the distance from the anode, the ion velocity drops as well. At a distance of $d = 2cm$ and $d = 15.5cm$, a relative wind velocity of $\vec{v}_{rot} = 50\frac{m}{s}$ and $\vec{v}_{wind} = 10\frac{m}{s}$ would dominate the deflection of the particles, respectively.

The next step in the model introduces the space charge into the domain and the two different scenarios are compared. In Figure 4.9, the temporal and spacial evolution of the positive ions with and without a high wind velocity of $\vec{v}_{wind} = 50\frac{m}{s}$ are illustrated. In Figure 4.9a, the wind has no influence in the corona discharge and the concentration of particles is symmetrically distributed around the conductor. The picture illustrates the situation after a simulation time of $t = 2.4ms$. The space charge has propagated around $10cm$ into the gap. The discharge process can be described as follows: In the first instant of the simulation, the electrical field around the conductor is above the onset corona field $\vec{E}_{cor}$ defined in the model parameters. In the following calculation steps, the model verifies if the electric field $\vec{E}$ on each of the boundaries of the conductor is still above $\vec{E}_{cor}$. If this is the case, positive space charge is injected into the gap, lowering the effective field around the conductor. Eventually, the electric field is stabilized around $\vec{E}_{cor}$. The first discharge impulse is the strongest, since the $\Delta\vec{E}$ is the biggest. Afterwards, smaller discharges are generated on the top of the cylindrical surface since the grounding plate is located on the top boundary. Therefore, the local electric field is highest at the top boundaries of the conductor. With no wind velocity, the space charge is evenly distributed at the top of the layer. The space charge is spreading out in an axial-symmetric triangular zone (2D) or in an axial-symmetric cone zone (3D) if point discharges are assumed.

In Figure 4.9b, the space charge is influenced by a high velocity field from the left boundary. In accordance with Figure 4.8, the ion velocity dominates in the close vicinity of the conductor, however, the wind velocity takes over the particle drift after few centimeters. The non-symmetric shape of the positive ions can be observed, leaving the left side of the conductor rather exposed compared to the right side. The difference in maximum concentration between Figure 4.9a and 4.9b can be explained with different diffusion of the particles. In the situation where no wind is applied, the space charge from the initial discharge, which lowered the electric field to $\vec{E}_{cor}$, is still concentrated in the domain. In comparison to this, the space charge where wind is applied is further diffused into the domain.

Plots of the electric field and the voltage of both scenarios are compared in Figure 4.10. Additionally, the voltage and field distribution of a scenario without space charge is taken into consideration to highlight the diversification. The quantities are extracted along the length of the lines which are indicated in Figure 4.9. The simulation without wind, illustrated in Figure 4.10a and 4.10b, highlights a lowered voltage gradient which is symmetric for both sides. Therefore, the voltage and electric field plots for left and right side are exactly aligned in the illustrations. Furthermore, the total resultant electric field is lowered on the conductor from a maximum value $\vec{E}_{max} = 126\frac{kV}{cm}$ to the onset corona

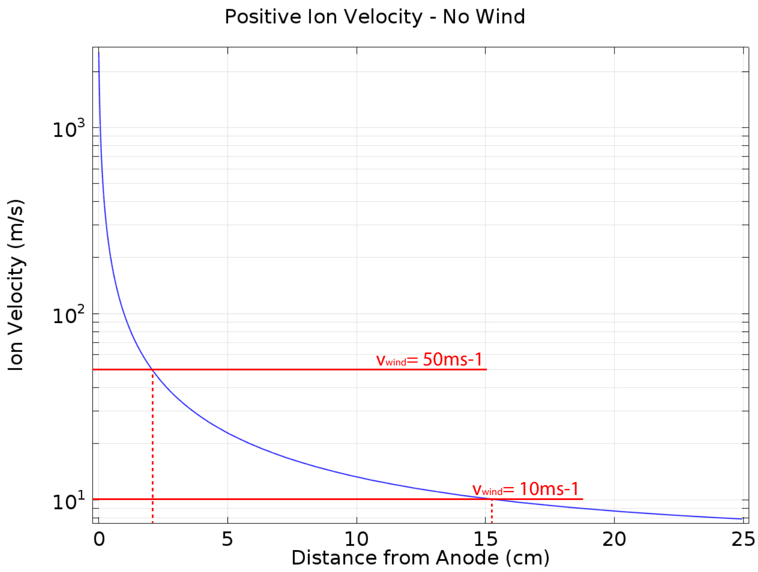

Figure 4.8: Ion velocity $\vec{v}_{ion}$ as a function of distance from anode

field $\vec{E}_{cor}$. Notice that the electric field with space charge (green line) in Figure 4.10b is lower in the vicinity of the anode($< 4cm$), compared to the situation of no space charge (red line). The development of streamer from the anode is hampered and the shielding of the electrode is improved. Further away from the electrode($> 4cm$), the electric field is enhanced since the background electric field and the electric field of the space charge superimpose.

In Figure 4.10c and 4.10d, the influence of the air flow is observable. The right side of the conductor is exposed to higher concentrations of space charge resulting in a higher shielding effect. At the left side from the conductor, however, the space charge is removed due to the wind and is transported to the right side. This is results in a higher voltage gradient compared to the situation without wind where the space charge is evenly distributed

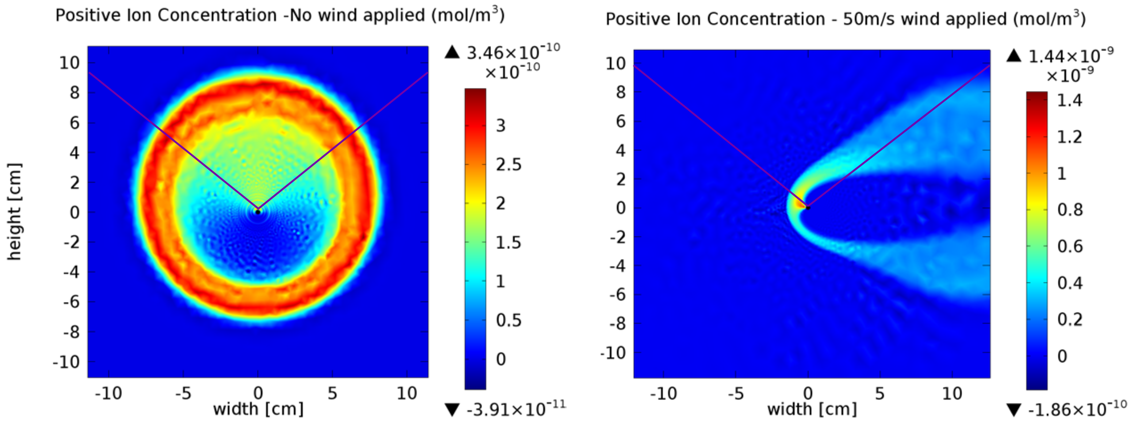

(a) No wind in boundary

(b) 50m/s wind applied to left boundary

Figure 4.9: Propagation of positive space charge due to corona discharge after a simulation time of $t = 2.4ms$. Purple lines illustrate the path where the voltage and electric field values are extracted (See Figure 4.10).

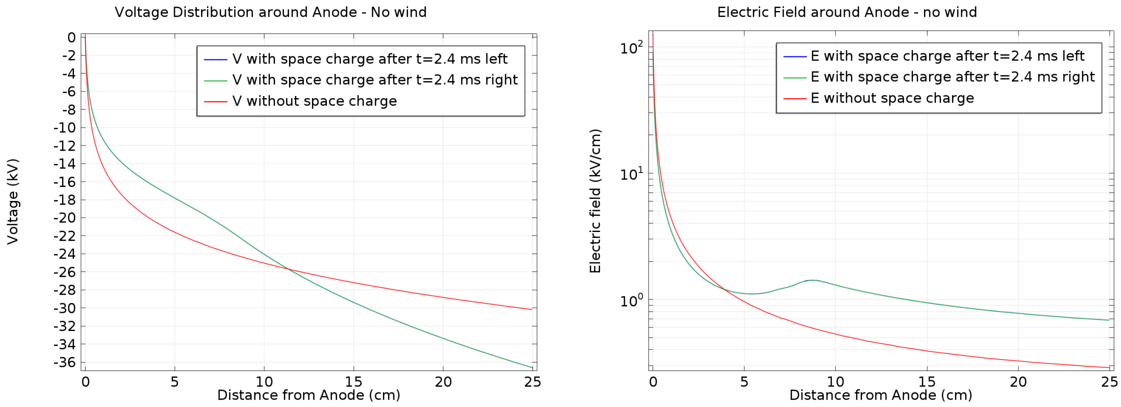

(a) Voltage Profile: Symmetric distribution on left and right side, Curves left/right are coincident

(b) E-Field Profile: Symmetric distribution on left and right side, Curves left/right are coincident

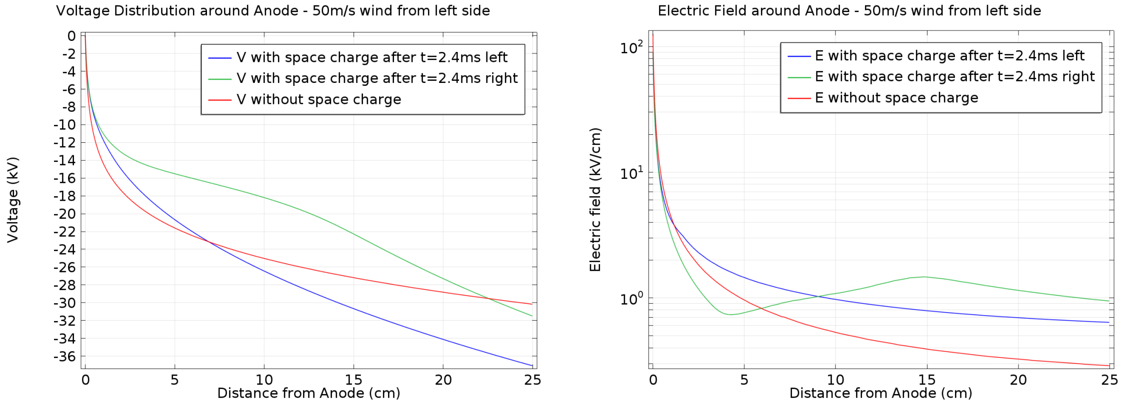

(c) Voltage Profile: Left side is less shielded by space charge, therefore higher voltage gradient. Right side, better shielded

(d) E-Field Profile: Left side, higher E-Field gradient, therefore higher exposure risk. Right side, better shielded in the vicinity of the anode

Figure 4.10: Voltage and electric field from the left and right cut line (See Figure 4.7)

around the top of the cylinder. If the situation is applied to the case of a wind turbine blade, the leading edge of the blade should be less shielded by the space charge compared to the trailing edge and the uniform shielding of a static tower, and therefore, be more exposed to lightning attachment. This statement only applies if the ambient wind speed is relatively low which centers the positive ions above the tower. In [109], the attachment probability of a wind turbine and its neighbor lightning protection tower was recorded in Japan during 5 winter months (2005-2010). Additionally, the ambient wind speed was recorded for each event. In total, 44 lightning discharges were observed. The author concluded that self-initiated upward lightning always started either from the stationary tower under larger wind speeds $\vec{v}_{wind} > 8\frac{m}{s}$ or from the rotating wind turbine blade. No attachment to the tower was recorded during lower wind speeds $\vec{v}_{wind} < 8\frac{m}{s}$ due to self-initiated upward lightning. This observations coincide with the shielding theory in this work. Other-triggered lightning flashes are triggered by inter-cloud or nearby lightning discharges, which employ a sudden change in electric field. There, the shielding effect of the space charge seems to loose the relevance. No regular pattern of attachment probability due to the wind could be determined.

4.5 Laboratory experiment - Discharge characteristics in inhomogeneous fields under air flow

In order to validate the effect of air flow to corona discharges experimentally, a laboratory experiment was performed in the premises of the high voltage laboratory in DTU. The content of this section relates to the publications [j.1] and [c.6].

4.5.1 Methodology

In this work two different measurement setups are used to quantify the effect of wind to the discharge behavior. In the first setup, a high voltage DC source is connected to a needle-plane electrode configuration and PD measurements and Ultraviolet (UV) photography are performed with and without air flow. The first experiment is a non-breakdown experiment, where only the different corona modes are investigated based on charge-time (Q-t) Pd-patterns. In the second experiment, breakdown of the gap is initiated by superposition of direct and impulse voltage for positive and negative polarity with and without wind. The following section describes the laboratory setup and provides more information regarding the methodology.

4.5.1.1 Measurement setup 1

In the first part of the experiment, a high voltage DC source up to $U_{DC} = 100kV$ with $I_O = 1mA$ maximum current output is connected to a needle-plane spark gap with a distance of $l = 20cm$. PD measurements are performed with and without wind across the spark gap. The schematic of the setup is illustrated in Figure 4.11. The purpose of this test is to investigate if and in which manner air flow changes the Q-t discharge patterns in the close vicinity of the needle tip. The needle had a shaft diameter of $d_n = 4mm$ and an approximate tip radius of $d = 0.5mm$. The PD measurements were performed through a Power Diagnostix ICM Measurement System with a bandwidth of $f = 40kHz$ to $f = 800kHz$ which detected the charge displacement across the spark gap via a measurement capacitor $C_M = 400pF$. Dead time between measurements was set to the lowest possible value of $t_d = 2\mu s$. Lower noise threshold was set to 2% of the respective PD measurement scale. Furthermore, acoustic measurements for PD localization were performed by means of an ultrasonic PD detector. A bleeding resistor $R_B = 330GW$ was added to ensure save discharge of the measurement setup when powered down. A variable DC voltage of up to $U_{DC} = 100kV$ applied to a needle-plane electrode configuration with $d = 20cm$ gap distance, representing near breakdown conditions for positive polarity, such that all corona modes could be studied. The room temperature during the measurements was between $T = 20.3řC$ and $T = 21.8řC$ and the relative humidity between $RH = 28.7\%$ and $RH = 34.1\%$. The wind source was a modified industrial fan for buildings connected to a frequency converter which produced an air flow velocity of maximum $v = 22m/s$ through a rectangular shaped nozzle with an air-outlet of 61 cm times 30 cm, which ensures laminar air flow across the gap. The needle-plane electrode configuration was mounted 40 cm away from the outlet. The methodology for the PD measurements was the following. Constant DC voltage was applied to the needle tip and the PD patterns were measured during 100 seconds. From $t = 0s$ to $t = 20s$ there was no air flow in the gap. At $t = 20s$ the industrial fan was turned on and the wind speed increased. The fan accelerated linearly from $n = 0rpm$ to $n = 1500rpm$ in ten seconds. From $t = 30s$ to $t = 40s$ the maximum wind speed of $v = 22m/s$ was applied. $Att = 40s$ the fan was turned off and the fan speed linearly decreased within ten seconds. It needs to be noticed that the air flow continued slightly in the gap after the fan reached idle state due to the inertia of the air. At $t = 60s$, the fan was switched-on again and the process was repeated in similar fashion. Both positive and negative DC voltages at the needle were evaluated and the results are presented the Figures 4.13 and 4.14. Each illustration contains nine diagrams which show the behavior at discrete voltage levels. On the top of each figure, the time dependent rotational speed of the fan is illustrated. The correlation between steady state wind speed and rotational speed of the fan is given in Table 4.2.

UV photographs show the needle tip area at different DC voltage levels. The UV camera was a Hamamatsu C8484-05G with a 05mm f/4 uv-micro-apo lens.

4.5.1.2 Measurement setup 2

The purpose of the second laboratory experiment is to investigate if space charges, mainly ions, which alter the electric field in the gap, can be distracted with air flow, leading to an altered breakdown voltage in the case of air flow. An illustration of the laboratory setup is given in Figure 4.12. A $100kV$ DC voltage source was connected in parallel to an $800kV$ impulse generator. The same needle-plane electrode configuration as described in Section 4.5.1.1 was used; however, the gap distance was increased to $d = 25cm$. The impulse voltage waveform was the standard lightning impulse voltage with a front time

Table 4.2: Rotational speed vs. wind speed of industrial fan.

Rotational Speed [rpm]	Wind Speed [m/s]
250	3.4
500	7.1
750	10.5
1000	14.2
1250	17.5
1500	22.0

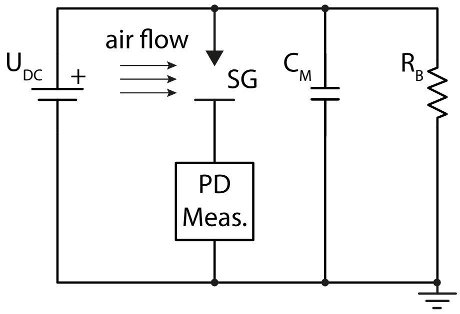

Figure 4.11: Circuit diagram for first laboratory setup. The DC voltage U_{DC} is varied between 0 and 100 kV. Partial discharges are measured with the PD measurement equipment across the measurement capacitor C_M . The bleeding resistor R_B acts as safety equipment.

T_f and a half value time T_h of $T_f/T_h = 1.2/50\mu s$. In order to ensure isolation between DC source and the impulse generator a separation capacitor $C_s = 400pF$, a protection resistor $R_p = 50M\Omega$ and a filter capacitor $C_p = 4nF$ are added to the circuit as illustrated in Figure 4.12. For each DC voltage, the flashover impulse voltage U_{50} was found by application of the Multi-level test method as described in [114]. Between five and nine levels were used to determine U_{50} depending on the resulting discharge characteristics. For each level, 15 shots were applied in order to identify the breakdown probability. The experiment was conducted for positive impulse and positive DC voltage (1335 discharges), as well as negative impulse and negative DC voltage (1500 discharges).

4.5.2 Results

4.5.2.1 Measurement setup 1 - PD measurements

Negative polarity Figure 4.13 illustrates the impact of air flow to the PD patterns under negative polarity at the needle. The PD-pattern is the charge-time distribution over the measurement period and the colors indicate the number of PD-pulses being detected.

The corona onset was determined for the negative polarity at $U_{DC} = -3kV$. Compared to the positive polarity, the PD started at lower voltages, since initiating electrons are readily available from the negatively charged electrode. If the DC voltage is increased gradually, the negative corona discharges develops through three different pulse modes, which are Trichel streamer(or Trichel pulses), pulseless negative glow and negative streamer (See Section 4.1.1). Trichel streamer corona was identified between $U_{DC} = -3kV$ to $U_{DC} = -40kV$, pulseless negative glow between $U_{DC} = -50kV$ to $U_{DC} = -60kV$ and negative streamer from $U_{DC} = -70kV$. The main discharge amplitude band of negative PD is located between a few picocoulombs and 137 picocoulombs. In the Trichel streamer mode between $U_{DC} = -3kV$ to $U_{DC} = -40kV$, the maximum amplitude increases between 5% and 100% depending on the DC voltage due to the air flow. When air flow is applied in

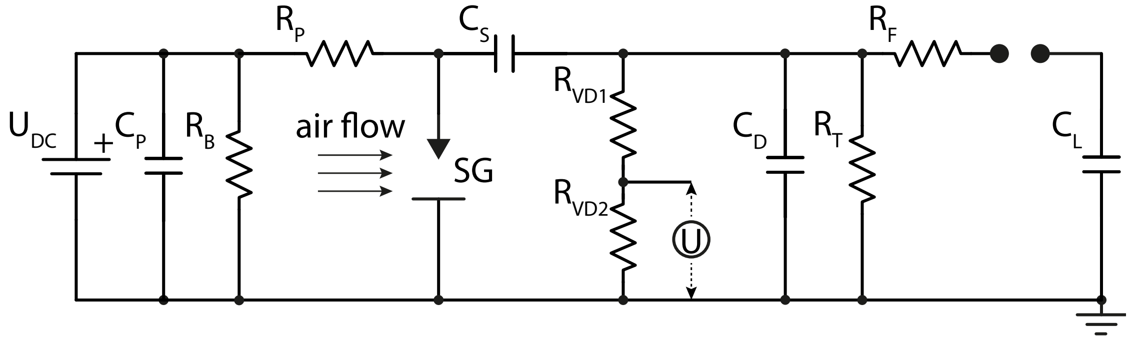

Figure 4.12: Circuit diagram for second laboratory setup. Combined DC and impulse voltage on needle-plane spark gap exposed to wind flow. U_{DC} is varied between 0 and 100 kV. The air flow can be varied in the spark gap. C_P = protection capacitor, R_B = bleeding resistor, R_P = protection resistor, C_S = separation capacitor, C_D = discharge capacitor, R_V = voltage divider resistor (measurement resistor not in schematic), R_T = tail resistor, R_F = front resistor, C_L = load capacitor.

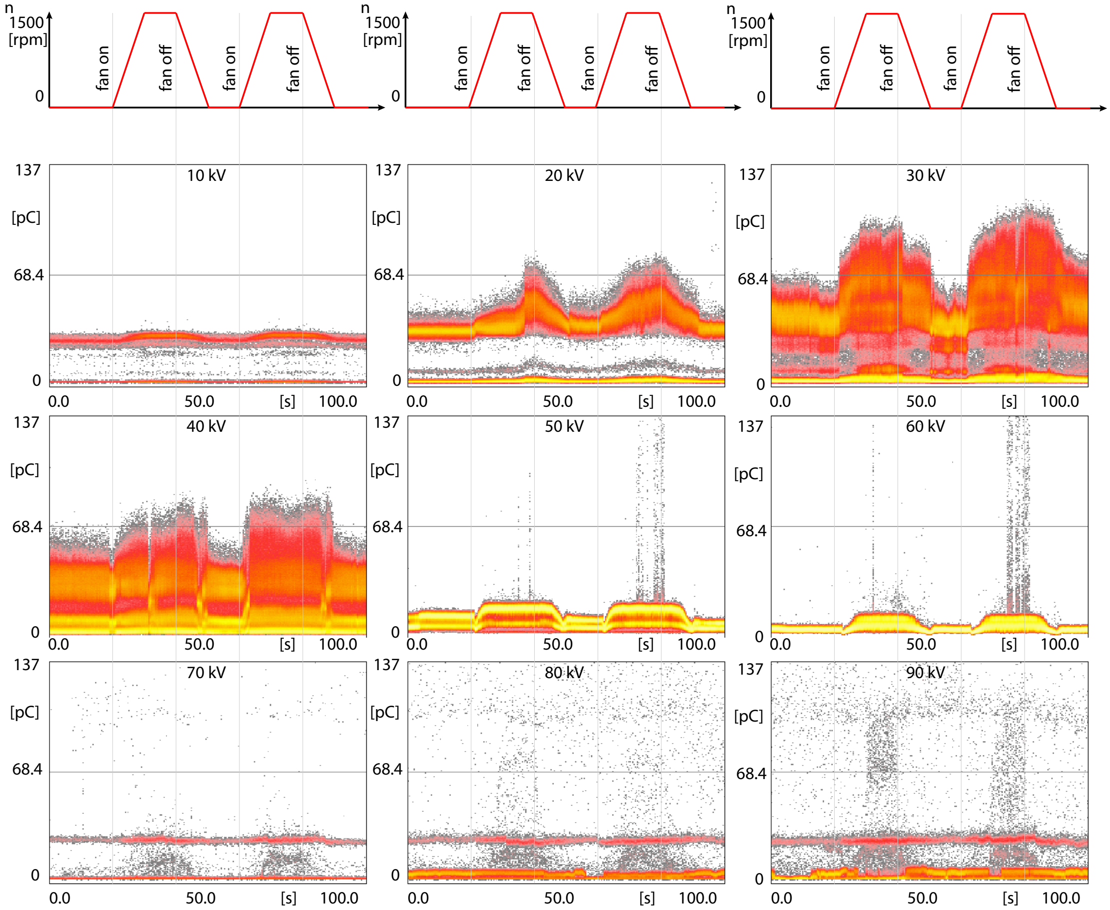

Figure 4.13: Negative polarity: Wind speed variations and corresponding changes in the charge-time (Q-t) PD pattern: 100 seconds of PD measurements with air flow from $t = 20s$ to $50s$ and $t = 60s$ to $t = 90s$. Trichel streamer corona mode from $U_DC = -3kV$ to $-40kV$, pulseless negative glow corona from $U_DC = -50kV$ to $-60kV$, streamer corona from $U_{DC} = -70kV$ to $-90kV$.

the negative glow corona state between $U_{DC} = -50kV$ to $U_{DC} = -60kV$, the characteristic high frequency PD pattern increases slightly in magnitude and various larger discharges are superimposed on the measurement. It can be seen that the air flow changes the PD pattern from pulseless negative glow to negative streamer corona. From $U_{DC} = -70kV$ to $U_{DC} = -90kV$, the air flow increases slightly the frequency and magnitude of the PD pattern.

Positive polarity Four different positive corona modes can be distinguished which are burst corona, onset streamer, glow corona, and breakdown streamer [113]. The measurement results are illustrated in Figure 4.14.

Corona onset for the positive polarity was determined to be $U_O = 12kV$. Burst corona and onset streamer corona can appear within a very short voltage range [113] and were determined simultaneously between a voltage range of $U_{DC} = 12kV$ to $U_{DC} = 14kV$. Compared to the negative polarity, the PD of the initial positive corona mode was

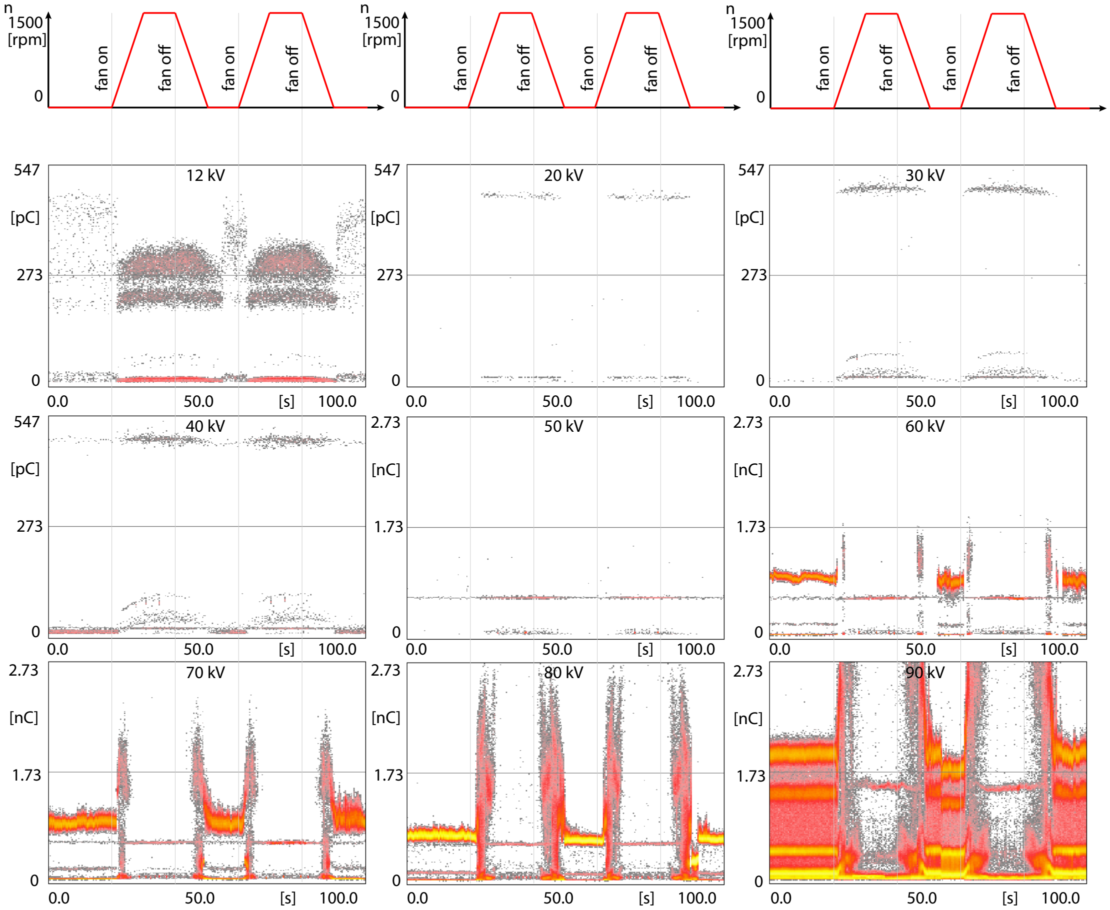

Figure 4.14: Positive polarity: Wind speed variations and corresponding changes in the charge-time (Q-t) PD pattern: 100 s of PD measurements with air flow from $t = 20s$ to $50s$ and $t = 60s$ to $t = 90s$. Burst corona and onset streamer corona mode from $U_{DC} = 12kV$ to $14kV$, positive glow corona from $U_{DC} = 14kV$ to $50kV$, breakdown streamer corona from $U_{DC} = 60kV$ to $90kV$.

characterized by a higher charge magnitude (up to $Q = 500pC$) and a lower frequency. This is in good agreement with the gas discharge theory, since continuous availability of starting electrons at the negative polarity enable more frequent discharges with a lower amplitude, whereas PD at positive biased electrodes is initiated based on random electrons in the ambient air [136]. The glow corona mode started at approximately $U_{DC} = 14kV$ and continued until $U_{DC} = 50kV$. Few positive glow corona discharges were detected with the PD-measurement equipment. The reason for this appearance is most likely the high frequency of glow corona pulses in DC fields of several Megahertz [117]. With an upper cut-off frequency of $f_c = 800kHz$ from the PD measurement equipment, a fraction pulses may be not able to be detected. Breakdown streamer corona starts at $U_{DC} = 60kV$ and continues until $U_{DC} = 90kV$. Notice, the y-axis scale in Figure 4.14 changes from $Q = 547pC$ to $Q = 2.73nC$. With increasing voltage, the frequency of the pulses as well as the magnitude increases.

The impact of the air flow is more pronounced at positive polarity as compared to negative polarity. The strongest impact can be seen in the burst corona, onset streamer and breakdown streamer mode as can be seen in Figure 4.14. The reason for the observation is that streamers propagate further into the gap and are not only contained around the vicinity of the gap. When partial discharge channel propagate further into the gap, also the air flow has higher impact since it can influence the movement of charged ions.

In the case of $U_{DC} = 12kV$ illustrated in Figure 4.14, the frequency of pulses increase significantly, whereas the magnitude of pulses decreases slightly. Glow corona from $U_{DC} = 20kV$ to $U_{DC} = 30kV$ could not be measured with the PD-measurement equipment without air flow, however, when air flow was applied, pulses clearly could be detected. A possible explanation is that the air flow removes the shielding ions from the electrode, leading to discharges which are higher in magnitude and lower in frequency. From $U_{DC} = 60kV$ to $U_{DC} = 90kV$ breakdown streamer corona appears. It can be observed that the magnitude of PD increase while the fan is starting up and the air flow is increasing in the gap. If the air flow reaches a critical wind speed, the occurrence of PD stops. The breakdown streamer corona is extinguished and possibly transformed into a reduced glow corona discharge pattern which takes place only in the vicinity of the electrode.

Breakdown streamer corona extinguished by high air flow In order to see the impact of air flow to a specific corona mode, in this case the breakdown streamer corona, a separate experiment was performed, where the wind magnitude was varied at a steady DC voltage of $U_{DC} = 70kV$. As can be seen in Figure 4.15, already at slight wind speeds of $v = 3.4\frac{m}{s}$ the magnitude of PD discharges increases as well as the frequency of the discharges. At $v = 7.1\frac{m}{s}$ the magnitude does not vary distinctly; however, the frequency (Number of discharges) of the PD decreases. At $v = 10.5\frac{m}{s}$, the magnitude of PD is further increased but the amount of discharges is significantly reduced. From $v = 14.2\frac{m}{s}$, the breakdown streamer corona is extinguished. There remains a high frequency PD pattern which is of similar nature to the glow corona mode. Notice, only a positive corona discharge can be extinguished by high air flow.

4.5.2.2 Measurement setup 1 - UV photography

Ultraviolet (UV) photographs from the corona discharges at various DC voltage levels were recorded with and without air flow, as illustrated in Figure 4.17. The positive polarity is more sensitive regarding air flow compared to the negative polarity. For the positive polarity, the visible corona glow started at around $U_{DC} = 40kV$. Beforehand, as indicated by the PD measurements, the discharges were so faint that glow was not able to be determined. Furthermore, there was no visible corona in the first corona mode at $U_{DC} = 12kV$. In the UV picture, the impact of the air flow becomes apparent at $U_{DC} = 60kV$ and above. Two different effects can be observed. First, due to the air flow, the luminosity of the corona discharge can be enhanced as can be seen in Figure 4.17 at $U_{DC} = 80kV$. Second, the corona discharge can be extinguished by high air velocities as can be observed at $U_{DC} = 100kV$. The stable breakdown streamer corona is suppressed into a smaller glow corona. The process of transformation is also illustrated in Figure 4.16. In this scenario, the wind was linearly increased from $v = 0\frac{m}{s}$ to $v = 22\frac{m}{s}$ and the discharges were in breakdown streamer mode at positive $U_{DC} = 100kV$. The recordings of the negative polarity did indicate no or only a weak effect of the air flow to the light

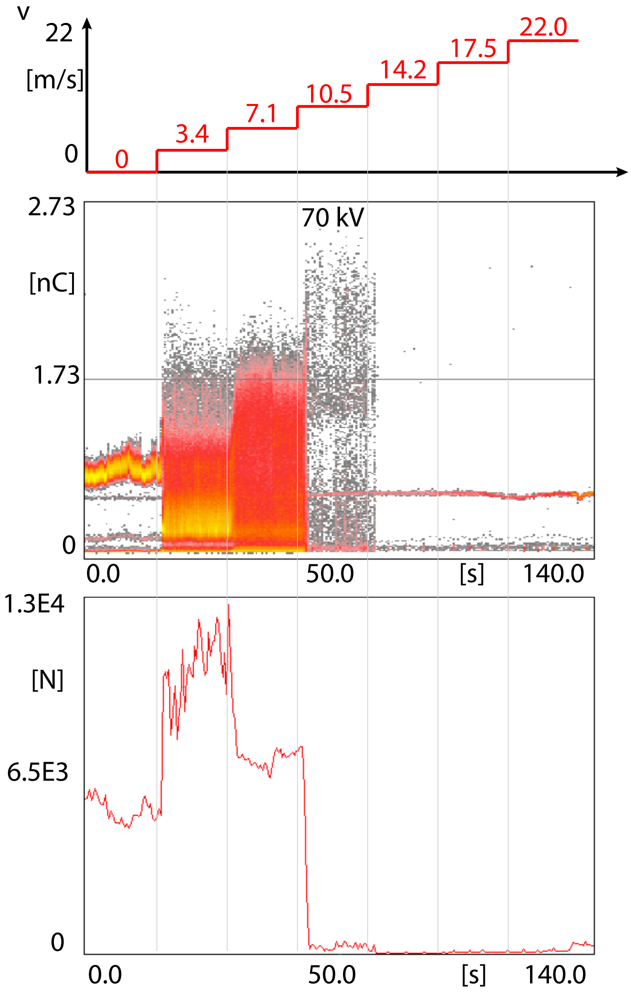

Figure 4.15: Breakdown streamer corona exposed to a variable amount of air flow. The magnitude of PD increases with increasing air flow and the frequency (number of discharges) of PD increases first at $v = 3.4\frac{m}{s}$ and decreases from $v = 7.1\frac{m}{s}$ until breakdown streamer corona is extinguished.

emission in the UV spectrum. With increasing negative voltage, the corona emission linearly increases in brightness around the tip of the electrode in a conical shape. Since negative corona discharges are driven by electron emissions from the nearby cathode, the air flow has only a weak impact and the ionization zone remains unaffected even if the electrode is exposed to high air flow velocities.

4.5.2.3 Measurement setup 2 - Combined impulse and DC voltages - Breakdown experiment

Negative DC + Negative impulse voltage The air flow has a distinct impact on the breakdown voltage of a negative biased electrode configuration. As can be seen in Figure 4.18a, the 50% Flashover voltage (FOV) is higher when air flow is applied to the needle electrode compared to the case without air flow. The effect is more pronounced when the DC voltage is higher. The results indicate that space charges created by a negative point discharge have the ability to reduce distinctly the breakdown voltage in the gap. The DC

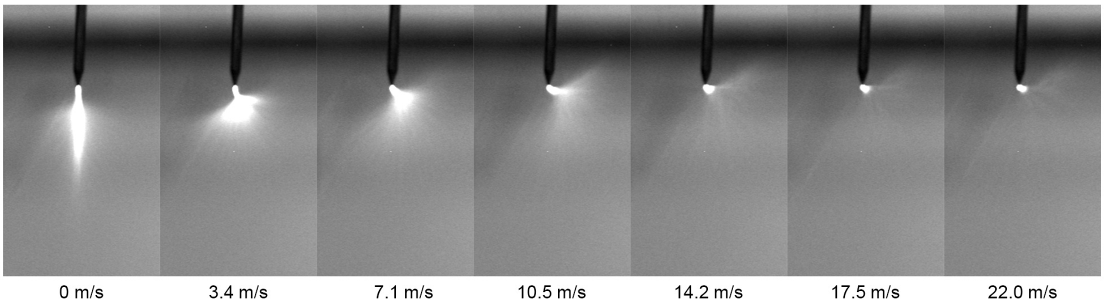

Figure 4.16: UV recordings of positive corona discharges at $U_{DC} = 100kV$ with increasing air flow.

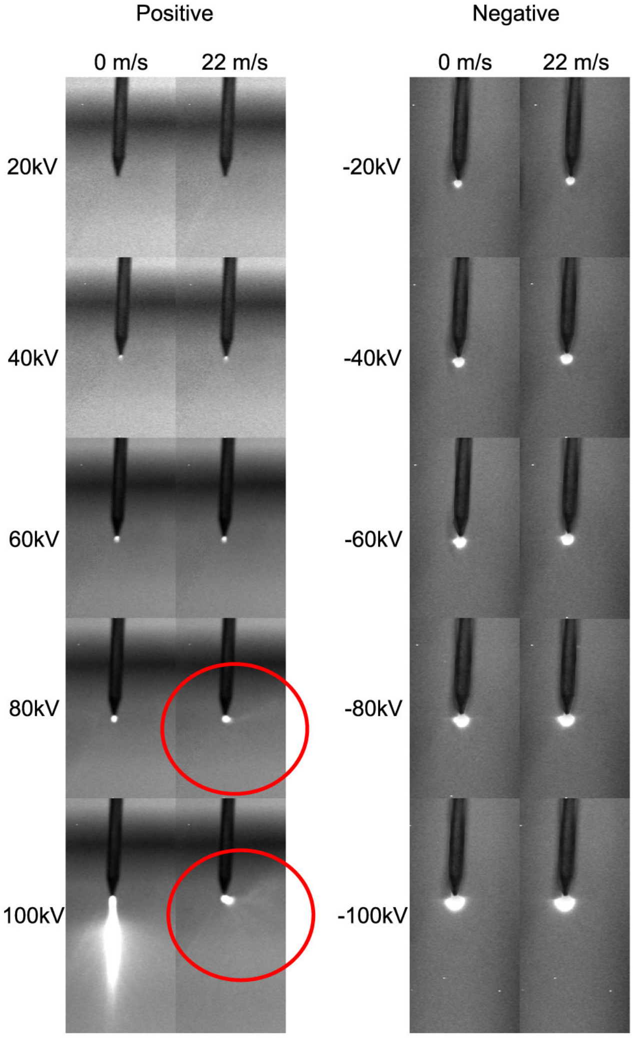

Figure 4.17: UV recordings of corona discharges of positive and negative tip polarity at various DC voltages with and without air flow. Red circles highlights the tilted corona stem due to air flow.

voltage range U_{DC} in this experiment was $U_{DC} = -40kV$ to $U_{DC} = -100kV$. Breakdown at $0kV$ and $-20kV$ could not be triggered reliably since the breakdown voltage exceeded the maximum rated voltage of the impulse generator.

Positive DC + Positive impulse voltage With positive DC and impulse voltage, the air flow has only a slight impact. The results align with the findings from [137] which stated that the impact of space charges from positive pre-stress can only be investigated for electrode distances larger than $0.5m$. As can be seen in Figure 4.18b, from $U_{DC} = 0kV$ to $U_{DC} = 90kV$, there is no effect between the measurement with and without air flow. At $U_{DC} = 100kV$ and without air flow, a stable breakdown streamer corona channel is established with a length of approximately $2.5cm$. This discharge reduces effectively the distance between the needle and the plane, resulting in a significant decrease in the 50% FOV. In the case of applied air flow, the stable breakdown streamer corona is extinguished as shown in the UV pictures in Figure 4.16, leading to an increase in FOV.

The effect of air flow to the reduction of FOV voltage The impact to the reduction of the FOV is illustrated in Figure 4.19. The difference between the solid and dashed lines represents the magnitude of the impact of the air flow. As can be seen, especially at the negative polarity the impact of air flow can be observed. If no air flow is applied, the space charges in the gap enable a drastic reduction in FOV with up to 44% at $U_{DC} = 90kV$. If the gap is exposed to relative high wind velocities, the space charges are swept away and the reduction of FOV is close to zero. At positive polarity, both curves are nearly identical and only at $U_{DC} = 100kV$ a distinct alteration is noticeable due to the extinguished corona discharge. The reason for the distinct difference between the polarities may be that negative point discharges are continuously filling up the gap with ions due to the abundance of initiating electrons. The negative streamers are supported in their propagation through the gap. When air flow is applied ions are removed from the gap leading to a reduced support in propagation and a higher FOV. On the other hand, at positive polarity, the frequency of discharges is lower but the magnitudes of pulses are bigger. Once a positive streamer develops from the anode, the propagation and development is governed mainly by the participating ions of the streamer and residual space charges from the preceding discharges are too weak to impact the discharge characteristic.

4.5.3 Summary - Laboratory experiment

The impact of air flow on discharge characteristics in inhomogeneous fields was verified. In the first experiment, a PD pattern analysis was performed and the impact of wind on the different corona modes was evaluated. The PD pattern of the positive polarity shows higher dependence on air flow compared to the negative polarity. Breakdown streamer corona was transformed into a smaller glow corona discharge if sufficient wind was applied to the needle electrode. Moderate air flow, on the other hand, can increase the amount and magnitude of PD pulses. UV photographs of the luminous corona confirm the susceptibility of the positive polarity to air flow, compared to the negative polarity which is largely unaffected. In the second experiment, combined DC and impulse voltages were applied to a needle-plane electrode configuration and the 50% flashover voltage U_{50} was determined

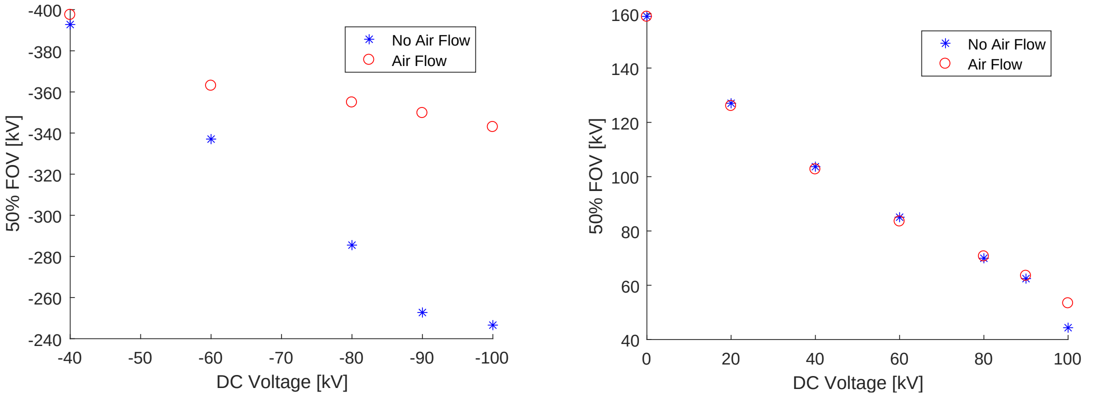

(a) Negative polarity. Scenario one (blue asterix) without air flow, Scenario two (red circle) with $v = 22\frac{m}{s}$ air flow applied

(b) Positive polarity. Scenario one (blue asterix) without air flow, Scenario two (red circle) with $v = 22\frac{m}{s}$ air flow applied.

Figure 4.18: 50% (FOV) with combined impulse and DC voltage.

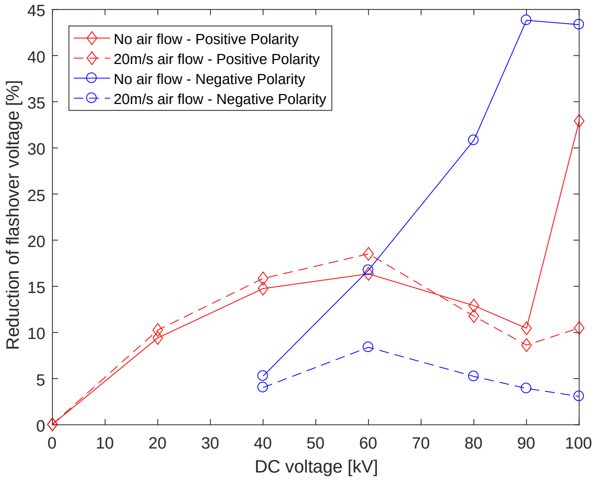

Figure 4.19: Combined impulse and DC voltages. Reduction of FOV due to DC voltage and space charge on electrode configuration with and without the impact of air flow.

with and without the impact of air flow. In the case of negative polarity and no air flow, the space charges created by the DC field decreased the flashover voltage U_{50} up to 44%. When air flow was applied to the gap, the space charges were removed from the gap and flashover voltage U_{50} showed only a negligible reduction. On the other hand, there is hardly any impact of air flow on the positive breakdown characteristics. Table 4.3 summarizes the results of this paper.

4.6 Discussion of results from FEA model and laboratory experiments and their implications to lightning attachment

In this chapter, a practical and theoretical investigation of the effects of high velocity air flow and space charges were performed. The background for this investigation is the

Table 4.3: Summary: Polarity dependent impact of air flow to corona discharges and flashover voltage.

	Negative	Positive
PD measurements at DC voltage	Slight	Yes, distinct
Optical UV observation at DC voltage	No	Yes
FOV at combined impulse and DC voltage	Yes, distinct	Only at 100kV

rotation of wind turbine blades which constantly exposes the metallic tip receptors to a relative air flow and removes space charges from the tip receptors.

Similar to the predictions of Wang [109] and Montanya [32], the FEA analysis showed that space charges effectively lower the resulting electric field in the immediate vicinity of the electrode. Even though the research by Becerra [138] showed that the field reduction is not enough to suppress answering upward lightning leaders in the instance of an approaching downward lightning leader, it could possibly hinder a self-initiated upward lightning discharge from developing on a static tower. On the contrary, wind turbine blades are exposed to constant high air velocity which removes the concentration of spaces charges on side, leaving the leading edge of a wind turbine blade more exposed compared to the situation on a tower. This could explain the observation made by Wang [109]. In his research, a lightning protection tower which is placed next to a wind turbine was less likely to be struck compared to a wind turbine when the ambient wind speed was rather low and space charge accumulated over the top of the tower.

The results of the second laboratory experiment, on the other hand, indicated a contradicting observation to the results of the FEA model and the observations of [109]. For the negative DC bias, breakdown of the gap was initiated at lower median FOV voltages when no air flow was applied and hence no space charge was removed from the gap. As soon as the fan was turned-on and the space charge was affected by the air flow, the median FOV voltage increased. The positive DC bias did not show a distinct impact of the air flow, except at the highest DC potential when breakdown streamer corona occurred and the corona discharge was suppressed. The reduction of FOV with combined voltage levels was also reported in with bigger electrode distances [137].

There might be several reasons responsible for the contradicting observation of simulation and laboratory experiment. The first crucial point to be made is that the distance between the spark gap electrodes used for the laboratory experiment is very small ($d = 25cm$). Due to this reason, there was only little accumulation of space charge in the gap which influenced the breakdown behavior. The space charge was swept away in the opposing electrode before the electric field was noticeably affected, as discussed in Section 4.3. In larger gaps, the space charge is slowed-down drastically in the low magnitude electric field regions and can accumulate. Second, the high velocity of the ions around the needle electrode distributed the space charge in the gap very evenly rather than surrounding (shielding) the electrode. When no air flow is applied, the entire gap is filled with ionized particles which enable an easier environment to create a discharge from the subsequently fired the impulse generator. When air flow is applied, the space charge is swept away and ionization in the gap is reduced. The higher impact of the DC bias from negative polarity compared to the positive polarity may be explained by the circumstance that positive oxygen ions created by positive corona (ionization) are likely to attach an electron and neutralize their charge. Negative ions created by negative corona (ionization) are already saturated and potentially more electrons are available in the gap to initialize an avalanche. Third, the small distance of the gap does not represent a similar environment of a lightning leader because the electric field is dominated by the potential of the electrode rather than the space charges. Lastely, the missing shielding effect of space charge could be attributed to the circumstance that there is not enough space charge in the gap since there was only one needle electrode in the laboratory experiment. An electrode configuration with several grounded pointy edges may have changed the outcome since corona current increases with the amount of corona points [139].

In order to observe the shielding effect of space charge, it is estimated that a substantial distance of several meters between the electrodes is likely to be necessary. In order to generate corona in such a gap, a DC voltage source of several hundred kilovolts is necessary and a multi-megavolt Marx-Generator is required to generate a flash-over. Unfortunately, laboratory facilities did not allow for the required test conditions for this study.

Nevertheless, the laboratory experiments verified that air flow influences the propagation of spaces charges. From the theory and the FEA model, a shielding effect from space charges can be expected.

5 ELITE - A MODULAR HIGH CURRENT IMPULSE GENERATOR

The previous chapters discussed various lightning related issues and enabled the reader to form a broader understanding of how lightning flashes and wind turbines interact and which local differences exist between different sites. The final chapter of this dissertation documents the design, implementation, and test of the novel high current impulse generator that enables realistic high current testing for lightning impact verification.

The chapter is divided into several sections. At first, the requirements from the industry and practical design guidelines for the generator are discussed. Subsequently, in order to dimension the generator, the maximum expected impedance of the test samples is determined. The section is followed by the fundamentals of high current testing which also calculates the limitations of high current testing. The design and control of the individual impulse generators are discussed and a practical validation of generator concept is given. The last section discusses the possibility of combined impulse testing and the resulting challenges.

5.1 Industry requirements and practical design guidelines for the generator

Before the design and development of the novel test generator started, the representatives of the advisory board of ELITE (Overview Appendix: A) were asked to formulate the expected wind turbine component developments in the next ten years. Following results were obtained for the survey:

1. Wind turbine blades are likely to exceed a length of 100 meters.
2. There is an increasing trend towards carbon fiber in wind turbine blades in order to decrease the weight of the blade.
3. The nominal power of nacelles increases to over 10 megawatt. Both direct drive and gear drive generator concepts exist. The physical size of nacelles will increase.
4. There will be a trend towards full-scale component testing in order to obtain the results of both direct and indirect effects of the lightning current in the component structure.
5. Due to the increased size of the components, there will be a need for flexible testing solutions which can be employed in the premises of the wind turbine manufacturer.

Additionally to the industry requirements, a brainstorm meeting was held with the involved staff of GLPS and DTU in order to receive feedback which functionalities need to be implemented in the test system. The meeting included the testing staff of GLPS that eventually will operate the new test system. Following key points were concluded from the meeting.

- A modular system for high current lightning tests is required in order to enable an easy laboratory setup preparation.
- The system shall be used for different loads - from full-scale to small-scale test items.
- A centralized control system that allows to operate the generator with a simple interface is essential. The control system needs to provide a common time reference in order to coordinate exact triggering of the individual actors of the generator.
- All signals and measurements need to be galvanically isolated.
- The manual operation during the testing procedure shall be reduced to a minimum and automated processes shall be included where possible. This includes charging of the generator, grounding, measurement, and triggering the system. All control features shall be implemented in a common user control interface. This will eventually decrease the pre-test preparations and reduce the setup time for the generator.
- The components of the generator shall fit into a regular transportation container.
- The main energy source for high current impulse testing are capacitors and batteries. The concept of inductive energy storage will not be a focus for the project.
- Automatic grounding of the high-voltage capacitors without manual interaction is essential.
- The measurement shall be integrated in the control interface.

In addition to this list of practical functionalities, the ELITE generator shall attempt to create the three most fundamental components of a lightning flash:

1. The first return-stroke of downward lightning flashes.
2. The continuous current sequence of downward and upward lightning flashes.
3. The subsequent return-stroke.

These individual current components are subjected to the natural limitations of high current testing that arise due to resistance and inductance of the test circuit. These properties are further discussed in the Section 5.2 and 5.3.

5.2 Test sample characteristics and return-conductor arrangement

Full-scale wind turbine components are, as any physical object, characterized by resistance, inductance, and capacitance to ground or between other conductors. Especially wind turbine blades are characterized by several tens of microhenries of self inductance that impedes the rise of current in the test sample. Because of this reason, wind turbine blades are defined as the highest expected load for the high current test generator and therefore the focus of this chapter. The construction of the down conductor system as well as the current return-cage has a significant impact on the total circuit inductance. Nacelles, on the other hand, are typically characterized as bulky structures where the current can distribute within the cast iron structure of the mainframe. The resistance and self inductance of the system is typically low, whereas the mutual inductance to the return-cage is high. This decreases the overall inductance of the test circuit as further discussed in Section 5.2.2.2.

This section is dedicated to the characteristics of test samples and the arrangement of the return-cage for high current testing. At first, different lightning protection methods for wind turbine blades are introduced. Subsequently, the analytic approximation of blade impedance is described. Afterwards, the resistance and inductance of different blade geometries are determined by means of a FEA analysis with varying return-conductor arrangements.

5.2.1 Lightning protection methods of wind turbine blades

Lightning protection of wind turbine blades may be performed in various ways. Figure 5.1 illustrates five different blade concepts with different protection methods. In the next section, the different methods are discussed.

- A) illustrates a wind turbine blade with no lightning protection. The protection concept was based-on the insulating nature of glass-fiber which does not conduct electricity in theory and hence no answering lightning leader will develop from the blade structure. Experience shows, however, that polluted structures, wet surfaces, and slightly conducting balsa wood enable lightning attachment to insulating wind turbine blades. Failure of the structural components of a blade was often reported. Due to this reason, modern wind turbines have always one of the following lightning protection means installed.
- B) since glass-fiber blades are never perfect insulators, a metal conductor can be placed inside or outside the wind turbine blade in order to enable a low impedance discharge path for the lightning current. The so called down conductor is a solid or stranded metal conductor which is usually made out of copper, aluminum, or steel. Recommendations of nominal cross- section can be found in [24]. Usually, the down conductor in a blade is connected to the hub/nacelle via sliding contacts or spark gaps. The conduction of lightning currents through pitch/azimuth bearings is usually avoided in order to prevent partial melting of ball bearings. At the tip section of the blade and usually within 1 meter of the tip, a disk receptor is placed and connected to the down conductor. Most of the lightning discharges attaches to this receptor as previously discussed in Chapter 3. Depending on the lightning protection design, several side receptors may be placed along the length of the blade that enable a better protection for low peak current lightning discharges as described in[8]. When designing lightning protection concepts with internal down conductors, special attention needs to be attributed to the insulation coordination and interfaces between the down conductor and the receptors. Especially in the tip area where the electric field is concentrated, discharges may start from unintended locations and punctures through the laminate of the blade may degrade the LPS.
- C) is similar to the concept B). Instead of a tip receptor, the tip is protected by a solid cap that provides an electrode with a bigger heat capacity. The design is advantageous in areas where frequent high charge lightning attachments are expected to connect to the blade (for instance winter lightning areas). Since the arc is pushed towards the trailing edge due to the rotation of blade, the majority of the charge interfaces with the receptor from the trailing edge. A solid metal cap has the advantage that the arc can directly attach to the outside of the receptor. Disk receptors, as indicated in concept B), drag the plasma channel of the lightning over the insulating composite

surface which can alter the conductivity of the laminate. This may also lead to unintended punctures in the tip area. Solid tip receptors need adequate mechanical implementation in the blade tip which can take the stress of the increased weight. Additionally, if conductive fixations are used to hold the tip in place, sharp edges need to be avoided and insulation coordination needs to be applied to eliminate the risk of punctures through the blade laminate.

- D) Recently, the trend to include structural carbon-fiber spars is apparent in the industry due to the enhanced physical performance for instance the stiffness/weight ratio. Also blade laminates can be made directly from carbon fiber. The material is an anisotropic conductor with an approximately 1000 times lower conductivity than aluminum [24]. The apparent conductivity depends on the manufacturing method of the fibers and the direction-dependent alignment. The conductivity perpendicular to the fibers is about two orders of magnitude higher than that of the conduction direction. Usually, a metallic down conductor system is placed in parallel to the carbon fiber laminate. Carbon fiber spars and laminates may be included to the lightning protection system via bonding or electrically isolated from the design; however, the design needs to address the conductivity of the material and one of the solutions has to be implemented. If the bonding solution is implemented, the difference in resistivity between down conductor and carbon fiber requires regular bonding points along the blade. Simulation of lightning current distribution can estimate bonding distances. If the isolation solution is implemented, the down conductor should be placed as far as possible from the carbon fiber elements.
- E) a mesh or surface protection in wind turbine blades provides protection independent from down conductor systems. This solution is primarily used to protect conductive carbon fiber laminates. Several surface protection methods exist for instance metal spray, metal fibers, or metal foil which are placed in or outside the outer layer of the blade skin. The disadvantage of this protection is the rather low thickness of the mesh. The arc diameter of a lightning stroke is usually lower than 10 cm. The high current density at the injection point leads to a high rate of evaporation of the mesh/foil which damages the lightning protection capability of the blade.

5.2.2 Resistance and inductance approximation with analytic expressions

In this section, expressions to determine resistance and inductance of large wind turbine blades are provided.

5.2.2.1 Resistance

The resistance per unit length of a material can be calculated by dividing the cross-sectional area A by the resistivity of the material ρ.

$$\frac{R}{l} = \frac{\rho}{A} \tag{5.1}$$

Commonly used materials for lightning protection purposes in wind turbines are metals like copper and aluminum as well as composite materials like GFRP and Carbon fiber

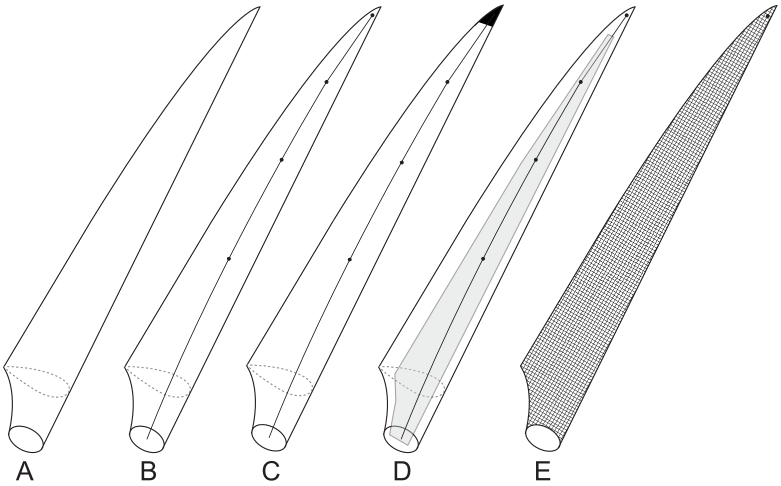

Figure 5.1: Different lightning protection designs. A) Isolation Design B) Down conductor design with disk receptors and optional side receptors C) Down conductor design with solid metal tip receptor and optional side receptors D) Down conductor system with carbon fiber spar caps, E) Conductive mesh design

reinforced plastic (CFRP). The latter material is characterized by anisotropic material properties which creates challenges in terms of current distribution in the test samples. Furthermore, CFRP is semi-conductive which means that it is neither a good insulator nor a good conductor. This creates challenges in terms of potential differences between parallel current paths.

Table 5.1 lists resistivities of materials used in wind turbine applications. The direction reference for CFRP materials is illustrated in Figure 5.2. It should be noted that the given resistivity values of CFRP are average values of generic test samples. Conductivity of carbon fiber can be increased with various techniques such as adding nano-particles or graphene-oxide into the polymer resin or directly to the carbon fibers.

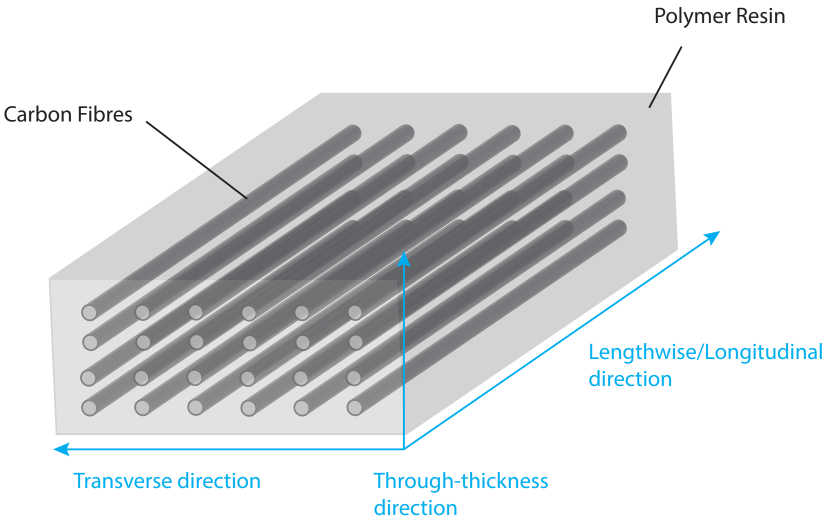

Figure 5.2: Direction reference for carbon fiber panels

Table 5.1: Resistivity values for various materials used in lightning protection of wind turbines.

Material	Resistivity $[\Omega m]$
Copper	$1.7 \cdot 10^{-8}$
Aluminium	$2.8 \cdot 10^{-8}$
Mild Steel	$1.5 \cdot 10^{-7}$
Stainless Steel	$6.9 \cdot 10^{-7}$
CFRP (Lengthwise)	$2.5 \cdot 10^{-5}$
CFRP(Through-thickness)	$2.5 \cdot 10^{-3}$
CFRP (Transverse direction)	$2.5 \cdot 10^{-2}$

5.2.2.2 Inductance

The term inductance is commonly defined as the property of an electric circuit, by which an electromotive force is induced in it, as the result of changing current or magnetic flux [30]. The term can be further split into self inductance and mutual inductance. Self inductance of a single component can be treated as a fraction of the inductance of a complete circuit. In the absence of magnetic materials, self and mutual-inductances are parameters that are independent of the magnitude of the current and depend solely on the geometry of the conductors [30]. Therefore, it is possible to calculate sequentially self inductance values for a system.

The self inductance L_o of a straight wire of non-magnetic material can be calculated analytically:

$$L_o = 2 * 10^{-7} l \left(ln \frac{4l}{d} - 0.75 \right) \tag{5.2}$$

where $l[m]$ represents the length of the conductor and $r[m]$ is the radius of the conductor [140].

For high frequencies, the change of inductance due to the skin effect can be accounted:

$$L_o = 2 * 10^{-7} l \left(ln \frac{4l}{d} - 1 + (\mu_r \delta 1e3 \right) \tag{5.3}$$

where μ_r is the relative permeability and δ is the skin-effect factor which can be calculated:

$$\delta = \sqrt{\frac{2\rho}{\omega \mu_0 \mu_r}} \tag{5.4}$$

where $\rho[\Omega m]$ is the material resistivity, $\omega[\frac{1}{s}]$ is the angular frequency, and μ_0 is the magnetic permeability constant of vacuum.

The term mutual inductance defines the linkage of flux created by one conductor to another one. It can also be expressed as a coupling between coils or conductors [140].

The mutual inductance M between two straight parallel wires of the same length can be analytically estimated with:

$$M = 2 * 10^{-7} l \left(ln \frac{2l}{D} - 1 + D/L \right) \tag{5.5}$$

where $D[m]$ is the distance between the two wires.

The total inductance L of a circuit can be calculated by sequential calculation of self inductances of all components and by subtracting all the mutual couplings [141].

$$L = L_{s1} + L_{s2} - 2M \tag{5.6}$$

As can be seen, an increase in mutual coupling in a circuit decreases the overall inductance of the system. High-current impulse testing typically involves a specially designed return-cage arrangement which enhances the mutual coupling between test object and current return path.

As a part of the ELITE project, the effect of a variable amount of return-conductors in the return-cage was analytically evaluated in [142]. In the model of the author, the self- and mutual inductances of one down conductor and N return conductors were determined which were arranged on the circumference of a $48.7m$ long cone. The narrow end had a radius of $30cm$ whereas the radius of the wide end was varied between $1m$ and $3m$. An illustration with eight return-conductors is depicted in Figure 5.3. The cone represents a simplified return conductor arrangement around a wind turbine blade. The down conductor was placed in the center of a circle, whereas the return conductors were distributed evenly on the circumference of the cone as depicted in Figure 5.3a.

The variation of return-conductors in the current return-path has a distinct impact on the resulting stray inductance in the system. As can be seen in Figure 5.4, with increasing amount of conductors, the stray in inductance is reduced. The biggest gradient in stray

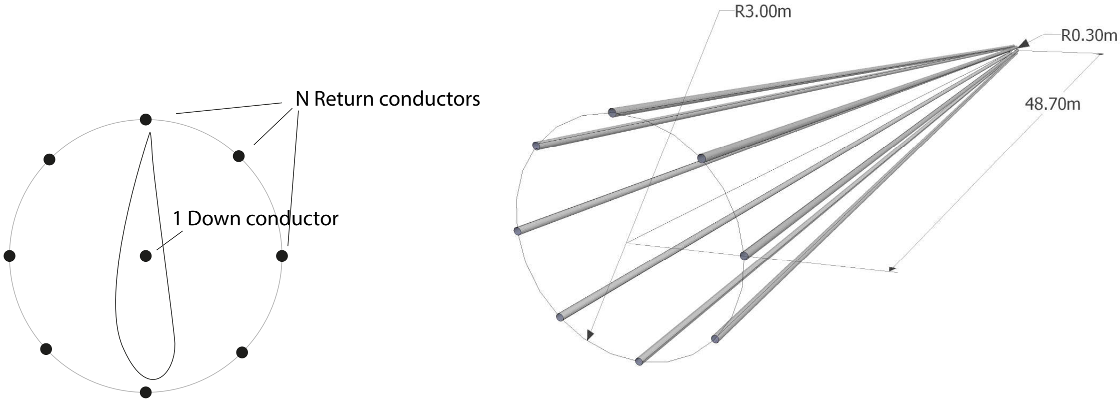

(a) 2D overview of the return-cage arragement. (b) 3D view of the cone shaped conductor arrangement.

Figure 5.3: Illustration of a return-cage with 8 return-conductors for analytic stray inductance evaluation.

inductance reduction can be seen if the number of return-conductors is increased from two to eight, whereas a further increase results in limited impact to the overall circuit inductance.

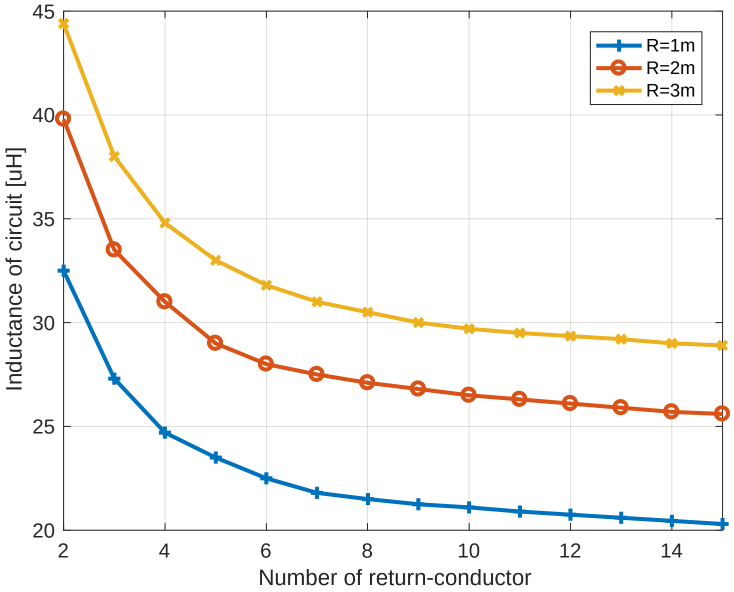

Figure 5.4: Impact of varying return-conductors to the overall circuit inductance. Conductors are arranged on the circumfrence of a cone with a narrow end of $30cm$. The radius of the wide end was varied between $1m$ ant $3m$ (Data from [142]).

For idealized conductor arrangements such as depicted in Figure 5.3, a solution of the total inductance of a system can be found analytically, however, if the LPS design of blades becomes more complex, FEA is a crucial step towards the load impedance estimation of new blade designs. In the next section, the resistance and inductance of several lightning protection solutions of wind turbine blades are computed by means of a FEA in Comsol.

5.2.3 Resistance and inductance approximation with FEA

In the frame of the ELITE project, generic blade resistances and inductances were calculated per unit length with an electromagnetic 2D FEA simulation in the Multiphysics software Comsol. The impedance values were obtained per meter length. The distance and the placement of the individual conducting elements were determined according to a realistic case of a 50 meter blade. This simulation provides insight which wind turbine blade designs are characterized by the highest and by the lowest impedance. In total, eight different lightning protection solutions were used for the evaluation which are:

- One down conductor inside the blade.
- Two parallel down conductors inside the blade.
- Four parallel down conductors inside the blade.
- One down conductor with electrically connected carbon fiber girders in parallel.
- Two parallel down conductors with two connected carbon fiber girders in parallel.
- Four down conductors with two connected carbon fiber girders in parallel.
- Two carbon fiber girders without metallic down conductor path.

- Four carbon fiber girders without metallic down conductor path.

Furthermore, the diameter of the down conductor (Down conductor (DWC)) was varied between $35mm^2$, $50mm^2$ and $70mm^2$. The material of the down conductors was copper for the first two cases and aluminum for the latter case. Additionally, the impact of a current return cage was evaluated and three different cases are investigated.

- Calculation without return path (The current flows back on the edges of the outside air domain). The outside domain is adjusted to a self inductance value of $L = 1.1\mu H$ for a single conductor. Therefore, this case represents the self inductance of a blade.
- Calculation with one steel return path
- Calculation with six steel return paths

The purpose of a current return cage is to enable an even distribution of magnetic fields during the instant of high current lightning test. Since the current flow is forced to return to the terminals of the source, the return path of the current is an important aspect which can alternate the impedance of the DUT.

In Figure 5.5, an illustration of the simulation is shown as an example for the simulation process. The geometric dimensions of a lightning protection design involving two down conductors and two carbon spar gaps is illustrated in Figure 5.5a. As can be seen, only conducting elements are modeled in this type of simulation and all non-conductive GFRP elements are excluded. The model is surrounded by six return conductors where the current is returning. Figure 5.5b shows the surface plot of the magnetic field intensity around the down conductor system when a current of one ampere at a frequency of 1 Hz is conducted. The impedance for the blade is determined at near DC conditions in order to avoid proximity effects between the current paths which would influence the inductance value. This method avoids the increase of resistivity due to the skin effects of the conductors, however, the impedance of the circuit is dominated by inductance at frequencies above $1kHz$ and the influence of resistance is insignificant. Since copper is a better conductor than carbon fiber, 87% of the current is flowing through the smaller down conductor whereas 13% is flowing through the carbon fiber profile. Due to this reason, the magnetic flux peaks in the vicinity of the copper conductor. The current density in the copper conductor is $J = 12.5\frac{kA}{m^2}$ whereas the current density is only $J = 6.8\frac{A}{m^2}$ in the carbon fiber spar.

Table 5.2 shows values for all mentioned cases with and without a return-conductor arrangement. The following conclusions can be drawn from the simulation of the different lightning protection solutions:

1. The inductance of a wind turbine blade is reduced if several parallel down-conductor paths are used for lightning protection purposes. The highest inductance is expected in a lightning protection solution with only one down conductor and no connected carbon fiber spars.
2. Increasing the number of current return-conductors reduces the inductance of the circuit. The distance between the return conductors and the lightning protection conductors should be as small as possible. Limitation of the distance is the shell of a DUT and the safety clearance due to the high voltage potential.

Table 5.2: Calculated resistance and inductance for different lightning protection designs in wind turbine blades. DWC = Down-conductor. Carbon-fiber (CF)= carbon fiber.

Impedance per unit length	Single DWC	Dual DWC	Four DWC	Single DWC - two CF girders	Dual DWC - two CF girders	Four DWC - two CF girders	Two CF girders as DWC	Four CF girders as DWC
Impedances calculated without return path								
35 mm2 Cu DWC		$L = 1.35\mu H$ $R = 0.24m\Omega$	$L = 1.02\mu H$ $R = 0.12m\Omega$	$L = 1.4\mu H$ $R = 0.37m\Omega$	$L = 1.15\mu H$ $R = 0.21m\Omega$	$L = 0.96\mu H$ $R = 0.11m\Omega$	$L = 0.9\mu H$ $R = 1.59m\Omega$	$L = 0.9\mu H$ $R = 0.73m\Omega$
50 mm2 Cu DWC	$L = 1.74\mu H$ $R = 0.34m\Omega$	$L = 1.33\mu H$ $R = 0.17m\Omega$	$L = 1\mu H$ $R = 0.1m\Omega$	$L = 1.45\mu H$ $R = 0.28m\Omega$	$L = 1.16\mu H$ $R = 0.15m\Omega$	$L = 0.97\mu H$ $R = 0.08m\Omega$	$L = 0.9\mu H$ $R = 1.59m\Omega$	$L = 0.9\mu H$ $R = 0.73m\Omega$
70 mm2 AL DWC	$L = 1.71\mu H$ $R = 0.62m\Omega$	$L = 1.31\mu H$ $R = 0.31m\Omega$	$L = 1\mu H$ $R = 0.15m\Omega$	$L = 1.3\mu H$ $R = 0.44m\Omega$	$L = 1.1\mu H$ $R = 0.26m\Omega$	$L = 0.96\mu H$ $R = 0.14m\Omega$	$L = 0.9\mu H$ $R = 1.59m\Omega$	$L = 0.9\mu H$ $R = 0.73m\Omega$
Impedance calculated with one steel conductor as return path								
35 mm2 Cu DWC		$L = 1.29\mu H$ $R = 0.44m\Omega$	$L = 1.05\mu H$ $R = 0.32m\Omega$	$L = 1.37\mu H$ $R = 0.41m\Omega$	$L = 1.13\mu H$ $R = 0.41m\Omega$	$L = 1\mu H$ $R = 0.31m\Omega$	$L = 0.9\mu H$ $R = 1.79m\Omega$	$L = 0.92\mu H$ $R = 1.42m\Omega$
50 mm2 Cu DWC	$L = 1.47\mu H$ $R = 0.53m\Omega$	$L = 1.27\mu H$ $R = 0.37m\Omega$	$L = 1.04\mu H$ $R = 0.28m\Omega$	$L = 1.43\mu H$ $R = 0.48m\Omega$	$L = 1.14\mu H$ $R = 0.35m\Omega$	$L = 1\mu H$ $R = 0.28m\Omega$	$L = 0.9\mu H$ $R = 1.79m\Omega$	$L = 0.92\mu H$ $R = 1.42m\Omega$
70 mm2 Al DWC	$L = 1.71\mu H$ $R = 0.58m\Omega$	$L = 1.25\mu H$ $R = 0.39m\Omega$	$L = 1\mu H$ $R = 0.35m\Omega$	$L = 1.38\mu H$ $R = 0.51m\Omega$	$L = 1.08\mu H$ $R = 0.46m\Omega$	$L = 0.98\mu H$ $R = 0.34m\Omega$	$L = 0.9\mu H$ $R = 1.79m\Omega$	$L = 0.92\mu H$ $R = 1.42m\Omega$
Impedance calculated with six steel conductors								
35 mm2 Cu DWC		$L = 0.69\mu H$ $R = 0.27m\Omega$	$L = 0.34\mu H$ $R = 0.15m\Omega$	$L = 0.69\mu H$ $R = 0.27m\Omega$	$L = 0.49\mu H$ $R = 0.24m\Omega$	$L = 0.32\mu H$ $R = 0.15m\Omega$	$L = 0.24\mu H$ $R = 1.62m\Omega$	$L = 0.24\mu H$ $R = 1.25m\Omega$
50 mm2 Cu DWC	$L = 1.13\mu H$ $R = 0.37m\Omega$	$L = 0.67\mu H$ $R = 0.2m\Omega$	$L = 0.35\mu H$ $R = 0.12m\Omega$	$L = 0.83\mu H$ $R = 0.31m\Omega$	$L = 0.5\mu H$ $R = 0.19m\Omega$	$L = 0.31\mu H$ $R = 0.11m\Omega$	$L = 0.24\mu H$ $R = 1.62m\Omega$	$L = 0.24\mu H$ $R = 1.25m\Omega$
70 mm2 Al DWC	$L = 1.09\mu H$ $R = 0.27m\Omega$	$L = 0.65\mu H$ $R = 0.22m\Omega$	$L = 0.34\mu H$ $R = 0.19m\Omega$	$L = 0.65\mu H$ $R = 0.22m\Omega$	$L = 0.44\mu H$ $R = 0.29m\Omega$	$L = 0.3\mu H$ $R = 0.17m\Omega$	$L = 0.24\mu H$ $R = 1.62m\Omega$	$L = 0.24\mu H$ $R = 1.25m\Omega$

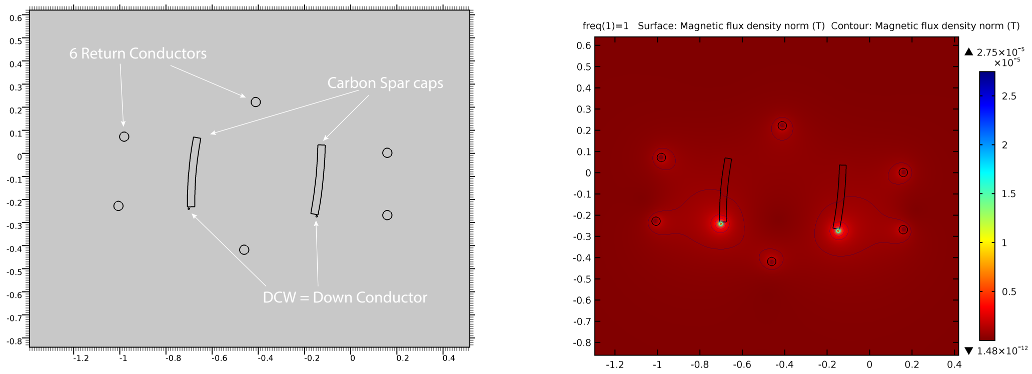

(a) Geometric dimensions of the simulated case. Dimensions in meters.

(b) Field lines of magnetic flux. Due to the opposing current direction, the magnetic field lines cancel-out and the total inductance of the circuit is reduced.

Figure 5.5: Geometry and magnetic flux field lines of a lightning protection system during current injection. The current is injected into the DWC and the carbon spar caps and it is return through the return conductor arrangement.

3. By increasing the cross section of the down conductor, the resistance of the system is reduced. Increasing the cross section does not substantially effect the inductance.

From Table 5.2, an approximation of the highest expected load for the impulse generator can be derived. Long wind turbine blades above 65 meters are most likely built with multiple carbon fiber spars in order to reduce the weight. The circuit inductance is therefore reduced to a value of $\frac{L}{s} = 0.3 - 0.5\frac{\mu H}{m}$. Therefore, the expected inductance of a large blade (60-100 meter) with an optimized return cage is defined as L=40μH and a resistance of $R = 50m\Omega$. This value can vary between the designs of different LPS and each blade needs to be evaluated before a high current test is performed.

5.3 Fundamentals of high current testing

A few fundamental characteristics of high current testing are provided in order to support the design process later in the chapter. In general, high current testing is governed by the law of energy conservation. The most simplified testing circuit is illustrated in Figure 5.6.

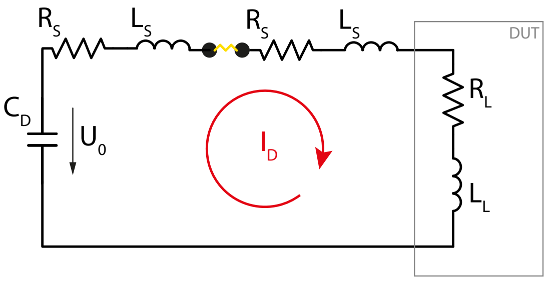

Figure 5.6: Basic high current testing circuit for oscillating current pulses

The circuit consists of one or several series/parallel connected discharge capacitors C_D, a spark gap, and a DUT, characterized by a certain load impedance defined by R_L and L_L. Furthermore, the stray resistance R_S and inductance L_S of the circuit needs to be accounted for. The resistance and inductance of the loop can be added together.

$$R = \sum R_i = R_s + R_L + ... \tag{5.7}$$

and

$$L = \sum L_i = L_s + L_L + ... \tag{5.8}$$

The discharge capacitor C_d is charged until a certain voltage. The spark gap switch triggers a discharge and the capacitor is discharged through the impedance of the DUT. The energy stored in the electric field of the capacitor is transformed into the magnetic energy. The resistance in the circuit transforms a fraction of the energy into heat which eventually dampens the oscillations.

$$\frac{1}{2}C * U^2 = \frac{1}{2}L * I^2 \tag{5.9}$$

A stepwise analysis and design for simple high current generators was performed in [143]. The following equations 5.10 - 5.15 are used from his work in order to introduce the reader to the fundamental equations which determine the type of high current testing.

The loop voltage of the circuit can be determined:

$$U_0 = Ri_D(t) + L\frac{di_D(t)}{dt} + \frac{1}{C}\int i_D(t)dt \tag{5.10}$$

The impedance Z of the loop determines the type of the discharge.

$$Z = \sqrt{|R^2 - 4\frac{L}{C}|} \tag{5.11}$$

By adjusting the resistance in the circuit, the current decay mode can be adjusted. If $R^2 > 4\frac{L}{C}$, the impedance Z becomes positive and the current decay is over-damped. If $R^2 < 4\frac{L}{C}$, the impedance Z becomes complex and the current decay is under-damped. For the matched case $R^2 = 4\frac{L}{C}$, a damped current decay is established.

Table 5.3: The properties of the current discharge depend on R, L, and C.

$R^2 - 4\frac{L}{C}$	Current decay
>0	over-damped
=0	damped oscillation
<0	under-damped

The magnitude of resistance in the test circuit is crucial for high current impulse waveform. In Figure 5.7, the implications of the different damping modes are illustrated. Damped and over-damped high current discharges are characterized as unipolar discharges. The high resistance in these circuits transforms most of the stored capacitor energy into heat which limits the peak current, charge, and specific energy. Therefore, the resistance of high current impulse generators is typically minimized as best as possible and the test impulse is characterized as an under-damped oscillation. With this approach, also the prospective peak current in the test circuit increases. Furthermore, the decay of the current waveform tail is reduced which effectively increase the amount of specific energy and charge in the DUT. The drawback of under-damped systems is the oscillating current impulse which does not represent the typical unipolar current waveform of a first return-stroke in a lightning flash. Interestingly, the impact of the resistance on the current rise time T_f, on the other hand, is insignificant.

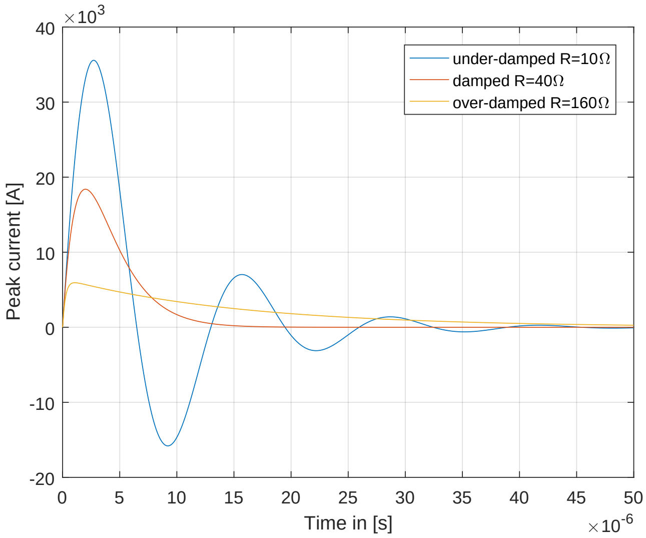

Figure 5.7: The damping possibilities of high current testing through varying resistance R. $C_D = 0.1\mu F$, $L = 40\mu H$, $U_0 = 1MV$

For the under damped case, the current waveform can be computed:

$$i_D(t) = \frac{2 * U_0}{Z} e^{-\frac{R}{2L}t} sin(2\pi f t) \tag{5.12}$$

where the frequency of the oscillation can be determined by:

$$f = \frac{Z}{4\pi L} \tag{5.13}$$

The rise time of the current from zero to the first peak of the oscillation can be calculated with:

$$T = \frac{2}{2\pi f} arctan\left(\frac{\sqrt{(4\pi f L)^2 - 1}}{4\pi f L}\right) \tag{5.14}$$

OR if Z and f are included in the equation.

$$T = \frac{-4L \arctan \frac{R - \sqrt{(|R^2 - \frac{4L}{C}| + R^2}}{\sqrt{|R^2 - \frac{4L}{C}|}}}{\sqrt{|R^2 - \frac{4L}{C}|}} \tag{5.15}$$

The current rise time T_f is then computed as a linear approximation between the $t_{10\%}$ and $t_{90\%}$ their intersections with the x-axis and the horizontal extension of the peak current value, as illustrated in Figure 5.8.

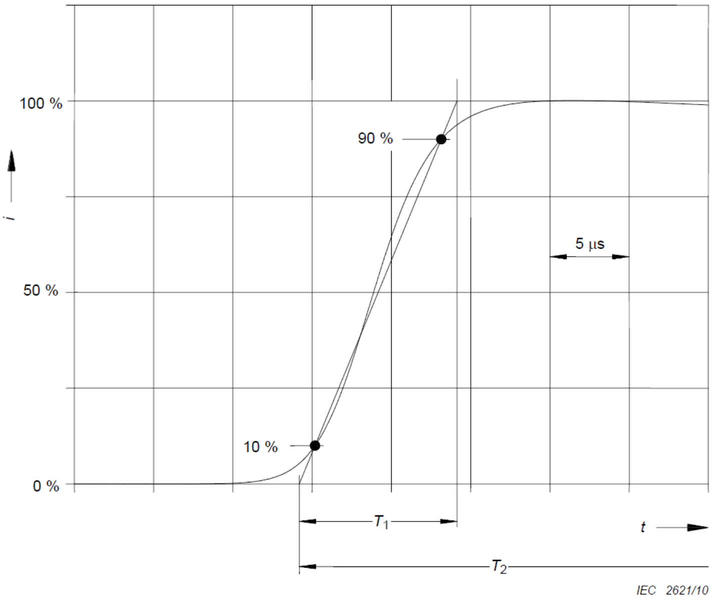

Figure 5.8: Rise-time definition for first return-stroke of positive polarity. Picture adapted from [55].

The maximum amplitude I_p of the current wave is:

$$I_{peak} = \frac{2U_0}{Z} e^{-\frac{R}{2L}T} sin(2\pi fT) \tag{5.16}$$

The energy in the pulse can be calculated by:

$$W = R * \int |i_D^2(t)| dt \tag{5.17}$$

The energy is therefore directly proportional with the resistance of the circuit multiplied by the square of the integrated current waveform.

This work focuses on under-damped high current impulse generators due to the previously indicated limitations of damped and over-damped impulse systems.

5.3.1 Current and voltage characteristics of under-damped impulse systems

Practical high current generators are typical under-damped impulse generators where the resistance in the test system is minimized as best as possible. In this section, the reader is introduced to the fundamental principles and challenges of high current impulse testing for wind turbine components with under-damped impulse systems.

In Figure 5.9, the equivalent circuit and the resulting transient current and voltage waveform of the most fundamental testing circuit is illustrated. It is comprised out of a capacitor, a spark gap and the load. The sequential operation of the generator can be described as follows: As soon as the switch establishes a connection between the charged capacitor and the impedance of the DUT, the current starts to rise with a frequency of:

$$f_0 = \frac{1}{2\pi\sqrt{LC}} \tag{5.18}$$

At the same time and with the same frequency, the voltage across the capacitors starts to decrease and an oscillating current impulse with close to 90° phase difference between voltage and current is created. The resonance between the capacitor and the inductive load provides a constant oscillation between magnetic energy stored in the DUT and the electric energy in the capacitor. Resistive losses are responsible for a transformation of electromagnetic energy into heat and hence a decrease of current amplitude.

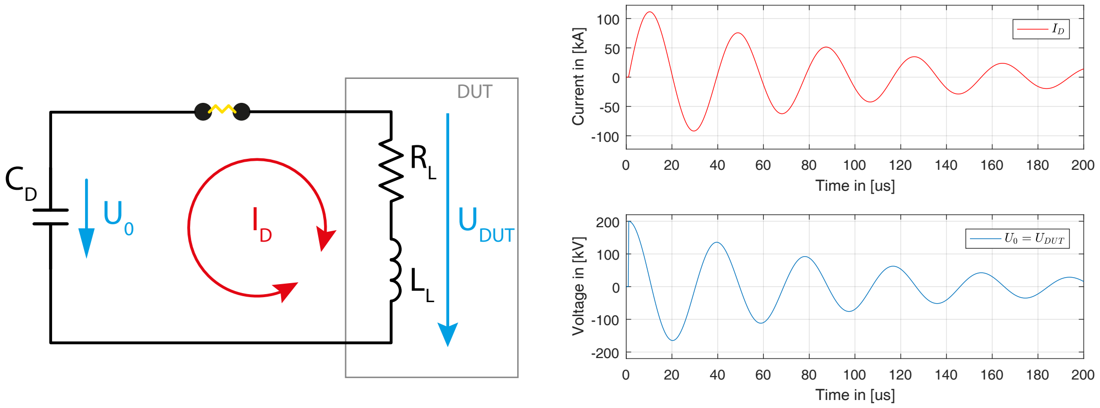

(a) Equivalent circuit of most simplified current test with oscillating current pulse ($C_D = 3.75\mu F$, $R_L = 200m\Omega$, $L_L = 10\mu H$).

(b) Time-domain current I_D and voltage U_{DUT} graphs for an oscillating impulse current. Notice the phase displacement of 90 degrees between voltage and current.

Figure 5.9: Idealized high current testing without impact of stray components.

Oscillating current pulses were used used for lightning testing of aircrafts from the 1970s [144]. With the simple generator setup, the peak current of lightning flashes were able to be created. However, lightning current impulses are characterized as unipolar pulses as described in Section 2.1. The most obvious difference between oscillating and unipolar current pulse testing is the difference in specific energy and charge for a given load and peak current. However, also the resonance of electric field due to the current is expected to change the partial discharge environment inside the blade which can, in turn, alter the outcome of the test.

Technical advances in the accurate triggering of spark gaps led to the development of crow-bar circuits which enabled a rectification of the current pulse of under-damped impulse generators.

Figure 5.10 illustrates the concept of high current testing with a crow bar circuit. Similar to the circuit depicted in Figure 5.9, the main spark gap triggers the discharge and the current I_D increases in the DUT. Simultaneously, the voltage U_{DUT} drops. At the instance of maximum current, the crow bar spark gap is triggered and starts the conduction process of I_{CB}. This process effectively short circuits the source capacitor C_D and eliminates the current flow of the capacitor. At the same time, the peak current from the load is transferred to the crow bar which instantaneous takes over the conduction process.

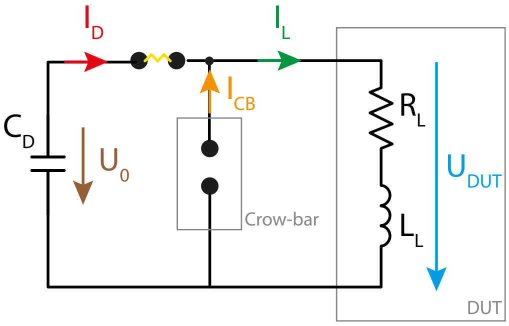

(a) Equivalent circuit of crow-bar generator for unipolar current pulse ($C_D = 3.75\mu F$, $R_L = 200m\Omega$, $L_L = 10\mu H$).

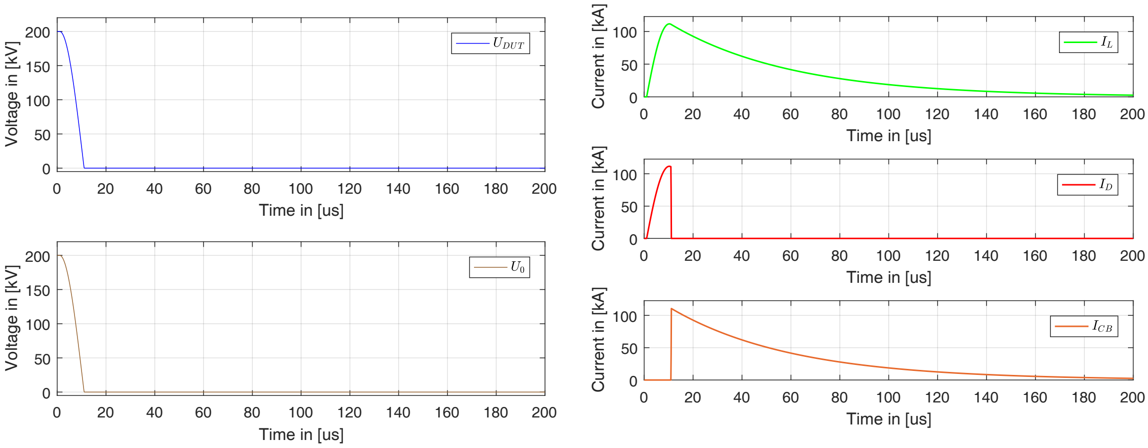

(b) Time-domain voltage waveforms.

(c) Time-domain current waveforms.

Figure 5.10: Circuit diagram, voltage and current waveform of idealized high current testing circuit. The crow-bar spark gap is triggered at the maximum peak current, effectively short circuiting the capacitors.

Unfortunately, the idealized circuit depicted in Figure 5.10a does not exist in physical applications. Each conductor is characterized by a specific parasitic inductance, resistance and capacitance to ground. During high current testing, especially the stray inductance is of crucial importance since it alters the voltage and current distribution inside the test circuit distinctly. Capacitive effects play also a role, however, the effects are only observable in very fast current components $< 1\mu s$ [31].

In Figure 5.11c the impact of a high current testing circuit with a crow-bar circuit and parasitic elements is illustrated. Parasitic inductance was added in the capacitor branch, the crow-bar branch and the load branch. Until the first peak of I_L the current and voltage waveforms are similar to the ideal case depicted in Figure 5.10. After the current peaked, the load current I_D shows distinct oscillation which is caused by the parasitic inductance of the crow-bar circuit which limits the instantaneous rise of current in the branch and oscillates with the discharged capacitor C_D. The maximum current magnitude I_{CB} is approximately 65% higher than the current magnitude I_L since, at this instance, negative current is sucked into the capacitor I_D while the inductance of the DUT drives the unipolar load current I_L through the test sample.

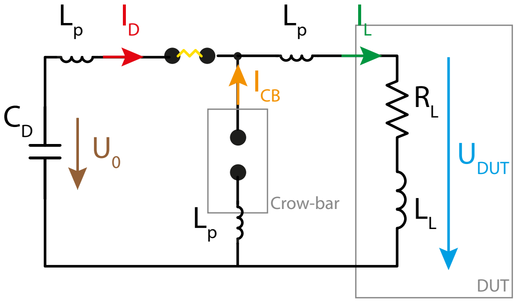

(a) Equivalent circuit of crow-bar generator for unipolar current pulse with parasitic stray inductance of the test setup ($C_D = 3.75\mu F$, $R_L = 200m\Omega$, $L_L = 10\mu H$,$L_p = 1\mu H$).

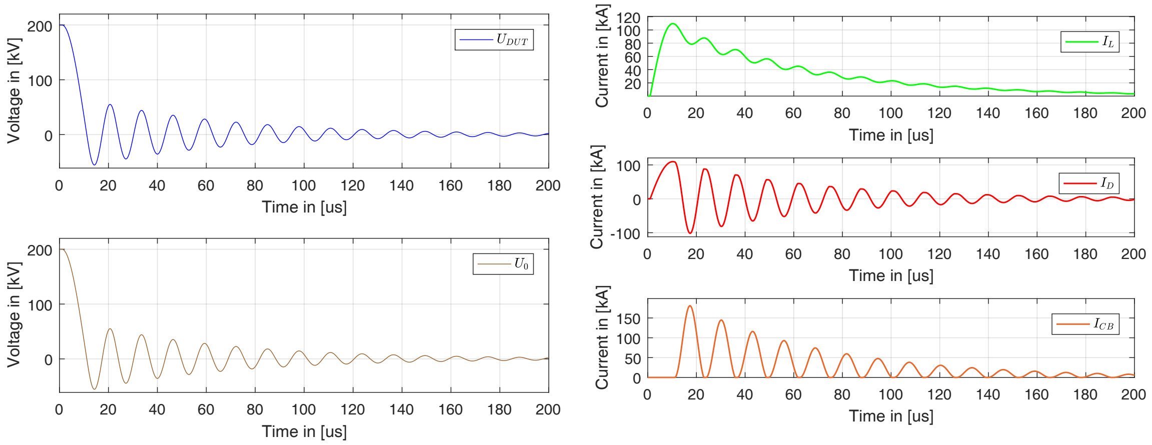

(b) Time-domain voltage waveforms.

(c) Time-domain current waveforms.

Figure 5.11: Circuit diagram, voltage and current waveform of idealized high current testing circuit. The crow-bar spark gap is triggered at the maximum peak current, effectively short circuiting the capacitors.

The last example shows that it is crucial to account for the effects of parasitic inductance which is implicit in a physical high current generator. Furthermore, transient oscillations between capacitors and stray inductance in the test system may overload certain components and need to be accounted for when dimensioning components. Stray inductance, on the other hand, may be reduced by considered design of equipment as can be seen on the example of coaxial cables.

5.3.2 Limitations of high current testing

The limitations of high current testing arise when specific current parameters are required in the DUT.

Equation 5.12, 5.14, 5.15 dictate the quantities which can be alternated to vary the current waveform of under-damped impulse systems. By adjusting the inductance, the capacitance, the resistance and the initial voltage of the circuit, any current waveform can be created in theory. Theoretical boundaries are created due to the natural electrical characteristics of conductors such as stray resistance R and inductance L as described in Section 5.2 or by the separation distance d between conductors for a given charging voltage U_0.

The impedance of the test circuit is defined by the circuit resistance R, the inductance L and the capacitance C which has in impact on both the current waveform $i_D(t)$ and the peak current I_{peak}. The zero to peak time T_p of the current, which is proportional to the front time of the current waveform T_f, is affected by the inductance L, the capacitance C_G (through f) and the resistance R of the generator but not by the initial DC voltage U_0. The resistance R, however, does nearly have no impact of the rise time even though it is a variable in equation 5.15. The maximum amplitude of the current depends on the voltage U_0, the resistance R, the inductance L, the capacitance, and the current time to peak T.

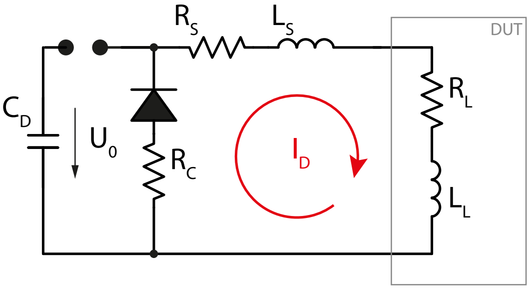

Figure 5.12: Test circuit with crow bar circuit for unipolar pulses

Lightning current waveforms are ideally unipolar pulses. Since the resistance of the test circuits need to be as low as possible in order to reach sufficient energy in the circuit, damped or over-damped circuits are not a feasible option in practical applications. Another approach to create unipolar current pulses exists utilization of a under-damped circuit and a crow bar circuit (See Figure 5.12). The concept is realized with a triggered spark gap or a diode. After the main spark gap is triggered, the voltage across the load drops until it reaches zero, effectively driving the discharge current $i_D(t)$ into the load impedance. At this instant the peak current I_{peak} crests in the test sample and the crow bar circuit takes over the load current. In case a diode is employed in the crow bar circuit, the current conduction is initialized as soon as the voltage across the load terminal becomes negative. In case a spark gap is used, a precise trigger mechanism is needed to activate the circuit. By employing a crow bar circuit, the discharge capacitor is effectively short circuited after the voltage reverses and does not contribute to the current waveform. The energy of the impulse is solely stored in the magnetic field of the stray inductance of the test sample. In case of very low inductive test samples, additional inductance may need to be added to the test circuit in order to limit the peak current. Furthermore, the stray inductance of the crow bar impacts the current waveform as further discussed in Section 5.3.1.

The unipolar current waveform can be computed similarly to the oscillating waveform. From 0 to T, the current waveform is governed by Equation 5.12. From time step $T + ts$

(after the peak current is reached) the circuit is driven by an inductive discharge process:

$$i_D(T + ts) = I_{peak} e^{-\frac{R}{L}t} \tag{5.19}$$

where R and L are the accumulated resistance and inductance of the crow bar and the test sample branch excluding the capacitor branch which is does not impact the current waveform.

With the information above, it is possible to calculate the idealized impulse generator capacitance/voltage ratio for both first return-strokes and subsequent return-strokes. At first, we need to define some realistic load impedance values. As explained in Section 5.2, a realistic load impedance for a wind turbine blade with adequate return-conductor arrangement is expected to be $L_L = 40\mu H$ and $R_L = 50m\Omega$. It needs to be noticed that arc resistance of spark gaps are not included in this simulation.

For first positive return-strokes, the maximum impulse current parameters were previously defined in Section 2.3 with peak current $I_p = 200kA$, a rise time $T_f = 10\mu s$, a charge content $C = 100C$, and a specific energy content of $\frac{W}{R} = 10\frac{MJ}{\Omega}$.

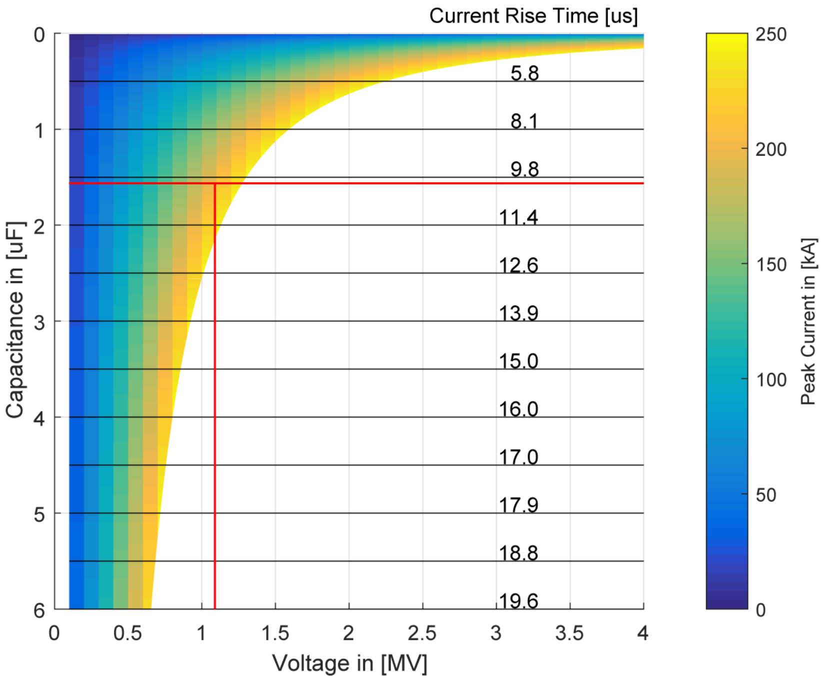

Figure 5.13: Determination of capacitance/voltage ratio in order to create 1st positive return-stroke current according to IEC 61400-24. The corresponding load for this scenario is $L_L = 40\mu H$ and $R_L = 50m\Omega$

From Figure 5.13 following conclusion can be drawn. High peak current values can be created with relatively low driving voltage U_0 and high generator capacitance C_D; however, the rise time is longer as specified in the requirements of the next test system. On the other hand, if the generator capacitance C_D decreases, also faster current rise times T_f are achieved; however, the voltage needs to be increased in order to fulfill the peak current I_p requirements.

The current rise time T_f is directly related to the capacitance of the impulse generator C_g and the inductance L of the entire circuit. The inductance can be minimized only until a certain degree. Therefore, the inductance is a parameter and not a variable for the purpose of defining the optimal generator configuration. The driving voltage U_0 of the circuit does not impact the rise time. In order to achieve a current rise time of $T_f <= 10 \mu s$, the driving capacitance of the generator can not exceed $C_D = 1.5 \mu F$. Furthermore, a minimum capacitor voltage of $U_0 = 1MV$ is needed to reach the required peak current value of $I_p = 200kA$.

Similar plots can be created for charge C and specific energy $\frac{W}{R}$, as illustrated in Figure 5.14. It can be concluded that both charge C and specific energy W/R requirements can be fulfilled with a rise time of $T_f = 10 \mu s$ if a generator capacitance of $C_g <= 1.5 \mu F$ is given with a driving voltage of $U_0 >= 0.8MV$.

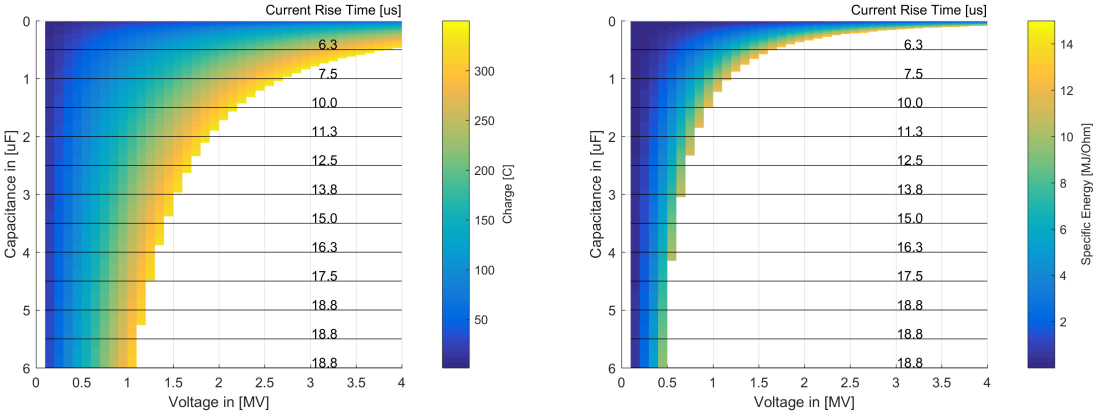

(a) Charge as a function of capacitance and voltage (b) Specific Energy as a function of capacitance and voltage

Figure 5.14: Potential charge and specific energy of the A-bank

For subsequent strokes, the requirements of Section 2.3 defines the current pulse with a peak current of $I_p = 30kA$ and a front/decay time of $T_f = 0.25 \mu s$. In order to create a subsequent lightning stroke into a full-scale test sample of $L_L = 40 \mu H$ and $R_L = 50 m\Omega$, the impulse generator needs to be characterized by a very low capacitance $C_G <= 0.9nF$ combined with a very high discharge voltage of $U_0 = 6.5MV$. Figure 5.15 illustrates the requirements for a subsequent impulse generator as a function of capacitance and voltage. The mentioned generator specification are unrealistic for most testing facilities globally. Even the largest Marx-type generators have typically resulting capacitance values of several tens of nanofarad [145]. Due to this reasons, it may be concluded that a full-scale test of wind turbine components with a subsequent lightning stroke current as defined by the requirements in Section 2.3 are not realistic with the budget of the ELITE project. It is therefore recommended to perform subsequent lightning tests on smaller test samples in order to reduce the inductance of the circuit.

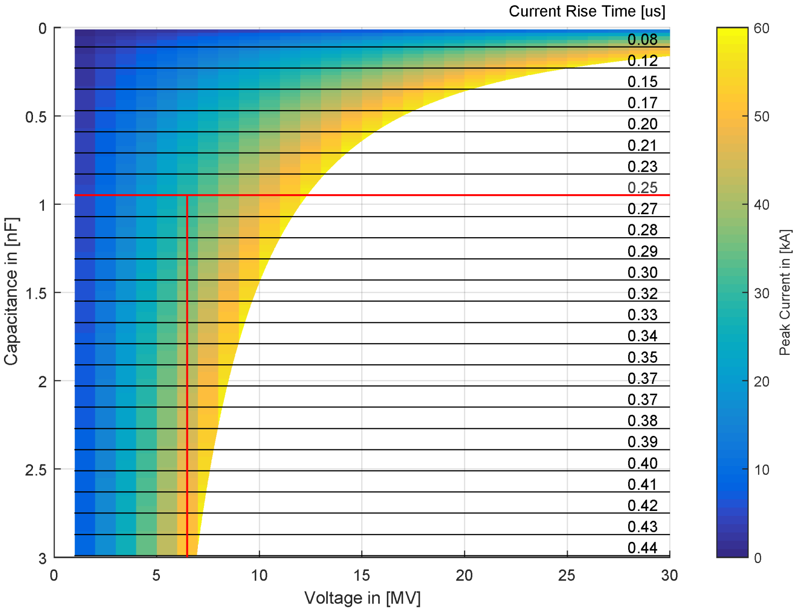

Figure 5.15: Determination of capacitance/voltage ratio in order to create a subsequent stroke current according to IEC 61400-24. The corresponding load for this scenario is $L_L = 40\mu H$ and $R_L = 50m\Omega$.

5.4 Design

In this section, the design and development of the novel high current test system is documented. In the previous chapters, lightning data and lightning related effects were documented that supported the argumentation of how to test a wind turbine component. At this point, the information of the lightning exposure of wind turbines is transformed into the premises of the high voltage lab. Technologies are employed which can imitate the current flow of real lightning conditions in a limited amount of space and within the budget of the project.

As it has been shown in Section 2.1, a downward lightning flash is characterized by a first return-stroke, and may be followed by a sequence of continuous currents and subsequent return-strokes. Furthermore, an upward lightning flash is typically characterized by an initial continuous current which may be superimposed by M-components and potentially followed by subsequent return-stroke sequences.

The properties of a lightning flash, independent of the propagation direction, can be itemized into three different components:

1. A first return-stroke sequence, which is characterized by a peak current of several hundred kiloamperes, a high charge, and a high specific energy. This component exposes the test item to the highest heating effect and the highest mechanical stress between the connections.
2. A continuous current sequence with a duration of up to a second and a magnitude of several hundred amperes. This component exposes the test item to the biggest quantity of surface erosion on the injection point if a spark gap is used to transfer the current in the form of an open arc.

3. A subsequent stroke sequence with a fast current impulse rise-time. This component is responsible for indirect current effects such as induced voltages in sub-circuits.

Each of these components are characterized by individual requirements in terms of current rise time, duration and decay time. Due to this reason, the design of the novel high current test system divided the generator into three different impulse generators, each capable of testing one specific component of the individual lightning impulse. The terminology from the Society of Automotive Engineers (SAE) committee on electromagnetic compatibility SAE-AE-4L was inherited which defined the improved lightning protection guidelines for aircrafts since 1972 [144]. The proposed lightning current waveform for wind turbine testing is illustrated in Figure 5.16. The A-bank component represents the first return-stroke current, the B/C-bank component creates the continuous current as well as the transition from the A-component, and the D-bank is used to create a subsequent current type component.

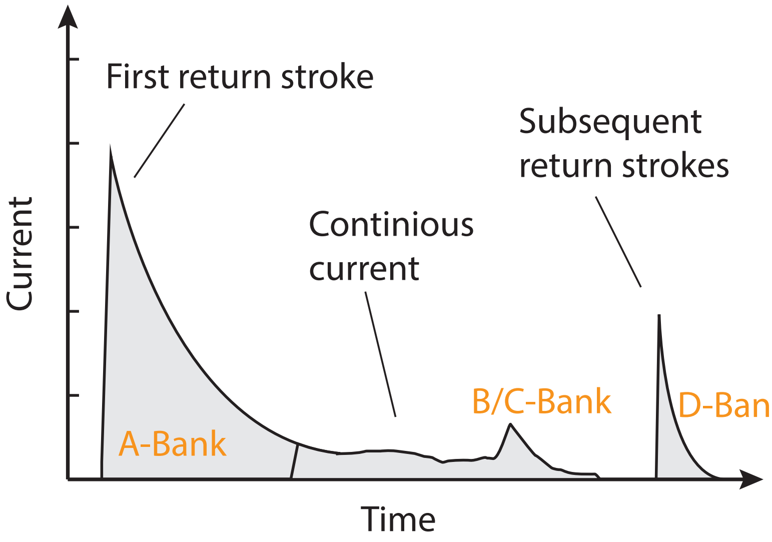

Figure 5.16: The novel high current test system is divided into three different test systems: A-bank, B/C-bank, and D-bank

In the next subsections, a deeper look into the three generator concepts are provided and the prospective performance of the generator on full-scale lightning blades is documented.

5.4.1 A-Bank

The A-bank, which is used to create the first return-stroke, consists out of 12 identical generation units. Each module is a stand alone high current generator with five intrinsic source capacitors, one encapsulated spark gap chamber with trigger, one crow-bar rectifier consisting out of 45 series connected rectifier didoes, one control cabinet, and one pressure controlled grounding. Illustrations of one A-bank module can be found in Figure 5.17. The main frame is fabricated out of insulating glass fiber and the physical dimensions of one module is (width x depth x height) 1794 x 1484 x 1565mm.

5.4.1.1 Design and used components

The A-bank is physically the largest impulse generator of the ELITE project. The unit can also be used to verify the conducted current and arc entry test of wind turbine components according to IEC 61400-24: Lightning Protection of Wind Turbines standard [24].

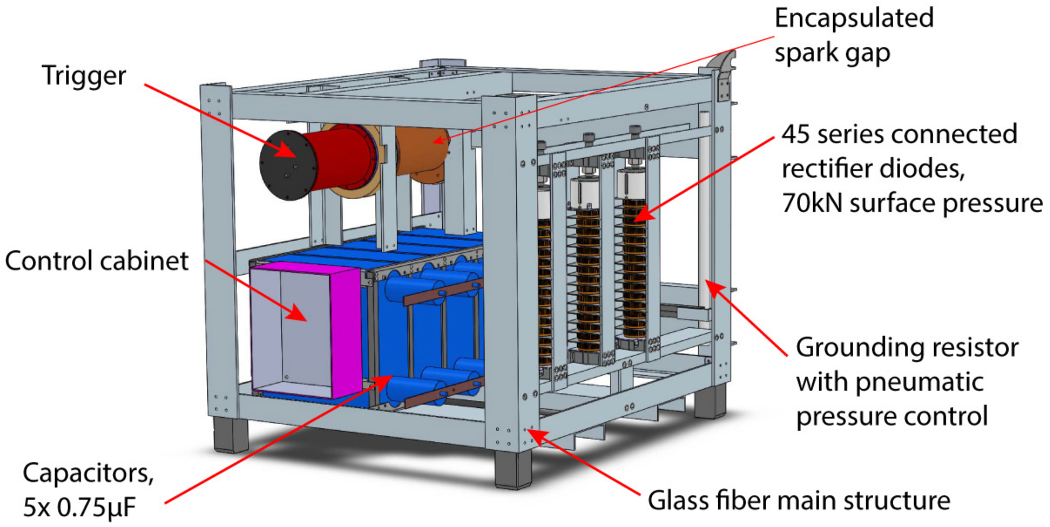

(a) 3D illustration

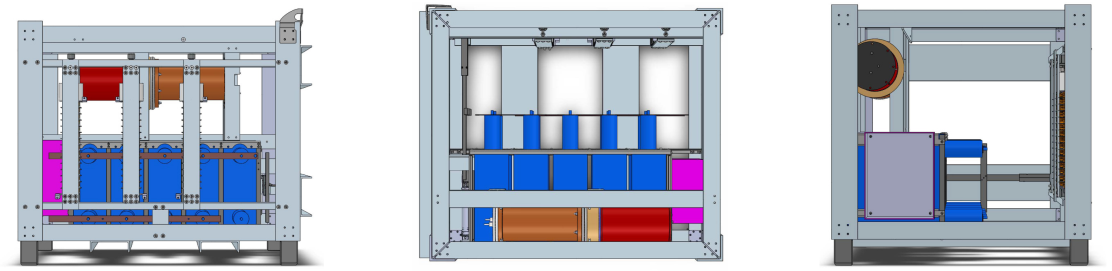

(b) Front (c) Top (d) Side

Figure 5.17: Physical appearance of one A-bank module. Each module is an independent high current impulse generator with capacitor bank, spark gap, trigger, diode crow bar, control cabinet and grounding resistor. Dimensions of module: 1794x1484x1565mm.

In Figure 5.18 the detailed overview of one A-bank module is illustrated. Each module consists out of five physical high voltage capacitors. Each capacitor is has two terminals (bushings) that are rated for 100kV, leading to two separate capacitors inside one housing with an individual capacitance of $C_D = 1.5\mu F$. The capacitor bushings are connected in series connection. Therefore, one physical capacitor unit has a capacitance of $C = 0.75\mu F$. Five capacitors are connected in parallel, resulting in a total capacitance of $C = 3.75\mu F$ per module. Each capacitor unit has a current rating of $I_{max-1Cap} = 25kA$, leading to a total discharge current of $I_{max-5Cap} = 125kA$. A drawing of one capacitor unit is illustrated in Figure 5.19.

The equivalent circuit model with included stray parameters of one module is depicted in Figure 5.20. The stray inductances L_S are representative for a physical A-bank module and the validation of the values are presented in Section 5.6.1.3. The stray inductance L_{S1}

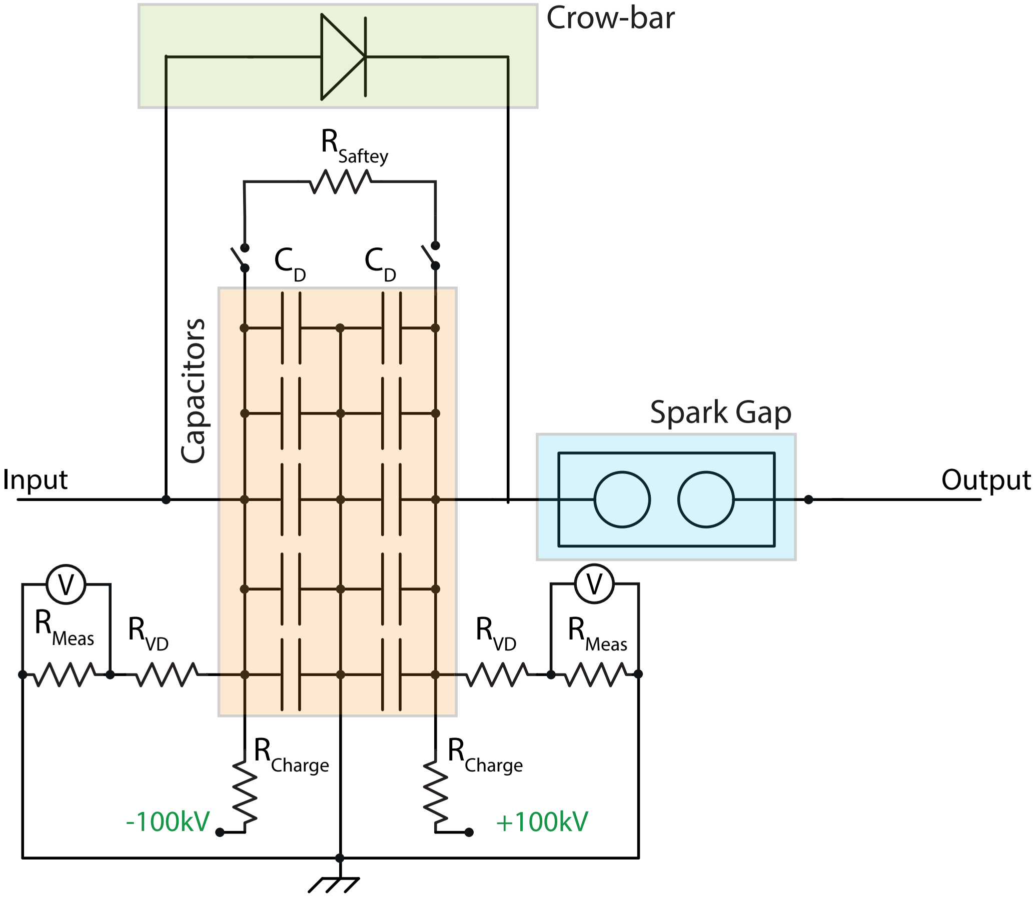

Figure 5.18: Detailed circuit diagram of one A-bank module. $C_D = 1.5\mu F$, $R_{Charge} = 60k\Omega$, $R_{VD} = 1G\Omega$, $R_{Meas} = 1k\Omega$, $R_{Saftey} \approx 1M\Omega$

- L_{S3} originate from the physical properties of the generator and is lumped in each specific branch. The resistance R_{S1} is characterized by the bus bar and the bushing resistance of the capacitors. R_{S2} is give by the forward resistance of the diode stack. R_{arc} is the current dependent arc resistance.

Diode Crow bar As can be seen in the circuit drawing in 5.18, the crow bar concept has been realized with a stack of 45 series connected rectifier diodes from the manufacturer Westcode. Each diode has a nominal repetitive blocking voltage of $U_{RRm} = 6000V$, leading to a total blocking voltage of $U_{Block} = 270kV$. The diode stack requires a mounting force of 75kN in order to achieve the correct operation.

In the datasheet of the diodes, also the current rating for the diodes can be found. Since rectifier diodes are typically used for 50 Hz applications, it is not straight forward to find an answer how much current they can conduct before the diode is irreversibly damaged. The maximum average forward current of the diode is stated as $I_{F(AV)M} = 4205A$ for a 50 Hz 180° half-sine wave at a heat sink temperature of $T_{sink} = 55°$. The peak non-repetitive surge current for a $10ms$ half-sine pulse at a reverse voltage of below $10V$ is stated as $I_{FSM} = 50kA$. The targeted conducted peak current for the diode crow bar is up to $I_{FSM} = 200kA$; however, the duration of the current impulse is also smaller than $1ms$.

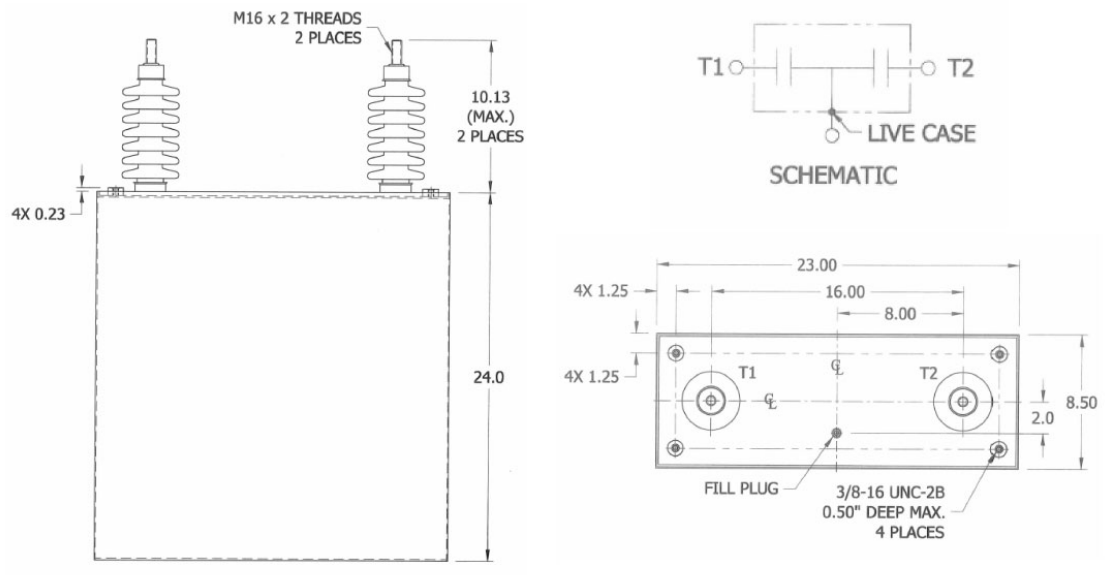

Figure 5.19: High voltage capacitor manufactured by NWL. Two bushings for two separate capacitors. Distance measurements in inch.

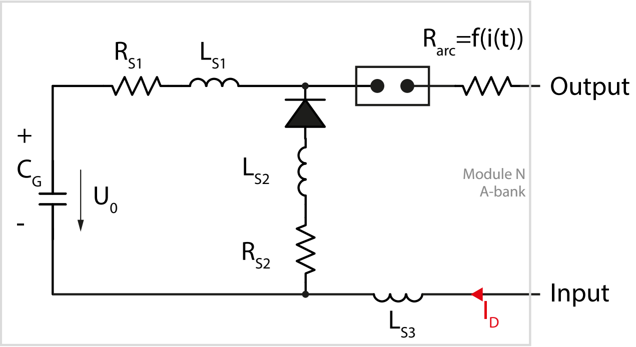

Parameter:

C_G = 3.75uF	U_0 = 200kV
R_{S1} =1mΩ	L_{S1}=2uH
R_{S2} =6mΩ	L_{S2}=2.4uH
R_{arc}=f(i(t))	L_{S3}=2.5uH

Figure 5.20: Stray resistance and inductance values for one A-bank module.

Research regarding the usability of diode concludes that peak current amplitudes of current impulses can exceeded multiple times the rating of the datasheet as long as the specific energy through the diode is not exceeded [146] and the junction temperature of the diodes remains within the specified operation condition. In the case of the ELITE generator, the fusing energy for the specific used diode is $12.5\frac{MJ}{\Omega}$. Simulations of the functionality of the A-bank concept show that the specific energy during operation remains below $5\frac{MJ}{\Omega}$ when the maximum current amplitude of $I_D = 125kA$ is injected into the test sample and circulates in the DUT and the crow bar circuit. Furthermore, consultations with semiconductor specialists emphasized that diodes are very robust components [147] as long as diodes are operated within the boundaries of the nominal voltage.

By utilizing diodes instead of spark gaps, the control of the crow bar is much simpler compared to a solution with a triggered spark gap. As soon as the main spark gap triggers and the voltage reverses due to the discharge characteristics, the diode instantaneously starts conducing. A second spark gap does not need to be triggered. As previously discussed in Section 5.11, the stray-inductance of the crow bar introduces a delay in the current rise time and subsequently a oscillations with the capacitor circuit. The peak current in the diode is therefore approximately 50% higher in the diode compared to the peak current in the load.

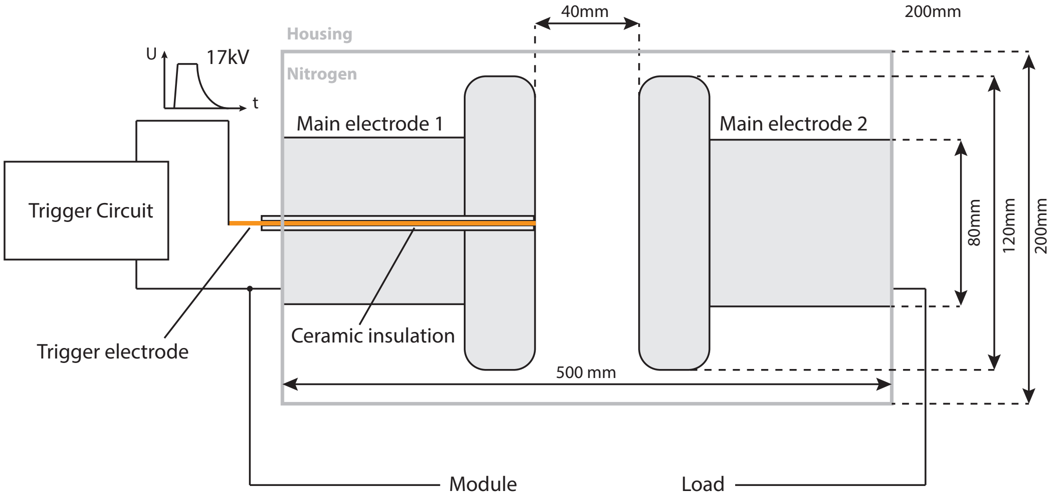

Figure 5.21: Electrical circuit illustration for triggered spark gap operation.

A triggered spark gap Each module is equipped with an encapsulated spark gap and a floating trigger unit which is connected in a Trigatron manner to one side of the spark gap, resulting in a three component electrode design as depicted in Figure 5.21. The electrodes are arranged in a fixed position and the flashover voltage can be adjusted by regulation of the nitrogen pressure in the discharge chamber. The electrodes are made out of a Tungsten/Wolfram alloy in order to reduce melting at the surface. The center pin electrode floats on the potential of the surrounding main electrode. Subsequently to a trigger signal, a differential high voltage impulse of approximately 17kV is generated through cascading two high voltage transformers. This creates a spark between the center pin electrode and the main electrode which ignites the main gap.

Nitrogen has been chosen as pressure regulating gas since it provides stable discharge characteristics, it is a non-toxic gas, it is relatively cheap, and it is with 78% already the major component in air.

Pressure increase in discharge chamber of spark gap In order to approximate the highest possible operating pressure in the spark gap, a calculation of the transient pressure increase due to the appearance of the arc has been performed. The evaluation is crucial for the sustainable operation of the ELITE generator since the control circuit as well as the design of the spark gap chamber is limited to a maximum pressure of $p_{max_{cc}} = 7bar$ and $p_{max_{sg}} = 13.8bar$, respectively.

Following parameters were used for the calculation:

- Potential different $\Delta U = 200kV$
- Maximum peak current $I_{max} = 125kA$

- Front and half time of current $\frac{T_f}{T_h} = \frac{10us}{350us}$
- Distance between electrodes $d = 40mm$ and geometry of gap according to Figure 5.21.
- Maximum steady state operating pressure $p = 35PSI$ (2.4 bar above atmospheric pressure) and extreme case of $p = 70PSI$ (4.8 bar above atmospheric pressure)

The first step towards a pressure estimation is to determine the arc resistance between the electrodes. The arc resistance is depending on the pressure and the distance of the spark gap. The latter is fixed in this design. Furthermore, there is a current dependency where higher currents are less resistive. Various general expressions for arc resistance can be found in the literature, however, most of the studies focus on air or SF6 as discharge gases or discuss low pressure systems [148][149][150]. Due to this reason, an arc resistance expression was used for a discharge in pressured air. A comparison between three different arc models is illustrated in Figure 5.22.

The first model considered was derived by Mesyats [151] and includes pressure, distance, and current dependency.

$$R(t) = \sqrt{\frac{pd^2}{2a\int_0^t i^2(t)dt}} \tag{5.20}$$

where p is the pressure in [atm], d is the distance in [cm], $a = 0.8$ is a correction coefficient.

Additionally to Mesyats model, the model of Stokes [148] and Paukerts[149] are used for a comparison. The latter are typically used for atmospheric pressure.

Stokes:

$$R(t) = \frac{20 + 0.534 * Z_g}{I_{arc}^{0.88}} \tag{5.21}$$

where Z_g is the gap length in [mm].

Paukert:

$$R(t) = 20.11 * I_{arc}^{-0.801} \tag{5.22}$$

which is valid for electrodes gaps of $d = 20mm$ and currents up to $I_p = 100kA$.

As can be seen, Mesyats model shows higher resistance values during the first few hundred microseconds. Subsequently, the resistance remains on a steady level of approximately 3 milliohm. On the other hand, the model of Stokes and Paukert, have lower resistance during the peak of the current and increase during the tail of the current.

For this calculation, the arc resistance equation from Mesyats was used [151]. In this model, the arc resistance drops during the front time of the pulse and remains on a low level after the crest of the current. Naturally, the arc resistance rises again after the peak current has been reached, however, since the majority of power loss is created during the first tens of microseconds ($P_L \propto I^2$), the model represents the worst case scenario.

Together with the arc current $i(t)$, the power loss due to the arc resistance can be calculated with:

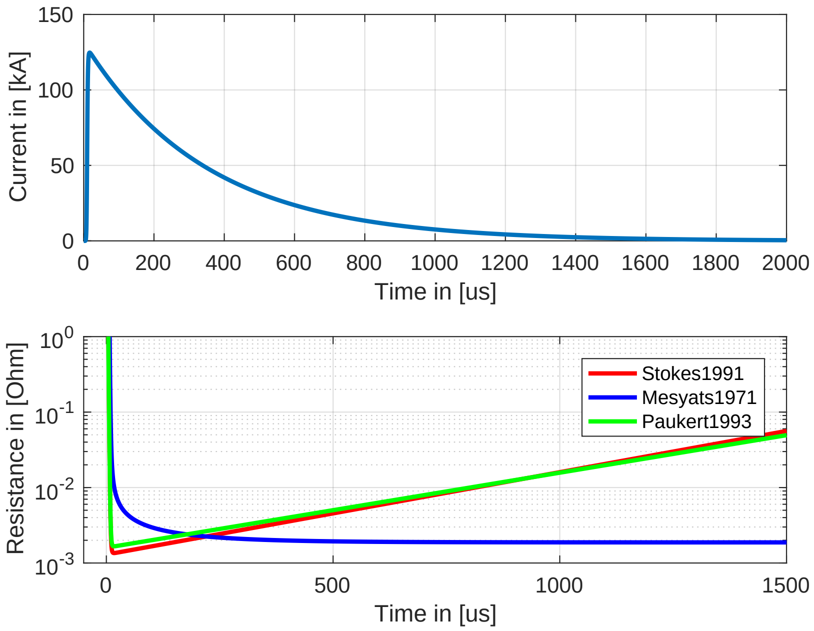

Figure 5.22: Comparison between arc models. Mesyats model is pressure dependent whereas Stokes and Paukerts model depend on the magnitude of the current. All three models depend on the distance. Parameters for Mesyats model are $d = 4cm$ and $p = 1[atm]$.

$$P_l(t,p) = I^2(t) * R(t,p) \tag{5.23}$$

The calculated transient current, resistance, and power loss in the discharge chamber is shown in Figure 5.23. The current waveform was calculated with the Heidler function [152] with a timestep interval of $t_s = 100ns$, a peak current of $I_p = 125kA$, a correction factor of $n = 1$, and time constants τ_1 and τ_2 of 10^{-5} and $3.5 \cdot 10^{-4}$, respectively. The graphs reveal that the maximum power loss is generated during the rise-time of the current with a maximum transient value of $P_{L_{max}} = 375$ and $530MW$, depending on the pressure level in the gap. As higher the pressure, as higher the expected power loss in the gap. The power loss decreases rapidly after the peak current has been reached.

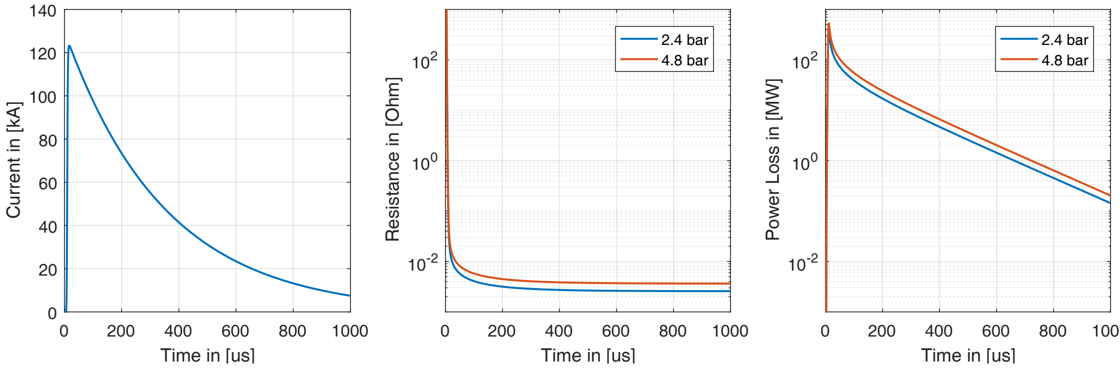

Figure 5.23: Current, resistance, and resistive power loss in discharge chamber for 2.4 and 4.8 bar.

A 2D axis symmetric model of the spark gap with the dimensions given in Figure 5.21 has been created in Comsol 5.2. The calculated transient power loss from the arc was included as a heat source in the model. In order to model the temperature increase and the connected pressure increase in the gap, the Conjugate Heat transfer module was used which includes convective and conductive heat transfer equations through the Heat transfer interface. Following equation governs the simulation:

$$\rho C_p \frac{\partial T}{\partial t} + \rho C_p u \cdot \nabla T + \nabla \cdot q = Q \tag{5.24}$$

further:

$$q = -k \nabla T \tag{5.25}$$

where ρ is the density of the element, C_p is the heat capacity, T is the temperature, t is the time, u is the fluid velocity field, k is the thermal conductivity, and Q is the heat gradient.

Additionally, the Laminar Flow interface for compressible gases enabled to investigate the pressure increase due to the generated heat in the gap. In this simulation, it is assumed that the heat is solely responsible for the pressure increase in the spark gap and that the discharge chamber is heating up evenly during the arc phase. Furthermore, an ideal pressure container without leaks from joints or the pressure control is assumed. The dimensions of the discharge chamber is illustrated in Figure 5.24.

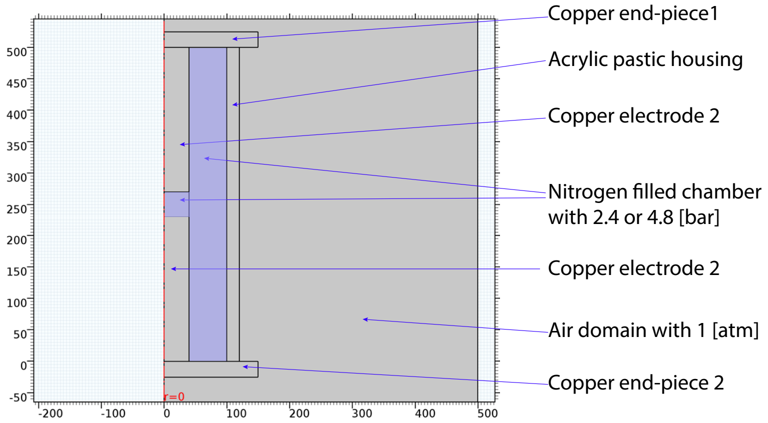

Figure 5.24: 2D axis symmetric model of the spark gap. Blue shade illustrates Nitrogen discharge chamber.

The results of the investigation are illustrated in Figure 5.25. It can be observed that the temperature increase is lower for the scenario with higher pressure ($4.8bar$) compared to the lower pressure case. The reason for this observation is that the density of the gas directly affects the temperature increase in the system as can be seen in Equation 5.24. On the other hand, the pressure increased with 83% at the higher pressure level (from $4.8bar$ to $8.8bar$), whereas the pressure increase was 116% at the lower pressure level (from $2.4bar$ to $5.2bar$).

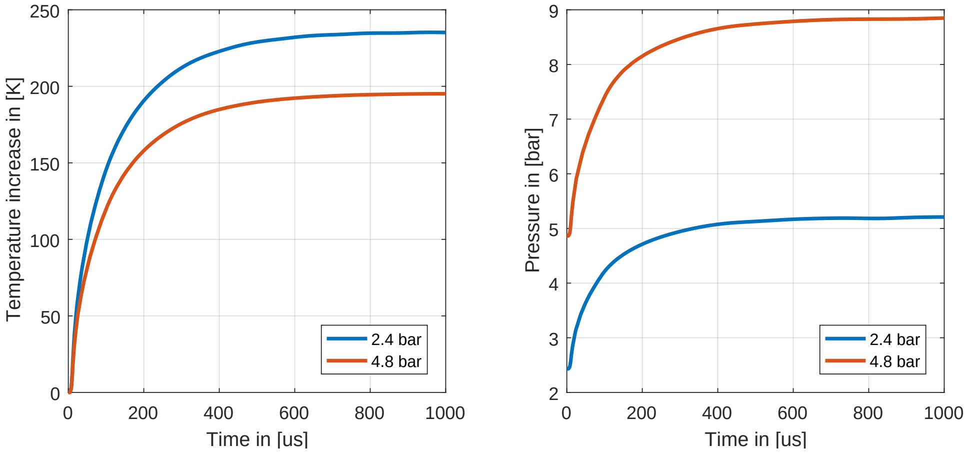

Figure 5.25: Expected temperature and pressure increase due to arc formation in discharge chamber. The temperature increase is lower at $4.8bar$ compared to $2.4bar$ due to the higher gas density.

After the simulation time of $1000\mu s$, the injected power to the system ceases and the temperature and pressure curve start to decay in a negative exponential manner similar to the discharge process of an RL or RC circuit. The half time of the temperature and pressure is reached within ten seconds.

This investigation shows that the presence of an arc increases the pressure in the discharge chamber to a maximum level of $8.8bar$ if the gap is initially biased with a constant pressure of $4.8bar$ or $70PSI$. The maximum tolerable pressure level of the gap is $13.8bar$ or $200PSI$. The pressure control of the spark gap, on the other hand, has a maximum tolerable pressure threshold of $7bar$. It is very likely that these components are severely stressed during the discharge.

5.4.1.2 Modularity

This section is dedicated to elaborate further on the modularity of the A-bank generator concept. The modules can be arranged in series, parallel or mixed configuration in order to adjust the current waveform to various load impedances or specific current properties. The total driving capacitance of the generator is highly adaptable and can be calculated with the number of series connected modules N_s and parallel connected strings N_p.

$$C_g = \frac{3.75uF}{N_s} \cdot M_p \tag{5.26}$$

If the modules are connected in a series connection, after one module is fired, the voltage across the remaining spark gaps in the string increases to the double value which effectively triggers all remaining modules. This principle is typically known from Marx-generators.

The performance of different series and parallel connections can be seen in Figure 5.26 and Figure 5.27. Circuit simulation of the possible configurations have been performed and the key parameters peak current I_p, Time to peak T_p, charge Q, and specific energy

$\frac{W}{R}$ are extracted. It shall be highlighted that the rise time T_f of the current is typically $T_f = 0.8...0.9 \cdot T_p$.

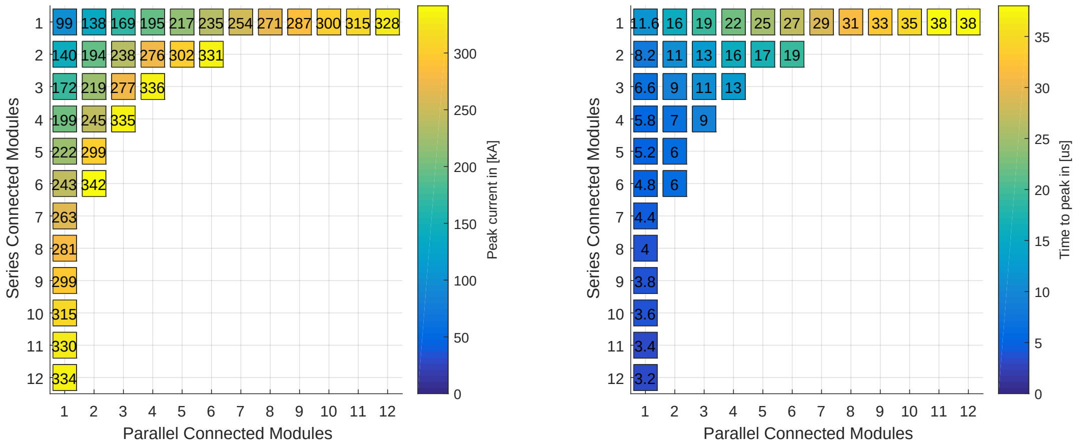

	1	2	3	4	5	6	7	8	9	10	11	12
1	99	138	169	195	217	235	254	271	287	300	315	328
2	140	194	238	276	302	331						
3	172	219	277	336								
4	199	245	335									
5	222	299										
6	243	342										
7	263											
8	281											
9	299											
10	315											
11	330											
12	334											

(a) Peak current I_p

	1	2	3	4	5	6	7	8	9	10	11	12
1	11.6	16	19	22	25	27	29	31	33	35	38	38
2	8.2	11	13	16	17	19						
3	6.6	9	11	13								
4	5.8	7	9									
5	5.2	6										
6	4.8	6										
7	4.4											
8	4											
9	3.8											
10	3.6											
11	3.4											
12	3.2											

(b) Time to peak T_p

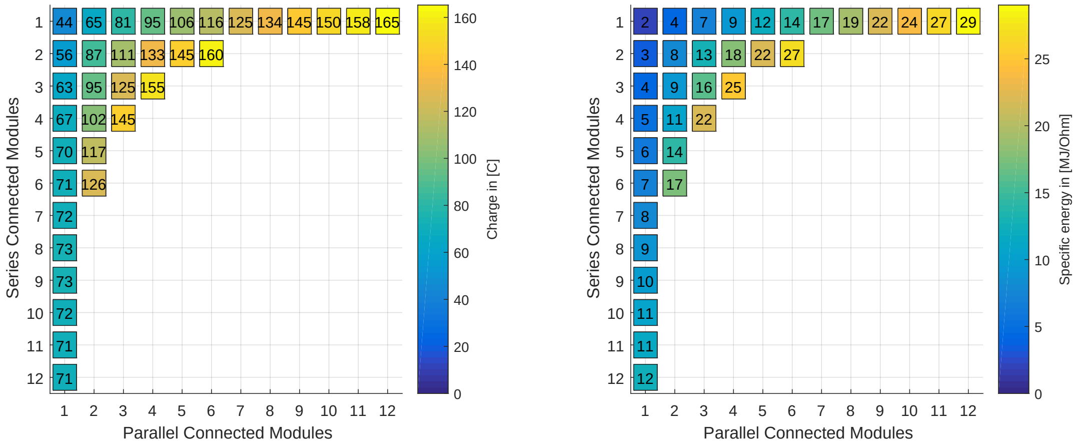

	1	2	3	4	5	6	7	8	9	10	11	12
1	44	65	81	95	106	116	125	134	145	150	158	165
2	56	87	111	133	145	160						
3	63	95	125	155								
4	67	102	145									
5	70	117										
6	71	126										
7	72											
8	73											
9	73											
10	72											
11	71											
12	71											

(c) Charge Q

	1	2	3	4	5	6	7	8	9	10	11	12
1	2	4	7	9	12	14	17	19	22	24	27	29
2	3	8	13	18	22	27						
3	4	9	16	25								
4	5	11	22									
5	6	14										
6	7	17										
7	8											
8	9											
9	10											
10	11											
11	11											
12	12											

(d) Specific energy $\frac{W}{R}$

Figure 5.26: Perspective performance of the ELITE generator with a total circuit impedance of $L = 15\mu H$ and $R = 25m\Omega$.

Two different load scenarios are described. A low load test sample (for example a segment of a blade or a nacelle) is defined with a circuit inductance of $L = 15\mu H$ and a resistance of $R_L = 25m\Omega$, whereas a high load test sample (a full-scale wind turbine blade) is defined with an inductance of $L = 40\mu H$ and a resistance of $R_L = 50m\Omega$. The circuit inductance is a fixed value in the circuit and includes stray inductance from the A-bank bank modules. Additionally to the $R_L = 25m\Omega$ and $R_L = 50m\Omega$ load resistance, the simulation includes the forward resistance of the diodes ($R_{S2} = 6m\Omega$) and the arc resistance R_{arc}.

$$R_{circuit} = R_L + \frac{R_{arc}(t, I, d) + R_{S2}}{N_p} * N_s \tag{5.27}$$

For the calculation, the arc resistance model of Paukert [149] (See Section 5.4.1.1) was selected since the resistance increases with the tail time of the current, unlike the model of Mesyats[151]. It needs to be noticed that Paukert's model does not consider the effect of pressure in the gap. Therefore, the reported values of charge Q and specific energy W/R in Figure 5.26 and 5.27 are expected to be lower in the laboratory. The amount of reduction is expected to be 5% to 35% depending on the configuration. A high number of series connected modules results in the highest loss due to the accumulated arc resistance.

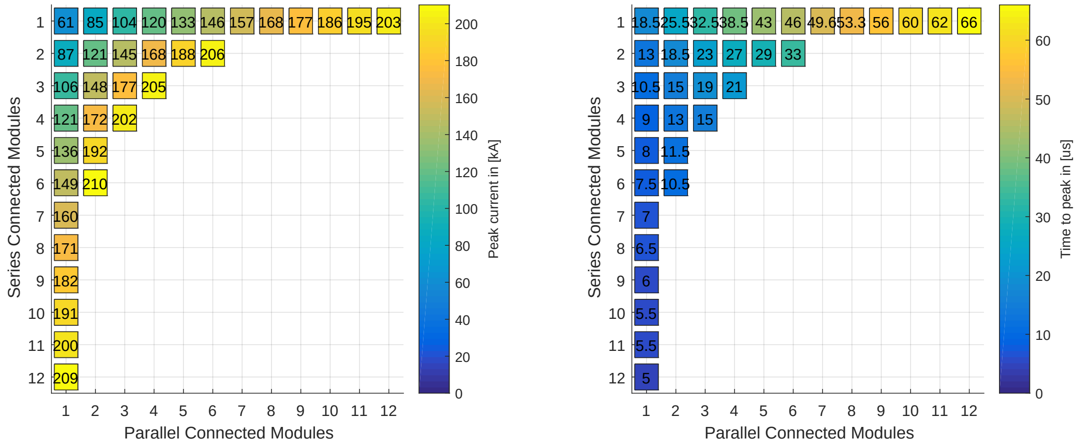

(a) Peak current I_p (b) Time to peak T_p

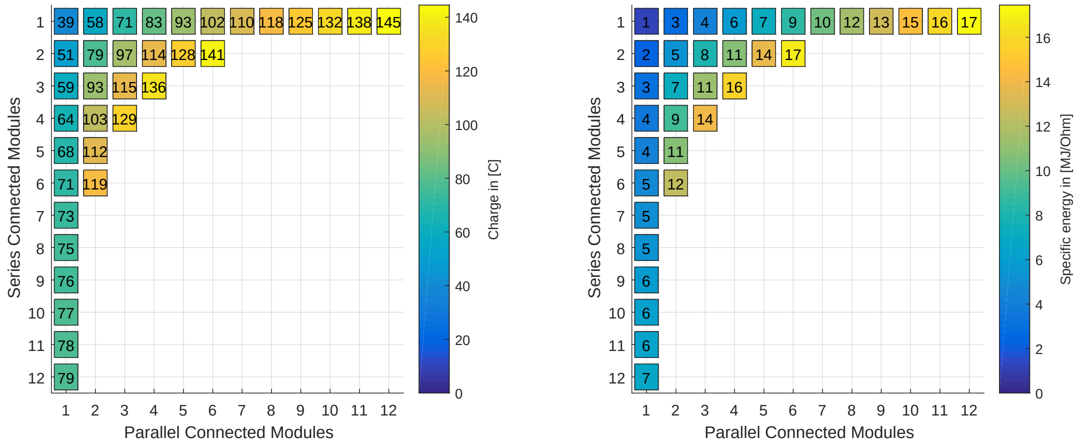

(c) Charge Q (d) Specific energy $\frac{W}{R}$

Figure 5.27: Perspective performance of the ELITE generator with a total circuit impedance of $L = 40\mu H$ and $R = 50m\Omega$.

For the calculation, it is further assumed that all spark gaps trigger at the same microsecond. The perspective current parameters do not consider component specific limitations such as capacitor current limits or diode fusing currents. If, for example, the current output per module needs to be limited to 125kA, the charging voltage should be decreased.

In the overview of Figure 5.26, the perspective performance of the generator is illustrated with a small test sample. As can be seen, very high currents up to $I_p = 328kA$, charge levels of up to $Q = 165C$, and specific energies of up to $\frac{W}{R} = 29\frac{MJ}{\Omega}$ are theoretical possible with the novel concept with the mentioned load specification. This requires to parallel all twelve modules. In this case, however, the time to peak of the current increases to a value of $T_p = 38\mu s$. This configuration, results in a total source capacitance of $C_g = 45\mu F$. On the other hand, a series connection of all twelve modules can significantly improve the time to peak value up to maximum level of $T_p = 3.2\mu s$. Theoretical currents of up to $I_p = 324kA$ are possible with pure series connection, however, the output current is limited to a maximum value of $I_p = 125kA$. This generator configuration results in a capacitance of $C_g = 0.3125$ at a driving voltage of $U_o = 2.4MV$. A combined connection of series and parallel modules merges high current capabilities, a fast rise time, and high specific energy.

Similar graphs were created for the case of a long wind turbine blade as depicted in Figure 5.27. In this scenario, the current parameters are limited to maximum values of $I_p = 210kA$, $T_p = 5\mu s$,$Q = 145C$, and $\frac{W}{R} = 17\frac{MJ}{\Omega}$. Certainly, the higher inductance limits the output current parameters distinctly. Therefore, as already discussed in Section 5.2.3, a properly designed and optimized return-cage around the test object is mandatory to decrease the circuit inductance as best as possible.

In order to reach the requirements for the first return-stroke as defined in Section 2.3, ($200kA$ peak current,$10\mu s$ rise-time, $100C$ charge, and $10\frac{MJ}{\Omega}$), the most promising configuration is to connect two parallel strings of six modules in series. The modules are arranged along the length of the wind turbine blade. A circuit diagram of this configuration is illustrated in Figure 5.28. The total resulting source capacitance of this generator unit is $C_g = 1.25\mu F$ at a total resulting driving voltage of $U_0 = 1.2MV$. The illustration in Figure 5.28 shows the scenario where the root-end of the wind turbine blade is fixed at ground potential. During the firing of the generator, the voltage of each module stacks with the previously fired modules and tip of the blade experiences the full potential of $U_0 = 1.2MV$. Due to this reason, the individual modules need to be isolated from ground in order to avoid flashover. In the literature, various publications regarding point-to-plane flashover voltages can be found and typical values of $U_{fov} = 0.5kV/mm$ can be found[153] [36]. A safety distance of $U_{fov} = 0.35\frac{kV}{mm}$ is recommended, leading to a separation distance of $d_s = 3.5m$ at an impulse voltage of $U_0 = 1.2MV$.

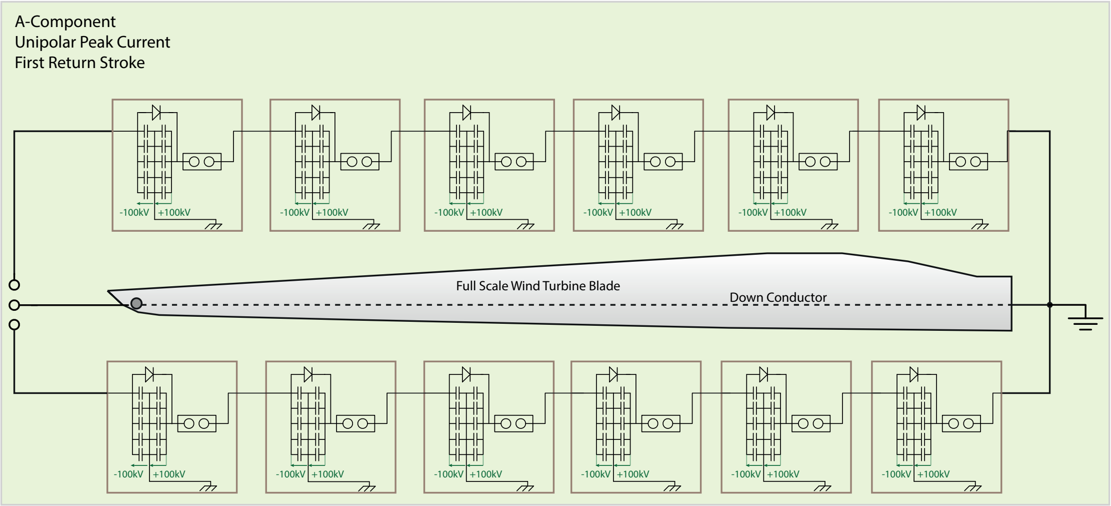

Figure 5.28: Twelve A-bank modules connected to a large wind turbine blade for high current test according to IEC 61400-24: Lightning Protection of Wind Turbines

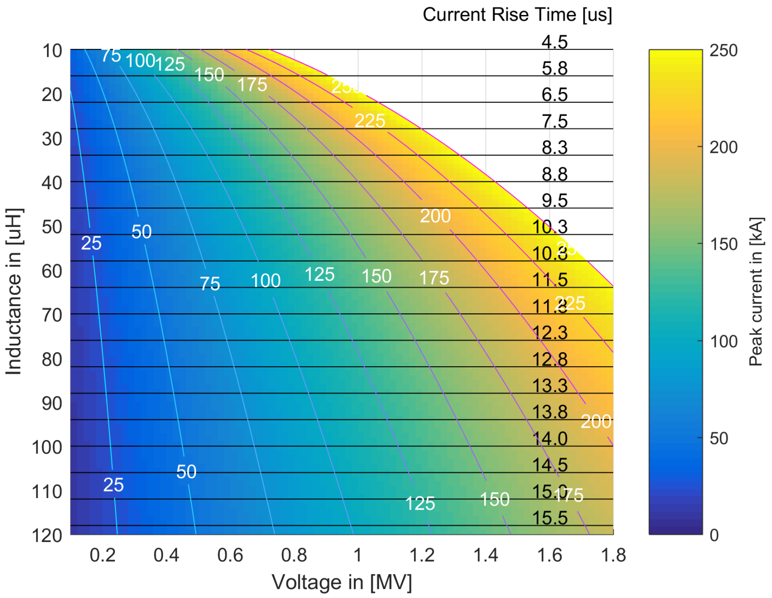

(a) Peak current I_p

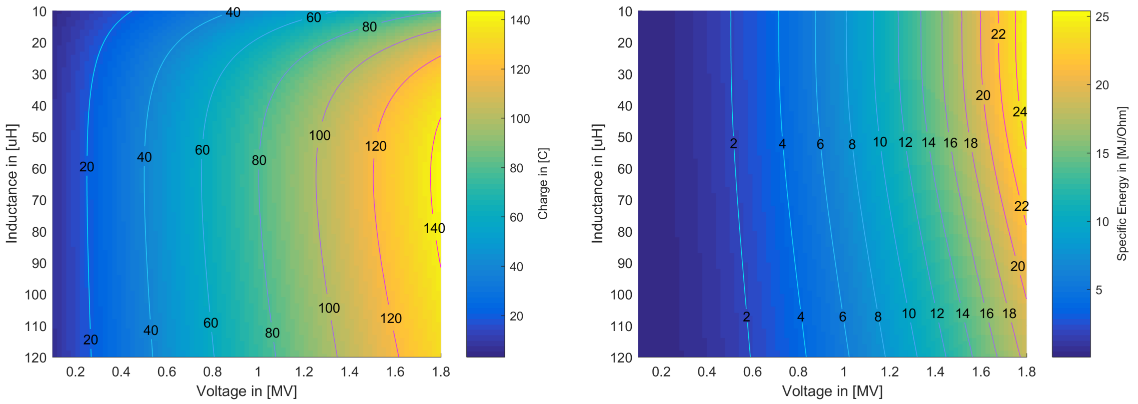

(b) Charge Q

(c) Specific Energy $\frac{W}{R}$

Figure 5.29: Peak current, rise-time, charge, and specific energy capabilities of A-bank generator with 2 parallel strings and 6 series connected modules (Valid for $C_g = 1.25\mu F$). Notice that the Charge Q and Specific Energy $\frac{W}{R}$ are calculated with a fixed circuit resistance of $R = 80m\Omega$.

If it is possible to isolate the DUT from ground, the test could also be performed with a floating setup and a bipolar test voltage of $U_0 = \pm 600kV$ which halves the amount of separation distance at the tip region. In this case both the root end and the tip region should be elevated to $d_s = 1.75m$. On the other hand, it might be challenging to control the firing of the modules precisely, leading to a possible imbalance in the potential distribution. The result could be that the root end is at an potential of 900kV, whereas the tip is at a potential of -300kV. It is therefore recommended to fix the potential on one side of the DUT or isolate both ends to the highest possible potential difference to ground.

With the A-bank configuration depicted in Figure 5.28, peak currents up to $I_p = 250kA$ can be generated combined with a fast rise-time and sufficient energy. In order to highlight the test capabilities of this particular configuration, voltage depended peak current I_p, rise time T_f, charge Q, and specific energy $\frac{W}{R}$ capabilities for a circuit load spectrum of $L = 10...120\mu H$ are illustrated in Figure 5.29. Notice, that here is is actually the rise time of the current (as defined by IEC 61400-24) and not previously mentioned the time to peak T_p.

As it can be seen by the graphs, the maximum circuit inductance with a driving voltage of $U_0 = 1.2MV$ is approximately $L = 45\mu H$ in order to reach the requirements of Section 2.3. If the load inductance increases further, additional A-bank modules would need to be added to the circuit, in order to ensure the correct peak current I_p and rise-time T_f. By adding a seventh series connected A-bank module to the setup, the effective voltage of the A-bank would increase to $U_0 = 1.4MV$ and the generator capacitance would decrease to $C_g = 1.07\mu F$. In order to investigate how additional modules effect the performance of the generator, the voltage scale is not limited to $U_0 = 1.2MV$ but is extended to $1.8MV$. However, since the generator capacitance would also be slightly altered, the graphs are only indicative above $U_0 = 1.2MV$.

5.4.1.3 Challenges

There have been two major practical challenges in the design of the A-bank generator. This section addresses these problems and suggestions are made how to tackle the issues.

Spark gap flashover characteristics The first issue is related to the breakdown characteristics of the spark gaps. Unfortunately, after various testing, the flashover characteristics of the spark gaps did not fulfill the documented values in the datasheet of the manufacturer. The difference between measured flashover performance and datasheet values are illustrated in Figure 5.30. Notice, the measured values originate from the prototype discharge chamber made out of ceramic, however, the flashover characteristics of the glassfiber discharge chamber showed the same characteristics after the discharge chamber was cleaned and coated. As it can be seen by the graph, there is a distinct difference between the documented and measured flashover characteristics. Especially the differences from the self-breakdown characteristics is striking with a reduction of more than 50% between datasheet and measurement values. Various attempts had been made to improve the discharge characteristics.

- Flushing the gap with Nitrogen.
- Evacuation of the discharge chamber with a vacuum pump which lowered the ambient pressure in the gap to approx.: $0.1bar$ and reduced the amount of oxygen molecules.
- Removal of the outer Teflon and silicon layer inside the discharge chamber.
- Application of various protective cylinders (PVC, clay, and glass cylinder) in order to prevent the arc from propagating on the glassfiber housing.
- Application of a coating for the outside of the discharge chamber.

For the latter point, several surface flashover tests were performed on glassfiber samples in order to evaluate which coating provided the highest surface flashover values (most insulating). Three different types of coating were tested which are a heat resistant paint, a heat resistant spray, and a specialized ceramic paint. After the coating was applied, each sample was equipped with an electrode pair of rounded-off copper tape with a distance of

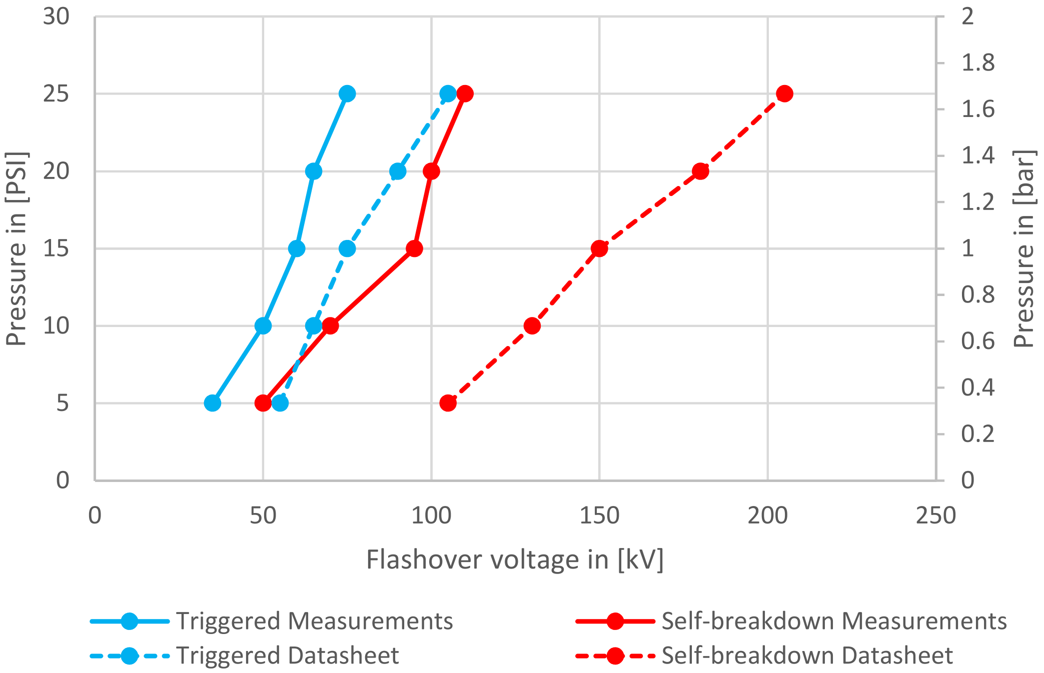

Figure 5.30: Spark-gap performance. Comparison between flashover/pressure characteristics of measurement and datasheet values. The y-scales are pressure difference above atmospheric level.

$50mm$. A high voltage DC source was connected to the electrode pairs and surface flashover characteristics were determined as is illustrated in Figure 5.31. The lowest surface flashover voltage was determined at the pure glassfiber sample whereas the highest surface flashover voltage was determined with the heat resistant paint. The spray exhibited initially good flashover characteristics; however, the flashover voltage decreased gradually after several applied shots. Due to this reason, the spark gaps were coated with the heat-resistant paint.

The reason for the discrepancy between datasheet and measurement values is that the spark gaps were obviously not manufactured and tested for high current applications. It is rather likely that the gaps were only tested with a high voltage source. After a few discharges, dust and byproducts from the discharge accumulated inside the discharge chamber which effectively lowered the flashover characteristics. Furthermore, burning marks on the outside of the discharge chamber indicated that the arc propagated on the outside of the housing rather than directly in between the electrodes. This was in particular a problem for the glassfiber discharge chambers.

Following recommendations are given in order to improve the discharge characteristics in the gap:

1. It is recommended to evacuate all discharge chambers and refill them with fresh nitrogen before between each single firing. A small vacuum pump should be installed in each control cabinet which is connected to the control system of the A-bank.
2. The condition of the heat resistant paint should be carefully monitored. In case the paint deteriorates after several discharges and dust is forming in the gap, a new coating has to be applied. Aluminum oxide coatings, for instance, may be more

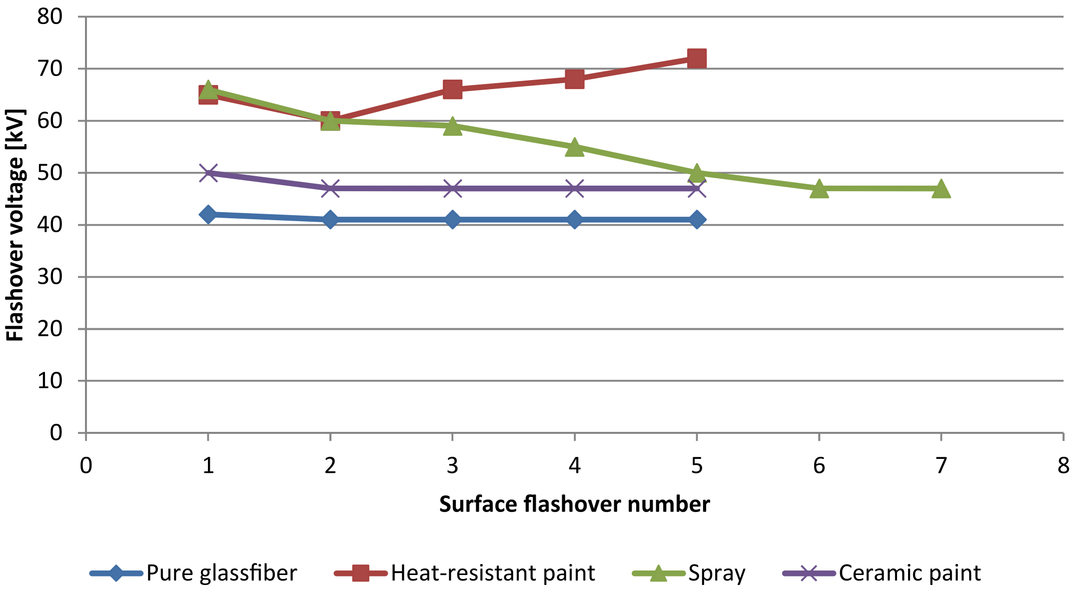

Figure 5.31: Surface flashover testing of various coatings to improve the flashover characteristics of the glassfiber discharge chamber.

suitable for the application.

3. Alternatively, replace the discharge chamber with a ceramic tube with a diameter of at least 25cm.
4. If these steps did not improve the flashover characteristics, the edges of the electrodes (as depicted in Figure 5.21) should be further rounded off.

Parallel triggering of the A-bank The second challenge relates to the parallel triggering of A-bank modules. A circuit diagram of two parallel branches and three series connected A-bank modules is depicted in Figure 5.32. Each module is charged to $U_0 = 100kV$ or $U_0 = \pm 50kV$.

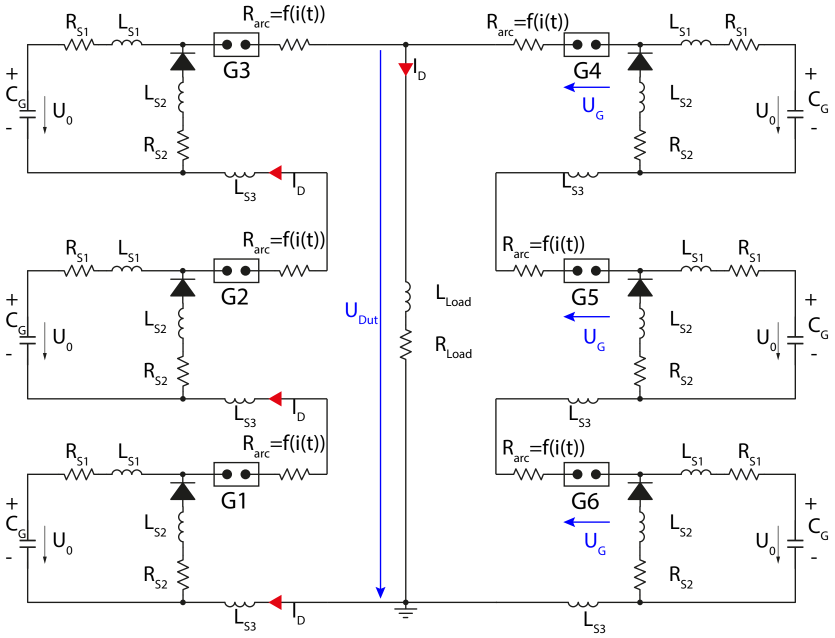

Figure 5.32: Schematic of parallel triggering of two branches. Gap $G1 - G3$ fire at $t = 0$. Trigger impulse of gap $G_4 - G_6$ is delayed due to possible jitter in arc formation and random delay. Parameters:($L_{Load} = 18\mu H$, $L_{S1} = 2\mu H$, $L_{S3} = 4\mu H$, $R_{Load} = 100m\Omega$, arc resistance model of Stokes [148]

Stray inductances are included in the model. Each A-bank module has an individual spark gap which receives the optic trigger impulse within the same microsecond. Furthermore, the Marx principle ensures that if one gap flashes over, the voltage across the remaining gaps of the branch is increased, leading to a series triggering. However, there may be a delay between when the optic trigger signal is received by the trigger and the main gap flashes-over of several hundred nanoseconds to a few microseconds. This can lead to a situation where only one branch of the A-bank ignites. The sudden increase in voltage over the DUT U_{DUT} lowers the voltage across the spark gaps U_G of the non-triggered branch which inhibits the firing. The situation is illustrated in Figure 5.33.

An in depth analysis of the jitter in the arc formation was performed in [154]. The author concluded that the spark gap should be operated near self-breakdown voltage in order to reduce the time delay of arc-initiation.

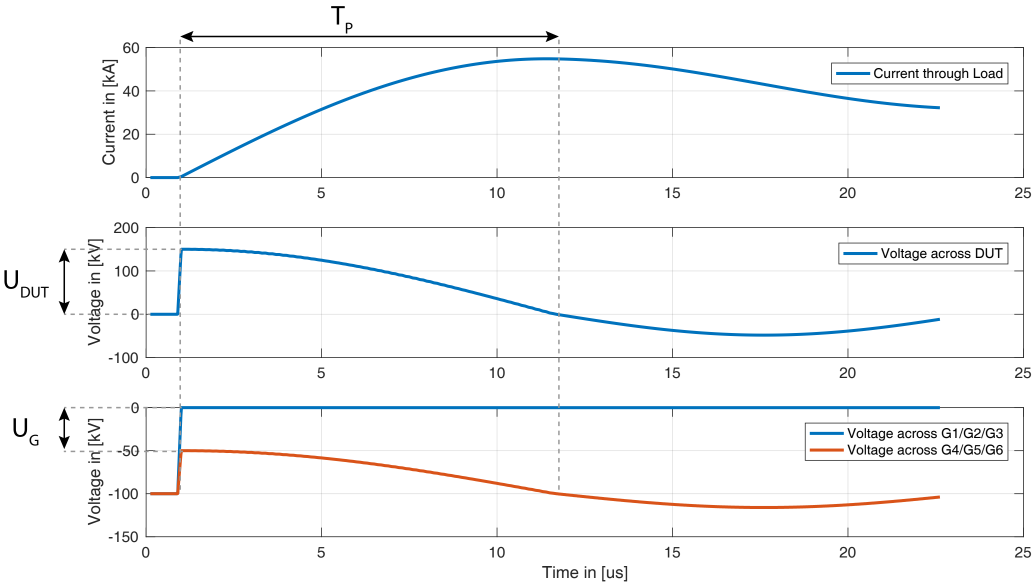

Figure 5.33: Current through $I_D(t)$ load L_{Load} , voltage across dut $U_{DUT}(t)$, and voltage across spark gaps $G1 - G6$. After the left side triggered, the voltage across the DUT is significantly decreased until $U_{DUT}(t) = 0$.

At $t = 1\mu s$, the left branch, depicted in Figure 5.32, flashes over and the voltage over the DUT increases instantaneously. At the same time, current starts to be conducted in the inductive test sample.

The voltage magnitude across the DUT U_{DUT} can be approximated after the first branch flashes over. Under the assumption the resistance in the circuit is much smaller than the reactance X_L of the test circuit

$$\sum R \ll X_L \tag{5.28}$$

or

$$\sum R_S + R_{load} \ll |(j\omega(\sum L_s + L_{load})| \tag{5.29}$$

the voltage across the DUT is approximately:

$$U_{DUT} = N_S * U_0 * \left(1 - \frac{N_S * (L_{S1} + L_{S3})}{N_S * (L_{S1} + L_{S3}) + L_{Load}}\right) \tag{5.30}$$

As can be seen in Figure 5.33, the voltage over the DUT U_{DUT} is approximately $150kV$ which is 50% of the charging voltage of the capacitors $(3 * U_0)$. This is the case if the stray inductance of the A-bank modules $(N_s * (L_{S1}L_{S3})$ is equal to L_{Load}. This applies to most of the practical testing cases since inductance is distributed in the entire circuit.

The recovery voltage across the spark gaps $G_4 - G_6$ after spark gaps $G_1 - G_3$ triggered is also dependent on the inductance distribution of the system and can be calculated by the ratio of stray inductance from the modules and the load.

$$U_G = \frac{N_S * U_0 * (L_{S1} + L_{S3})}{L_{Load} + N_S * (L_{S1} + L_{S3})} \tag{5.31}$$

or simply

$$U_G = \frac{U_{DUT}}{N_s} \tag{5.32}$$

As can be seen in Figure 5.33, the voltage across the non-triggered gaps is reduced from $-100kV$ to $-50kV$. This hinders the arc formation drastically and the second branch is unlikely to trigger.

The voltage over the gaps U_G recovers after a time period T_p determined by the capacitance C_g and the inductance L of the circuit:

$$T_p = \frac{\pi}{2}\sqrt{(N_s * (L_{S1} + L_{S3}) + L_{Load}) * \frac{C_G}{N_S}} \tag{5.33}$$

After the time T_p, the voltage across U_{DUT} becomes negative and the diodes start conducting the current. Since the stray inductance in the diodes branches limits the di/dt, the voltage across the U_{DUT} becomes slightly negative. This effectively increases the voltage U_G above the initial charging voltage U_0. It is expected that the second branch triggers at this instance automatically.

Unfortunately, a sequential triggering after a time period T_p limits the rise-time of the current in the DUT and distributes the current in the diodes unequally. Therefore, it is crucial to enable an aligned triggering of parallel branches.

Two solutions are proposed to enable parallel triggering of several A-bank modules.

The first solution relates to a physical separation of the branches by individual spark gaps in each branch. If both branches in Figure 5.32 were separated at the location of the ground symbol, a firing of one bank would not lower the potential of the second branch. Figure 5.34 shows the potential arrangement of a separation spark gap which enables a parallel triggering of up to three branches. The electrodes from the parallel branches are arranged in a circular manner around the center electrode connected to the DUT. Notice that the distance of all the electrodes is d to the center electrode, where it is $\sqrt{2}d$ between the electrodes of the branches (electrode diameter neglected). The separation distance d is adapted to the half the charging voltage of the capacitors $1.1\frac{U_0}{2}$ plus an margin of 10%. Up to five parallel branches may be connected if the spark gap are arranged in a hemispherical manner. If more than five parallel branches are to be connected, the spacing between the branch electrodes is decreased and additional insulation needs to be applied between the branches.

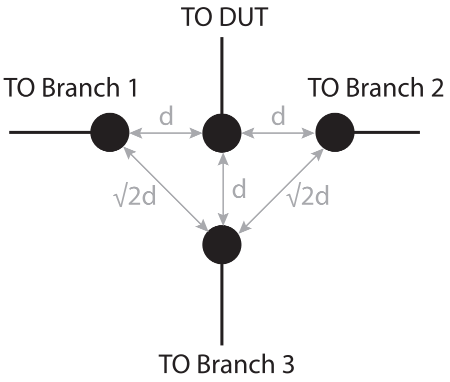

Figure 5.34: Proposed spark gap design for parallel triggering of three branches. Branch 3 does not apply to the example in Figure 5.32.

The second solution to enable parallel triggering is to modify the triggering circuit of the spark gaps $G1 - G6$. In the original design of the trigger circuit, the main gap is triggered by a short-duration current impulse which ionizes the main gap. This impulse is created by a high voltage pulse transformer. If the circuit was modified that instead a constant DC arc was created between trigger electrode and main electrode, the likelihood of ignition of the main gap is distinctly enhanced. If enough ionized particles are in the main gap, the main spark gap is likely to ignite even though the voltage across the gap U_G is reduced to half the voltage.

5.4.2 B/C-Bank

The B/C-bank is responsible for creating the continuous current component in a lightning flash. The duration of this current component can extend to a duration of $t = 1.5s$ and a current amplitude of $I_p = 2kA$. Extremely high charge levels of up to $3000C$ can be created within one test. Unlike the A-bank, the electrical source of the B/C-bank is realized by a battery bank of 35 series connected $24V$ car batteries with a total resulting driving voltage of approximately $800V$ as depicted in Figure 5.35.

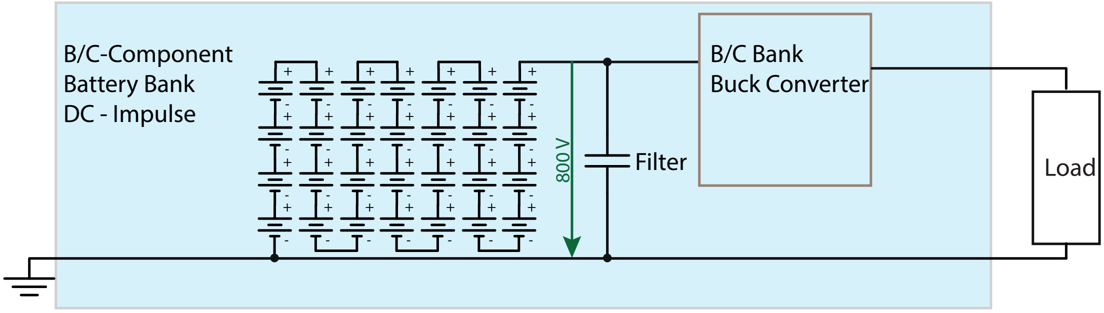

Figure 5.35: Overview of the battery fed B/C-bank switching concept.

A more detailed circuit diagram of the B/C-bank is illustrated in Figure 5.36. The structure is similar to a typical low-voltage DC/DC buck-converter, however, the components are rated for the expected high current magnitude. Particularly the Insulated-gate bipolar transistor (IGBT) and the freewheeling diode are stressed with the full DC discharge current. A RLC snubber circuit protects the IGBT from overvoltages through the snubber capacitance C_{snub}, whereas the rate of change of current in the IGBT during turn-on operation is controlled by the snubber inductance L_{snub}. The snubber resistor R_{snub} is used to dampen oscillations which are generated due to energy stored in the magnetic field of the stray inductance in the circuit. It is essential to control the rate of rise of current in the IGBT since the reverse recovery current of the freewheeling diode would otherwise exceed the current limitation of the IGBT during the turn-on operation. The values for the snubber components were determined with the software Snubdim which calculates the suggested components based on the performance characteristics of IGBT and freewheeling diode found in the data-sheet. Additionally, an input filter is used to stabilize the supply voltage during the turn-on phase of the IGBT. The physical layout is shown in Figure 5.37 and the used components in the B/C-bank are listed in Table 5.4. As can be seen, all the components are mounted on a grounding plate in order to reduce stray inductance to ground as best as possible.

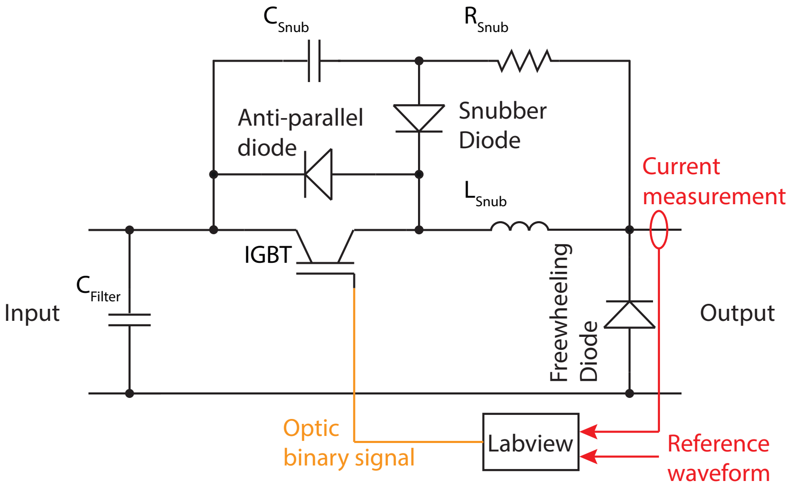

Figure 5.36: Circuit diagram of the B/C-bank. The configuration acts as a buck-converter. Values of the components: $C_{Filter} = 2.35mF$, $C_{snub} = 13.6nF$, $R_{snub} = 125m\Omega$, $L_{snub} = 0.28\mu H$.

In principle, a duty cycle control of an IGBT switch regulates the voltage across the load. A current measurement from a Rogowski coil in the load branch is compared to the desired reference waveform and an analog digital interface combined with Labview is used to generate the optic binary signal. The switching frequency can be selected from a range between $f = 1kHz$ to $f = 3kHz$. The duty cycle control of the buck converter enables to vary the amplitude of the continuous current waveform and various amount of charge and specific energy can be inserted into the DUT.

Table 5.4: Component list of B/C-bank.

Component	Manufacturer	Type	Quantity
IGBT	ABB	5SNA 3600E170300	1
Gate Driver	Concept	1SP0635V	1
Freewheeling diode	ABB	5SLA 3600E170300	1
Snubber diode	ABB	5SLA 3600E170300	1
Snubber resistor	Vishay	LPS0300H1R00JB	7
Snubber inductor	Self-made		1
Snubber capacitor	WIMA	FKP1U011505B00	8
Filter capacitor	KEMET	ALS3(1)(2)472NP400	8

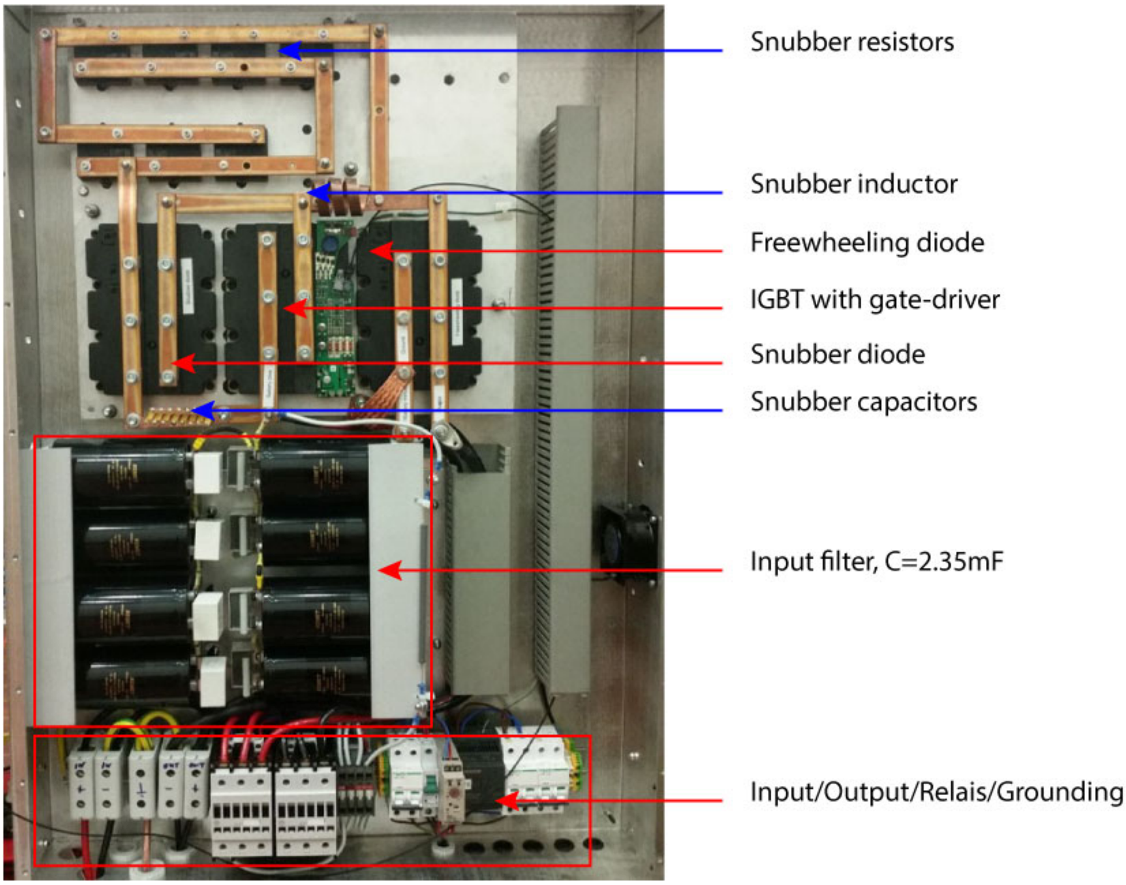

Figure 5.37: Layout of B/C-bank with parts explained.

The switching operation of the IGBT and the current flow during each possible switching state is illustrated in Figure 5.38. During the turn-on phase of the IGBT (Figure 5.38a), the full battery voltage is applied to the load and current flows directly between battery and load. The current derivative in the test sample is limited by the inductance of the test circuit. During the turn-off process of the IGBT (Figure 5.38b), the full dc current flow (up to $I_p = 2kA$) is interrupted within $t_{d(off)} = 1\mu s$, which creates transient overvoltages with a magnitude of $\Delta U = L * \frac{di}{dt}$ on both the load and the battery side of the IGBT. The magnitude of overvoltage is proportional to the stray inductance in the circuit and hence the magnetic energy stored in the system. Due to this reason, the bus bar and grounding layout has been optimized for minimum lead length and hence minimum stray inductance. On the battery side, the transient overvoltages oscillate with both the filter capacitor C_{Filter} as well as the snubber capacitor C_{snub}. On the load side, the energy trapped in L_{snub} is able to circulate through R_{snub} and the snubber diode. After the closing process of the IGBT is finished, the current is conducted through the freewheeling diode and the load (Figure 5.38c). During the IGBT opening instance (Figure 5.38d), the diode switches from conducting state to blocking state. During this time, a reverse recovery current flows caused by the charge storing pn-junction. The peak magnitude can reach a value of up to 70% of the forward current I_F [155] and depends on the current-rise time in the diode. The faster the $\frac{di}{dt}$ in the diode, the higher the reverse current. The negative current in the diode is controlled by the magnitude of L_{snub}. Without the inductor, the current limit of the IGBT may be reached during IGBT turn-on.

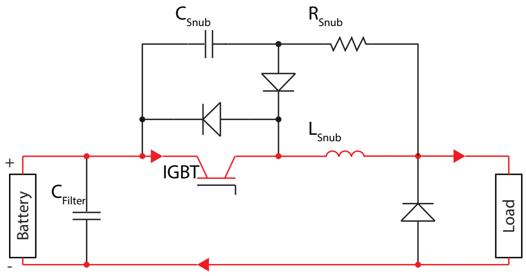

(a) IGBT conducting

(b) IGBT closing: During the closing instance, the energy from the snubber inductance is dissipated by the resistance R_{snub}. C_{snub} limits the $\frac{dV}{dt}$ across the terminals of the IGBT.

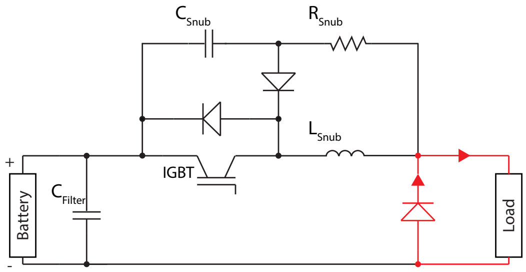

(c) Freewheeling diode conducting

(d) IGBT opening: During the opening instance, the snubber inductance L_{snub} limits the rate of rise of current in the IGBT from the reverse recovery current of the diode that switches from conduction to blocking state. After the reverse recovery current in the diode ceased, the excess energy in the stray inductance is dissipated by the snubber resistor R_{snub}. C_{snub} limits the $\frac{dV}{dt}$ across the terminals of the IGBT.

Figure 5.38: Switching operations of B/C-bank and relevant snubber components.

5.4.3 D-Bank

The D-bank is able to create a faster current impulse compared to the A-bank which attempts to represent the current properties of a subsequent stroke. The generator is a typical Marx-type high voltage impulse generator with 10 capacitor stages of each

$C_S = 100nF$ at a charging voltage of $U_0 = 100kV$ per stage. The capacitors are charged in parallel and discharged in series, leading to a total resulting capacitance of $C_g = 10nF$ at a voltage of up to $U_g = 1000kV$. The maximum output current is $I_p = 20kA$. The capacitor bank is equipped with an encapsulated spark gap chamber including spark gap switches. Similar to the A-bank, the pressure in the discharge chamber can be regulated and hence the flashover voltage adjusted. The D-bank does not have a crow-bar circuit and therefore, it can only create oscillating current components. An illustration of the D-bank circuit and a picture of the physical D-bank is depicted in Figure 5.39. The impulse generator was manufactured by an Indian high voltage component supplier.

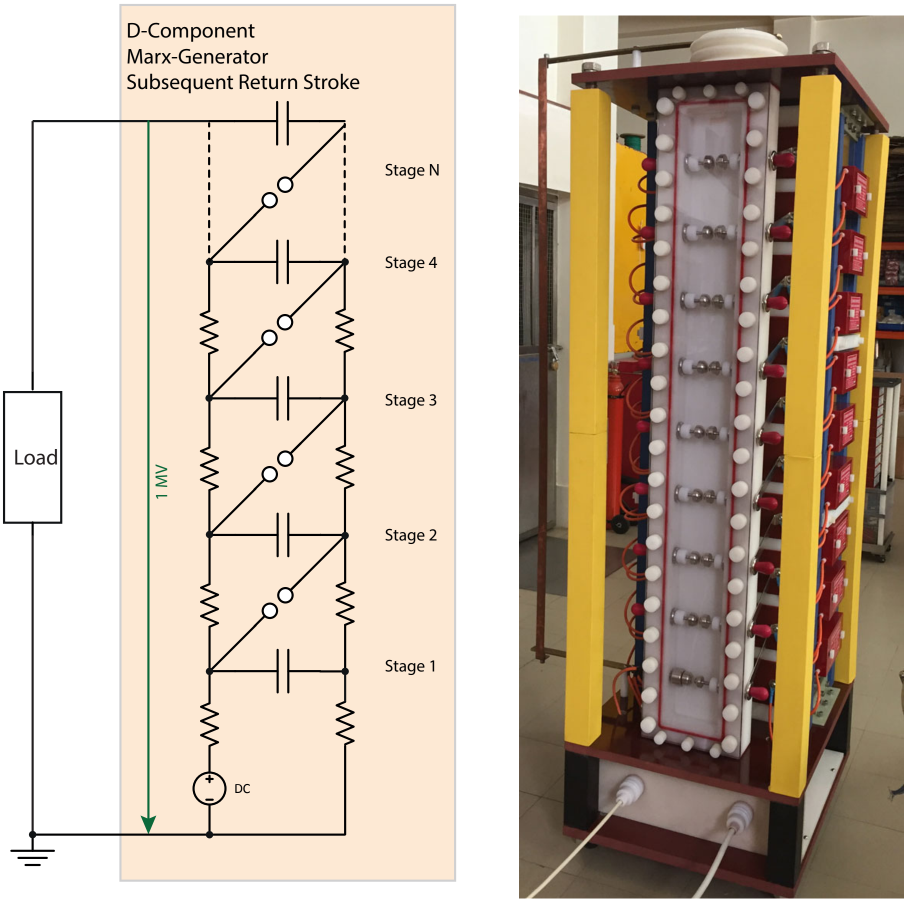

(a) Schematic of D-bank.

(b) Picture of D-bank. View shows encapsulated spark gaps and resistors. Terminals are short circuited.

Figure 5.39: Illustrations of D-bank

As has been previously discussed in Section 5.3.2, the current waveform of the D-bank is not expected to reach current properties of a subsequent return-stroke in a full-scale structure. However, it is able to inject a faster current pulse compared to the A-bank module. This test is especially valuable if nacelles are tested and an evaluation of induced voltages in electronic circuits are performed during the test. The optimization of signal cable routing and cabinet placement in the nacelle can help to prevent malfunction of components due to induced voltages of fast current components. Furthermore, Electromagnetic compatibility (EMC) related tests of electronic equipment as defined in IEC 61000-4-10: Testing and measurement techniques - Damped oscillatory magnetic field immunity test [156] may be performed.

Similar to the A-bank, the expected peak current and rise time of the current impulse was calculated and Figure 5.40 illustrates the expected performance of the D-bank. The smallest possible circuit inductance of the D-bank generator can be approximated by the physical dimensions of the Marx-generator. The height of the generator is $h = 1.85m$ and the side width is $l = 0.85m$. The inductance of a rectangular loop of this dimension ($w = 2 * l$ due to safety distance to the generator) and a wire diameter of $r = 0.001m$ can be calculated according to [157]:

$$\begin{aligned} L = \frac{\mu_0}{\pi}(-h \cdot log(1 + \sqrt{(1 + (\frac{w}{h})^2)}) - w \cdot log(1 + \sqrt{(1 + (\frac{h}{w})^2)}) + \\ h \cdot log(\frac{2w}{r}) + w \cdot log(\frac{2h}{r}) + 2\sqrt{(h^2 + w^2)} - 2w - 2h) \end{aligned} \tag{5.34}$$

and results in a inductance value of $L = 10\mu H$. Furthermore, the some extra inductance is expected due to the connection leads of resistors and capacitors. The minimum stray inductance of the D-bank is therefore approximated to a value of $L = 13uH$. From Figure 5.40, the smallest expected rise-time can be determined with a value of approximately $T_f = 0.4\mu s$ at peak current value of $I_p = 20kA$. Such an inductance value represents the generator in short circuit conditions when a conductor is placed between the terminals. If a small test item $L = 15\mu H$ is connected to the terminals, the perspective characteristics are $I_p = 20kA$ at a current rise-time of $T_f = 0.45\mu s$. If the load inductance is similar to a full-scale blade with $L = 45\mu H$, a perspective current magnitude of $I_p = 15kA$ with a current rise-time of $T_f = 0.9\mu s$ can be reached.

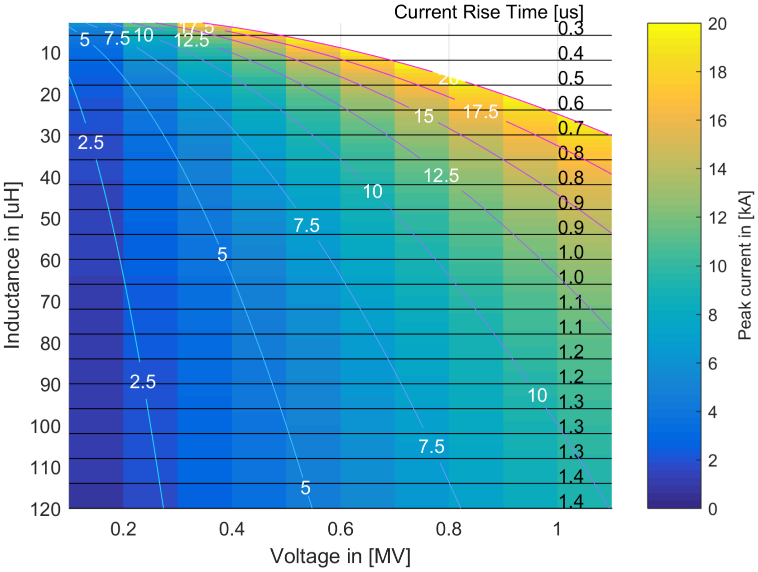

Figure 5.40: Peak current and rise-time capabilities of the D-bank generator as a function of load impedance.

5.5 Control and measurement of the impulse generator

This section elaborates on the control and measurement of the ELITE generator. The backbone of the system is based on the Ethercat network, a real time high-speed Ethernet network from the automation hardware provider Beckhoff. It offers a flexible, modular, and synchronized network interface which is able to send and receive data to partner devices. Fiber optic connection between the modules ensures galvanic isolation to the control cabinet.

The system is a hardware-implemented network bus and consists of one reference module and an arbitrary number of slave modules. Data packages are sent from the reference module to the slave modules via a chain connection. The individual modules only process the relevant data for their operation and send irrelevant data further to the next segment. The last Ethercad module returns the fully processed frame back to the first unit, which in turn, informs the reference module that the operation is fully executed. The synchronization frequency f_s between the modules is about 10kHz for the A-bank and D-bank, and 20kHz for the B/C-bank. Each module has further an individual clock which is aligned with f_s each time a command is executed. Distributed impulse testing requires exact time correlated commands between the modules. In order to achieve that signals are executed within the same microsecond, the information is send to the individual modules several milliseconds before the event. After each module has received the information, a countdown is initiated and the individual synchronized clocks in the modules execute the desired operation at the same time instance. The advantage of this system is that the amount of transferred data in the instance of the triggering is significantly reduced which increases the speed of the network and the jitter between the modules. The slave modules are connected to input/output devices which execute actions or record data. In the ELITE generator, pressure control, and fiber optic signal input/output devices are used.

The control and measurement network structure of the ELITE generator is illustrated in Figure 5.41. As can be seen, the different generator banks have each an individual bus, however, all the different modules could also be connected to into a one bus system.

In the following section, the control variables are explained for each of the ELITE banks.

5.5.1 A-Bank

The control of the A-bank is the most complex system of all the ELITE banks. It consists out of the reference module which links m high voltages sources and n A-bank modules.

As can be seen in Figure 5.41, to each A-bank module, there is one fiber optic input, one fiber optic output, and one nitrogen pressure connection. Through the fiber optic connection, several pressure valves can be enabled or disabled in order to adjust the pressure inside the spark gap or remove the grounding system from the bus bars. Furthermore, the trigger can be activated and fired via fiber optic connection. Additionally, there is a voltage measurement on both capacitor bus bars realized with a voltage divider $\frac{R_1}{R_2} = \frac{1G\Omega}{1k\Omega}$. The analog voltage measurement from the low voltage side is converted to a fiber optic pulse train which is further processed in the A-bank control cabinet and available in the ELITE measurement interface. Furthermore, a safety echo variable which continuously

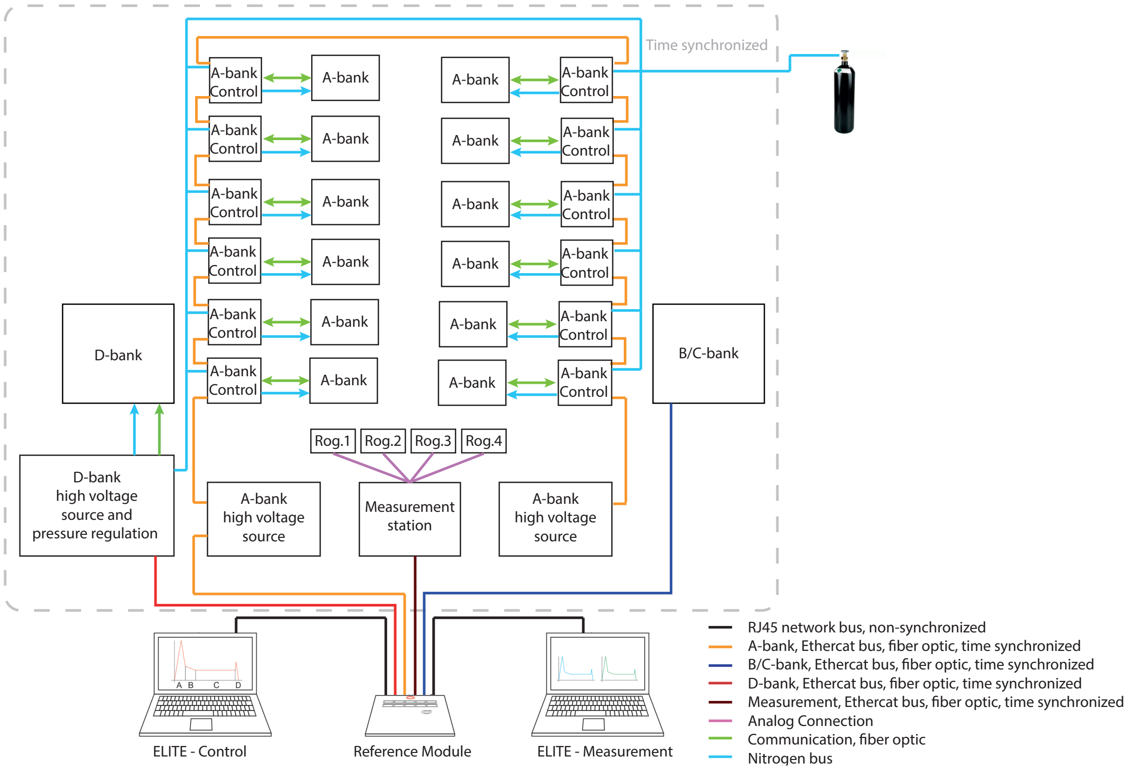

Figure 5.41: The control system of the ELITE generator.

verifies the functionality of the controls system is available. In case of low voltage on the battery supply terminals, as well as component faults, the safety echo provides a negative feedback and informs the operator.

The control variables for the A-bank control cabinet are:

- Enable/disable the pneumatic grounding
- The nitrogen pressure in the spark gap chamber
- Bus bar voltage measurement via fiber optic connection
- Enable the spark gap trigger
- Fire the spark gap trigger
- Safety echo

Additionally, in the individual A-bank modules, the high voltage sources are connected in the A-bank Ethercad and following parameters can be controlled.

- Enable high voltage output
- Set the output current from 0 to 22mA
- Set the output voltage from 0 to 100kV
- Voltage/current echo of the high voltage sources
- Safety echo

5.5.2 B/C-Bank

In order to create a variable current waveform from the B/C-bank, a duty cycle control with a Pulse width modulation (PWM) algorithm was implemented. The control circuit is based on a Labview control program. An illustration of the implementation is depicted in Figure 5.42. The output current of the B/C-bank is measured and subtracted from the reference current waveform. The resulting error is then fed to a digital comparator which calculates the binary IGBT operation on base of a sawtooth reference signal. The output is fed to a power Light-emitting diode (LED) which creates the optic signal for the IGBT gate driver. The switching frequency of the IGBT can be varied between one and three kHz and is adjusted by increasing or decreasing the frequency of the sawtooth reference signal.

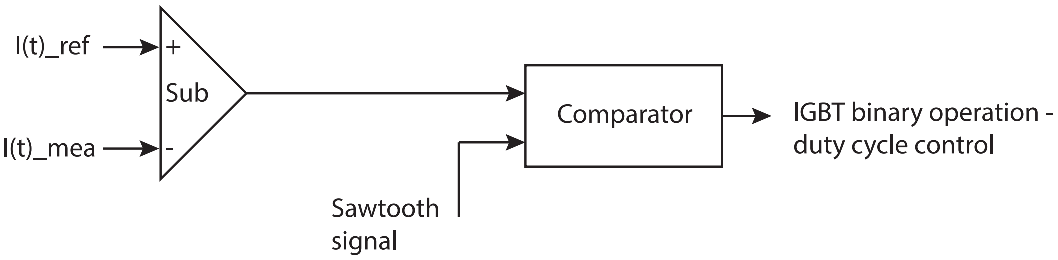

Figure 5.42: Duty cycle control based on output current measurement.

Additionally, the voltage at the input of the B/C-bank is measured and a safety echo is returned to the reference module.

The control variables for the B/C-bank are:

- Measurement of the input voltage in B/C bank
- Measurement of output current for control
- Reference signal for PWM duty cycle control
- Safety echo

5.5.3 D-Bank

The D-bank voltage and pressure control is located in the high voltage source. Similar to the A-bank, the fiber optic bus transmits the control variables and the signals are processed locally.

The control variables for the D-bank are:

- Pressure control for spark gap
- Set the output current from 0 to 22mA
- Set the output voltage from 0 to 100kV
- Voltage/current output echo of the high voltage sources.
- Fire the spark gap trigger
- Safety echo

5.6 Practical validation of the ELITE concept

This section documents the practical validation of the ELITE generator.

5.6.1 Validation 1: A-Bank single module laboratory test

The first A-bank module verification was performed at the high voltage laboratory of the Technical University of Denmark in August 2016. Before all twelve modules were constructed, a prototype module was built in order to verify the performance of a single module. There are several differences between the prototype A-bank module and the finalized version:

- The prototype A-bank impulse generator consisted in a parallel configuration of four instead of five capacitors and was therefore characterized by a capacitance of $C = 3\mu F$ and a maximum discharge current of $I_p = 100kA$. The finalized version of one A-bank module employs five parallel connected capacitors with a capacitance of $C = 3.75\mu F$ and a maximum discharge current of $I_p = 125kA$. Furthermore, in the prototype module, the spark gap was connected in the capacitor branch instead of the output branch. With this configuration, the arc does not have an influence on the tail current since the current flows only in the didoes and the test object. In the final design, the spark gap is connected in the output branch, since it is required for successful triggering of several series connected modules.
- The prototype of the A-bank module was equipped with a ceramic discharge chamber manufactured by the Indian high voltage component supplier. The gap provided good insulating properties, however, the overall weight of the discharge chamber and the electrodes exceeded a value of $100kg$ which hampered the handling process. Furthermore, the interface between metal electrode and ceramic cylinder failed at a pressure level of $50PSI$. Due to this reason, it was decided to change the discharge chamber from a ceramic structure to a lightweight glass fiber structure.
- In the capacitor branch, a discharge resistor of $R = 100m\Omega$ was placed in order to reduce the oscillations between stray inductance and capacitor.

Despite the changes, the flashover characteristics as well as the operation remain the same between prototype module and the finalized version because the distance and structure of the spark gap and trigger are identical.

The perspective performance of the A-bank with oscillating and unipolar current pulses are documented in the next pages.

5.6.1.1 Oscillating current waveform: Voltage-current characteristics of spark gap

The first performance evaluation was conducted by firing more than five hundred oscillating current impulses into a low inductive test load with an approximate resistance of $R = 30m\Omega$ and and inductance of $L = 1.7\mu H$. The crow-bar diode was disconnected from the generator for this test. The purpose of the test was to evaluate the performance of the spark gap and to identify related pressure voltage diagrams. Furthermore, the peak current and rise-time

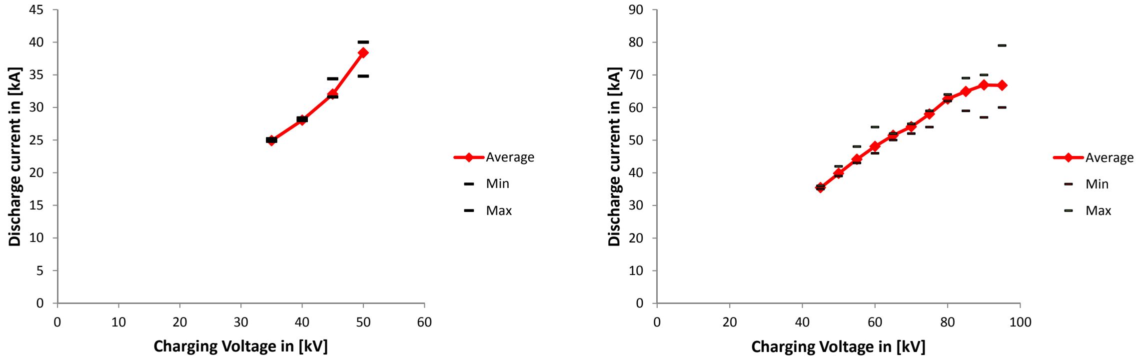

(a) Voltage-Current graph at 0.34 bar or 5 PSI above atmospheric pressure

(b) Voltage-Current graph at 0.69 bar or 10 PSI above atmospheric pressure

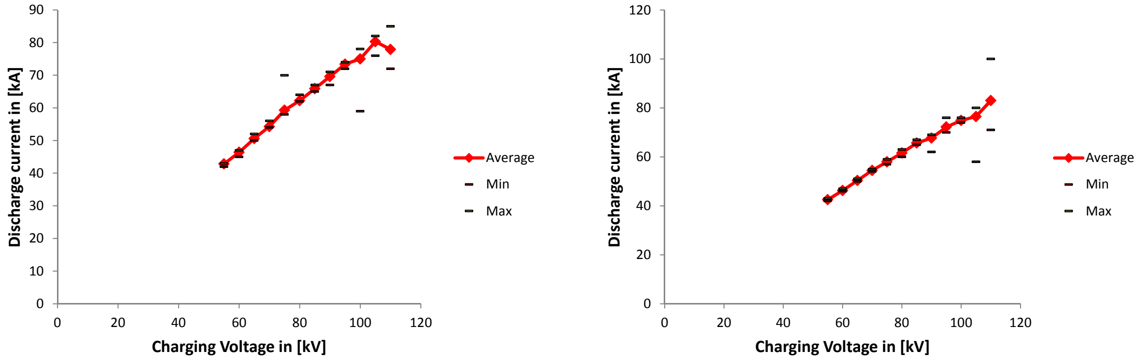

(c) Voltage-Current graph at 1.03 bar or 15 PSI above atmospheric pressure

(d) Voltage-Current graph at 1.38 bar or 20 PSI above atmospheric pressure

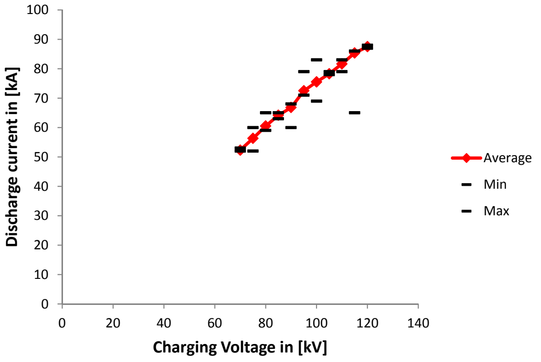

(e) Voltage-Current graph at 1.72 bar or 25 PSI above atmospheric pressure

Figure 5.43

performance of the impulse generator was verified. The current waveform were measured with Rogowski coils.

In Figure 5.43, the voltage-current capabilities of one A-bank module can be seen for different nitrogen pressure levels. For each charging level, ten discharges were triggered and the average, minimum and maximum current magnitude is illustrated.

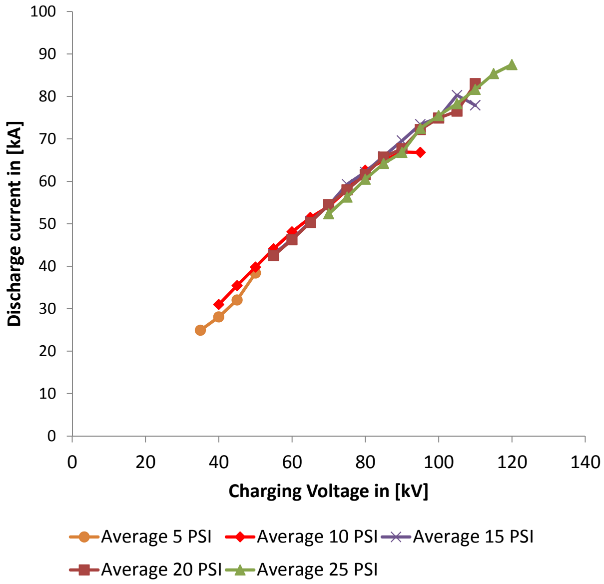

Figure 5.44: Merged voltage-current characteristics.

As can be seen, the variance between minimum and maximum readings increases with increasing charging voltage.

If all graphs from Figure 5.43 are plotted in one graph, the total voltage-current capability for one load scenario can be plotted. As can be seen from Figure 5.44, a good linearity can be observed between voltage and current. The smallest current injected was $I_P = 25kA$. By adjusting voltage and pressure, a current magnitude of $I_p = 90kA$ was able to be injected into the test sample.

This measurement demonstrated that the capacitors are able to reach 90% of the maximum current rating.

5.6.1.2 Unipolar current waveform: Diode performance

At the next stage of testing, the diode crow-bar was connected to the module and therefore, the automated rectification of the current impulse was enabled. This test was performed directly in order to evaluate the performance of the diode stack.

The A-bank was tested with 39 documented unipolar test impulses in August 2016; however, the amount of actual performed discharges is more than double. Not all current waveforms were recorded during the prototyping phase since the measurement equipment needed a processing time of 10 minutes after three shots were fired. Furthermore, the data needed to be retrieved manually from inside the restricted high-voltage test area.

The current waveform of three firings is depicted in Figure 5.45 and the properties of the current are given in the captions. The current was recorded in the DUT as well as in the diode stack. The charging voltage of the capacitors was $U_o = 50kV$, $U_o = 63kV$, and $U_o = 70kV$. As previously explained in Section 5.3.1, the stray inductance in the capacitor and diode branch triggers an oscillation with the capacitors, leading to an overshoot in current at $t = 2 * t_{peakDUT}$. The diode branch needs to conduct 55% more peak current

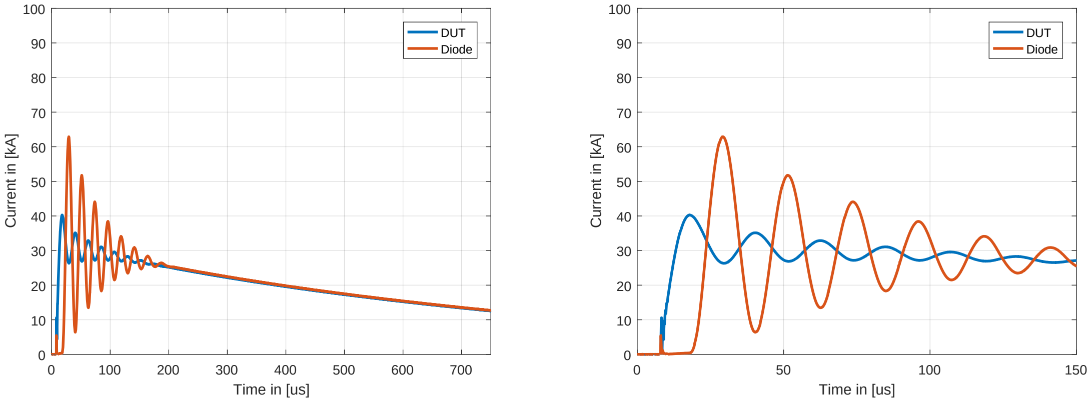

(a) $U_0 = 50kV$, $Q = 22.7C$, $\frac{W}{R} = 0.4\frac{MJ}{\Omega}$ (b) $U_0 = 50kV$,zoomed, $I_p = 40.3kA$,$T_f = 8.6\mu s$

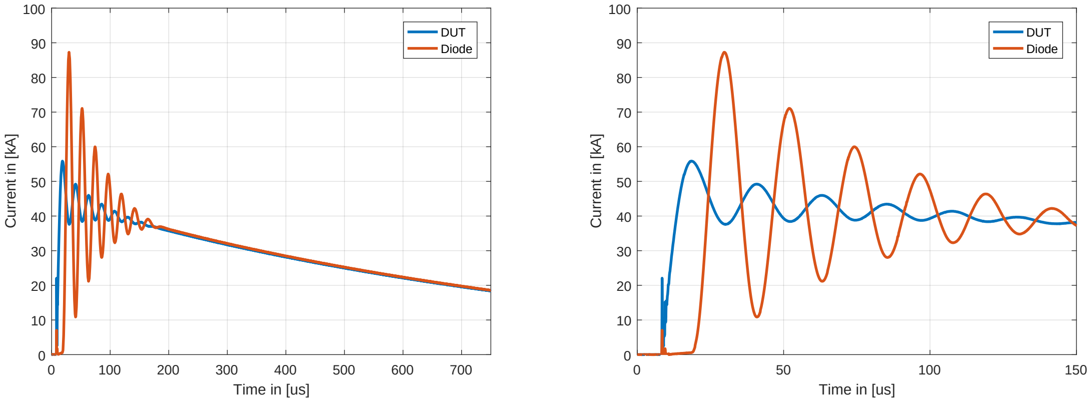

(c) $U_0 = 63kV$, $Q = 33.7C$, $\frac{W}{R} = 0.8\frac{MJ}{\Omega}$ (d) $U_0 = 63kV$,zoomed, $I_p = 55.8kA$, $T_f = 8.5\mu s$

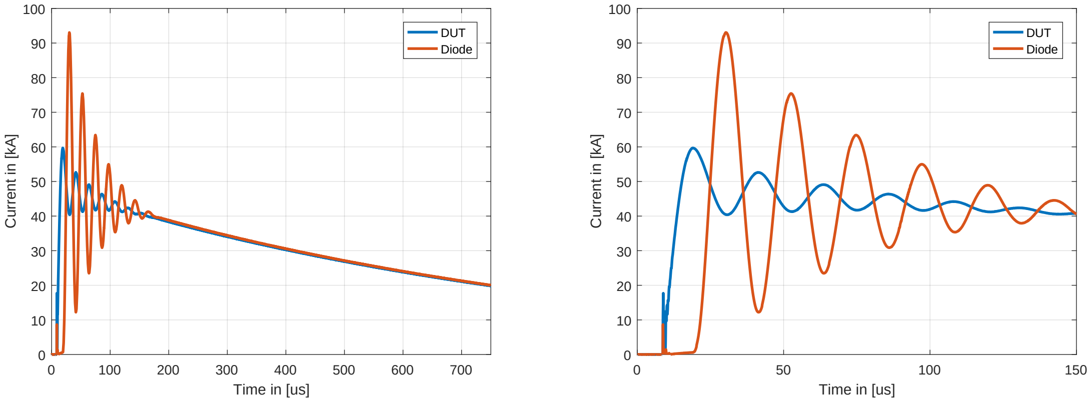

(e) $U_0 = 70kV$, $Q = 36.4C$, $\frac{W}{R} = 1\frac{MJ}{\Omega}$ (f) $U_0 = 70kV$,zoomed, $I_p = 59.6kA$, $T_f = 8.7\mu s$

Figure 5.45: Current measurement of unipolar current impulse from A-bank. Prototype module with $C = 3.0\mu F$. Three charging levels of capacitors $U_0 = 50kV, 63kV, 70kV$. Left large focus, right zoomed. Load resistance/inductance: $R = 10m\Omega$, $L = 10\mu H$.

compared to the actual current through the DUT. The oscillations between the capacitor and the stray inductance are fully damped within the first $200\mu s$. From the frequency of the oscillations or the period time T, the stray inductance in the capacitor and diode branch can be estimated:

$$L_s = \left(\frac{\left(\frac{T}{2\pi}\right)^2}{C} \right) \tag{5.35}$$

with a period time $T = 22\mu s$, the stray inductance from the two branches is:

$$L_s = \left(\frac{\left(\frac{22us}{2\pi}\right)^2}{3uS} \right) = 4.1uH \tag{5.36}$$

In August 2017, after the new iteration of the spark gap was delivered, an additional extensive testing period followed with 122 documented unipolar discharges. The same diode stack which was previously used in the prototype module was used for the test. Similar to 2016, several changes in the generator design were made during the test, so that many current impulses of the A-bank were not documented. It is estimated that the first diode stack in the prototype A-bank was tested with more than 300 unipolar discharges. During this time, the diode stack always performed in accordance, even though the current magnitude in the diodes reached more than 100 kiloamperes. It was therefore concluded that the stacked semiconducting diodes are in fact a suitable solution which enable an automated rectification of the lightning current impulse.

5.6.1.3 Stray inductance and resistance estimation of one A-bank module

From the current measurements of the prototype, a circuit simulation model was derived which was used to estimate the current and voltage distribution of the full-scale setup including diode crow-bar. The impact of stray inductances from leads and bus bars plays a critical role in the behavior of the system. As a rule of thumb, the self inductance of 1 meter straight conductor in air is approximately $L = 1.1\mu H$ [144]. If the return path of the current is in proximity of the straight conductor, the total inductance is typically smaller than $L = 1\mu H$ due to the impact of flux mitigation from mutual coupling with the return path. Figure 5.46, illustrates the circuit with indicated stray resistance and inductance positions. The resistor $R_B = 100m\Omega$ is the blocking resistor for damping the oscillations between crow-bar and capacitor branch. The load in this experiment was a circular wound air core inductor with 25 turns and an approximated resistance of $R_L = 10m\Omega$ and $L_L = 10\mu H$. Furthermore, the labels I_{DUT} and I_D in the circuit diagram indicate the position of the current measurements which are used to determine the characteristics of the model.

For determination of the stray inductance and resistance, the values of measurement and simulation have been compared. Iteratively, the values for $R_{S1} - R_{S3}$ and $L_{S1} - L_{S3}$ were determined. Similar to Section 5.4.1.1, the resistance of the arc R_{arc} was modeled according to the expression by Paukert [149]. Varying each parameter separately, the shape of the current impulse is fitted. For instance, the resistance of the output branch has a crucial impact on the tail time of the current, whereas the inductance in the crow bar is characteristic for the magnitude of current in the diode branch.

In Table 5.5, all stray parameters are listed and Figure 5.47 shows the result of a simulated and measured curve.

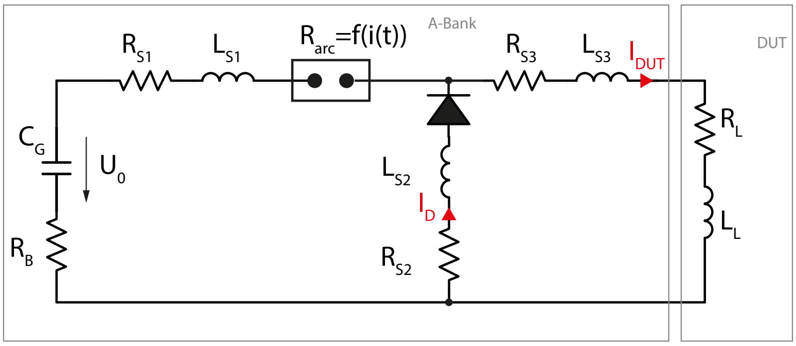

Figure 5.46: Circuit diagram for stray impedance estimation of the prototype A-bank

Table 5.5: Stray inductance and resistance in one A-bank module

Parameter	Unit	Value	Parameter	Unit	Value
R_{S1}	$[m\Omega]$	1.0	L_{S1}	[uH]	2
R_{S2}	$[m\Omega]$	6.0	L_{S2}	[uH]	2.4
R_{S3}	$[m\Omega]$	1.2	L_{S3}	[uH]	2.5

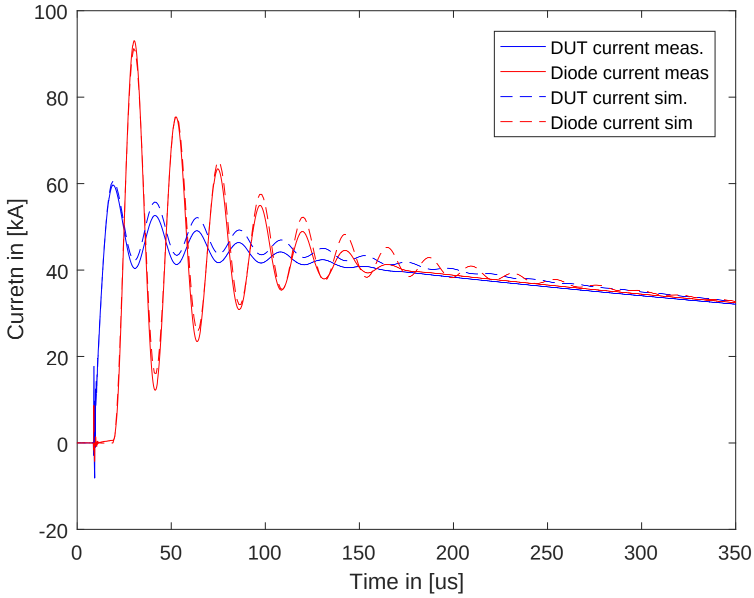

Figure 5.47: Result of the estimated simulation model fitted to the current measurements. Charging voltage: $\pm 70kV$, Load: $L_L = 10\mu H$ and $R_L = 10m\Omega$

The determined values in Figure 5.5 show that each A-bank module adds approximately 4.5 microhenry of stray inductance per module to the overall test circuit. This value may be decreased if the module is placed close the DUT. Another important aspect is the resistance of the diodes. It is shown that each module is characterized $R_{S3} = 6m\Omega$ in the crow-bar branch. The high resistance is attributed to the forward resistance r_f of the diodes. For one single diode in standard operating conditions, the forward resistance is $r_f = 0.19$ as given in the datasheet. Since 45 diodes are series connected for one module, the actual resistance of the diode stack is in-fact slightly lower than is defined in the datasheet.

By determination of the stray parameters in one A-bank module with current measurements, the transient overvoltages inside a module can be calculated which are naturally difficult to measure. Furthermore, it is possible to evaluate the performance of several modules in a parallel or series connection before the physical setup is realized.

5.6.2 Validation 2: B/C-Bank laboratory test

The performance of the B/C-bank has been validated in the premises of GLPS. The battery bank was connected to a battery bank consisting out of 35 series connected $24V$ car batteries. Figure 5.48 shows the scope readings from a discharge performed with the B/C-bank. The blue line shows the switching signal for the IGBT. The red line indicates the input voltage to the DC/DC-converter. The initial voltage is about $880V$. After the discharge is initiated, the voltage drops about 20% due to the sudden load on the terminals. The green line represents the output current measured with a Rogowski coil. In this test, the reference current amplitude is set to $800A$. After approximately $15ms$, the output current reaches the targeted of the reference signal. A switching frequency of $1kHz$ was used. The duration of the current waveform can be adjusted and is in theory only limited by the lower battery voltage threshold.

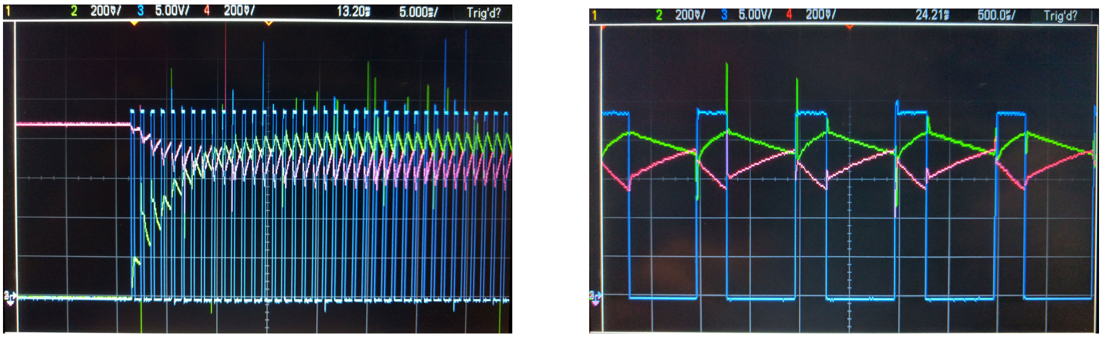

(a) Ramp-up: $5ms/div$ (b) Zoomed: $500\mu s/div$

Figure 5.48: Scope plots for B/C-bank validation. Red: Input voltage B/C-bank ($200V/div$, Green: Output current ($200A/div$), Blue: Switching Signal for IGBT.

A DC arc was fired into a flat resistive test sample. Figure 5.49 shows two pictures of the developed arc. The discharge was initiated with a thin conductive wire which evaporates as soon as the current increases and an open arc is formed.

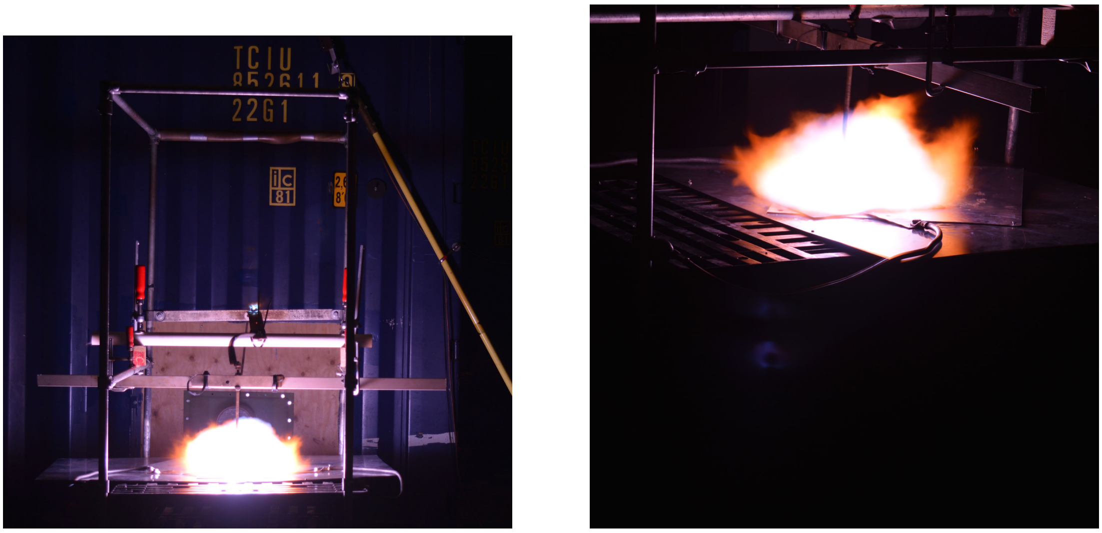

(a) Overview test

(b) Zoomed view

Figure 5.49: Pictures of a DC arc in air created by the B/C-bank.

5.6.3 Validation 3: D-Bank laboratory test

The performance of the D-bank was validated in the laboratory of GLPS. Over 200 discharges were initiated and the pressure-voltage characteristics were recorded. As can be seen in Figure 5.50, the pressure increase (Nitrogen) in the discharge chamber increases the charging voltage. The highest gain in charging voltage was noticed between the difference of 0 and $5PSI$. Between self-breakdown and triggered-breakdown, there is a margin of 8 to $15kV$ where the impulse generator can be operated. By linear extrapolation of the self-breakdown curve between $5PSI$ and $15PSI$, the highest possible charging voltage of $100kV$ may be reached at a pressure level of $40PSI$.

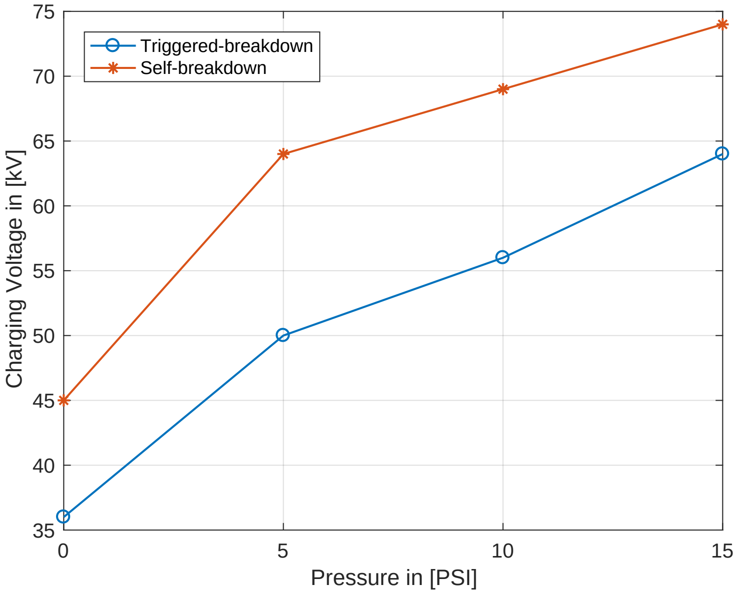

Figure 5.50: Pressure-voltage plot for the D-bank.

Furthermore, current recordings of the performance of the D-bank were available with short circuited terminals as previously depicted in Figure 5.39b.

In Figure 5.51, a $20kA$ $(1kA = 0.1V)$ oscillating current impulse with a time to peak of $T_p = 0.54\mu s$ is illustrated. The initial phase of the current component is superimposed by induced noise. Nevertheless, the performance of the impulse generator can be deduced. The rise-time of the D-bank was estimated in Section 5.4.3 with approximately $T_r = 0.4\mu s$. Considering that T_p is typically $10-15\%$ lower compared to the rise-time T_r, the estimation of the circuit inductance of $L = 13uH$ with shorted terminals (As discussed in Section 5.4.3 seems appropriate. Figure 5.40 can be used to predict the performance for varying values of inductance in the load branch.

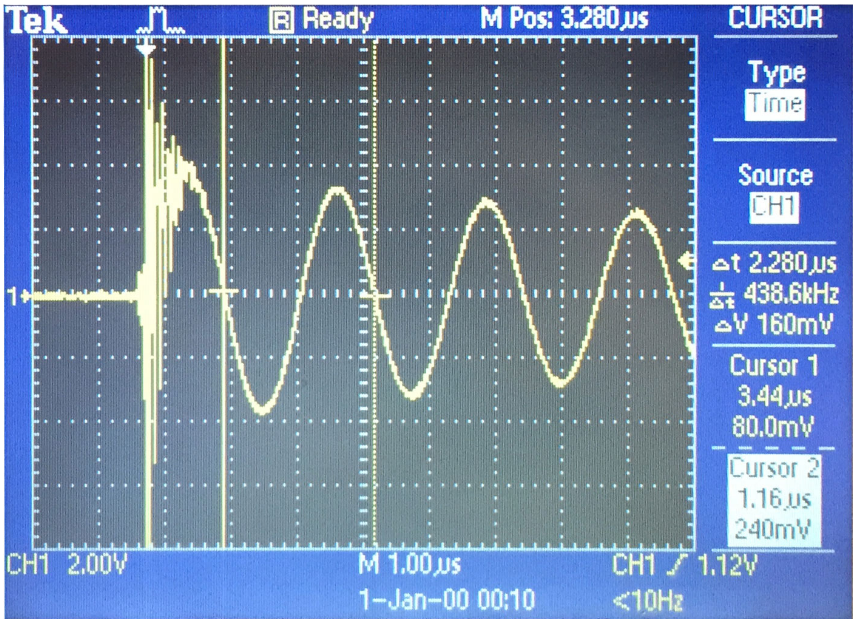

Figure 5.51: Current time plot of D-bank.

5.6.4 Validation 4: A-Bank full-scale laboratory test

At the 9th of October 2017, a full-scale demonstration test of the A-bank was performed at the mechanical wind turbine blade test center Blæst in Aalborg, Denmark. Blæst typically performs mechanical blade test such as parameter analysis, static proof tests, or fatigue tests; however, a perspective cooperation between GLPS and Blæst may also introduce lightning verification tests to the portfolio in the future. The advantage of performing multiple wind turbine tests within one laboratory is the reduced transportation effort of wind turbine components to various test facilities which is especially expensive for large structures.

The demonstration test was used to show the functionality of the ELITE concept to the project funding representatives of EUDP as well as to interested participants from the wind turbine industry. The test was performed with ten A-bank modules which were connected in two parallel strings with each five series connected modules. A photograph of the test setup is shown in Figure 5.52. The resulting capacitance of the generator was $C_G = 1.5\mu F$. The modules were aligned closer to the tip of the blade, rather then fully distributed along the length of the blade. The reason for this configuration was the limited space around the root of the blade.

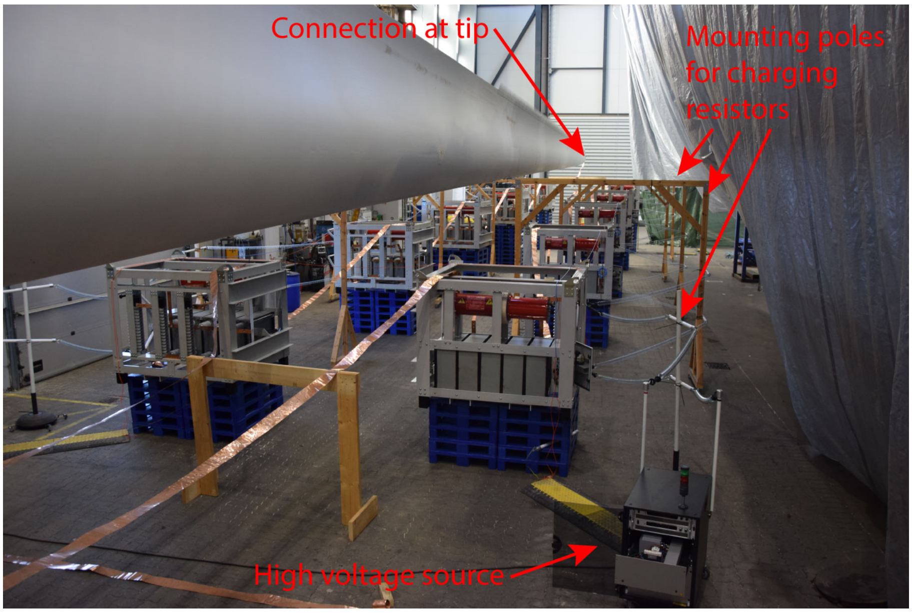

Figure 5.52: A-bank photograph of full-scale test.

A structural overview of the test is illustrated in Figure 5.53. The DUT was a 67 meter blade which was mounted on a static blade hub steel structure. The mounting socket implied that the root end of the blade is on ground potential and that the voltage builds-up towards the tip of the blade. A spark gap at the tip of the blade isolates the blade from the charging voltage. Additional pictures from the test setup can be found in Appendix D.

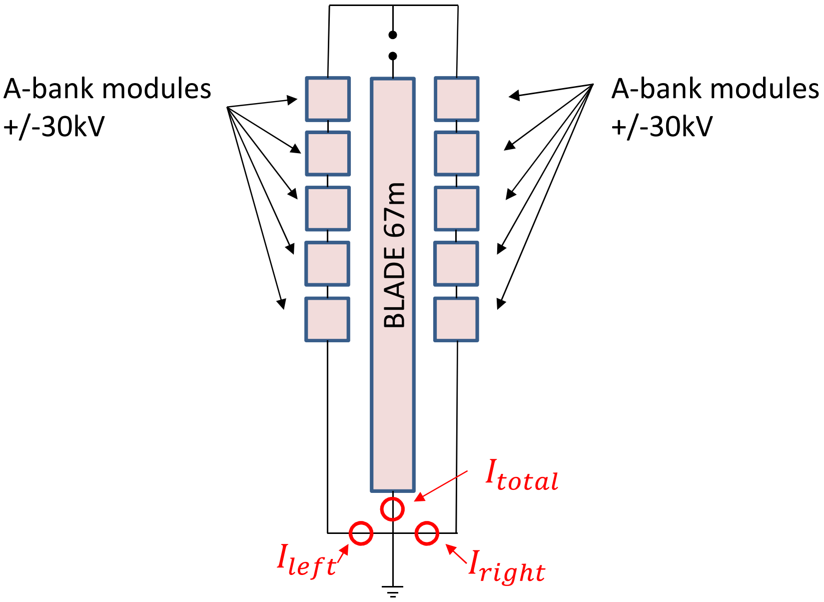

Figure 5.53: Structural overview of the A-bank full-scale demonstration test in Aalborg with indicated current measurement positions.

During the full-scale testing in Blæst, each A-bank module was charged to a voltage of $U_0 = \pm 30kV$ at a pressure level of $p = 0.69bar$ above atmospheric pressure, instead of the rated $U_0 = \pm 100kV$. There were three reasons for the reduced voltage for the demonstration test. First, the budget and time limitations of the project did not allow to build an optimized return cage for the blade. The current return path was distributed in the vicinity of the ground rather than at the exterior of the blade. The resulting circuit inductance of the demonstration test was $L = 120\mu H$. Due to this reason, a current impulse with the targeted current properties as defined by Section 2.3, was not realistic for this test. For future testing, a return-cage optimized to the blade perimeter must be installed in order to lower the inductance of the circuit. Second, as discussed in Section 5.4.1.3, the spark gap flashover characteristics of the A-bank varied distinctly from the expected performance. The maximum blocking voltage which could have been achieved is $U_0 = \pm 60kV$ with a gap pressure of $60PSI$. This pressure level, however, would stress the control components to the operational limit. Contact with the supplier of the gaps was established and there is an ongoing debate how to establish the flashover characteristics of the spark gap as presented in the datasheet. Third, the high current test was attended by a selected audience from the industry and safety considerations were first priority.

The performance of three measured current impulses created with the ELITE high current impulse generator is further discussed. Current measurements were taken from the two branches and the total current through the DUT as indicated in Figure 5.53. Besides the measurements, a circuit simulation of the A-bank with ten modules was performed in order to cross-correlate measurements and simulation. The circuit diagram can be found in Appendix C. It incorporates the stray parameters determined for single modules as well as the current dependent arc resistance as previously discussed in Section 5.4.1.

The expected time to peak T_p of the current with a test load of $L = 120\mu H$ and a generator capacitance of $C = 1.5\mu F$ is:

$$T_p = \frac{\pi}{2}\sqrt{LC} = \frac{\pi}{2}\sqrt{120uH * 1.5uF} = 21.1us \tag{5.37}$$

By utilizing equation 5.16, the expected peak current $I_p = 33.3kA$ can be calculated.

Figure 5.54 shows a current waveform where both branches trigger within the same microsecond. As expected, the total current is peaking after $21\mu s$ with a magnitude of $32.2kA$. Interestingly, the current in the two branches increases with a different slope where the left branch reacts faster than the right branch. Compared to the simulation of the left branch, the measured time to peak is even faster. One possible explanation is that the left side triggered a few hundred nanoseconds before the right side. In this time, the active impulse generator capacitance is only $C = 0.75\mu F$, leading to a rise time of $14.9\mu s$. By the time the right side starts conducting, the current rise-time is already dominated by the smaller capacitance of the left side. The rise-time of the right current is delayed to an extend that the total current reaches the expected current waveshape with an amplitude of $33.3kA$ and a rise-time of $21\mu s$.

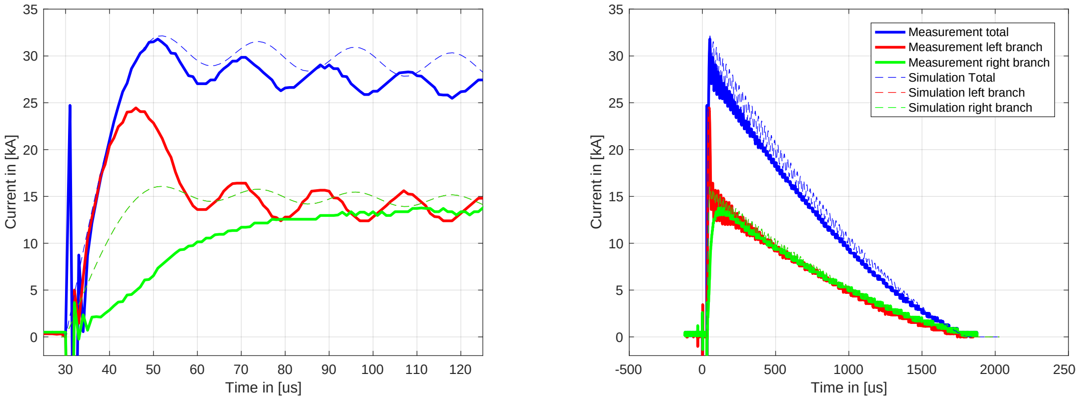

(a) Timeframe: $t = 25 : 125\mu s$ (b) Timeframe: $t = -500 : 2500\mu s$

Figure 5.54: Current waveforms of simultaneous triggering of two parallel branches with five series connected A-bank modules.

From the comparison between measurements and simulation, the arc resistance in the gaps can be determined. Following the style of the arc resistance equation of Stokes (See equation 5.21, an additional factor of $k = 5$ need to be included in order to align the current waveforms.

Stokes:

$$R(t) = \frac{20 + 0.534 * k * Z_g}{I_{arc}^{0.88}} \tag{5.38}$$

With this factor, the arc resistance in the A-bank is 4.4 times higher compared to the Stokes equation. The reason for the increase of resistance is the increased pressure in the gap and the variation in the type of gas. A comparison between the resistance equation of Stokes and the determined curve is illustrated in Figure 5.55. The increased arc resistance is expected to reduce the overall charge and specific energy in the test sample by $5 - 30\%$ compared to the expected output, as depicted in Figure 5.26 and 5.27. However, it is also estimated that this arc resistance characteristic varies with different pressure levels. Therefore, it is difficult to predict the amount of energy reduction. Arc resistance should be determined with varying pressure levels in future tests.

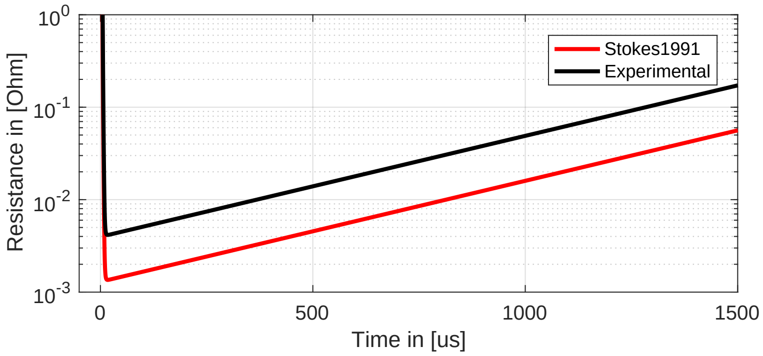

Figure 5.55: Comparison between arc resistance by Stokes and experimentally determined.

There is a special case that needs to be considered if the spark gaps of both branches do not ignite within the same microsecond.

As previously discussed in Section 5.4.1.3, if the parallel strings are not separated by an individual spark gap, as soon as one string flashes over a little earlier than the other, the voltage across the inactive spark gaps of the second string is reduced to half the voltage.

As a result, even though the trigger generator is firing, the second branch is not able to firing until the voltage recovers after one to three LC periods. Figure 5.56 and 5.57 show measurements and simulations of a delayed firing of the second branch of $\Delta t = 16\mu s$ and $\Delta t = 42\mu s$, respectively.

This effect increases substantially the rise-times of the current, whereas peak current, charge, and specific energy are only slightly affected. Another negative impact of this delayed triggering is that the current is distributed unequally between the branches. The diodes in one side need to conduct substantially more current compared to the other side. This is unproblematic for low peak currents; however, if a current impulse of $10\frac{MJ}{\Omega}$ is conducted, the diodes are close to their rated fusing currents of $12.5\frac{MJ}{\Omega}$.

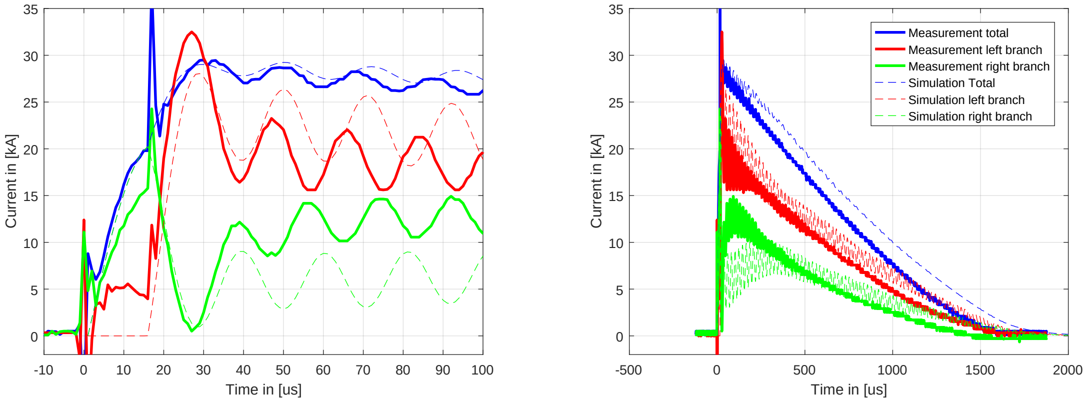

(a) Timeframe: $t = -10 : 100\mu s$ (b) Timeframe: $t = -500 : 2000\mu s$

Figure 5.56: Current waveforms with a trigger delay of $\Delta t = 16\mu s$ of two parallel branches with five series connected A-bank modules.

In both cases, the right branch triggers first and the left branch triggers with a delay of Δt seconds. In both figures, there is a $5kA$ DC current signal from the left branch before the firing which is most likely electrical noise in the measurement signal.

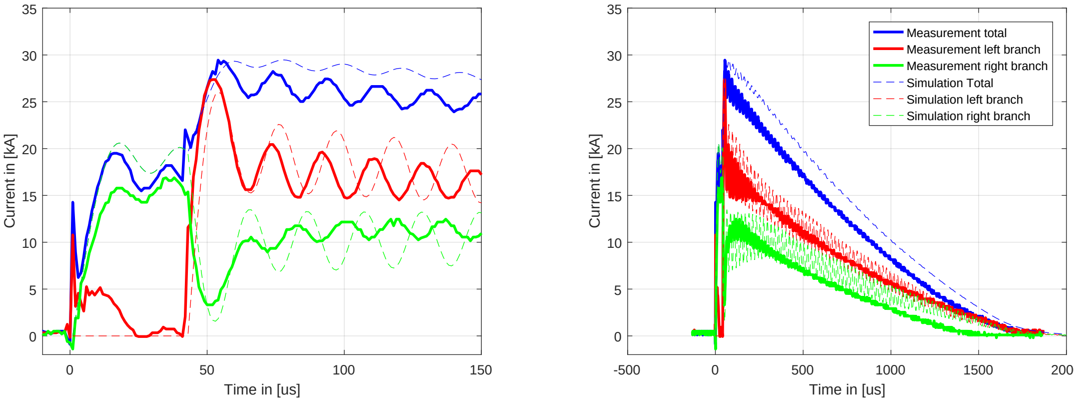

(a) Timeframe: $t = -10 : 150\mu s$

(b) $t = -500 : 2000\mu s$

Figure 5.57: Current waveforms with a trigger delay of $\Delta t = 42\mu s$ of two parallel branches with five series connected A-bank modules.

In the ELITE demonstration test, the parallel strings were not separated by individual spark gaps but the output of both strings were connected together and separated to the DUT by one common spark gap, as illustrated by Figure 5.53. In order to avoid the unequal firing depicted in Figure 5.56 and 5.57, it is highly recommended to isolate each parallel string with an individual spark gap.

5.7 The future of testing: Combined impulse

At this point, a brief look into the future of high current testing for lightning verification purposes shall be performed. In the previous chapters, three separate high current impulse generators were introduced, each of them designed to create a characteristic current component of a real lightning flash. All three generators were physically built and are ready to test the individual current components.

In future applications, there is also the option to connect all three test generators together in order to perform a combined test impulse. An illustration of a combined test generator with A, B/C, and D-bank is depicted in Figure 5.58. All generators are controlled via the same ELITE reference module. A current measurement at the down conductor of the DUT enables the sequencing of the individual banks. For instance, it would be possible to represent the current waveform of a typical downward lightning flash. At first, the A-bank initiates the flash with a high current impulse of several hundred kiloamperes and a rise-time of several tens of microseconds, representing the first return-stroke. After the current magnitude in the DUT is lower than $I(t) = 2kA$, the B/C-bank starts operating and creates a continuous current impulse of several hundreds of milliseconds. Finally the D-bank impulse is triggered which represents the subsequent return-stroke sequence. On the other hand, also a typical upward lightning flash could be created. In this sequence, the B/C-bank initiates the current sequence, representing the initial continuous current of an upward lightning discharge. Then, either A- or D-bank could be fired in order to create subsequent current impulses with different current magnitude and rise-times.

In such a test, a careful instigation of the return-path would need to be performed in order to connect all banks with the lowest possible stray inductance. Especially the incorporation of the D-bank is only useful for low inductance test circuits.

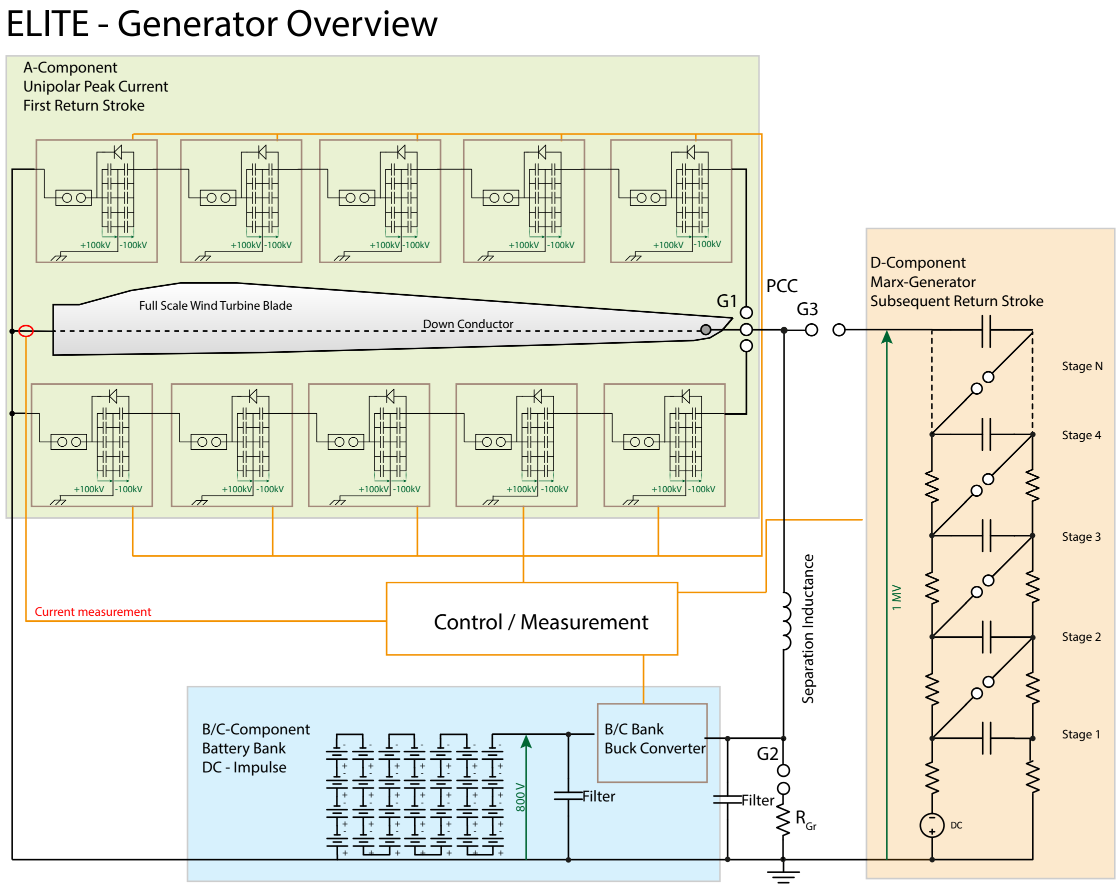

Figure 5.58: Conceptual overview of the novel ELITE generator for combined impulse current testing.

The most challenging part of a combined current impulse test is to protect the individual impulse generators from the current and voltage impulses of the other banks. At this point, some considerations regarding the practical implementation are given.

First of all, there are three different spark gaps $G_1 - G_3$ (apart from the A-bank gaps) which are necessary for the harmonized operation of the impulse generators. The spark gaps are adjusted to the following flashover voltage (The distance depends on the electrode geometry of the gaps):

1. G_1: The electrodes of G_1 are adjusted to a flashover voltage of $110kV$.
2. G_2: The electrodes of G_2 are adjusted to a flashover voltage of $0.9kV$.
3. G_3: The electrodes of G_3 are adjusted to a flashover voltage of $800kV$.

The A- and D-bank are characterized by a total discharge voltage of up to $U_0 = N_S * 0.2MV$ and $U_0 = 1.0MV$, respectively. The maximum voltage over the DUT is determined by the sum of stray inductance of the active impulse generator branch (A- or D-bank) and the stray inductance of the load. In case of the A-bank, if it is assumed that the stray inductance of the impulse generators are equally distributed to the load, the voltage across the DUT can be calculated according to Equation 5.31. The highest expected voltage at the Point of common coupling (PCC) should not exceed a value of $700kV$ if the trigger impulse voltage is $U_0 = 1MV$. This high voltage magnitude is in particular dangerous for the B/C-bank which is operating at a DC voltage of $800V$.

A large separation inductance ($L \approx 10mH$) is necessary in order to protect the B/C-bank from high voltage on the terminals. As soon as a fast current impulse is triggered on the blade, the voltage rises across the separation inductance. The spark gap G_2 initiates a discharge at $0.9kV$. The current through the spark gap is limited during the fast current components by the large separation inductance and during the low frequency tail part of the impulse by the grounding resistor $R_{GR} \approx 10\Omega$. The resistor would need to be selected in order to endure a high impulse power. The approximate current through R_{GR} during A-bank firing of a $1MV$ peak voltage is estimated to a maximum of $700A$ at a voltage of $7kV$ as can be seen in Figure 5.59. A water resistor or a parallel array of high power wirewound cement coated resistor could be appropriate for the purpose.

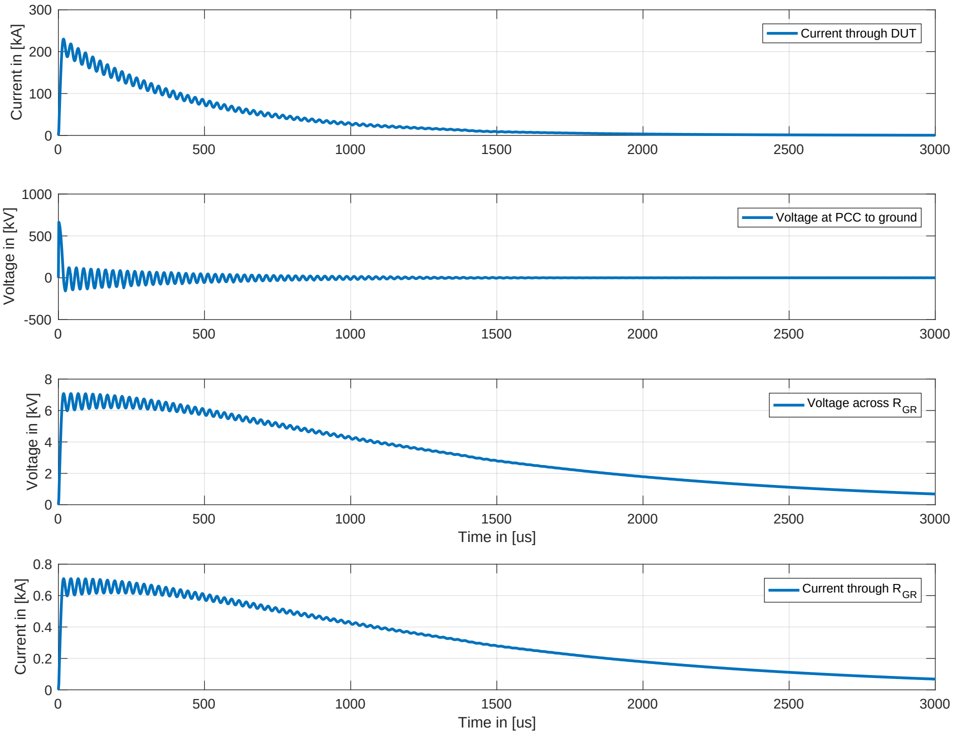

Figure 5.59: Current through DUT, voltage at PCC, voltage across R_{GR}, and current through R_{GR}

.

Transient over-voltages are expected at the time when G_2 is extinguished due to the energy trapped in the large separation inductance. One possibility to handle these oscillations is given by applying a RC filter at the output of the B/C-bank. Another option would be to open the IGBT of the buck converter, use the transient energy to charge the batteries, and start the switching sequence of the DC current component through the DUT before the arc is extinguished.

If the energy trapped of the separation inductance causes too high voltage transients, another option would be to replace the inductance by a spring/pneumatic controlled mechanical switch which physically separates the B/C bank from the test setup.

As can be seen, a combined current impulse imposes several challenges to the executing application engineer. Eventually, the demand of the industry will determine if such a test is requested in the future. From an academic point of view, a study of the implications of combined testing would be most desirable.

6 CONCLUSIONS

The outcome of this thesis contributes with new knowledge regarding the real lightning exposure of wind turbines which can further increases the reliability and performance of wind turbines in the future. The findings are implemented in a physical test system that can inject realistic current impulses of first return-strokes and continuous currents in full-scale wind turbine components. Current impulses resembling subsequent strokes currents can be injected in partial wind turbine components since the inductance of full-scale items limits the peak and rise-time of the current. The project was funded by the public Danish foundation EUDP and the private corporation GLPS.

6.1 Current parameters of lightning discharges

The first step towards a high current impulse generator for validation of realistic lightning exposure was to determine the current parameters the system needs to be able to create. In order to approach a solution, various data sources of lightning discharges to tall structures and wind turbines were reviewed. It is found that wind turbines are exposed to both downward and upward lightning. The properties of the lightning current waveform and the current derivatives of both types vary distinctly.

The current waveform of downward lightning flashes is composed out of the first return-stroke, possibly followed by a continuous current and/or multiple subsequent return-strokes. So far, there are no current measurement campaigns performed on wind turbines which published current parameters of downward lightning flashes. Due to this reason, current measurements on tall towers are used to justify the current parameters. It is found that up till today, the most comprehensive dataset of downward lightning flashes was measured by Berger in the 1970s [12], including current components of positive and negative first return-strokes, as well as subsequent return-strokes. Lightning protection standards such as IEC 61400-24 [24] base their test values for high current testing of positive first return-strokes on the highest 5% of measured lightning currents by Berger. Since there is only one comprehensive dataset of downward lightning flashes, it is difficult to argue that current parameters should be different from the already defined values. It is therefore concluded that current parameters of first return-strokes from downward lightning flashes are appropriately represented in the lightning protection standard IEC 61400-24 [24] and the same values are adopted for the new impulse system.

The current waveform of upward lightning flashes are composed out of an initial continuous current, possibly followed by a return-stroke sequences. They can be separated into self-initiated and other-triggered upward lightning discharges [44] and sorted whether they are characterized with pulses, return-strokes, or only with initial continuous currents [14]. Comprehensive current measurements of upward lightning discharges were performed on wind turbines during a five year measurement campaign in Japan [9]. A direct comparison between Japanese measurements and measurements on the Austrian Gaisberg tower indicates that charge of negative upward lightning flashes are in fact comparable. The Gaisberg tower reports 50% and 5% values from the cumulative frequency distribution of charge of $38C$ and $300C$ [14], respectively, whereas measurements of negative upward lightning flashes measured on Japanese wind turbines report values of $35C$ and $200C$ [10]. The difference between European and Japanese winter thunderstorms are the high ratio of positive and bipolar flashes in Japan which are characterized by statistically higher values of specific energy [10]. Winter thunderstorms in Europe and Japan are capable to lower extensive amount of charge towards the ground. As an example, within one year, the Gaisberg tower lowered $8800C$ to ground [66]. A wind turbine constructed in a similar environment is expected to be heavily affected by those quantities of charge.

Due to these reasons, it is concluded that both downward and upward lightning pose a threat to the reliability of wind turbines. In terms of current derivatives, downward lightning is characterized by higher amplitudes of peak current and specific energy, whereas upward lightning is potentially harmful due to extensive accumulated amount of charge which can be lowered to the ground within the operational time of a wind turbine.

In order to verify the effects of both flash types, a realistic lightning exposure system needs to be able to create the current waveform of both downward and upward lightning.

For an overview of the proposed current parameters and further justification for the requirements of the novel lightning exposure system, please refer to the conclusion on current parameters for the new lightning exposure system in Section 2.3.

6.2 Lightning exposure to wind turbines

The second focus of this work was to analyze which factors determine how often a wind turbine is struck by lightning and which type of lightning attaches to the wind turbines. Furthermore, the consequences for the Lightning protection system of a wind turbine are discussed if frequent lightning flashes attach to the turbine.

Lightning location system (LLS) data are a valuable tool in order to investigate the movement of thunderstorms and discharge pattern around wind turbines. There are different LLS technologies available, each of them characterized by individual performance indicators. It is found that mid-range LLS such as the LINET or the NLDN are the most suitable tool to verify lightning activity on wind turbines. Typically, they are able to detect a fraction of upward lightning discharges [50].

The amount of downward lightning attachments a wind turbine receives depends mainly on the convective thunderstorm activity of the area. LLS data of summer thunderstorms shows that the lightning pattern are typically spread within the observation area and are not focused around the wind turbines. The striking distance of downward lightning depends on the perspective peak current of the first return-stroke, the height of the structure, and the lateral position of the downward leader [69]. Downward lightning can be detected by LLS with high reliability.

The factors that determine the amount of upward lightning discharges to a wind turbine are more complex. Summer thunderstorms mainly initate other-triggered upward lightning discharges [23][49], whereas winter thunderstorms trigger both self-initiated and other-triggered lightning events [44]. Four factors are observed to increase the amount of upward lightning discharges experienced by a wind turbine. The first relation was established by Eriksson [70] which utilizes the height of a structure to calculate the percentage of upward lightning flashes a structure receives, the second is the topography of a wind power plant [45] [71], the third are the meteorological properties of a site [10][72][73] [74] , and the fourth, the ground flash density [46]. All four factors are, to some level, interconnected and determine whether a structure is exposed to upward lightning or not.

Particularly the meteorological parameters of a site seem deterministic for frequent upward lightning attachment on tall structures as documented by Diendorfer [66] and Ishii [10]. Due to this reason, a meteorological analysis of five wind power plants was performed and the meteorological characteristics of summer and winter thunderstorms were further defined.

The particular threat of a winter thunderstorm can be illustrated with LLS data. Even though those thunderstorms generate less frequent lightning discharges compared to summer thunderstorms [104] [105], each flash attaches on tall structures where the electric field is highest. Often the same wind turbine or tower is struck multiple times. Summer thunderstorms, on the other hand, show distributed lightning pattern in the entire observation area and the potential threat is rather distributed.

Based on the gathering of meteorological parameters of cold season thunderstorms, a map was developed utilizing data from radio soundings which indicates areas where self-initiated cold season lightning may affect wind power plants.

A dedicated section to winter lightning in Japan elaborates on the special lightning environment of the country. Two particular studies are included in this section. The first relates the amount of LLS detection to the current parameters of a particular storm type. There is a tendency that more active winter thunderstorms are also characterized by higher current parameters. The second study shows the lightning attachment position and duration of 172 upward lightning discharges on rotating wind turbines. It is shown that upward lightning attaches mostly on vertical blades, however, also horizontal attachments are reported. A correlation was made that attachment to horizontal blades are predominantly triggered by nearby lightning activity. Finally, the last section addresses the question why potentially frequent damages are reported in the winter lightning areas of Japan and how to improve the reliability in those areas.

6.3 On the impact of air flow to electric field altering space charge

The third focus of this thesis was to determine the impact of air flow to the distribution of space charges created by ionization of air due to the electric field of a thundercloud. One of the reasons to investigate the phenomena is to determine if current measurement of lightning discharges performed on towers are representative for wind turbines. Furthermore, since air flow constantly removes generated space charges on the blades, a potential space charge cloud can not accumulate above the structure. A shielding effect is not established and the wind turbine is theoretically more exposed to lightning attachment.

After the relevant literature regarding ionization and corona modes was reviewed, a 2D Finite Element Analysis simulation was developed which evaluated the impact of the space charges to the electric field around a grounded conductor when affected by an air flow of $v = 50\frac{m}{s}$. The results showed that the propagation of space charges are in fact heavily dependent on the ambient wind speed and that the electric field around the conductor is substantially different between the scenario. When no air flow is applied, the space charge is accumulating around the grounded conductor and travels slowly towards the high voltage potential (cloud), whereas the air flow tilts the space charges towards the outlet of the air domain in the scenario with air flow. The electric field in the vicinity of the grounded conductor is lower in the scenario without air flow compared to scenario with air flow. Potentially, self-initiated upward lightning discharges may be inhibited by a reduced electric field.

Two laboratory experiments were performed in an attempt to verify the shielding effect of the space charge and the impact of air flow. The first experiment evaluated the effect of air flow to Partial discharge/s patterns on a needle-plane electrode configuration with a distance of $20cm$. It was found that the positive polarity is more affected by air flow compared to the negative polarity. A positive corona discharge may be excited, suppressed, or visually tilted depending on the magnitude of air flow. A negative corona discharge, on the other hand, may be excited by air flow but is visually unaffected by it. In the second experiment, space charges were created by means of a $100kV$ high voltage DC source and breakdown experiments were performed with a $800kV$ Marx generator. Breakdown of the gap was initiated at reduced median flashover voltages when no air flow was applied and hence no space charge was removed from the gap. As soon as the fan was turned-on and the space charge was affected by the air flow, the median flashover voltage increased. In other words, the space charge reduced the median flashover voltage, whereas a removal of space charges increased the median flashover voltage. This is the opposite effect as predicted by the model. The reason for this observations is most likely attributed due to the small gap distance in the laboratory experiment. It is estimated that much larger distances and voltages are necessary in order to verify the shielding effect due to inhibited leader development. A thorough discussion regarding the results from the FEA simulation and the laboratory results can be found in Section 4.6.

6.4 ELITE - A modular high current impulse generator

In the final chapter of this thesis, the knowledge obtained the from preceding chapters is transformed into a physical impulse generator for realistic lightning exposure on full-scale wind turbine components such as blades and nacelles. The chapter includes solutions regarding the theoretical and practical challenges related to the generator design.

The chapter is initialized by reviewing the requirements of future testing expected from the industry. Blades exceeding 100 meters in length and nacelles of 10 megawatt are expected to be in the market within the next 10 years. Lightning protection solutions are likely to incorporate more semi-conductive carbon fiber composites in order to reduce weight.

The next step led to the characterization of the impedance from full-scale DUTs. Wind turbine blades are expected to exhibit the highest load since the extended physical dimensions increase the stray inductance. After a review of lightning protection solutions for blades, analytic and computational methods to determine the stray resistance and inductance of a DUT are introduced. Resistance and inductance values per meter are calculated for different lightning protection solutions. Furthermore, the possibility to reduce stray-inductance of the circuit is highlighted by optimizing the location and the number of return-cage conductors.

The requirements on the test systems in terms of current derivatives were previously defined in Section 2. It was stated that a realistic lightning exposure system needs to be able to create a first return-stroke sequence with an amplitude of $I_p = 200kA$, a rise-time of $T_f = 10us$, a charge of $100C$ and a specific energy of $10\frac{MJ}{\Omega}$; a DC current component with a amplitude of up to $I_P = 2kA$ and a duration of up to one second; and a subsequent return-stroke with a current amplitude of $I_p = 30kA$ and a current rise-time of $T_f = 0.25us$ (rounded from $T_f = 0.22us$). In order to reach these, parameters a section about the fundamental limitations of high current testing discusses if these values are realistic to be injected into full-scale wind turbines components. First return-stroke currents are likely to be injected into a full-scale component; however, the requirements to inject subsequent return-strokes in full-scale components are beyond the budget of this project.

As can be seen, each stroke component is characterized by distinct current derivatives. Therefore, it was decided to separate the exposure system into three different impulse generators.

- The A-Bank, responsible to inject the current impulse representing the first return-stroke
- The B/C-Bank, responsible to inject the current impulse representing the DC current component
- The D-Bank, responsible to inject the current impulse representing the subsequent return-stroke (limited peak current and rise-time, depending on the inductance of the DUT)

The A-Bank consists of 12 individual high current impulse generators, each equipped with a capacitor bank, a triggerable spark gap, a diode crow bar, a grounding system, and a control cabinet. Each unit is characterized by a capacitance of $C = 3.75\mu F$, a maximum charging voltage of $U_0 = \pm 100kV$, and a maximum discharge current of $I_p = 125kA$. The modules can be connected in series or parallel connection, leading to generator setup with a total resulting discharge voltage of up to $U_0 = 2.4MV$ and a capacitance of $C = 0.3125\mu F$ with a series connection of 12 modules. 12 parallel connected modules lead a total resulting discharge voltage of up to $U_0 = 200kV$ with a capacitance of $C = 45\mu F$. A connection of multiple parallel connected modules allows to create high peak currents, whereas a series connection creates a shorter rise-time duration of the current. The performance characteristics for each possible configuration possibility was calculated.

The B/C-Bank is a DC/DC buck converter which controls the voltage from a battery bank over the DUT. It employs an IGBT, a snubber circuit, a freewheeling diode, and a filter capacitor. DC currents up to 2kA are able to be conducted.

The D-Bank is a typical Marx-type high voltage impulse generator with 10 capacitor stages of each $C = 100nF$ at a maximum charging voltage of $U_0 = 100kV$ per stage. The maximum current output is $I_p = 20kA$ with shorted terminals. The capacitors are charged in parallel and discharged in series.

Two challenges regarding the A-Bank were discussed in particular. The first relates to the flashover characteristic of the spark gap which only could be used to block 60% of the nominal blocking voltage. The second relates to difficulties regarding the triggering of parallel modules. The reasons for the issues were discussed for both cases and recommendations are provided in order to solve the issues.

Finally, the performance of each individual lightning impulse bank was documented and the functionality of the A-bank was demonstrated on a 67 meter full-scale wind turbine blade.

Each impulse generator (A-Bank, B/C-Bank, D-Bank) can be used to verify the effects of one particular stroke of the lightning current individually, or as proposed in the last section, connected together, in order to make a combined lightning current impulse as measured in the field.

Further information regarding design, challenges during prototyping, and control of the generator banks are highlighted in Chapter 5.

6.5 Towards improved testing procedures to enhance wind turbine reliability

In order to enhance the reliability of wind turbines, it is crucial to know the real properties of lightning discharges. Downward and upward lightning flashes are characterized by different current wave shapes which also affect the resulting damage modes for the LPS. Even though current derivatives of upward lightning flashes are lower compared to downward lightning flashes, the possible high attachment frequency of upward lightning in certain regions of the world can lead to frequent damages as a result of accumulated charge transfer. The high exposure needs to be accounted for in the LPS design of a wind turbine blade.

In order to test the effect of both downward and upward lightning discharges, a new lightning test system was developed which enables wind turbine manufacturers to verify their lightning protection solution in the laboratory. The generator was designed to perform full-scale tests of wind turbine components to further improve reliability of wind turbines. The system is based on the concept of modularity and can be extended if larger test subjects are required to be tested in the future.

The flexible design of the ELITE impulse generator and the possibility to interconnect the individual banks allow the concept to set a new standard within the lightning testing industry.

7 FUTURE WORK

This section elaborates on related issues of this thesis that needs further attention by the next generation of researchers and private companies.

The following points can be named:

- The lack of lightning data directly measured on wind turbines is an issue in order to classify the real risk of lightning flashes to wind turbines. Recently, GLPS introduced a commercial lightning current measurement system (Lightning Key Data System (LKDS)) that records the current waveform through each blade by means of three independent Rogowski coils. Since wind turbines are distributed around the world and operate in various meteorological conditions, the system could potentially establish the worlds largest lightning current database.
- Meteorological parameters that define winter lightning should be reviewed. Radio sounding data as source for winter lightning tracking may be a too coarse tool with 12 hours between the soundings and lateral distances of several hundred kilometers between two radio sounding stations. More meteorological expertise would be beneficial to evaluate the winter lightning properties. A meteorological model that uses recalculated weather data as an input and projects them to a smaller grid size could enhance the validity of the results.
- The leader inhibiting effect of space charge due to a field reduction around the pointy electrode should be quantified in a laboratory.
- A validation of a combined test of the A-Bank, B/C-Bank, and D-Bank is desired and to create a realistic lightning current impulse as it is observed in downward and upward lightning.
- This thesis considered the maximum current parameters a realistic lightning current exposure system needs to deliver, however, it does not answer the question how often a specific current component should be tested in order to account for realistic exposure. Is the methodology of testing representative for the real lightning exposure of wind turbines? Are a few lightning discharges of $200kA$, $10/350\mu s$ representative for frequent downward lightning exposure with a median peak current of $30kA$. Regarding upward lightning, the question arises how the variation of exposure among several sites may be accounted in the testing procedure recommendations of the IEC 61400-24 standard.

REFERENCES

[1] ADOPTION OF THE PARIS AGREEMENT - Paris Agreement. Technical report, United Nations, Paris, 2015. URL `http://unfccc.int/files/essential_background/convention/application/pdf/english_paris_agreement.pdf`.

[2] Report of the Conference of the Parties on its twenty-first session, held in Paris from 30 November to 13 December 2015 Part one: Proceedings. Technical report, United Nations, 2015. URL `http://unfccc.int/resource/docs/2015/cop21/eng/10.pdf#page=30`.

[3] L. Fried. Global Wind Statistics 2016. Technical report, Global Wind Energy Council, 2017. URL `http://www.gwec.net/wp-content/uploads/vip/GWEC_PRstats2016_EN_WEB.pdf`.

[4] GCube. GCube Insurance Services » Top 10 Causes for Turbine Failure. URL `http://www.gcube-insurance.com/en/uncategorized/top-10-causes-for-turbine-failure/`.

[5] F. Rachidi, M. Rubinstein, J. Montanyà, J. Bermúdez, R. R. Sola, G. Solà, and N. Korovkin. A Review of Current Issues in Lightning Protection. *IEEE Transactions on Industrial Electronics*, 55(6):2489–2496, 2008.

[6] G. Diendorfer. On the risk of upward lightning initiated from wind turbines. *2015 IEEE 15th International Conference on Environment and Electrical Engineering, EEEIC 2015 - Conference Proceedings*, pages 872–876, 2015. doi: 10.1109/EEEIC.2015.7165278.

[7] V. Peesapati, I. Cotton, T. Sorensen, T. Krogh, and N. Kokkinos. Lightning protection of wind turbines – a comparison of measured data with required protection levels. *IET Renewable Power Generation*, 5(1):48, 2011. ISSN 17521416. doi: 10.1049/iet-rpg.2008.0107.

[8] S.F. Madsen and H.V. Erichsen. Numerical model to determine lightning attachment point distributions on wind turbines according to the revised IEC 61400-24. In *International Conference on Lightning and Static Electricity (ICOLSE)*, pages 1–13, 2009.

[9] NEDO report 20150000000080, "Research and Development of Next- Generation Wind Power Generation Technology for Technology Corresponding to Natural Environment etc. for Measures of Lightning Protection (FY2008-FY2012)," Annual Report of NEDO, Japan,. Technical report, 2015.

[10] M. Ishii. NEDO R & D Project for Measures of Lightning Protection of Wind Turbines in Japan. In *International Symposium on Lightning Protection (SIPDA)*, 2015.

[11] K. Berger. Methoden und Resultate der Blitzforschung auf dem Monte San Salvatore bei Lugano in den Jahren 1963-1971. *Bulletin der Schweizerischen Vereinigung fur Elektrotechniker*, 63(24):1403–1422, 1972.

[12] K Berger, R.B Anderson, and H. Kroninger. PARAMETERS 0F LIGHTNING FLASHES. *Electra*, 1(No. 41):23–37, 1975.

[13] K. Berger. Blitzstrom - Parameter von Aufwartsblitzen. *Bull. Schweiz. Elektrotech.*, 69:353–360, 1978.

[14] G. Diendorfer, H. Pichler, and M. Mair. Some parameters of negative upward-initiated lightning to the gaisberg tower (2000-2007). *IEEE Transactions on Electromagnetic Compatibility*, 51(3 PART 1):443–452, 2009. ISSN 00189375. doi: 10.1109/TEMC.2009.2021616.

[15] F. Heidler, M. Manhardt, and K. Stimper. Upward positive lightning measured at the Peissenberg Tower, Germany. *2013 International Symposium on Lightning Protection, SIPDA 2013*, pages 82–90, 2013. doi: 10.1109/SIPDA.2013.6729214.

[16] C. Romero, F. Rachidi, M. Paolone, and M. Rubinstein. Statistical distributions of lightning currents associated with upward negative flashes based on the data collected at the Saentis (EMC) Tower in 2010 and 2011. *IEEE Transactions on Power Delivery*, 28(3):1804–1812, 2013. ISSN 08858977. doi: 10.1109/TPWRD.2013.2254727.

[17] K. L. Cummins and M. J. Murphy. An Overview of Lightning Locating Systems : History , Techniques , and Data Uses , With an In-Depth Look at the U.S. NLDN. *IEEE Transactions on Electromagnetic Compatibility*, 51(3):499–518, 2009.

[18] A. Nag, M. J. Murphy, W. Schulz, and K. L. Cummins. Lightning location systems: Insights on characteristics and validation techniques. *Earth and Space Science*, (April):65–93, 2015. doi: 10.1002/2014EA000051.

[19] M. Saito, A. Sugita, and D. Natuno. Lightning Strokes Forming Hot Spots observed by LLS in Winter in Japan. In *International Conference on Lightning Protection (ICLP)*, pages 1–5, 2012. ISBN 9781467318976.

[20] V. March. Upward lightning observations on a wind turbine and its implications to environmental factor for risk assessment. In *Asia-Pacific International Conference on Lightning (APL), Nagoya, Japan*, pages 510–516, 2015.

[21] M. Saito and M. Ishii. Application of LLS to Detection of Winter Lightning Flashes Hitting Wind Turbines. In *33rd International Conference on Lightning Protection*, 2016.

[22] J. Schoene, M. A. Uman, M. Aurele, K. J. Rambo, J. E. Jerauld, and G. Schnetzer. Testing of the OBO Bettermann Peak Current Sensor System for Lawrence Livermore National Laboratory. Technical report, Lawrence Livermore National Laboratory, 2005.

[23] A. C. Garolera, K. L. Cummins, S. F. Madsen, J. Holbœ ll, and J. D. Myers. Multiple Lightning Discharges in Wind Turbines Associated With Nearby Cloud-to-Ground Lightning. *IEEE Transactions on Sustainable Energy*, 6(2): 526–533, 2015. ISSN 19493029. doi: 10.1109/TSTE.2015.2391013.

[24] IEC 61400-24. IEC 61400-24 - Wind turbines - Part 24: Lightning Protection ed1.0. Technical Report Edition 1.0, IEC, 2010.

[25] J. M. Tobias. Testing of ground conductors with artificially generated lightning current. *IEEE Transactions on Industry Applications*, 32(3):594–598, 1996. ISSN 00939994. doi: 10.1109/28.502171.

[26] P. L. Bellaschi. Lightning strokes in field and laboratory — III. *Electrical Engineering*, 60(12):1248–1256, 1941. ISSN 0016-0032. doi: http://dx.doi.org/10.1016/S0016-0032(40)90871-7.

[27] M. Iwata, T. Ohtaka, Y. Kuzuma, and Y. Goda. Development of a method of calculating the melting characteristics of opgw strands Due to DC arc simulating lightning strike. *IEEE Transactions on Power Delivery*, 28(3):1314–1321, 2013. ISSN 08858977. doi: 10.1109/TPWRD.2013.2260567.

[28] A. Kern. Simulation and measurement of melting effects on metal sheets caused by direct lightning strikes. In *International Aerospace and Ground Conference on Lightning and Static Electricity, Volume 1; 10 p*, pages 1–10, 1991.

[29] TC 88. IEC 61400-24 - Wind turbines - Part 24: Lightning Protection - Committee Draft 88/613/CD towards ed. 2.0. Technical Report 2, IEC, 2017.

[30] F.W Grover. *Inductance Calculations*. Dover Publications, Inc., 1973.

[31] A. C. Garolera, J. Holbœ ll, and S. F. Madsen. Lightning transient analysis in wind turbine blades. In *International Conference on Power Systems Transients (IPST)*, 2013.

[32] J. Montanya, O. Van der Velde, and E. Williams. Lightning discharges produced by wind turbines. *Journal of Geophysical Research*, 119:1455–1462, 2014. ISSN 0148-0227. doi: 10.1002/2013JD020225.Received.

[33] V. A. Rakov and M. A. Uman. *Lightning: Physics and Effects*. Cambridge University Press, 2003.

[34] E. R. Jayaratne, C. P. R. Saunders, and J. Hallett. Laboratory studies of the charging of soft hail during ice crystal interactions. *Quarterly Journal of the Royal Meteorological Society*, 109:609–630, 1983. ISSN 00359009. doi: 10.1002/qj.49710946111.

[35] V. Cooray. *The lightning flash; 2nd ed.* IET power and energy series. The Institution of Engineering and Technology, Stevenage, 2014.

[36] F.H Kreuger. *High Voltage Engineering*, volume II. Delft University Press, Delft, 1991. ISBN 9062755615.

[37] I. Gallimberti. The mechanism of the long spark formation. *Le Journal de Physique Colloques*, 40(C7):C7–193–C7–250, 1979. ISSN 0449-1947. doi: 10.1051/jphyscol:19797440.

[38] L. Arevalo and V. Cooray. Streamer to leader transition criteria for propagation of long sparks and lightning leaders. In *International Conference on Lightning Protection, (ICLP)*, pages 480–483, 2014. ISBN 9781479935444. doi: 10.1109/ICLP.2014.6973171.

[39] R. E. Orville. Spectrum of the lightning stepped leader. *Journal of Geophysical Research*, 73(22):6999–7008, 1968. ISSN 2156-2202. doi: 10.1029/JB073i022p06999.

[40] C. Perera, M. Fernando, and V. Cooray. Length of the Final Jump/Upward Connecting Leader of the Lightning Flashes Striking the Sea. *Lightning Protection (ICLP), 2012 International Conference on*, 2012.

[41] V. Cooray. The stepping process of the negative lightning stepped leaders. In *2014 International Conference on Lightning Protection (ICLP), Shanghai, China The*, pages 19–21, 2014. ISBN 9781479935444.

[42] M. Ishii, M. Saito, M. Toru, D. Tanaka, S. Takatoshi, A. Asakawa, H. Motoyama, T. Sonehara, Y. Suzuhigashi, and H. Taguchi. Observation of Downward and Upward Lightning Flashes at 634-m Tower. In *International Conference on Atmospheric Electricity*, number 1, pages 15–20, 2014.

[43] M. F. Saba, W. Schulz, T. A. Warner, L. Z. S. Campos, R. Orville, E. P. Krider, K. L. Cummins, and C. Schumann. High-speed video observations of positive lightning flashes. *JOURNAL OF GEOPHYSICAL RESEARCH*, 115(D24201):1–9, 2010. ISSN 01480227. doi: 10.1109/ICLP.2010.7845879.

[44] D. Wang, N. Takagi, T. Watanabe, H. Sakurano, and M. Hashimoto. Observed characteristics of upward leaders that are initiated from a windmill and its lightning protection tower. *Geophysical Research Letters*, 35(2):19–23, 2008. ISSN 00948276. doi: 10.1029/2007GL032136.

[45] A. Garolera, S. Vogel, J. López, S. F. Madsen, and K. Bertelsen. EFFECT OF LOCAL TOPOGRAPHY ON LIGHTNING EXPOSURE OF WIND TURBINES. In *ICOLSE - International Conference on Lightning and Static Electricity*, pages 1–7, 2015.

[46] T. A. Warner, K. L. Cummins, and R. E. Orville. Upward lightning observations from towers in Rapid City , South Dakota and comparison with National Lightning Detection Network data , 2004 – 2010. *JOURNAL OF GEOPHYSICAL RESEARCH*, 117(D19109):2004–2010, 2012. doi: 10.1029/2012JD018346.

[47] P. Lalande, A. Boundiou-Clergerie, G. Bacchiega, and I. Gallimberti. Observations and modeling of lightning leaders. *Applied physics*, 3(1):1375–1392, 2002.

[48] M. Manhardt, F. Heidler, and K. Stimper. The electric field of negative upward lightning strikes at the Peissenberg tower, Germany. *2012 31st International*

Conference on Lightning Protection, ICLP 2012, (lCC), 2012. doi: 10.1109/ICLP.2012.6344205.

[49] F. Heidler, M. Manhardt, and K. Stimper. Self-initiated and other-triggered positive upward lightning measured at the Peissenberg Tower, Germany. In *4th International Symposium on Winter Lightning*, pages 1–6, 2017. ISBN 9781479935444. doi: 10.1109/ICLP.2014.6973113.

[50] G. Diendorfer, H. Pichler, and W. Schulz. LLS Detection of Upward Initiated Lightning Flashes. In *9th Asia-Pacific International Conference on Lightning*, pages 1–5, 2015.

[51] C. Romero, M. Rubinstein, F. Rachidi, M. Paolone, V. A Rakov, and D. Pavanello. Some characteristics of positive and bipolar lightning flashes recorded on the S{ä}ntis Tower in 2010 and 2011. *Lightning Protection (ICLP), 2012 International Conference on*, pages 1–5, 2012. doi: 10.1109/ICLP.2012.6344271.

[52] M. Azadifar, M. Paolone, D. Pavanello, F. Rachidi, V. A. Rakov, C. Romero, and M. Rubinstein. An Update on the Charaterictics of Positive Flashes Recorded on the Säntis Tower. (May 2010):494–498, 2014.

[53] T. Miki, T. Shindo, A. Asakawa, H. Motoyama, Y. Suzuhigashi, K. Fukuda, M. Ishii, and M. Chihara. Measurement of lightning currents at TOKYO SKYTREE and observation of electromagnetic radiation caused by strikes to the tower. In *31st International Conference on Lightning Protection, ICLP 2012*, pages 1–5, 2012. ISBN 9781467318976. doi: 10.1109/ICLP.2012.6344298.

[54] D. Tanaka, A. Asakawa, and H. Motoyama. Upward and Downward Lightning Observed at Tokyo Skytree Overall observation results of current waveform and charge transfer. In *International Conference on Lightning Protection (ICLP)*, number July, pages 1426–1431, 2014. ISBN 9781479935444.

[55] IEC 62305-1. IEC 62305-01 - Protection Against Lightning - General principles ed2.0. Technical report, 2013.

[56] Y. M. Hernández, K. Stimper, W. Zischank, and B. Lewke. An experimental approach of the effects of lightning currents on rotor blade tips of wind turbines. In *31st International Conference on Lightning Protection, ICLP*, 2012. ISBN 9781467318976. doi: 10.1109/ICLP.2012.6344367.

[57] M I Baranov and M A Nosenko. INFLUENCE OF THE THERMAL ACTION OF ARTIFICIALLY-INITIATED LIGHTNING CURRENT ON SPECIMENS OF THE METAL SKIN OF AN AIRCRAFT. *Journal of Engineering Physics and Thermophysics*, 82(5):972–980, 2009.

[58] Global lightning protection services - lightning key data system. `http://global-lightning.com/en/products/`. Accessed: 2017-07-03.

[59] V. a. Rakov. Lightning parameters for engineering applications. In *Asia-Pacific Symposium on Electromagnetic Compatibility*, number 1, pages 1120–1123, 2010. ISBN 9781424456215. doi: 10.1109/APEMC.2010.5475697.

[60] Cigre Wg C4.407. *Lightning parameters for engineering applications (TB 549)*. Number August. 2013. ISBN 9782858732449.

[61] R.B Anderson and A. J Eriksson. Lightning Parameters for Engineering Application. *Electra*, 1(No. 69):65 –102, 1980.

[62] S. Visacro. Statistical analysis of lightning current parameters: Measurements at Morro do Cachimbo Station. *Journal of Geophysical Research*, 109(D1):D01105, 2004. ISSN 0148-0227. doi: 10.1029/2003JD003662.

[63] J. Takami and S. Okabe. Observational results of lightning current on transmission towers. *IEEE Transactions on Power Delivery*, 22(1):547–556, 2007. ISSN 08858977. doi: 10.1109/TPWRD.2006.883006.

[64] M. Azadifar, F. Rachidi, M. Rubinstein, M. Paolone, and D. Pavanello. An update on experimental data obtained at the Santis Tower. In *2015 IEEE 15th International Conference on Environment and Electrical Engineering, EEEIC 2015 - Conference Proceedings*, number December 2013, pages 1009–1012, 2015. ISBN 9781479979936. doi: 10.1109/EEEIC.2015.7165302.

[65] D. R. Poelman, W. Schulz, G. Diendorfer, and M. Bernardi. European cloud-to-ground lightning characteristics. In *International Conference on Lightning Protection (ICLP)*, pages 1953–1958, 2014. ISBN 9781479935444. doi: 10.1109/ICLP.2014.6971989.

[66] G. Diendorfer. Review of seasonal variations in occurrence and some current parameters of lightning measured at the Gaisberg Tower. In *International Symposium on Winter Lightning*, pages 1–6, 2017.

[67] MeteoSwiss. Federal Office of Meteorology and Climatology. URL `http://www.meteoswiss.admin.ch`.

[68] V. Cooray, V. Rakov, and N. Theethayi. The lightning striking distance-Revisited. *Journal of Electrostatics*, 65(5-6 SPEC. ISS.):296–306, 2007. ISSN 03043886. doi: 10.1016/j.elstat.2006.09.008.

[69] M. Becerra, V. Cooray, and F. Roman. Lightning striking distance of complex structures. *Generation, Transmission & Distribution, IET*, 2(1):131–138, 2008. ISSN 17518687. doi: 10.1049/iet-gtd:20070099.

[70] A. J. Eriksson. The incidence of lightning strikes to power lines. *IEEE Transactions on Power Delivery*, PWRD-2(3):859–870, 1987.

[71] F. A. M. Rizk. Modeling of lightning incidence to tall structures Part I: Theory. *IEEE Transactions on Power Delivery*, 9(1):172–193, 1994. ISSN 08858977. doi: 10.1109/61.277690.

[72] N. Kitagawa and K. Michimoto. Meteorological and electrical aspects of winter thunderclouds. *Journal of Geophysical Research: ...*, 99(D5):10713–10721, 1994. ISSN 0148-0227. doi: 10.1029/94JD00288.

[73] F. Fujii, M. Ishii, M. Saito, M. Matsui, and D. Natsuno. Characteristics of winter lightning threatening wind turbines in coastal area of the sea of Japan. *Electrical Engineering in Japan (English translation of Denki Gakkai Ronbunshi)*, 184(2): 44–50, 2013. ISSN 04247760. doi: 10.1002/eej.22357.

[74] H. Zhou, G. Diendorfer, R. Thottappillil, H. Pichler, and M. Mair. The Influence of Meteorological Conditions on Upward Lightning Initiation at the Gaisberg Tower. In *International Conference on Lightning Protection (ICLP)*, pages 923–926, 2014. ISBN 9781479935444.

[75] J. López, J. Montanyà, M. Maruri, D. De la Vega, J. A. Aranda, and S. Gaztelumendi. Lightning initiation from a tall structure in the Basque Country. *Atmospheric Research*, 117(0):28–36, 2012. ISSN 0169-8095. doi: http://dx.doi.org/10.1016/j.atmosres.2011.07.006.

[76] M. Ishii, M. Saito, F. Fujii, M. Matsui, and D. Natsuno. Frequency of upward lightning from tall structures in winter in Japan. In *2011 7th Asia-Pacific International Conference on Lightning, APL2011*, pages 933–936, 2011. ISBN 9781457714665. doi: 10.1109/APL.2011.6111049.

[77] A. Smorgonskii, M. Rubinstein, F. Rachidi, and G. Diendorfer. Prediction of Lightning Incidence to Tall Structures Before Construction. In *International Symposium on Winter Lightning*, pages 1–3, Joetsu, Japan, 2017.

[78] S. F. Abarca, K. L. Corbosiero, and T. J. Galarneau. An evaluation of the Worldwide Lightning Location Network (WWLLN) using the National Lightning Detection Network (NLDN) as ground truth. *Journal of Geophysical Research Atmospheres*, 115(18):1–11, 2010. ISSN 01480227. doi: 10.1029/2009JD013411.

[79] R. Said and M. Murphy. GLD360 Upgrade : Performance Analysis and Applications. In *24th International Lightning Detection Conference*, 2016.

[80] H. D. Betz. *Lightning : principles, instruments and applications : review of modern lightning research.* Springer, 2009. ISBN 9781402090783.

[81] V. Cooray, M. Fernando, T. S Sørensen, T. Götschl, and A Pedersen. Propagation of lightning generated transient electromagnetic fields over finitely conducting ground. *Journal of Atmospheric and Solar-Terrestrial Physics*, 62(7):583–600, 2000. ISSN 1364-6826. doi: http://dx.doi.org/10.1016/S1364-6826(00)00008-0.

[82] V. Cooray and V. Rakov. On the upper and lower limits of peak current of first return strokes in negative lightning flashes. *Atmospheric Research*, 117(1):12–17, 2012. ISSN 01698095. doi: 10.1016/j.atmosres.2011.06.002.

[83] W. Rison, M. Stock, P. Krehbiel, M. Stanley, H. Edens, and R. Thomas. OBSERVATIONS OF LIGHTNING USING A BROADBAND INTERFEROMETER. In *International Conference on Lightning and Static Electricity*, pages 1–8, 2015.

[84] M. Azadifar, F. Rachidi, M. Rubinstein, M. Paolone, G. Diendorfer, H. Pichler, W. Schulz, D. Pavanello, and C. Romero. Evaluation of the Performance Characteristics of the European Lightning Detection Network EUCLID in the Alps Region for Upward Negative Flashes Using Direct Measurements at the Instrumented Säntis Tower. *Journal of Geophysical Research: Atmospheres, Journal of Geophysical Research. Atmospheres, J. Geophys. Res. Atmos*, 121:595–606, 2015. ISSN 21698996, 2169897x. doi: 10.1002/2015jd024259.

[85] Hans D Betz and Baptiste Meneux. LINET Systems - 10 Years Experience. In *International Conference on Lightning Protection (ICLP)*, pages 1553–1557, 2014. ISBN 9781479935444.

[86] K. L. Cummins, M. J. Murphy, E. Bardo, W. L. Hiscox, R. B. Pyle, and A. E. Pifer. A Combined TOA/MDF Technology Upgrade of the U.S. National Lightning Detection Network. *Journal of Geophysical Research*, 103(D8):9035, 1998. ISSN 0148-0227. doi: 10.1029/98JD00153.

[87] K. L. Cummins, D. Zhang, M.G. Quick, A. C. Garolera, and J. Myers. Performance of the U.S. NLDN during the Kansas Windfarm2012 and 2013 Field Programs. In *International Lightning Detection Conference*, 2014.

[88] University of Wyoming - Global Radio Sounding Data. URL `http://weather.uwyo.edu/upperair/sounding.html`.

[89] National Oceanic and Atmospheric Administration (NOAA). URL `https://ruc.noaa.gov/raobs/`.

[90] Jon W Zeitler and Matthew J Bunkers. Operational Forecasting of Supercell Motion: Review and Case Studies Using Multiple Datasets. *National Weather Digest*, 29:81–97, 2005.

[91] J. Montanya, F. Fabro, O. Van Der Velde, V. March, E. Williams, N. Pineda, D. Romero, G. Sola, and M. Freijo. Global distribution of winter lightning: A threat to wind turbines and aircraft. *Natural Hazards and Earth System Sciences*, 16(6): 1465–1472, 2016. ISSN 16849981. doi: 10.5194/nhess-16-1465-2016.

[92] S. Vogel, J. Lopez, A. C. Garolera, and S. F. Madsen. Lightning Location System Data from Wind Power Plants Compared to Meteorological Conditions of Warm- and Cold Thunderstorm Events. In *International Colloquium on Lightning and Power Systems*, 2016.

[93] N. Takagi and D. Wang. Characteristics of Winter Lightning that Occurred on a Windmill and its Lightning Protection Tower. *IEEJ Transactions on Power and Energy*, 131(7):532–535, 2011. ISSN 0385-4213. doi: 10.1541/ieejpes.131.532.

[94] Y. Yasuda, T. Fujii, K. Yamamoto, N. Honjo, and S. Yokoyama. Classification of wind turbine blade incidents regarding lightning risk management. In *International Conference on Lightning Protection (ICLP)*, pages 986–991, 2014. ISBN 978-1-4799-3544-4. doi: 10.1109/ICLP.2014.6973266.

[95] Ministry of Economy Trade and Industry. Ministry of Economy Trade and Industry, "Document 4.1 - 4.7 in 1st Meeting of Working Group on Icident Correspondence of Structure Enhancement for New Energy Generation Facilities). Technical report, 2014. URL `http://www.meti.go.jp/committee/sankoushin/hoan/denryoku_anzen/newenergy_hatsuden_wg/001_haifu.html`.

[96] M. Ishii and M. Saito. Lightning Electric Field Characteristics Associated With Transmission-Line Faults in Winter. 51(3):459–465, 2009.

[97] A. Sugita and M. Matsui. Lightning Occurrence Characteristics in 2015 in Japan as Observed by the JLDN. In *24th International Lightning Detection Conference (ILDC), San Diego, USA*, 2016.

[98] T. Takeuti and M. Nakano. On Lightning Discharges in Winter Thunderstorm. In *Electrical Processes in Atmospheres*, pages 614–617, Heidelberg, 1976. Steinkopff. doi: 10.1007/978-3-642-85294-7_95.

[99] T. Takeuti, M. Nakano, M. Brook, D. J. Raymond, and P. Krehbiel. The Anomalous Winter Thunderstorms of the Hokuriku Coast. *JOURNAL OF GEOPHYSICAL RESEARCH*, 83(7):2385–2394, 1978.

[100] M. Brook, M. Nakano, P. Krehbiel, and T. Takeuti. The Electrical Structure of the Hokuriku Winter Thunderstorms. *Journal of Geophysical Research*, 87(C2): 1207–1215, 1982.

[101] D. Wang, T. Wu, and N. Takagi. Charge Structure of Winter Thunderstorm in Japan : a Review and an Update. In *International Symposium on Winter Lightning*, pages 1–5, 2017.

[102] T. Suzuki, Y. Matsudo, T. Asano, M. Hayakawa, and K. Michimoto. Meteorological and electrical aspects of several winter thunderstorms with sprites in the Hokuriku area of Japan. *Journal of Geophysical Research Atmospheres*, 116(6):1–19, 2011. ISSN 01480227. doi: 10.1029/2009JD013358.

[103] Kunihiko Miyake, Toshio Suzuki, Masao Takashima, Masao Takuma, and Takashi Tada. Winter Lightning on Japan Sea Coast - Lightning Striking Frequency to Tall Strcutures. *IEEE Transactions on Power Delivery*, 5(3):1370–1376, 1990.

[104] E. Williams. Lightning Activity in Winter Storms: A Meteorological and Cloud Microphysical Perspective. In *4th International Symposium on Winter Lightning*, pages 1–11, 2017.

[105] K Michimoto. The Nature of Winter Thunderstorms in the Hokuriku Coastal Area of Japan. In *International Symposium on Winter Lightning*, number 1, pages 1–5, 2017.

[106] Personal conversation with Nobuyuki HONJO - Wind turbine operator in Japan, J-Power, Tokyo, Japan, 2016-11-30.

[107] S.F. Madsen. *Interaction between electrical discharges and materials for wind turbine blades – particularly related to lightning protection*. Ph.d. thesis, Technical University of Denmark, 2006.

[108] R. B. Standler and W. P. Winn. Effects of coronae on electric fields beneath thunderstorms. *Quarterly Journal of the Royal Meteorological Society*, 105(443): 285–302, 1979. ISSN 00359009, 1477870x.

[109] D. Wang and N. Takagi. Characteristics of winter lightning that occurred on a windmill and its lightning protection tower in japan. *Ieej Transactions on Power and Energy, Ieej Trans. Power Energy*, 132(6):568–572, 2012. ISSN 13488147, 03854213. doi: 10.1541/ieejpes.132.568.

[110] M.A. Uman. *Lightning*. Dover Books on Physics Series. Dover Publications, 2012. ISBN 9780486150956.

[111] D. Jhawar and J. Chalmers. Point-discharge currents through small trees in artificial fields. *Journal of Atmospheric and Terrestrial Physics*, 29(11):1459–1463, 1967. ISSN 00219169.

[112] S. Soula. Transfer of electrical space-charge from corona between ground and thundercloud - measurements and modeling. *JOURNAL OF GEOPHYSICAL RESEARCH-ATMOSPHERES*, 99(D5):10759–10765, 1994. ISSN 2169897X.

[113] N. G. Trinh. Partial Discharge XIX: Discharge in Air Part I: Physical Mechanisms. *IEEE Electrical Insulation Magazine*, 11(2):23–29, 1995. ISSN 08837554. doi: 10.1109/MEI.1995.1025997.

[114] E. Kuffel, W.S. Zaengl, and J. Kuffel. *High Voltage Engineering Fundamentals*. Butterworth-Heinemann, second edi edition, 2000. ISBN 978-0-75-063634-6. doi: 10.1016/B978-075063634-6/50010-1.

[115] S. Chauzy and P. Raizonville. Space-charge layers created by coronae at ground-level below thunderclouds - measurements and modeling. *JOURNAL OF GEOPHYSICAL RESEARCH-OCEANS AND ATMOSPHERES*, 87(NC4): 3143–3148, 1982. ISSN 01480227, 21562202.

[116] S. Chauzy and C. Rennela. Computed response of the space-charge layer created by corona at ground-level to external electric-field variations beneath a thundercloud. *JOURNAL OF GEOPHYSICAL RESEARCH-ATMOSPHERES*, 90(ND4): 6051–6057, 1985. ISSN 2169897X.

[117] R. Morrow. The theory of positive glow corona. *JOURNAL OF PHYSICS D-APPLIED PHYSICS*, 30(22):3099–3114, 1997. ISSN 00223727, 13616463. doi: 10.1088/0022-3727/30/22/008.

[118] S. Dhali and P. Williams. Two-dimensional studies of streamers in gases. *JOURNAL OF APPLIED PHYSICS*, 62(12):4696–4707, 1987. ISSN 00218979, 10897550. doi: 10.1063/1.339020.

[119] P. Vitello, B. Penetrante, and J. Bardsley. Simulation of negative-streamer dynamics in nitrogen. *PHYSICAL REVIEW E*, 49(6):5574–5598, 1994. ISSN 1063651x, 10953787, 1063651X.

[120] D. Ariza, O. Montero, F. Roman, and O. Escobar. Influence of the wind for positive corona in a single-needle-electrode on thunderstorm-like conditions. In *Lightning Protection (XI SIPDA), 2011 International Symposium on*, pages 101–106, Oct 2011. doi: 10.1109/SIPDA.2011.6088455.

[121] E. M. Bazelyan, Y. P. Raizer, N. L. Aleksandrov, and F. D'Alessandro. Corona processes and lightning attachment: The effect of wind during thunderstorms. *ATMOSPHERIC RESEARCH*, 94(3):436–447, 2009. ISSN 01698095. doi: 10.1016/j.atmosres.2009.07.002.

[122] M. Abdel-Salam, H. Abdallah, S. Abdel-Sattar, and M. Farghally. Positive corona in point-plane gaps as influenced by wind. *IEEE Transactions on Electrical Insulation*, EI-22(6):775–786, 1987. ISSN 00189367, 1557962x. doi: 10.1109/TEI.1987.298940.

[123] S. Soula and S. Chauzy. Multilevel measurement of the electric field underneath a thundercloud: 2. Dynamical evolution of a ground space charge layer. *Journal of Geophysical Research*, 96(D12):22327, 1991. ISSN 0148-0227. doi: 10.1029/91JD02032.

[124] E. M. Bazelyan, Y. P. Raizer, and N. L. Aleksandrov. Corona initiated from grounded objects under thunderstorm conditions and its influence on lightning attachment. *Plasma Sources Science and Technology*, 17(2):024015, 2008. ISSN 0963-0252. doi: 10.1088/0963-0252/17/2/024015.

[125] R. B. Toland and B. Vonnegut. Measurement of maximum electric field intensities over water during thunderstorms. *Journal of Geophysical Research*, 82(3):438, 1977. ISSN 0148-0227. doi: 10.1029/JC082i003p00438.

[126] J.S. Townsend. *ELECTRICITY IN GASES*. 1915.

[127] R T Waters and W B Stark. Characteristics of the stabilized glow discharge in air. *Journal of Physics D: Applied Physics*, 8(4):416–426, 2001. ISSN 0022-3727. doi: 10.1088/0022-3727/8/4/014.

[128] P. Levin. Comparison of the donor cell method to other computational techniques for the duct electrostatic precipitator. *JOURNAL OF ELECTROSTATICS*, 25(2): 201–220, 1990. ISSN 03043886, 18735738. doi: 10.1016/0304-3886(90)90027-S.

[129] S. Cristina, G. Dinelli, and M. Feliziani. Numerical computation of corona space charge and v-i characteristic in dc electrostatic precipitators. *IEEE Transactions on Industry Applications)*, 27(1):2007–2013, 1991. ISSN 01972618.

[130] F.W. Peek, editor. *Dielectric phenomena in high-voltage engineering.* McGraw-Hill Book Co, 1929.

[131] F. D'Alessandro. Experimental study of the effect of wind on positive and negative corona from a sharp point in a thunderstorm. *JOURNAL OF ELECTROSTATICS*, 67(2-3):482–487, 2009. ISSN 03043886, 18735738. doi: 10.1016/j.elstat.2008.12.003.

[132] R. T. Waters and W. B. Stark. Characteristics of the stabilized glow discharge in air. *Journal of Physics D (Applied Physics)*, 8(4):416–426, 1975. ISSN 00223727, 13616463. doi: 10.1088/0022-3727/8/4/014.

[133] X. Qie, S. Soula, and S. Chauzy. Influence of ion attachment on the vertical distribution of the electric field and charge density below a thunderstorm X. *Annales Geophysicae*, 12(1):1218–1228, 1994.

[134] K. Georgii. Simulation and analysis of corona currents in large scale coaxial geometry due to triangular voltages, 2013. 52.

[135] G. Raju. *Gaseous electronics : theory and practice.* CRC, Taylor Francis, 2005. ISBN 0849337631, 9780849337635.

[136] L. B Loeb. *Electrical coronas.* University of California Press, Cambridge University Press, 1965.

[137] N.L. Allen, C.F. Huang, K.J. Cornick, and D.A. Greaves. Sparkover in the rod–plane gap under combined direct and impulse voltages. *IEE Proceedings - Science, Measurement and Technology*, 145(5):207, 1998. ISSN 13502344. doi: 10.1049/ip-smt:19982208.

[138] M. Becerra. Corona discharges and their effect on lightning attachment revisited: Upward leader initiation and downward leader interception. *Atmospheric Research*, 149:316–323, 2014. ISSN 01698095. doi: 10.1016/j.atmosres.2014.05.004.

[139] A. Jaworek and A. Krupa. Electrical characteristics of a corona discharge reactor of multipoint-to-plane geometry. *Czechoslovak Journal of Physics*, 45(12):1035–1047, 1995. ISSN 00114626. doi: 10.1007/BF01691996.

[140] H. Hertwig. *Induktivitäten.* Verlag Fuer Radio-Foto-Kinotechnik GmbH, Berlin-Borsigwalde, 1954.

[141] E. B. Rosa. The self and mutual inductances of linear conductors. *Bulletin of Materials Science*, 4(2):301–344, 1905.

[142] N. D. C. W. *Impulse Generator Design for Large Scale Wind Turbine Testing.* Master thesis, Technical University of Denmark, 2015.

[143] I. Gonos, N. Leontides, and F. Topalis. Analysis and design of an impulse current generator. In *WSEAS International Multiconference on Circuits, Systems, Communications and Computers*, pages 3601–3606, 2002.

[144] F. A. Fisher, J. A. Plumer, and R. A. Perala. *Lightning Protection o f Aircraft.* Lightning Technologies Inc, second edi edition, 1999.

[145] T. Naka, N. J. Vasa, S. Yokoyama, A. Wada, A. Asakawa, H. Honda, K. Tsutsumi, and S. Arinaga. Study on Lightning Protection Methods for Wind Turbine Blades. *IEEJ Transactions on Power and Energy*, 125(10):993–999, 2005. ISSN 0385-4213. doi: 10.1541/ieejpes.125.993.

[146] B. L. Maas, N. D. Clements, and V. Rinaldi. Short pulse, peak current ratings of diodes. *IEEE Transactions on Magnetics*, 29(1):1017–1020, 1993. ISSN 0018-9464. doi: 10.1109/20.195719.

[147] Meeting with semiconductor experts from astrol/switzerland (a.stoeckli, f. foster). Meeting/Minutes of Meeting. Accessed: 2015-05-05.

[148] A. D. Stokes and W. T. Oppenlander. Electric arcs in open air. *Journal of Physics D: Applied Physics*, 24(1):26–35, 1991. ISSN 0022-3727. doi: 10.1088/0022-3727/24/1/006.

[149] J. Paukert. The arc voltage and the resistance of LV fault arcs. *International Conference on Switching Arc Phenomena. Part 1: Conference Materials*, 1993.

[150] K. Takaki, D. Kitamura, T. Fujiwara, K. Takaki, T. Murakami, S. Mukaigawa, S. Kohno, Y. Teramoto, I. V. Lisitsyn, and H. Akiyama. The Resistance of a High-Current Pulsed Discharge in Nitrogen . *Japanese Journal of Applied Physics Koichi Takaki and Hidenori Akiyama Jpn. J. Appl. Phys. Jpn. J. Appl. Phys*, 40 (2B):979–983, 2001.

[151] G. A. Mesyats. *Techniques of Shaping High Voltage Nanosecond Pulses, FTD-HC-23-643-70, Foreign Technology Division, Wright Patterson Air Force Base.* PhD thesis, 1971.

[152] F. Heidler. Analytische Blitzstromfunktion zur LEMP- Berechnung, paper 1.9. In *Munich*, pages pp. 63–66, 1985.

[153] R. T. Waters and R. E. Jones. The Impulse Breakdown Voltage and Time-Lag Characteristics of Long Gaps in Air. II. The Negative Discharge. *Philosophical Transactions of the Royal Society of London. Series A, Mathematical and Physical Sciences*, 256(1069):185–212, 1964. ISSN 00804614.

[154] V. R. Larsen and J. Holbø ll. *Parallel coupling and control of a module based impulse generator*. Danish diplom thesis, Technical University of Denmark, 2017.

[155] ABB. Datasheet ABB - HiPak Single DIODE Module - 5SLA 3600E170300, 2012.

[156] TC77/SC 77B. IEC 61000-4-10:2016 Electromagnetic compatibility (EMC) - Part 4-10: Testing and measurement techniques - Damped oscillatory magnetic field immunity test. Technical report, 2016.

[157] C. R. Paul. *Inductance : loop and partial.* Wiley, 2010. ISBN 0470461888.

REFERENCES OF OWN PUBLICATIONS

Journal Papers

[j.1] S. Vogel and J. Holbøll, “Experimental evaluation of discharge characteristics in inhomogeneous fields under air flow,” *IEEE Trans. Dielectr. Electr. Insul.*, *Submitted, waiting for acceptance*

[j.2] S. Vogel, M. Ishii, M. Saito, and D. Natsuno, “Upward lightning attachment analysis on wind turbines and correlated current parameters,” *IEEJ Spec. issue Winter Light.*, *Submitted, waiting for acceptance*

Conference Papers

[c.1] S. Vogel, J. Lopez, J. Holbøll, S. F. Madsen, A. C. Garolera, and K. Bertelsen, “Numerical Simulation of the effect of wind removing the corona space charge over grounded structures under thunderstorm conditions,” *in International Conference on Lightning and Static Electricity (ICOLSE)*, Toulouse, France, 2015.

[c.2] S. Vogel, J. Holbøll, J. López, A. C. Garolera, and S. F. Madsen, “Lightning Attachment Estimation to Wind Turbines by Utilizing Lightning Location Systems,” in *International Lightning Detection Conference (ILDC)*, San Diego, United States, 2016.

[c.3] S. Vogel, J. Lopez, A. C. Garolera, and S. F. Madsen, “Lightning Location System Data from Wind Power Plants Compared to Meteorological Conditions of Warm- and Cold Thunderstorm Events,” in *International Colloquium on Lightning and Power Systems (ICLPS)*, Bologna, Italy, 2016.

[c.4] S. Vogel, J. Holbøll, J. López, A. C. Garolera, and S. Find, “European cold season lightning map for wind turbines based on radio soundings,” in *International conference on lightning protection (ICLP)*, Estoril, Portugal, 2016.

[c.5] S. Vogel, M. Ishii, M. Saito, E. Power, D. Natsuno, and T. Co, “Upward lightning attachment analysis on wind turbines and correlated current parameters,” in *International Symposium on Winter Lightning (ISWL2017)*, Joetsu, Japan, 2017.

[c.6] S. Vogel and J. Holbøll, “Discharge characteristics in inhomogeneous fields under air flow,” in *Nordic Insulation Symposium on Materials, Components and Diagnostics (Nordis)*, Vä sterås, 2017.

[c.7] S. Vogel, M. Ishii, M. Saito, A. Sugita, and D. Natsuno, “Correlations of current parameters with flash density from winter thunderstorms in Japan,” in *International Conference on Lightning and Static Electricity (ICOLSE)*, Nagoya, Japan, 2017.

[c.8] K. Bertelsen, J. Lopez, S. Vogel, S. F. Madsen, and H. I. Park, “Enhanced lightning effects testing for optimized wind turbine reliability,” in *EWEA OFFSHORE*, Copenhagen, Denmark, 2015.

[c.9] S. F. Madsen, S. Vogel, J. Lopez, A. C. Garolera, and K. Bertelsen, “Enhanced Lightning Effects Testing Capabilities,” in *International Conference on Lightning and Static Electricity (ICOLSE)*, Toulouse, France, 2015.

[c.10] A. C. Garolera, S. Vogel, J. Lopez, S. F. Madsen, and K. Bertelsen, “Effect of Local Topography on Lightning Exposure of Wind Turbines,” in *International Conference on Lightning and Static Electricity (ICOLSE)*, Toulouse, France, 2015.

[c.11] M. SAITO, S. Vogel, M. Ishii, “Relationship between aerological data and characteristics of upward lightning hitting wind turbines in winter,” in *International Conference on Lightning and Static Electricity (ICOLSE)*, Nagoya, Japan, 2017

Presentations

[p.1] S. Vogel, S. F. Madsen, and J. Holbøll, “High Current Full Scale Testing as Fundamental Element to Ensure Wind Turbine Reliability,” in *Wind Energy Science Conference (WESC)*, Lyngby, Denmark, June 2017.

[p.2] S. Vogel, “Winter Lightning Exposure to Wind Turbines” at *CIGRE WG C4.36 - Winter Lightning – Parameters and Engineering Consequences for Wind Turbines*, San Diego, United States, April 2016

[p.3] S. Vogel, “Upward Lightning Attachment Analysis on Wind Turbines and Correlated Current Parameters” at *CIGRE WG C4.36 - Winter Lightning – Parameters and Engineering Consequences for Wind Turbines* Joetsu, Japan, April 2017

A THE ELITE PROJECT

Due to the existing limitations of lightning testing of wind turbines, in July 2014, the so called ELITE project was established as a cooperation between DTU and GLPS with the goal to develop next generation lightning test equipment which can be used to create realistic lightning flash sequences as they appear in natural thunderstorms. This PhD thesis is a part of the project which contains the academic findings of the advancements in the field.

The ELITE project was structured with five work packages:

1. **Project management, dissemination and exploration.** The first part of the project focused on starting up the project, the overall management, and the risk management of the project. Responsibilities were assigned to individuals on sides of DTU and GLPS. Furthermore, strategies of exploitation and dissemination of the project results were defined.
2. **Requirements and specification of the novel lightning test equipment** The second work package contained the major research focus of the PhD thesis. Before the novel test generator is designed, the requirements towards the real lightning exposure of wind turbines needed to be defined. At first, lightning data documented in the literature was reviewed from tall structure and wind turbines. Subsequently, lightning data from wind turbines were obtained, analyzed and interpreted. Special focus between the differences of downward and upward lightning strikes is attributed. From the industry, the requirements and trends for the next generations of wind turbine components were determined. The results were used as the input for the design of the new test equipment.
3. **Design of the new lightning test system** The third work package focused on the design of the test system which fulfills the technical and industrial requirements defined by work package 2. Various generator designs concepts were considered and the optimal technology for testing large wind turbine components is selected. Key design attributes in this section are the energy storage, the triggering of the impulse and the creation of an uni-polar current impulse. Furthermore, control, safety and operational features need to be considered.
4. **Prototyping and assembling the test generator** The fourth work package focuses on test and assembly of testing solutions and identifying the practical feasibility of different approaches.
5. **Demonstration of the novel testing solution** The generator concept was tested on industrial size samples in order to verify the testing procedure.

From this structure, the academic focus was set mainly to the second and third work package, whereas work package one was dedicated to administration, and four and five were dedicated mainly to technical implementation of the generator design.

The ELITE project was supported with a collaboration of external wind industry partners. Status meetings were held typically every six months.

Following companies and persons were involved.

1. Dong Energy / Wind turbine operator: Hans V. Erichsen
2. EDP Renewables / Wind turbine operator: Justin Johnsen
3. LM Wind Power / Blade manufacturer: Lars Bo Hansen, Boas Eiriksson
4. Siemens Wind Power / Wind turbine manufacturer: Per Hessellund Lauritsen, Henrik Abild Jensen
5. Vestas Wind System / Wind turbine manufacturer: Anders Niels Hansen

B Current parameters by Berger 1975

Bergers [12] lightning current measurements are recognized as the fundamental source in many lightning related standards. Especially the extreme values (5% and 95%) there can be differences between linearized data and the actual data.

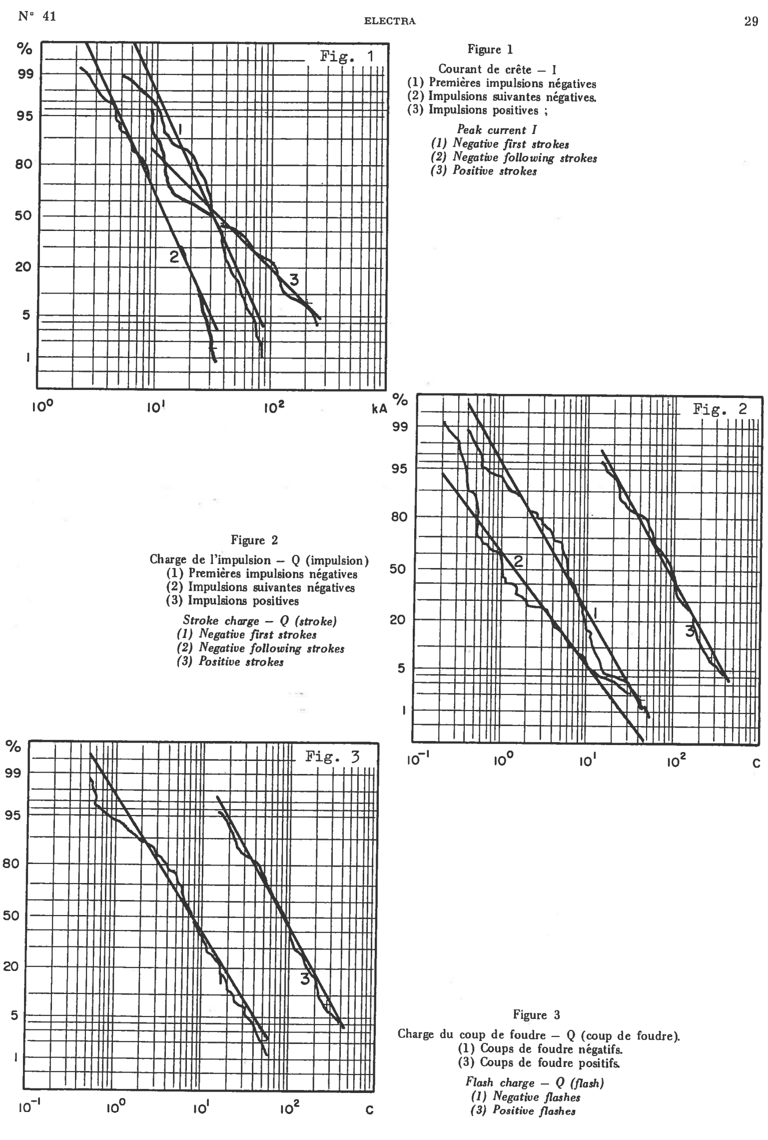

N° 41 ELECTRA 29

Figure 1

Courant de crête — I
(1) Premières impulsions négatives
(2) Impulsions suivantes négatives.
(3) Impulsions positives ;

Peak current I
(1) Negative first strokes
(2) Negative following strokes
(3) Positive strokes

Figure 2

Charge de l'impulsion — Q (impulsion)
(1) Premières impulsions négatives
(2) Impulsions suivantes négatives
(3) Impulsions positives

Stroke charge — Q (stroke)
(1) Negative first strokes
(2) Negative following strokes
(3) Positive strokes

Figure 3

Charge du coup de foudre — Q (coup de foudre).
(1) Coups de foudre négatifs.
(3) Coups de foudre positifs.

Flash charge — Q (flash)
(1) Negative flashes
(3) Positive flashes

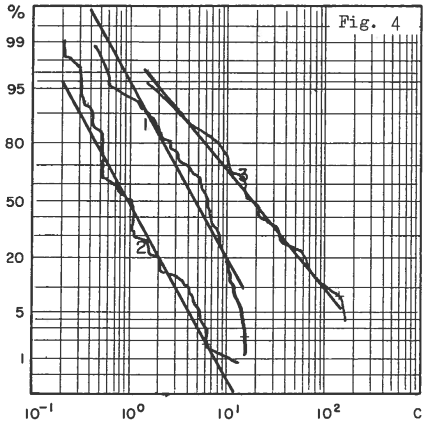

Figure 4

Charge du choc – Q (choc)
(1) Premières impulsions négatives
(2) Impulsions suivantes négatives
(3) Impulsions positives

Impulse charge Q (impulse)
(1) Negative first strokes
(2) Negative following strokes
(3) Positive strokes

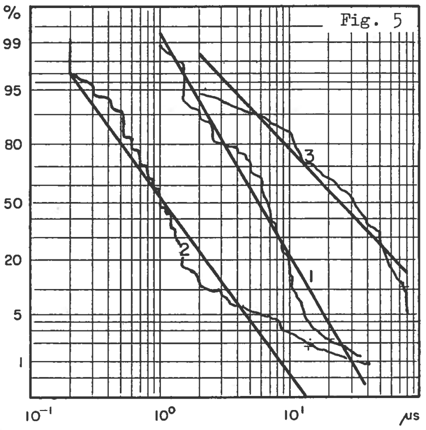

Figure 5

Durée de front – T (front)
(1) Premières impulsions négatives
(2) Impulsions suivantes négatives
(3) Impulsions positives.

Front duration – T (front)
(1) Negative first strokes
(2) Negative following strokes
(3) Positive strokes

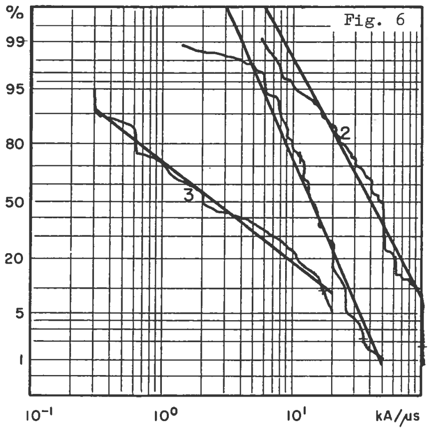

Figure 6

Vitesse de montée maximale du courant – di/dt (raideur de front du courant)
(1) Premières impulsions négatives
(2) Impulsions suivantes négatives.
(3) Impulsions positives.

Maximum rate of rise of current di/dt (current steepness)
(1) Negative first strokes
(2) Negative following strokes
(3) Positive strokes

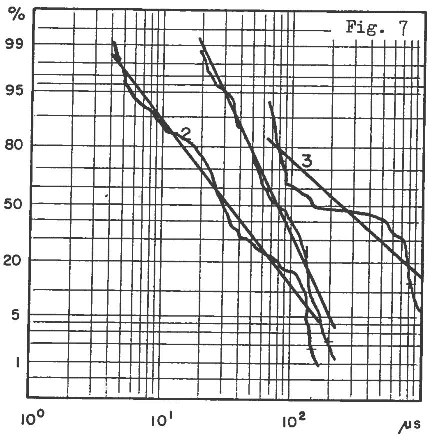

Figure 7

Durée de l'impulsion – T (queue)
(1) Premières impulsions négatives
(2) Impulsions suivantes négatives
(3) Impulsions positives

Stroke duration – T (tail)
(1) Negative first strokes
(2) Negative following strokes
(3) Positive strokes

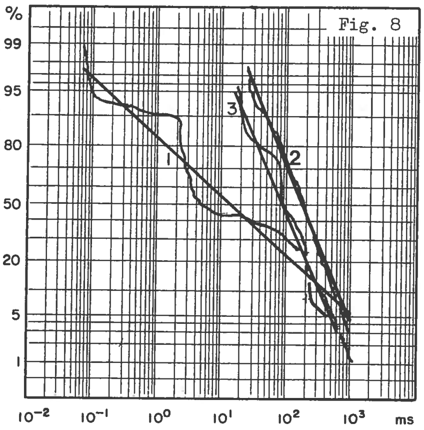

Figure 8

Durée du coup de foudre – T (coup de foudre)
(1) Coups de foudre négatifs y compris les coups de foudre simples.
(2) Coups de foudre négatifs non compris les coups de foudre simples.
(3) Coups de foudre positifs.

Flash duration T (flash)
(1) Negative flashes including single strokes
(2) Negative flashes excluding single strokes
(3) Positive flashes

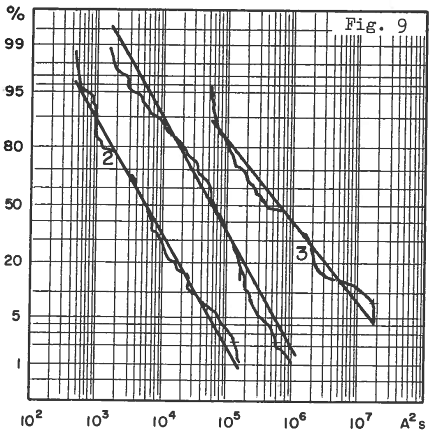

Figure 9

Energie présumée – $\int i^2 \, dt$
(1) Premières impulsions négatives
(2) Impulsions suivantes négatives
(3) Impulsions positives

Prospective energy – $\int i^2 \, dt$
(1) Negative first strokes
(2) Negative following strokes
(3) Positive strokes

C A-BANK FULL-SCALE CIRCUIT MODEL

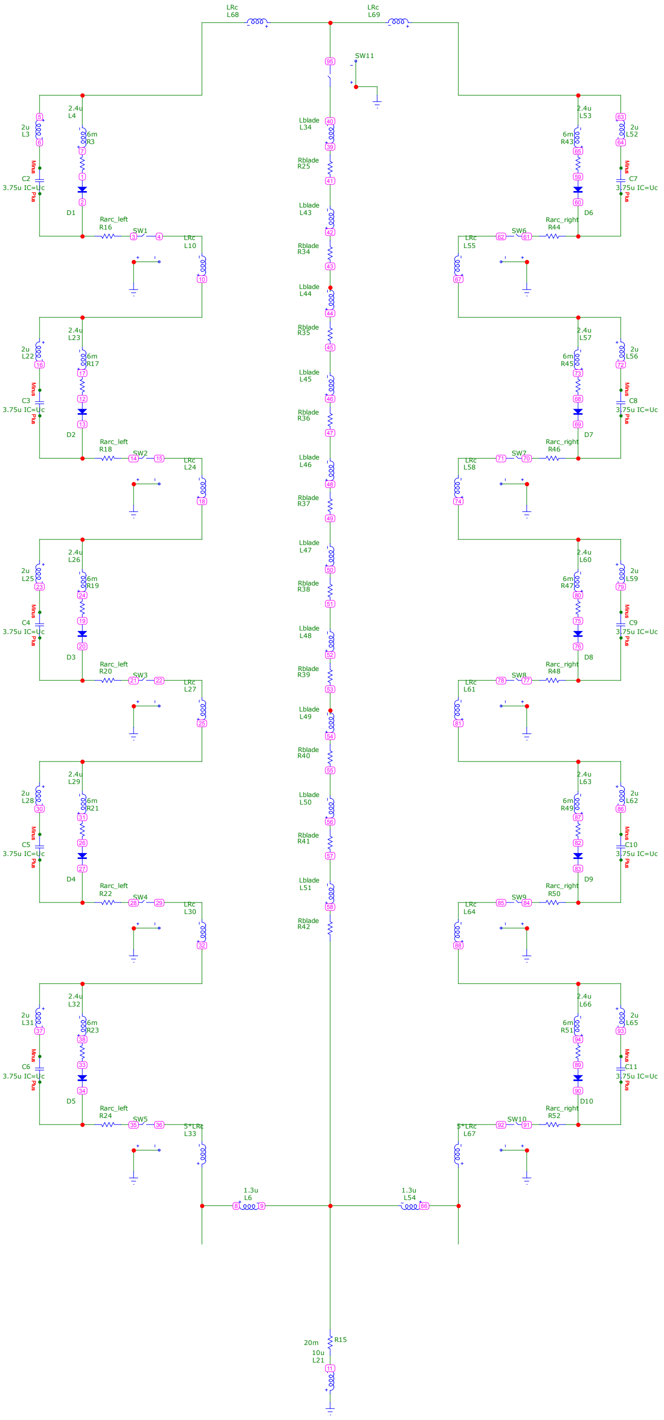

Figure C.1: Circuit model of A-bank during full-scale testing

D PICTURES FROM FULL-SCALE DEMONSTRATION TEST

Figure D.1: The tip of the blade with spark gap and A-bank modules on isolating plastic pallets.

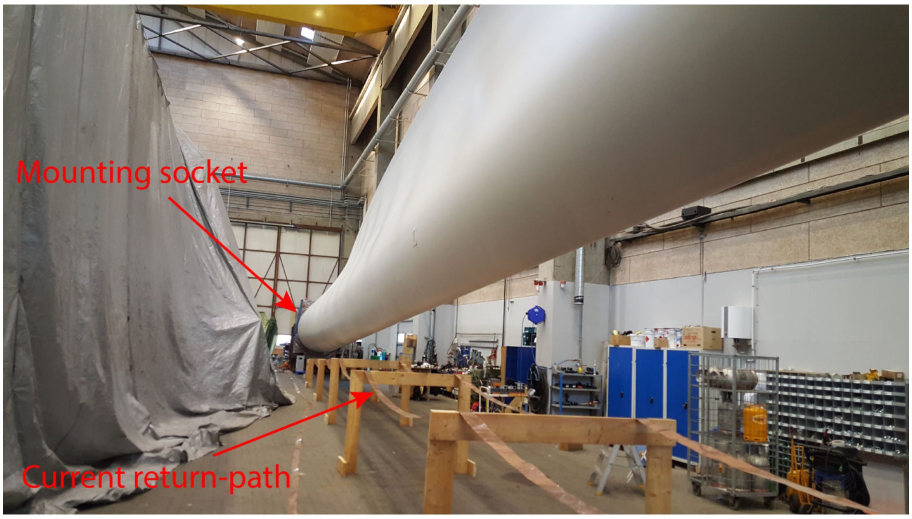

Figure D.2: A picture from the middle to the root end of the blade. The current return path is not optimized to the blade geometry. The mounting socket elevates the blade.

Figure D.3: Picture from the root end towards the tip of the blade. Current measurement is performed with Rogowski coils. The root of the blade is grounded.

Department of Electrical Engineering
Centre for Electric Power and Energy (CEE)
Technical University of Denmark
Elektrovej, Building 325
DK-2800 Kgs. Lyngby
Denmark

`www.elektro.dtu.dk/cee`
Tel: (+45) 45 25 35 00
Fax: (+45) 45 88 61 11
E-mail: `cee@elektro.dtu.dk`